Jet Energy Scale Corrections and their Impact on Measurements of the Top-Quark Mass at CMS

Dissertation

zur Erlangung des Doktorgrades

des Department Physik

der Universität Hamburg

vorgelegt von

Henning Kirschenmann

aus Hamburg

Hamburg

2014

Gutachter der Dissertation:	Prof. Dr. Peter Schleper
	Dr. Isabell-Alissandra Melzer-Pellmann
Gutachter der Disputation:	Jun.-Prof. Dr. Christian Sander
	Prof. Dr. Erika Garutti
Datum der Disputation:	25. September 2014
Vorsitzender des Prüfungsausschusses:	Dr. Georg Steinbrück
Vorsitzende des Promotionsausschusses:	Prof. Dr. Daniela Pfannkuche
Leiter des Fachbereichs Physik:	Prof. Dr. Peter Hauschildt
Dekan der Fakultät für Mathematik, Informatik und Naturwissenschaften:	Prof. Dr. Heinrich Graener

Kurzfassung

Der Endzustand vieler physikalischer Prozesse am „Large Hadron Collider“ (LHC) ist dominiert von Jets, der experimentellen Signatur von Quarks und Gluonen. Die genaue Messung ihrer Energie ist eine Grundvoraussetzung für das Verständnis solcher Prozesse. In dieser Arbeit wird die Bestimmung von Jetenergiekorrekturen bei CMS in Zweijetereignissen erläutert sowie die Untersuchung einer weiteren Korrektur beschrieben, die auf die Verbesserung der Rekonstruktion von b-Jets bei Messungen der Topquarkmasse zugeschnitten ist.

Zweijetereignisse werden untersucht, um die Jetenergieantwort relativ zum zentralen Detektorbereich als Funktion der Pseudorapidität η in Daten und in der Simulation zu bestimmen. Zwei komplementäre Schätzer der Energieantwort werden eingeführt und detaillierte ergänzende Studien durchgeführt, so z.B. eine Analyse der zeitlichen Beständigkeit der Jetenergieantwort. Für die Datennahme im Jahr 2011 werden bei systematischen Unsicherheiten von unter 1% MC/Daten-Unterschiede von weniger als 5% im Bereich des Spurdetektors festgestellt.

Darüber hinaus wird eine Studie von b-Jeteigenschaften in Daten aus dem Jahr 2012 vorgestellt. Die Korrelation verschiedener solcher Eigenschaften mit der Jetenergieantwort wird ausgenutzt, um die Messung der b-Jetenergien zu verbessern. Eine Auflösungsverbesserung von etwa 10% kann erreicht werden und die Auswertung systematischer Unsicherheiten auf die Energieskala von b-Jets (b-JES) weist auf eine Verbesserung von ungefähr 30% hin. Diese zusätzliche Korrektur wird im Rahmen einer bestehenden Messung der Topquarkmasse im Myon+Jets-Kanal angewandt. Sie führt zu einer Verbesserung der statistischen Genauigkeit um etwa 10% und einer Verringerung der systematischen Unsicherheiten im Zusammenhang mit der b-JES von 0.6 GeV auf 0.3 GeV.

Abstract

The final state of many physics processes at the Large Hadron Collider (LHC) is dominated by jets, the experimental signature of quarks and gluons. The precise measurement of jets is a prerequisite to understand these processes. In this thesis, the determination of jet-energy corrections at CMS using dijet events is described, and the investigation of a correction specifically tailored to improve the reconstruction of b-jets in top-quark mass measurements is presented.

Dijet events are used to determine the response relative to the central detector region in data and simulation as a function of the pseudorapidity η. Two complementary response estimators are introduced and detailed supplementary studies, e.g. of the time stability of the response, are performed. For the 2011 data-taking period, the MC/Data differences are found to be below 5% in the tracker-covered detector region with systematic uncertainties of less than 1%.

Furthermore, a study of b-jet properties in 2012 data is presented. The correlation of various such observables with the response is exploited to improve the jet-energy measurement of b-jets. A resolution improvement of about 10% can be achieved, and the evaluation of b-jet specific jet-energy scale uncertainties (b-JES) indicates improvements of about 30%. This additional correction is applied to an existing measurement of the top-quark mass in the muon+jets channel. It leads to a statistical sensitivity improvement of about 10% and a reduction of systematic uncertainties related to the b-JES from 0.6 GeV to 0.3 GeV.

Contents

List of frequently used abbreviations and acronyms

ATLAS	A Toroidal LHC ApparatuS
BJER	B-jet Energy Regression
CERN	European Organization for Nuclear Research
CMS	Compact Muon Solenoid
CMSSW	CMS Software (framework)
CSV	Combined Secondary Vertex (b-tagging discriminator)
ECAL	Electromagnetic Calorimeter
FSR	Final State Radiation
HCAL	Hadronic Calorimeter
HF	Hadronic Forward (calorimeter)
HEP	High Energy Physics
ISR	Initial State Radiation
JEC	Jet Energy Corrections
JER	Jet Energy Resolution
JES	Jet Energy Scale
JSF	Jet (Energy) Scale Factor
LHC	Large Hadron Collider
MC	Monte Carlo (simulation)
MPF	Missing-E_T Projection Fraction
OOT	Out-Of-Time (pileup)
PDF	Parton Distribution Function
PF	Particle Flow
pp	Proton-proton
PRIVATE WORK	Label used for most plots with personal work not made public by CMS
PU	Pileup
RR	Relative response
SM	Standard Model of Particle Physics
SV	Secondary Vertex
TMVA	Toolkit for Multivariate Data Analysis

Coordinate system and units

The coordinate system used by CMS has the origin centred at the nominal collision point inside the experiment. The x-axis is pointing radially inward towards the centre of the LHC, the y-axis is pointing vertically upward. The z-axis points along the beam direction toward the Jura mountains. The azimuthal angle φ is measured from the x-axis in the x-y plane (also called the transverse plane). The polar angle θ is measured from the z-axis. The transverse momentum p_{T}, often used throughout the following, is defined as

$$p_{\mathrm{T}} = p \cdot \sin(\theta) \tag{1}$$

η denotes the pseudorapidity and is defined as

$$\eta = -\ln\left[\tan\left(\frac{\theta}{2}\right)\right] \tag{2}$$

The pseudorapidity ranges from infinity (parallel to the beam axis) to 0 (transverse to the beam axis) in this context. The pseudorapidity for massless particles is equal to the rapidity defined as

$$y = \frac{1}{2}\ln\left[\frac{E+p_z}{E-p_z}\right] \tag{3}$$

where E denotes the energy of the particle and p_z its momentum along the z-axis.

Throughout the thesis, natural units $\hbar = c = 1$ are used. As a consequence, energies, masses, and momenta have the dimension of energy (factors of c are ommited) and are expressed in units of electron volt (eV). Electric charges are given in units of the elementary charge e. Cross sections are given in units of barn with $\mathrm{b} = 10^{-28}\mathrm{m}^2$.

Chapter 1

Introduction

From a historical perspective, there have been many commonly adopted descriptions of the world. The idea of “atomism” (from Greek $\alpha\tau o\mu o\nu$, “indivisible”) appeared at many different places and times throughout human history. Today, we refer to atoms in the context of chemistry. “Our” atoms are indivisible by means of chemical agents and classified in the periodic table of elements as introduced in its current form in 1869/1870 [1, 2]. According to our current understanding of physics, all distinct atoms in the periodic table of elements are made up of smaller units, protons and neutrons in the nucleus, and electrons in the atomic shell. Particle physics takes our understanding of the building blocks of nature to even smaller distance scales, probing what we now understand as the fundamental constituents of matter and their interactions. The current knowledge of particle physics is condensed in the Standard Model of Particle Physics (SM) which has been tested with extreme precision at energy scales between a few eV and several TeV in the last decades.

Operating at the edge of technical feasability, the high-energy frontier in this endeavour is pushed forward in proton-proton (pp) collisions at the Large Hadron Collider (LHC). 2012 marks the year of the discovery of the Higgs boson as the latest impressive confirmation of the SM, established at the general-purpose experiments at the LHC [3, 4].

Experimental signatures vital to the understanding of a large fraction of LHC physics are jets. This term refers to collimated sprays of particles that are initiated by high momentum quarks or gluons, exactly those particles which form the protons and neutrons of atomic nuclei. Quarks and gluons carry a color charge and are subject to the strong interaction as described by Quantum Chromodynamics (QCD). Free quarks and gluons are not observed in nature as the coupling of the strong interaction increases with distance and the formation of a spray of particles is energetically favorable.

At the Compact Muon Solenoid (CMS) experiment at the LHC, the jet constituents traversing the detector leave signals in the tracker, the calorimeter and possibly the muon system. However, the signals in the detector can not be translated directly to the energy of the jet constituents. Effects like a non-linear detector response will generally lead to a mismeasurement if no calibration is applied. Therefore, the study of jet-energy corrections (JEC) is vital for the success of all analyses depending on jets. It is the aim of these corrections to relate the initial particles produced instantly after the *pp* collisions, described by simulations, to the signals measured in the detector.

While the bulk of jet-energy corrections at CMS is derived from simulations, tuned to extensive test beam measurements, only the validation with data makes it possible to rely on the jet-energy corrections for actual physics analyses. A large part of this thesis is devoted to this validation using dijet events, comparing the jet-energy scale at different detector regions relative to a reference region in the central part of the detector. The small discrepancies between the jet-energy scale measured in data and in simulation are corrected for in the form of residual corrections, only applied to data. For combinations of precision measurements in which jet-energy scale uncertainties play a role, it is often necessary to take into account possible correlations of uncertainties between different experiments. An effort to understand such correlations between ATLAS and CMS at a center-of-mass energy of 7 TeV will be summarized here.

A second part of the thesis is devoted to the third generation of quarks, namely the top- and bottom-quarks. The top-quark is by far the heaviest fermion known in the SM and was discovered as late as 1995. Its extremely short lifetime of about $5 \cdot 10^{-25}\,\mathrm{s}$ and high mass of about 173 GeV imply a special role in many aspects of the SM. For example, it is often regarded as a bare quark as it decays before it can hadronize, and virtual loops involving the top quark contribute significantly to higher-order corrections of the W and Z boson mass.

The precise measurement of the top-quark mass is important to understand these higher-order corrections and is an important input to global electroweak fits of the SM. Top quarks almost exclusively decay via the weak interaction into bottom quarks, which themselves hadronize into jets. Such b-jets typically contain B-hadrons with a measurable lifetime, leading to characteristics of these jets that differ from jets initiated by light quarks or gluons. For example, displaced secondary decay vertices and low jet-energy response tails due to neutrinos are typical signatures of b-jets. In measurements of the top-quark mass, systematic uncertainties related to the jet-energy scale of b-jets have been found to be among the leading systematic uncertainties.

In an effort to improve the understanding of these uncertainties, b-jet properties are studied in detail in $\mathrm{t\bar{t}}$ events and an additional jet-energy correction specifically tailored for b-jets is derived. This b-jet energy regression (BJER) exploits the correlation of b-jet properties with the jet-energy response using boosted regression trees to improve the energy resolution and average scale of b-jets. Systematic uncertainties of the b-jet energy scale are compared with and without applying the regression correction. Ultimately, the regression correction is applied to the existing top-quark mass analysis in the lepton+jets channel [5–7] in order to quantify gains in the statistical precision and systematic uncertainties if applying the correction.

This thesis is organized as follows. Aspects of the SM particularly relevant for jets and top quarks are summarized in Chapter 2. The experimental setup of the LHC and of CMS is discussed in Chapter 3.

Chapter 4 reviews the event reconstruction at CMS and puts a focus on an overview of jet-energy corrections at CMS. Personal contributions presented in this chapter are a Particle Flow composition study and the investigation of flavor response uncertainties for the 2012 data-taking period.

The determination of residual corrections from dijet events relative to the central detector region as well as additional studies related to this determination are discussed in Chapter 5. I have extended the existing calibration framework of the University of Hamburg CMS group to determine these corrections and was the main analyst for the 2011 and early 2012 data-taking period, providing this part of the jet-energy corrections to the CMS collaboration. The responsibility to provide these corrections and the corresponding uncertainties using that framework is taken now by other members of the University of Hamburg CMS group. I have continuously supported this work and performed supplementary studies on 2012 data which will also be covered in this context.

Then, a short summary of the discussion on correlations of the systematic jet-energy scale uncertainties between ATLAS and CMS is given in Chapter 6. I have been one of the two CMS contacts in the joint group of both collaborations working out the recommendations.

The studies on the b-jet response and the derivation and application of a b-jet energy regression are summarized in Chapter 7 and the impact of the regression correction on the top-quark mass analysis is discussed in Chapter 8. This work builds upon the existing analyses of the top-quark mass in the University of Hamburg CMS group. I have added more b-jet specific observables to the analysis framework and studied their description in $\mathrm{t\bar{t}}$ events in detail. The training and testing of the BJER has been performed by me, and the resulting correction has been implemented in the existing top-quark mass analysis in the lepton+jets channel to evaluate its impact on the measurement.

Chapter 9 summarizes and concludes the thesis.

Chapter 2

Jets and top quarks in the standard model of particle physics

The Standard Model of Particle Physics (SM) is a description of the world down to extremely small distance scales ($\lessapprox 1\,\mathrm{fm}$). It unifies the previously existing models of electromagnetic, weak, and strong interactions in the framework of relativistic quantum field theories to give a coherent picture of matter and interactions at small distance scales. Textbooks discussing various experimental and theoretical aspects of particle physics in general and the Standard Model in particular include [8–11].

A scheme of the particles considered in the standard model of particle physics is shown in Figure 2.1.[1] There are three generations of matter particles, all spin-1/2 fermions, subdivided into quarks and leptons. The particles in different generations have identical properties, except for their different mass and flavor. In the SM, the interactions between particles are mediated by force-carriers which are bosons with an integer spin.

The weak force, mediated by W and Z bosons, couples to all matter particles. The electromagnetic interaction is mediated by photons and couples to particles with an electric charge. The strong interaction is mediated by gluons and couples to the color charge only found in quarks or gluons.

A detailed account of the "birth" of the SM is given by one of its creators in [13] and outlines the important advances taken in the 1960s and 1970s to arrive at our current understanding of particle physics. The quark model [14, 15] allowed to systematically categorize the "zoo" of hadrons that was discovered at ever more powerful particle accelerators and gave us e.g. the simplified picture of protons and neutrons made up of up/down-type quarks.

The development of the unified electroweak theory [16–20] was awarded with the Nobel prize in 1979 [21] after the experimental confirmation of weak neutral currents [22, 23]. The SM has an outstanding record of confirmed predictions and has been tested to unprecedented precision. For example, the existence of the W and Z bosons, the gluons, the charm, bottom, and top quarks was predicted before their experimental discovery.

---

[1] If no explicit citation is given in the figure captions of this thesis, the plots without a label or with the label "private work" are inofficial, i.e. prepared by the author and not officially approved by CMS.

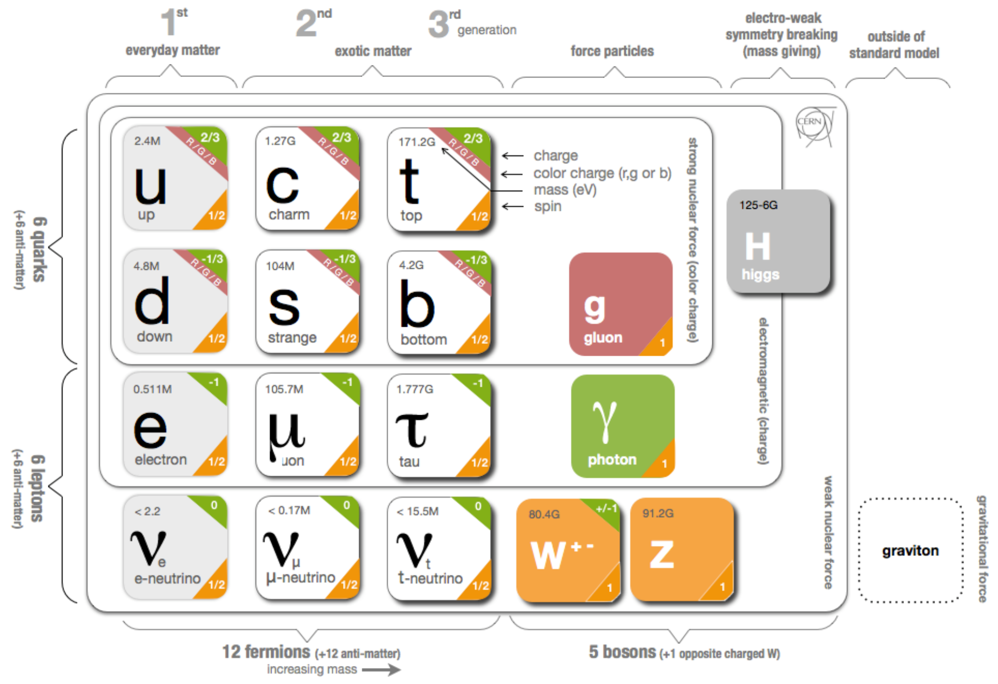

Figure 2.1.: Sketch of the elementary particles considered in the standard model of particle physics. Antiparticles are not explicitly shown, the graviton is a hypothetical particle not covered by SM. Taken from [12]

The latest addition to this decadeslong success is the experimental discovery of the Higgs boson at the LHC [3, 4]. The Higgs boson was postulated as early as in the 1960s to give mass to the a-priori massless gauge bosons (W and Z) in the process of electroweak symmetry breaking. Its prediction was awarded with the Nobel prize last year [24]. Direct searches at LEP, the Tevatron, and LHC had previously ruled out large Higgs mass ranges. Global fits to electroweak precision data [25] narrowed down the expected mass range to low Higgs masses. Such global fits of the standard model [26] are now performed including the measurements of the Higgs boson and provide important consistency checks of the SM.

Even though the Standard Model has proven so successful, it still has some considerable drawbacks and some kind of "new physics" is expected to emerge at the TeV scale, probed by the Large Hadron Collider. For example, astronomical observations like that of galactic rotation curves [27] as early as in the 1930s or the bullet cluster [28] in the early 2000s suggest that in addition to the known luminous matter there is “dark matter” not understood in the SM. The analysis of anisotropies in the cosmic microwave background (CMB) [29] suggests that indeed only a small fraction about 5% of the energy content in the universe is due to baryonic matter described by the SM. Instead, the energy content is dominated by dark energy (proposed to explain the accelerating expansion of the universe) about 65% and dark matter amounting to ≈ 28.3% of the energy content [29].

A popular extension of the SM is the introduction of supersymmetry, described in detail in [30]. For all existing particles, partners are postulated that have a different spin (all fermions have bosonic partners and vice versa). Such supersymmetric extensions often contain dark matter candidates matching the cosmological requirements and give a natural explanation to the "hierarchy problem". In addition, the introduction of new particles at the TeV-scale would make it possible for the coupling constants of the gauge groups relevant in the SM (SU(3), SU(2), U(1)) to meet at extremely high energy scales. This so-called "grand unification" would suggest that at these scales the electroweak and strong interactions could be described by a new common theory with higher-dimensional symmetry groups. Other possible extensions of the SM such as large extra dimensions [31] attempt to adress the weakness of gravity in comparison to other interactions. They predict neutral resonances at the TeV scale whose decays would result in clear signatures in data. Results obtained at the LHC at an increased center-of-mass energy will probe these and many more proposed extensions of the Standard Model by examining phase space regions unaccessible at previous collider experiments and at Run I of the LHC.

The search for new physics beyond the SM in hadronic final states critically relies on the precise understanding of the properties of jets. The detailed study of properties of the top-quark and their comparison to SM predictions can hint at new physics. The production of $\mathrm{t\bar{t}}$ resonances is a signature found in several SM extensions. So even though this thesis is not devoted to searches for physics beyond the SM, the ever more precise studies of SM physics are a prerequisite of such searches. Jets and the top-quark phenomenology will be discussed in more detail in the following. A fairly detailed account of jet physics and calorimetry has also been given in [32].

2.1. Jets

High-energy phenomena in Quantum Chromodynamics (QCD) [33,34] are discussed in terms of quarks and gluons. However, quarks and gluons are not observed freely in nature. Instead, the process of hadronization leads to a collimated spray of color neutral hadrons which is referred to as jet. The definition of jets and their connection to the initial partons is conceptually difficult and has been a matter of study for over 30 years [35].

Due to the running of the strong coupling constant α_s, which becomes large at low energies, perturbation theory is not applicable for the full evolution of the high-energy partonic process to the end of jet formation. Instead, a factorized approach as depicted in Figure 2.2 is used for the description of such processes. It relies on the factorization theorem [36], according to which the perturbative description of the high energy partonic processes can be combined with phenomenological models of the subsequent low-energy processes. Comprehensive reviews of this factorized approach and jet physics in general can be found e.g. in [37–40].

In this factorized approach, two constituents (quarks or gluons) of the colliding protons interact with each other in a hard interaction such that perturbation theory

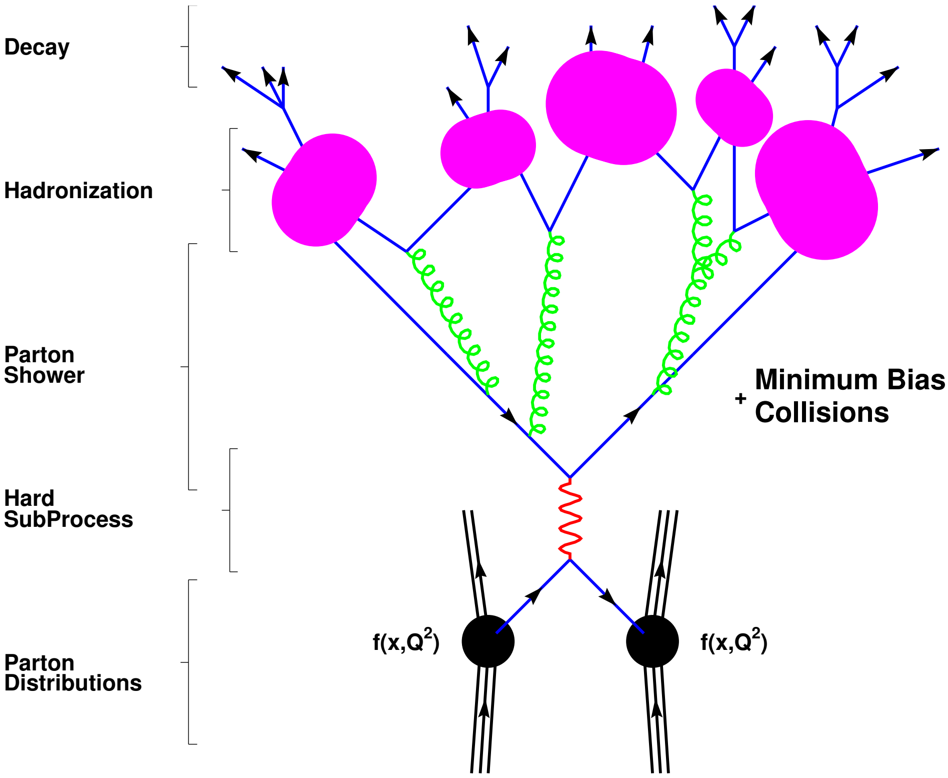

Figure 2.2.: Schematic illustration of the basic structure of event generation in pp collisions, taken from [41]

can be used to calculate the matrix element. The probability that determines which of the constituents interact, is governed by the empirically determined parton distribution functions (PDF). The outgoing partons will typically radiate further partons in a process called parton showering. In the process of hadronization the partons combine to colorless hadrons, such that only color neutral objects are observed in nature (color confinement). Most of the heavier hadrons have a short life time and decay quickly so that jets observed in particle physics detectors consist of relatively few particle types. Each of the above steps is described in more detail in the following.

2.1.1. Proton structure: Parton distribution functions

In contrast to lepton colliders in which the initial state is well defined by the beam energy and the colliding elementary particle, the initial state of the fundamental particles in pp collisions is not as well defined. Protons are compound objects and their constituents (valence quarks, sea quarks, and gluons) interact when jets are formed. This is described by parton distribution functions (PDF) $f_i(x, Q^2)$ for a parton of type i, which depend on the momentum fraction x of the interaction parton and the momentum transfer squared Q^2.

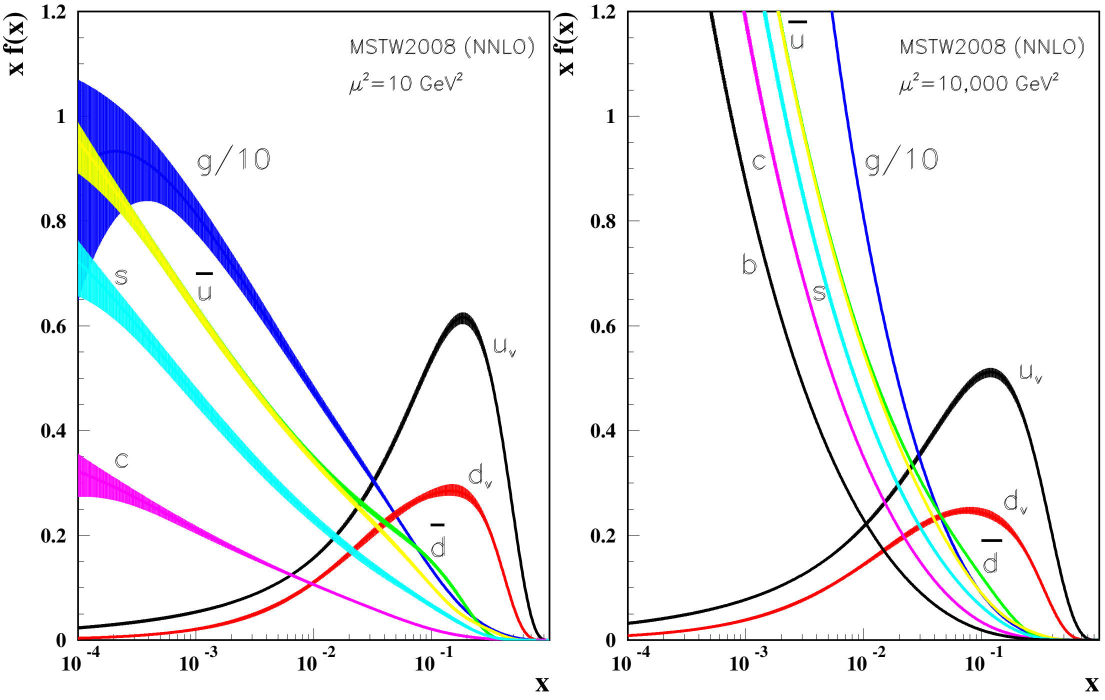

Figure 2.3.: Distributions of x multiplied by the unpolarized parton distributions $f(x)$ (where $f = u_v, d_v, u, d, s, c, b, g$ and their associated uncertainties using the NNLO MSTW2008 parameterization at a scale $\mu^2 = 10\,\mathrm{GeV}^2$ and $\mu^2 = 10000\,\mathrm{GeV}^2$); [40]

The PDFs can not be calculated by perturbative QCD and are instead obtained using experimental data from different experiments and processes, such as results from deep inelastic scattering (DIS) at HERA which cover a large phase space in Q^2 and x. The factorization scale μ separates the proton non-perturbative dynamics absorbed in the PDFs from the perturbative calculation of the cross section. Its choice is arbitrary in the range between about 1 GeV, at which the perturbative treatment becomes unreliable, and Q^2. The evolution between different scales is described by the DGLAP equations [42–44]. PDFs experimentally determined at a given x and Q^2 can be evolved to higher Q^2 values.

Most of the collaborations compiling sets of PDFs, such as CTEQ [45] and MSTW [46], use experimental data from various collider experiments and different processes to constrain the PDFs in global fits. HERAPDF [47] relies on the well understood DIS data obtained at HERA. As a widely used example, the MSTW parameterization is depicted in Figure 2.3 for two different scale parameters μ^2 (Q^2). For high-momentum-transfer reactions, the PDFs are dominated by gluons leading to the fact that many physics processes observed at the LHC are gluon-dominated, such as the production of QCD-jets or top quarks.

The reach of searches for high mass resonances, signatures of beyond-the-SM-physics, at the LHC depends on the probability to find partons with a sufficiently high x to initiate the production. These parton luminosities depend on the center-of-mass energy: An increased center-of-mass energy results in a significantly enhanced sensitivity due to the increased production rates. The ratios of parton luminosities in the 2010/2011 and 2015 data-taking period relative to the LHC energy in 2012 as function of the parton-parton center-of-mass energy is depicted in Figure 2.4. It indicates the significantly enhanced reach of such searches in the upcoming LHC run.

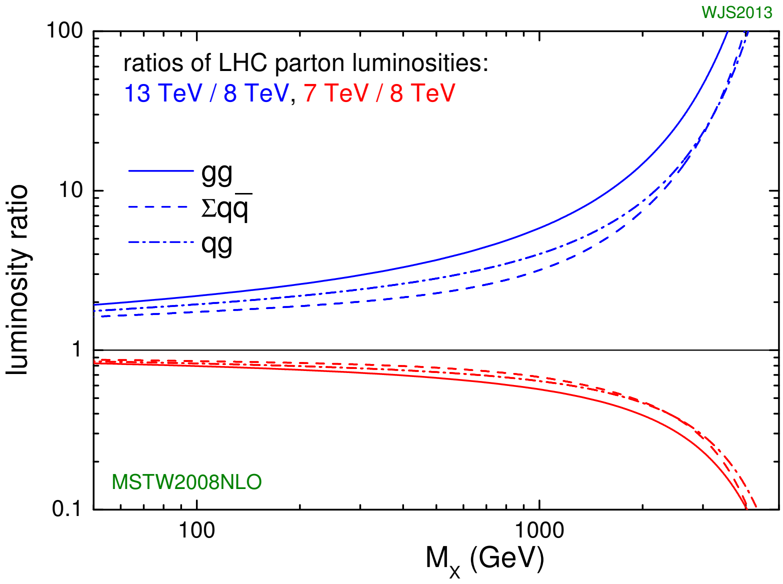

Figure 2.4.: Ratio of parton luminosities at different center-of-mass energies of the LHC. An increased center-of-mass energy results in significantly parton luminosities for high mass resonances. Taken from [48]

2.1.2. Hard interaction of partons

The factorization theorem of QCD [36] allows to separate high-Q^2 (perturbative) and low-Q^2 (absorbed in parton distribution functions) processes and calculate the cross section of physics processes as

$$\sigma_{pp\to kl} = \sum_{i,j} \int dx_1 dx_2 f_i^1(x_1, Q^2) f_j^2(x_2, Q^2) \hat{\sigma}_{ij\to kl} \tag{2.1}$$

with the longitudinal momentum fraction of the interacting partons $x_{1/2}$, the momentum transfer Q^2, the perturbative QCD cross section $\hat{\sigma}_{ij\to kl}$ for the process $ij \to kl$, and the parton distribution functions $f_i^{1/2}(x, Q^2)$ for colliding beams 1 and 2 [38].

Many different processes contribute to the inclusive jet production. Some of the leading order dijet production Feynman diagrams are depicted in Figure 2.5, while higher

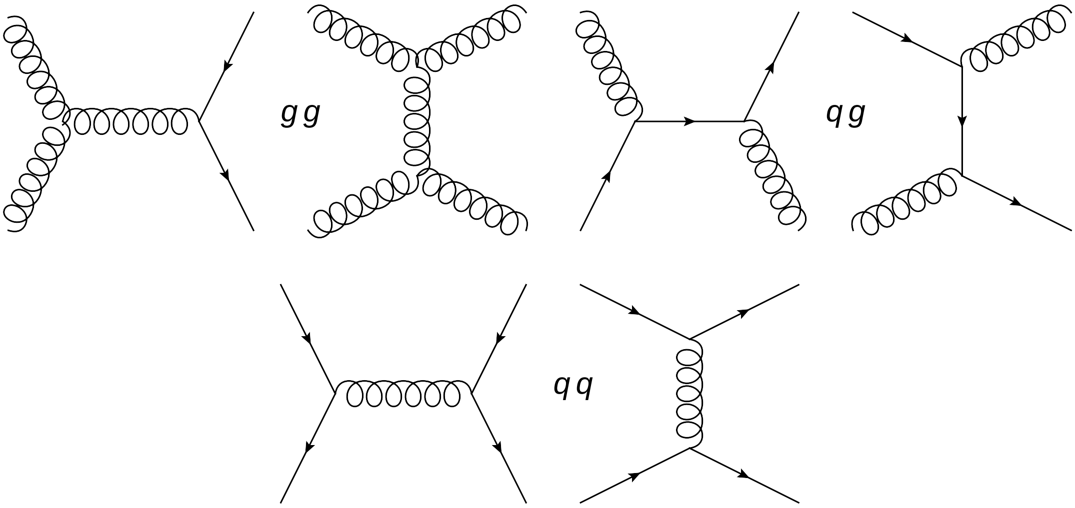

Figure 2.5.: Feynman diagrams of some of the leading order 2 → 2 QCD processes contributing to jet production

order diagrams with additional hard radiations result in higher jet multiplicities. The partons resolved from the incoming protons can be gluons (dominating the PDFs at low x) or quarks. While the inclusive jet cross section is dominated by gg as initial partons, it becomes dominated by qq at high jet p_{T} as depicted in Figure 2.6.(a). General purpose Monte Carlo event generators such as PYTHIA [49] or HERWIG [50] have the analytical formulae for a large number of physics processes implemented. For the general purpose event generators the implementation is often limited to lowest order calculations, but they can be interfaced with specialized matrix element generators [41] such as ALPGEN [51] or MadGraph [52] that include Next-to-Leading Order (NLO) or even higher-order perturbative calculations. The good description of the inclusive jet production in hadron-introduced processes at different center-of-mass energies is shown in Figure 2.6.(b), which compares the measured cross sections at the LHC and previous experiments with theory expectations.

2.1.3. Parton showering and hadronization

The hard scattering discussed for the dijet production involves 2 → 2 processes. Higher jet multiplicities can either be modeled by calculating higher order diagrams or by introducing the parton shower concept as adopted by current general purpose Monte Carlo (MC) event generators: The radiation of gluons from quarks and the splitting of gluons into $q\bar{q}$-pairs is approximated using the DGLAP-equations [44] which give the probability for a parton to branch.

This branching can occur iteratively, leading to softer and softer splittings. As the description becomes invalid for too-soft splittings (α_s approaching 1), a lower cutoff-scale is introduced at the order of $Q^2 = 1\,\mathrm{GeV}^2$, and the branching probabilities are weighted with the Sudakov form factor in order to avoid unphysical behavior. The parton

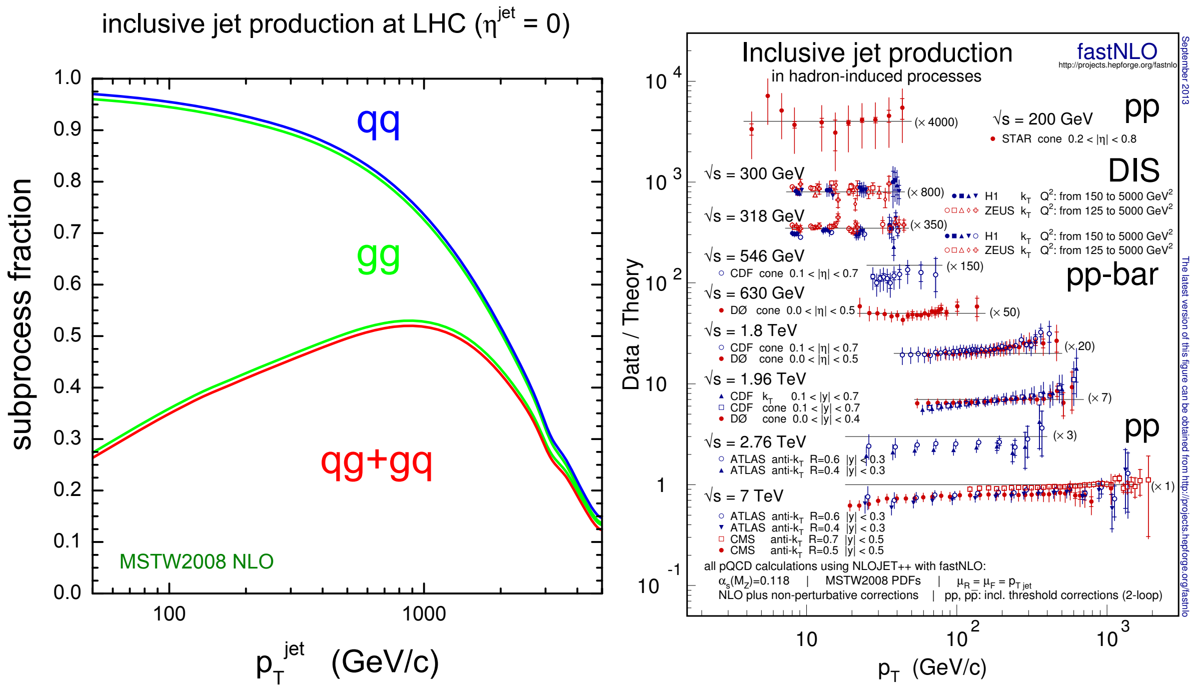

(a) (b)

Figure 2.6.: (a) Parton subprocess decomposition of the inclusive jet cross sections at the LHC: At low transverse momenta, the jet production is dominantly induced by gluons. At transverse momenta well above 1 TeV, the production is dominated by quarks in the initial state. Taken from [48]; (b): Ratios of experimental data and theory predictions for inclusive jet cross sections as a function of the transverse momentum of the jet. The different ratios are scaled by arbitrary factors as indicated in parentheses. Theoretical predictions at Next-to-Leading Order accuracy with parameters as given at the bottom of the plot, updated version of [53]. Taken from [54].

showering is described in more detail in [?, 49]. In case of 2 → 2 processes as considered for the dijet production, no particular matching procedure between the leading order matrix element and parton shower is needed. However, when using matrix element generators like MadGraph, e.g. for the production of top quark MC samples with high jet multiplicities, a specific matching procedure to avoid double counting is needed.

For increasing distances resulting in large α_s, the parton shower approach is not applicable anymore. Similarly to the approach of parton distribution functions to describe the initial state of the reaction, the transition from a few-parton to the many-hadron state (particle jet) is described using phenomenological models of the haronization.

Two different approaches are widely used in general purpose MC event generators, namely the string model by pythia and the cluster model by herwig. The string hadronization model is centered on a description of the color field between partons that are increasing their distance from each other. As a consequence of the confinement inherent to QCD, the assumed potential increases linearly with the distance, and it becomes energetically favorable for the color flux tubes between the partons to break up by producing additional $q\bar{q}$-pairs. The pairs are produced according to the tunnelling probability $\exp(-\pi m_{q,\perp}^2/\kappa)$, which depends on the transverse mass squared $m_{q,\perp}^2 \equiv m_q^2 + p_{q,\perp}^2$, where $p_{q,\perp}^2$ is the non-perturbative transverse momentum with an average value of $\approx (250\ \text{MeV})^2$, and the string tension $\kappa \approx 1\,\text{GeV/fm}$. The behavior is governed by the string-fragmentation function $f(z)$ with two empirical parameters that are adjusted to agree with data. This model suppresses the production of heavy quarks (mass in tunnelling probability) and is thus adapted to be in agreement with experimental observations.

The cluster hadronization model is used by herwig. It takes the remaining gluons at the end of the parton shower evolution and splits them non-perturbatively into quark-antiquark pairs, assuming a local compensation of color. Clusters of quarks and antiquarks with a typical mass of a couple of GeV are formed and then decay directly into two hadrons (or to a single hadron, when they are too light, or into two clusters when they are too heavy). The cluster hadronization has a very compact description with a few parameters. The different implementations of parton shower and hadronization models are subject to tuning of the event generators to experimental measurements and are main reasons for differences in the description of physics processes.

The hadronization process results in a large variety of different hadron species. Most of the hadrons have a very short lifetime and their decay is handled directly by the MC event generators using decay tables for particles with an average decay length of $c\tau < 10\,\text{mm}$.

2.1.4. Underlying event

Any processes other than the hard interaction as discussed above contributes to the underlying event (UE). It is caused by the proton remnants that carry a net color charge or by additional multiple parton interactions (MPI) initiated by partons other than those involved in the hard interaction. This underlying event typically adds a significant number of soft particles to the event, increasing in multiplicity and average p_T with center-of-mass energy and momentum transfer Q^2 of the reaction. Studies of the underlying event activity at CMS showed average contributions of 1–2 GeV per unit of pseudorapidity and per radian to jets with p_T up to 100 GeV at 7 TeV [55].

2.2. Top quark

The top-quark is the heaviest quark in the SM and has, often connected to its high mass, a number of unique properties. Comprehensive reviews of top-quark physics are given in [56–58].

The existence of a third generation of quarks, namely the top-quark and the bottom quark, was theorized in 1973 [59] to explain the CP violation observed in kaon decays. While the bottom quark as down-type quark of the third generation was found in 1977 [60], it took about two decades to discover the top-quark.

After the discovery and precise measurement of the W and Z bosons, electroweak precision fits indicated a very high top-quark mass as shown in Figure 2.7. This meant that the center-of-mass energy available in $\mathrm{e}^-\ \mathrm{e}^+$ colliders did not suffice to produce $\mathrm{t\bar{t}}$ pairs. Instead, the Tevatron experiments put more and more stringent lower bounds on the top-quark mass.

In 1995, 22 years after its prediction, the top-quark was established by both Tevatron experiments, CDF and D0 [62, 63]. Since then, the phenomenology of the top-quark could be studied in great detail in $p\bar{p}$ collisions. Since the start of LHC operations, top-quarks are produced at very high rates as shown in Figure 3.3, making the LHC known as a “top-quark factory” [64]. With the abundance of top-quarks produced in LHC pp collisions, even more detailed studies of the top-quark properties are possible.

2.2.1. Production

In hadronic collisions, top-quarks are most often produced in $\mathrm{t\bar{t}}$ pairs by the strong interaction. The production of single top-quarks is mediated by the weak interaction. Just as in the case of jet production, the initial state of the protons is approximated by the parton distribution functions and the hard scattering can be calculated perturbatively according to the factorization theorem [36].

Leading order Feynman diagrams for the $\mathrm{t\bar{t}}$-production are shown in Figure 2.8. At the Tevatron about 85% of the total cross section is due to $q\bar{q}$ annihilation. This is due to the relatively high momentum fraction $x = 2 \cdot m_\mathrm{t}/\sqrt{s} \approx 0.2$ needed for the production at the Tevatron center-of-mass energy of about 2 GeV. At this x, the valence quarks

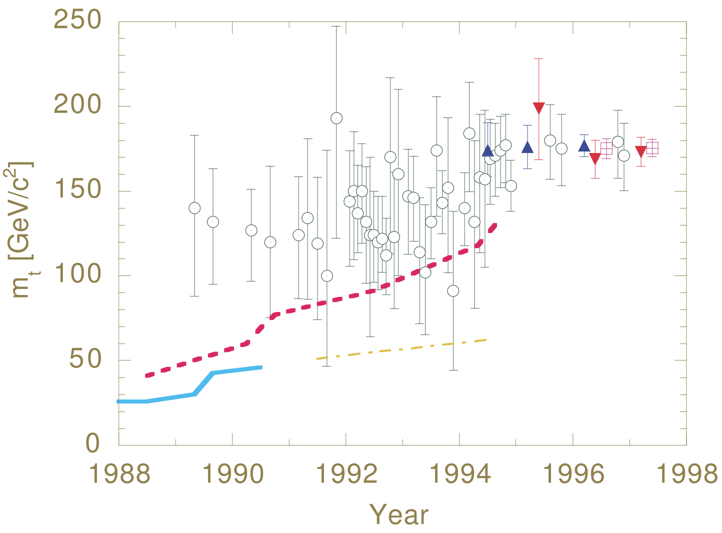

Figure 2.7.: History of the limits on or measurements of the top-quark mass: (○) Indirect bounds on the top-quark mass from precision electroweak data; (⊟)World-average direct measurement of the top-quark mass (including preliminary results); (▲) published CDF and (▼) D0 measurements; Lower bounds from $p\bar{p}$ colliders $Sp\bar{p}S$ and the Tevatron are shown as dash-dotted and dashed lines, respectively, and lower bounds from e^- e^+ colliders (Petra, Tristan, LEP and SLC) are shown as a solid light blue line. Taken from [61].

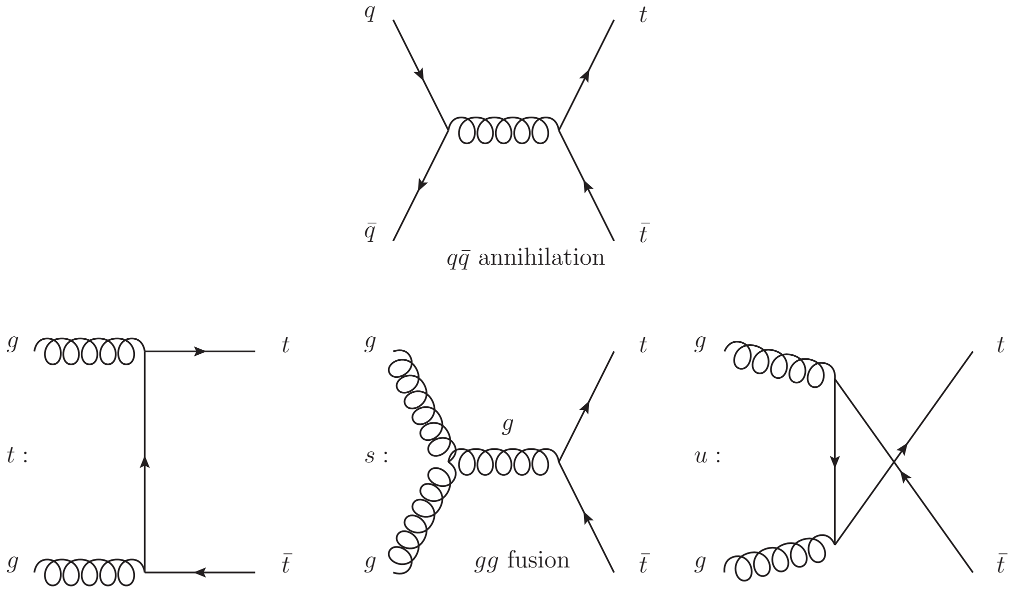

Figure 2.8.: Leading order Feynman diagrams for the production of $t\bar{t}$ pairs via $q\bar{q}$ annihilation and gg fusion (t, s, and u channel)

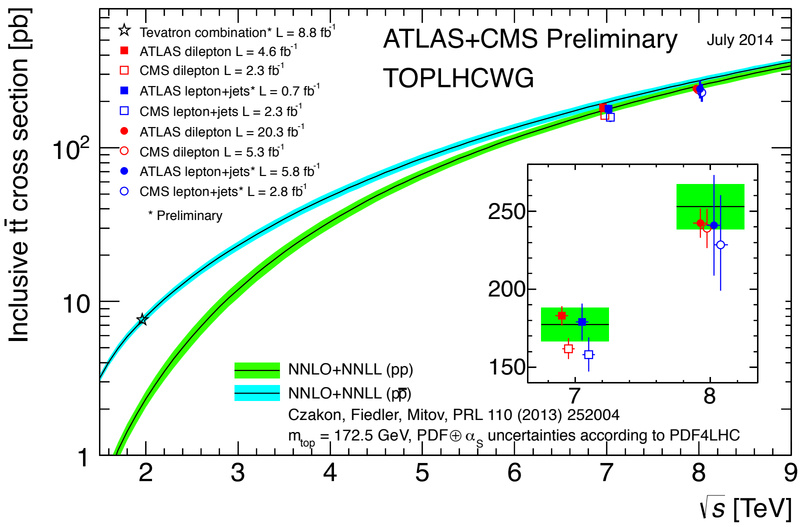

Figure 2.9.: Summary of LHC and Tevatron measurements of the top-pair production cross-section as a function of the center-of-mass energy compared to the NNLO QCD calculation complemented with NNLL resummation (top++2.0). The theory band represents uncertainties due to renormalization and factorization scale, parton density functions and the strong coupling. The measurements and the theory calculation is quoted at $m_{\mathrm{t}} = 172.5\,\mathrm{GeV}$. Measurements made at the same center-of-mass energy are slightly offset for clarity. [66]

of the p ($\bar{p}$) dominate the PDFs. The gg fusion dominates the production at higher center-of-mass energies in pp collisions at the LHC for relatively low invariant masses $m_{\mathrm{t\bar{t}}}$. In contrast to the Tevatron $p\bar{p}$ collisions providing $\bar{q}$ valence quarks from the antiprotons, the production via $q\bar{q}$ annihilation is suppressed at the LHC and only becomes relevant for high $m_{\mathrm{t\bar{t}}}$.

The partonic cross section for $\mathrm{t\bar{t}}$ production depends on the scale at which it is evaluated, the center-of-mass energy and the top-quark mass. The theoretical prediction at next-to-next-to leading order (NNLO) with next-to-next-to-leading-log (NNLL) soft gluon resummation (evaluated assuming $m_{\mathrm{t}} = 172.5\,\mathrm{GeV}$) is compared to experimental measurements at 1.98 TeV, 7 TeV, and 8 TeV in Figure 2.9. At 8 TeV, the predicted cross section is $\sigma_{\mathrm{t\bar{t}}} = 251.7^{+6.4+6.3}_{-8.6-6.5}\,\mathrm{pb}$ where the first uncertainty is due to scale dependence and the second due to PDF uncertainties [65]. The predictions at all center-of-mass energies are in good agreement with the available measurements.

2.2.2. Decays

Within the SM, top-quarks decay almost exclusively via the weak interaction into a bottom quark and a W boson. The corresponding matrix element $V_{tb} \approx 1$ in the quark mixing or CKM matrix [59]. Direct decays into the first two generations (down/strange)

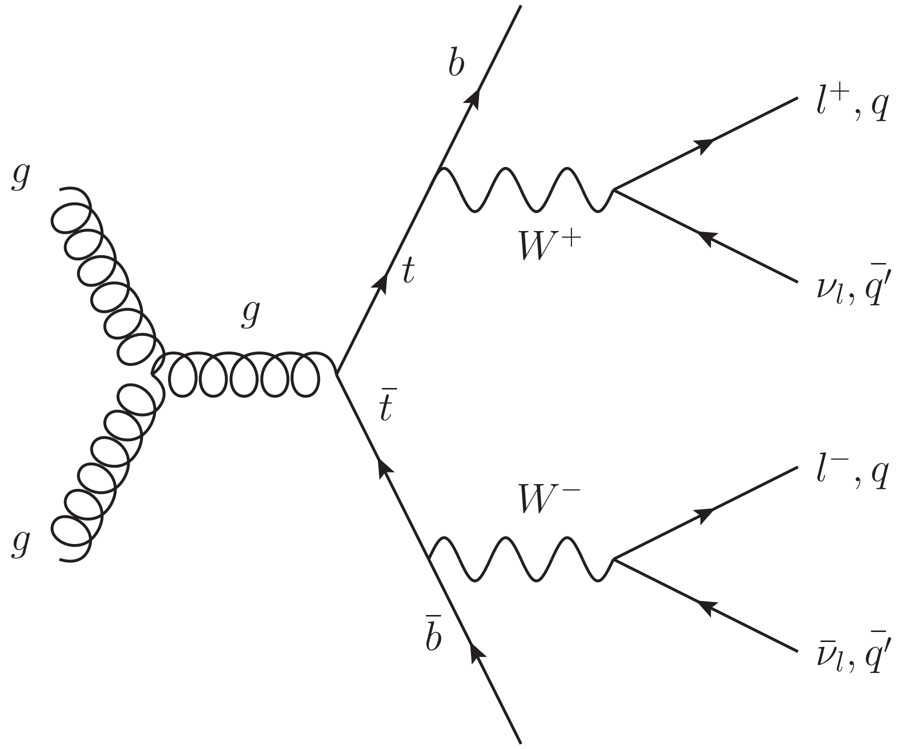

Figure 2.10.: Sample Feynman diagram of the t$\bar{\text{t}}$ production via gg fusion and subsequent decay, indicating the different W boson decay possibilities

are strongly CKM-suppressed. Due to its very high mass the top-quark decays into a real W boson, leading to a small decay width and thus an extremely short lifetime of $\tau_t \approx 5 \times 10^{-25}$ s. This is much shorter than the characteristic time of hadronization $\tau_{had} \approx 1/\Lambda_{QCD} \approx 3 \times 10^{-24}$ s.

As a consequence, no bound states with the top-quark such as top mesons or baryons can form and the top-quark can be treated as a bare quark in perturbative calculations of its properties. Due to this feature, the spin orientation is passed on to the decay products and leads to angular distributions of the decay products specific for the initial spin configuration.

A t$\bar{\text{t}}$ event is typically characterized by two b quarks and two W bosons. Each of the W bosons either decay leptonically into a lepton and its corresponding neutrino or into a pair of quarks as depicted in Figure 2.10. The hadronic decay is enhanced by the three different color charges carried by the quarks as illustrated in Figure 2.11 summarizing the decay channels and branching fractions of the t$\bar{\text{t}}$ pair decays.

The all-jets, channel has the largest branching ratio of 45.7%. However, such top-quark events are generally hard to distinguish experimentally from the huge background of QCD multijet events.

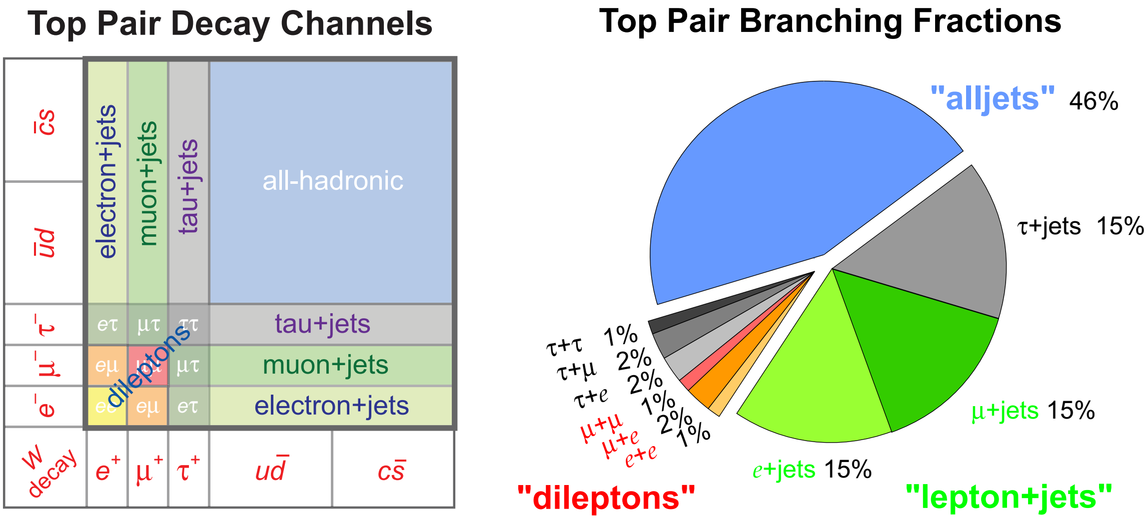

Figure 2.11.: Visualization of the top pair decay channels and branching fractions [67].

The dilepton channel has a very clean signature due to the presence of two isolated leptons which help to tell them apart from QCD events. Disadvantages for analyses of this decay channel are the relatively small branching ratio of $\approx 4.8\%$ (when neglecting τ decays) and the lack of fully constrained kinematics due to the two neutrinos produced by the leptonically decaying W bosons.

The lepton+jets channel is regarded as a good compromise in terms of background contamination and branching fraction. Due to practical considerations linked to the difficult identification of τ leptons, most analyses focus on the muon+jet and electron+jet channels with a branching ratio of 14.6% each. Background processes with similar signatures include W/Z+jets, single top-quarks, and QCD multijet events.

2.2.3. Mass

The special role of the top-quark in the SM is mainly linked to its high mass, being a factor of about 40 times heavier than the bottom quark, the next heaviest quark. However, the exact top-quark mass definition is not universal. Due to its extremely short lifetime, it is usually interpreted as a bare quark whose on-shell or pole mass is given by the real part of the top-quark propagator. However, the bottom quark resulting from the top decay carries on the color charge and hadronizes. This leads to an intrinsic ambiguity of the pole mass of the order of $\Lambda_{QCD} \approx 200\,\text{MeV}$.

Most of the experimental techniques to determine the top-quark mass at hadron colliders are based on the invariant mass of the top-quark decay products and rely on MC simulations for calibration. Their results are commonly identified with the pole mass. However, with systematic uncertainties of these experimental measurements below 1 GeV [7, 70–72], any ambiguities in the definition become more and more important.

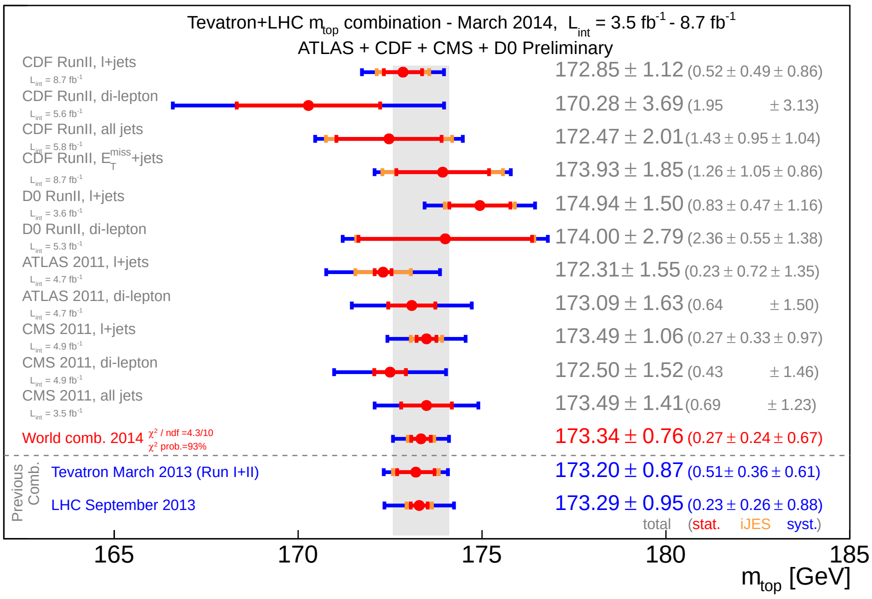

Figure 2.12.: Input measurements of the top-quark mass and the result of the March 2014 world combination, compared with the Tevatron and LHC combined mass values [68, 69]. Taken from [70]

Complementary approaches like that of determining the pole mass directly from the $t\bar{t}$ production cross section [73] are important cross-checks and help to reduce remaining ambiguities.

The results of the first world combination of the top-quark mass considering Tevatron and LHC results using standard techniques is shown in Figure 2.12.

2.2.4. Tests of the SM and searches for physics beyond the SM

Due to its high mass, close to the scale of electroweak symmetry breaking, the Yukawa coupling is close to one, closely intertwining the now established Higgs boson and the top-quark. For example, the Higgs boson is predominantly produced in gg fusion involving a top-quark loop at the LHC and higher-order corrections of many processes depend on virtual top-quark loops.

With the final puzzle piece – the Higgs boson – put in place, consistency tests of the SM such as [26] can now use the measured Higgs-boson mass and other measured SM parameters to predict the W-boson and top-quark mass as shown in Figure 2.13.(a). The experimental measurements and the prediction from other SM parameters agree well within the given uncertainties. The p-value of 0.20 for the the SM fit in [74], including the experimental information on the Higgs-boson mass, indicates the self-consistency of the

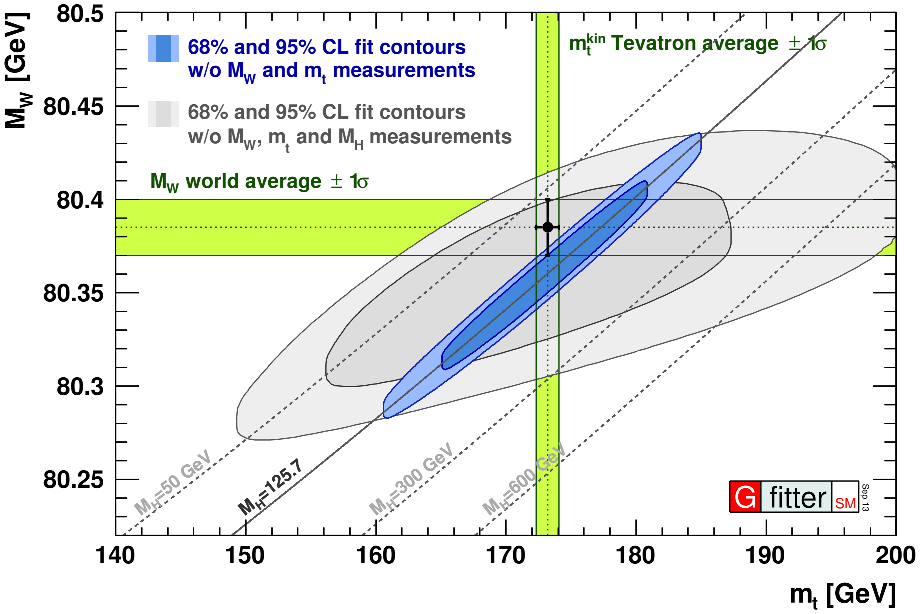

Figure 2.13.: Prediction of the W-boson and top-quark masses in a global fit of SM parameters including (blue area) or not including (grey area) the experimental Higgs boson mass measurements and comparing them to the experimentally determined values (green bands). Taken from [74], updated version of [26].

SM after the discovery of the Higgs boson. In the future, even more precise measurements of the W-boson and top-quark mass will help to further constrain such global fits.

Due to their high mass, top-quarks often play an important role in searches for physics beyond the SM. For example, heavy resonances decaying into $t\bar{t}$ pairs could show up in the $t\bar{t}$-invariant-mass distributions. Stringent limits on many exotic models have been set by both LHC experiments [75–77]. For example, CMS excludes Z' resonances decaying to $t\bar{t}$ pairs up to masses of about 2 TeV. An increased center-of-mass-energy in the upcoming LHC run will extend the reach of many new physics searches considerably.

Chapter 3

Experimental Setup

The progress in particle physics research is closely intertwined with the development of powerful particle accelerators. The Large Hadron Collider (LHC) [78, 79] is the most powerful particle accelerator to date and hosted by CERN, the European Organization for Nuclear Research. At the LHC, the unprecedented center-of-mass energy of 13 TeV (close to the design of 14 TeV) is expected to be achieved after the completion of currently ongoing extensive upgrade activities in 2015.

The physics program at the LHC is focused on the investigation of electroweak symmetry breaking and the discovery of physics beyond the SM. Four large detectors have been constructed for the physics program of the LHC. CMS (Compact Muon Solenoid) and ATLAS (A Toroidal LHC ApparatuS, [80, 81]) are general purpose detectors, LHCb (Large Hadron Collider beauty, [82, 83]) concentrates on the study of CP violation in B-hadron decays, and ALICE (A Large Ion Collider Experiment, [84, 85]) is specifically designed to investigate the results of the collisions of heavy ions.

A short account of the LHC accelerator is given in Section 3.1. In Section 3.2, the requirements of general purpose experiments at the LHC are discussed and the ATLAS detector is described briefly. The CMS detector, which has recorded the data analyzed in this thesis, is discussed in detail in Section 3.3.

3.1. The Large Hadron Collider

The LHC is a two-ring hadron accelerator and collider with a circumference of 26.7 km. A detailed account of the accelerator and its performance is given in [78, 79, 86].

The LHC is installed in the tunnel that was originally constructed between 1984-1989 for LEP, the “Large Electron Positron Collider” with the highest center-of-mass energies achieved in $e^- e^+$ collisions to date. LEP was in operation between 1989-2000. Among the most important results of LEP operation were strong constraints on the mass of the Higgs boson and the detailed study of W- and Z-bosons at the production thresholds, constraining the number of light neutrinos to three [88, 89].

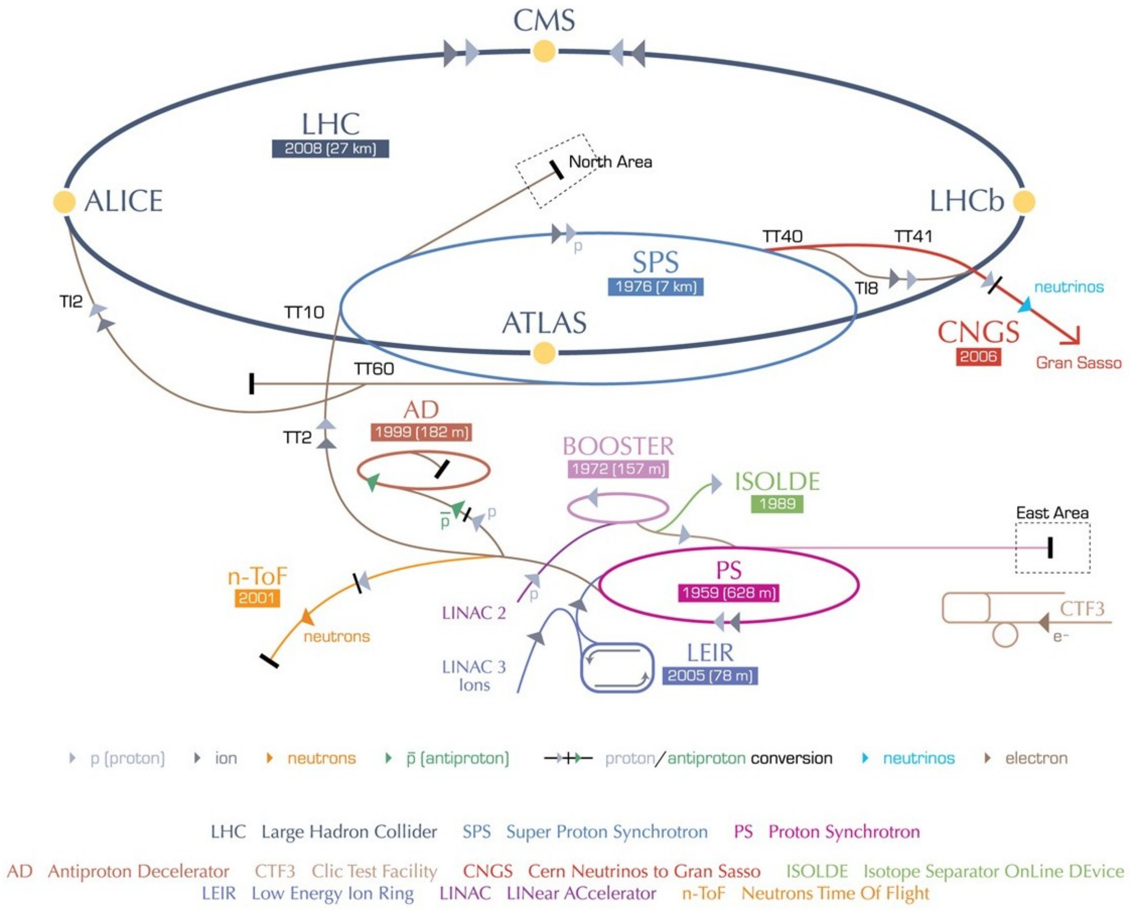

Figure 3.1.: Sketch of the accelerator facilities at CERN, showing the complete preaccelerator chain of the Large Hadron Collider: Proton beams originate from the linear accelerator Linac 2 (50 MeV) and are subsequently accelerated to 1.4 GeV (Proton Synchrotron Booster - PSB), 26 GeV (Proton Synchrotron - PS) and 450 GeV (Super Proton Synchrotron - SPS) before being injected into the LHC, where they are further accelerated to up to 7 TeV [87]

The LEP/LHC tunnel is situated 45-170 mbelow ground, crossing the Swiss/French border twice near Geneva. With the LHC being a particle-particle collider, the protons have to circulate in two separate beam pipes. They are guided and focused by 1232 superconducting NbTi dipole magnets and 392 superconducting quadrupole magnets. Only in the interaction regions the two beams share common beam pipes, each approximately 130 min length.

The LHC is supplied with protons from the pre-accelerator chain depicted in Figure 3.1: Starting with the Linac 2, accelerating the protons up to 50 MeV, the protons are transferred via the Proton Synchrotron Booster (PSB, 1.4 GeV), the Proton Synchrotron (PS, 26 GeV), and the Super Proton Synchrotron (SPS, 450 GeV) to the LHC. The acceleration of the protons from the injection energy (450 GeV) to the design energy of 7 TeV per beam is done using superconducting radio-frequency (RF) cavities operating at 400 MHz with a field strength of 5.5 MV/m. The ramping up to the full energy takes about 20 minutes. For a full refill of the LHC with proton bunches, 12 cycles of the SPS are needed, for which in turn 3 to 4 cycles of the PS are necessary. The expected average turnaround time of seven hours for a complete refill could be reduced to an average of three hours in 2012 LHC operations [86].

A single bunch in the beam typically consists of $1.5 \cdot 10^{11}$ protons (design: $1.15 \cdot 10^{11}$) and has an average length of 8 cm. The nominal beam size at the CMS interaction point is $\approx 20\,\mu\mathrm{m}$. A maximum number of 2808 bunches is foreseen for LHC operations. For this, every tenth RF bucket is filled with a bunch (corresponding to 25 ns bunch spacing). Several gaps between batches of bunches are needed to accommodate the time needed for the response of the injection kicker magnets (225 ns). In addition, a single 3 µs gap is mandatory to allow the beam in the LHC to be cleanly dumped after a normal run or in case of abnormal behavior of magnets or the beam.

In 2011 and 2012 data-taking a bunch spacing of 50 ns instead of 25 ns limited the number of filled bunches to 1380. In order to collect a large dataset, a relatively high average number of *pp* collisions per bunch crossing had to be coped with by the LHC experiments. The additional *pp* collisions in a bunch crossing overlaying the relatively rare hard processes, in which the experiments are mostly interested, are referred to as pileup.

The integrated luminosity in *pp* collisions delivered by the LHC and recorded by CMS amounts to $44.2\,\mathrm{pb}^{-1}$in 2010, $6.1\,\mathrm{fb}^{-1}$in 2011, and $23.3\,\mathrm{fb}^{-1}$in 2012 as depicted in Figure 3.2.(a). While the 2010 data-taking was done with minimal pileup, the average number of *pp* collisions per bunch crossing increased to about 9 in 2011 and about 21 in 2012. The maximum number of simultaneous interactions regularly exceeded 30 events in 2012 data-taking as illustrated in Figure 3.2.(b).

After the restart of the LHC in 2015, an operation with a bunch spacing of 25 ns is foreseen. Such a 25 ns bunch spacing or luminosity leveling could keep the pileup at an acceptable level while achieving even higher instantaneous luminosities and a faster accumulation of large datasets than in LHC Run I. Whether such a 25 ns operation can be performed successfully depends on the control of electron cloud and UFO (unidentified falling object) effects which significantly affected the LHC availability in 2011 and 2012 and could become a major performance limitation for future LHC operation [91, 92].

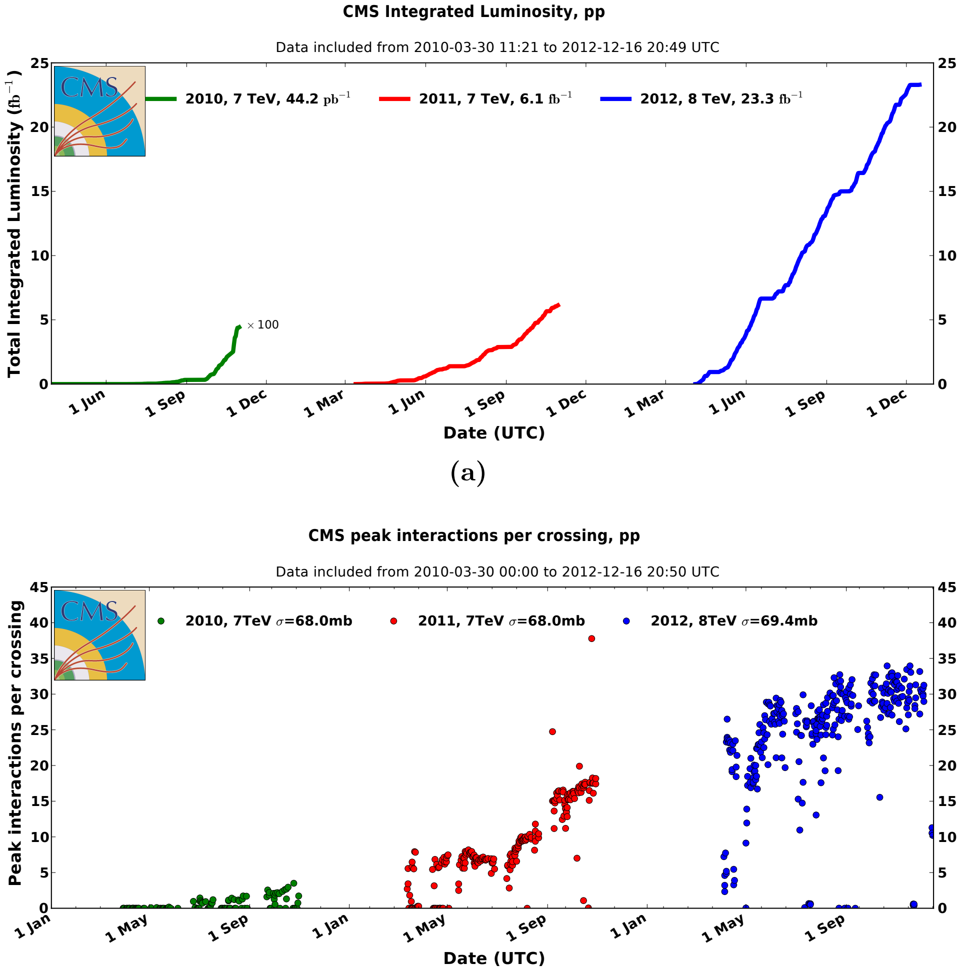

(a)

(b)

Figure 3.2.: (a): Integrated luminosity in 2010, 2011, and 2012 CMS data-taking; (b): Peak number of interactions per bunch crossing in 2010, 2011, and 2012 at CMS. [90]

3.2. General purpose experiments at the LHC

At the LHC, two general purpose detectors are in operation. Besides CMS, which is the detector described in detail in Section 3.3 and used for the analyses in this thesis, the ATLAS experiment ("A Toroidal LHC ApparatuS", described in detail in [80, 81]) has a very similar physics program. This constrains the desired physics performance of both experiments to a comparable level [93].

The LHC general purpose experiments have both been designed to study the process of electroweak symmetry breaking and possible beyond the standard model processes in detail. As a consequence of the high energy and high luminosity machine operation of the LHC, the detectors have to cope with unprecedented particle multiplicities and radiation doses. Even under these harsh conditions, an excellent momentum resolution for leptons and photons has to be achieved in order to successfully cover key processes like $H \to \gamma\gamma$ or $H \to 4l$.

In order to detect most of the produced particles, e.g. to infer missing transverse energy, a generic requirement for these detectors is to cover the pseudorapidity range up to $|\eta| < 5$. For precise measurements of the decay products of high mass resonances, the instrumentation of the "central" or "barrel" detector region ($|\eta| < 1.3 - 1.5$ in both experiments) is of particular importance. However, processes involving vector boson fusion have a specific signature with jets at high rapidities, indicating that a detector coverage up to high $|\eta|$ is important to exploit the full variety of physics processes.

An efficient trigger system is a prerequisite for all LHC experiments as the total inelastic cross section of pp collisions of $\approx 60\,\mathrm{mb}$ is many orders of magnitude higher than that of processes like $\mathrm{t\bar{t}}$ or Higgs production. A number of relevant cross sections and expected event rates per second at 1/10 of the LHC design luminosity are depicted in Figure 3.3. Relatively rare events like the production of Higgs bosons, occurring approximately once per second in the 2012 run, have to be filtered efficiently from the $\approx$ 1 billion other collision events occurring every second. The number of events which can be stored permanently by the experiments is of the order of 300 per second.

While the conditions provided by the LHC are the same for both experiments (about 25 pp collisions every 25 ns at design luminosity), many design choices differ between the two experiments. The two separate collaborations and different detector designs introduce an element of complementarity and competition. This is particularly important given the fact that the LHC is expected to be the only facility providing pp collisions at such a high center-of-mass energy for a long time. The confirmation of the discovery of new physics phenomena or precision measurements is needed by either experiment as the experimental setup can not easily be reproduced elsewhere.

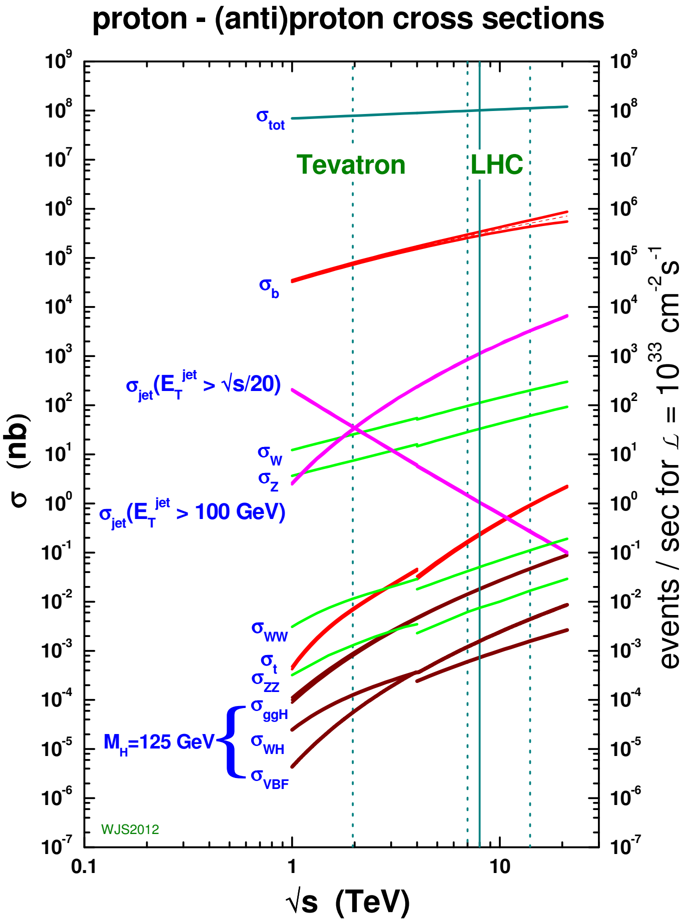

Figure 3.3: Cross section of various processes including the 125 GeV Higgs boson in (anti)proton-proton collisions and event rates at 1/10 of design luminosity of the LHC; [48]

3.2.1. ATLAS

ATLAS is the largest high energy physics experiment ever built. It is 46 m long, has a diameter of 25 m and weighs about 7000 t. The inner detector consists of three subsystems. Closest to the interaction region is a silicon pixel detector with about 140 mio. channels subdivided into three barrel layers and 5 endcaps on each end. Due to the requirements for a precise tracking, but also due to the high particle flux and radiation doses, very short strips or pixels are mandatory components for both general purpose LHC experiments. At larger radii, a silicon strip tracker with 4 barrel layers and 9 endcaps on either side with 6.2 mio. channels is installed. At a radial distance of 56-107 cm from the interaction region, a transition-radiation tracker improves the momentum determination and particle identification by continuous tracking. The inner tracking volume covers the $|\eta| < 2.5$ region and is immersed in a 2 T magnetic field by the surrounding superconducting solenoid magnet.

In the outer part of the detector, there are eight superconducting barrel loops and two endcap magnets producing an intense, but not uniform, toroidal magnetic field. Highly granular liquid-argon electromagnetic sampling calorimeters are installed outside of the central solenoid magnet and cover the $|\eta| < 3.2$ region. These calorimeters have an excellent performance in terms of spatial and energy resolution. In the central region up to $|\eta| < 1.7$ a scintillator-tile calorimeter with steel as absorber medium is installed, providing a radial depth of ≈ 7.4 nuclear interaction lengths (λ). In the endcap and forward regions $1.5 < |\eta| < 4.9$ the hadronic calorimetry (and forward electromagnetic calorimetry) is instrumented with a copper/liquid-argon detector and a copper-tungsten/liquid-argon detector.

The largest part of the ATLAS volume is taken by the muon instrumentation surrounding the calorimeters. Muon tracks are deflected by the toroidal field and precise tracking chambers provide for a second muon momentum measurement. Separate trigger chambers complete the muon spectrometer.

With the finely segmented calorimeter, ATLAS is able to achieve a jet-energy resolution of better than 10% at $p_{\mathrm{T}} \approx 100\,\mathrm{GeV}$ only using calorimeter information which is clearly superior to calorimeter jets at CMS. ATLAS jet-energy corrections and jet-energy scale uncertainties are discussed in more detail in Chapter 6 in the context of the correlation of jet-energy scale uncertainties between ATLAS and CMS in the 2011 data-taking.

3.3. CMS

The “Compact Muon Solenoid” (CMS) is the second general purpose detector at the LHC. It is described in detail in [95–97]. With a total weight of 12500 t, a length of 21.5 m and a diameter of 15 m it is the much more compact albeit much heavier counterpart of the ATLAS detector. Some of the basic design principles of the detector are expressed in its name: **Compact:** The full tracking and calorimetry are contained in a cylinder with a radius of 2.5 m within the solenoid magnet. The volume taken is only an eighth of that taken by the ATLAS detector. **Muon:** Highly energetic muons often originate from the decay of heavier particles and are regarded as good indicators for physics processes of interest. Their clean signature is particularly useful for triggering. **Solenoid:** A specialty of the CMS detector is its large superconducting solenoid immersing the tracking system and calorimeters with a 3.8 T magnetic field. With 2.6 GJ, the stored energy is an order of magnitude larger than in any other solenoid magnet used in high energy physics experiments to date.

CMS is constructed in onion-like layers. Closest to the beam pipe is the tracking system, consisting of all-silicon pixel and strip detectors. The tracking system is surrounded by the electromagnetic and the hadronic calorimeters, all contained within the solenoid magnet. Outside of the magnet, the iron return yokes are interleaved with the muon spectrometer providing a means of muon identification and a second momentum measurement. The detector layout and signatures of particles passing through the detector are shown in Figure 3.4 and 4.1. The different detector components are discussed in Sections 3.3.1 to 3.3.4.

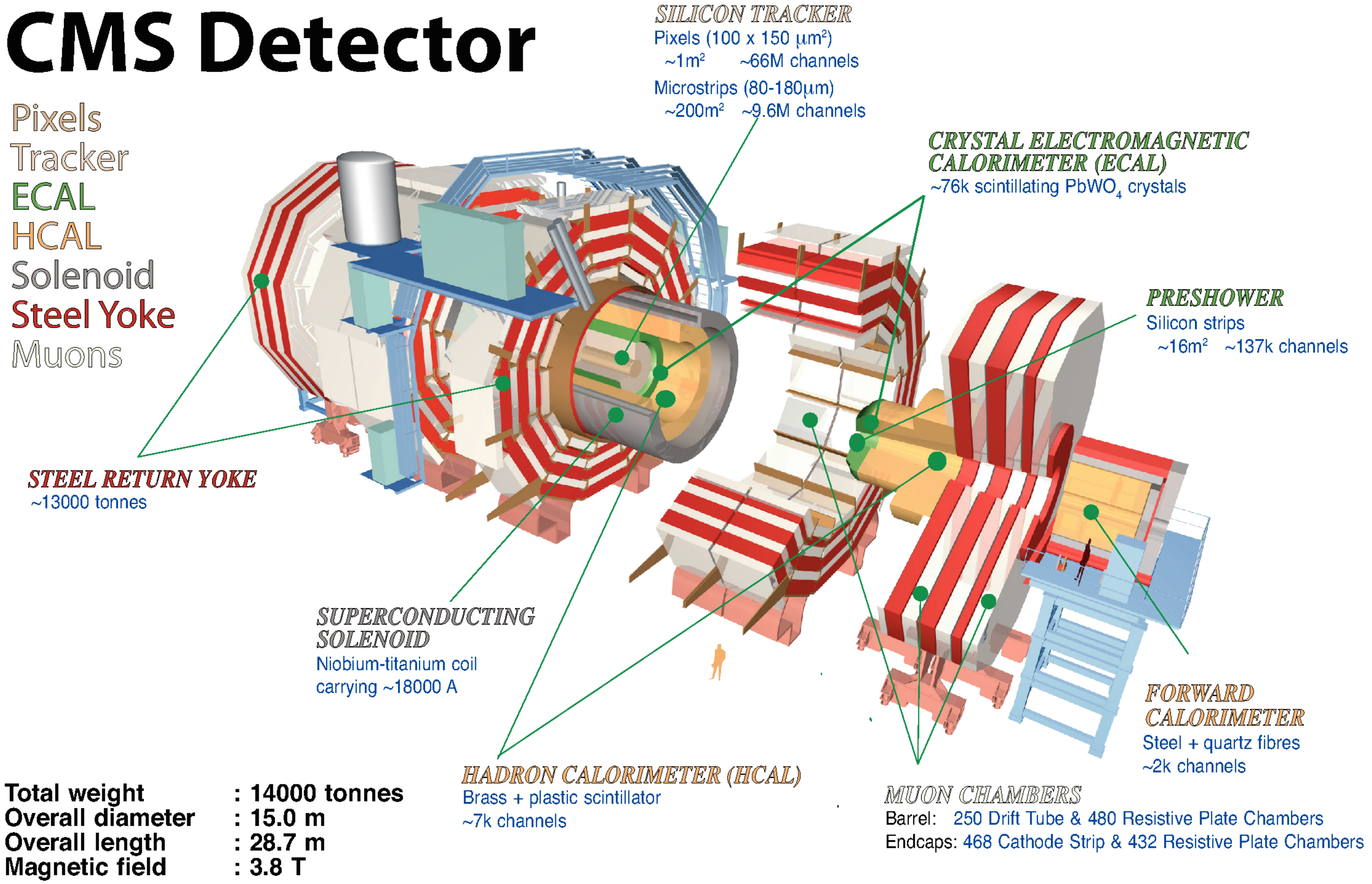

Figure 3.4.: Sketch of the CMS detector with key parameters and individually labelled subdetectors. Figure taken from [94]

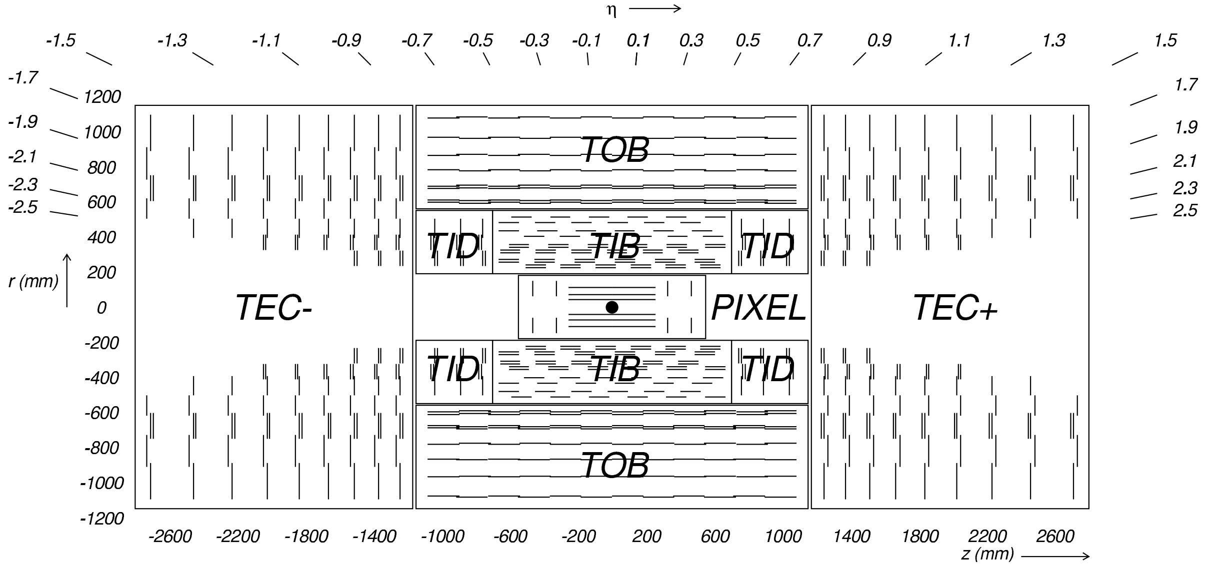

Figure 3.5.: Layout of the CMS tracking system showing the pixel detector, Tracker Inner Barrel/Disc (TIB, TID), and Tracker Outer Barrel/Endcap (TOB, TEC), taken from [98]

In order to identify the particles passing through the detector, the specific signatures left in the subcomponents are combined in an optimized way using the Particle Flow (PF) event reconstruction discussed in Section 4.3. The rate of pp collisions is so high that it is impossible to store all events permanently. Instead, the trigger system described Section 3.3.5 carefully preselects events of interest.

3.3.1. Tracker

The tracking system of CMS is composed of silicon-based sensors detecting the ionization caused by the passage of charged particles. The hits detected in different layers of the detector have to be linked in order to reconstruct the trajectories of particles. From these trajectories, bent by the magnetic field of the solenoid magnet, the transverse momentum of the charged particles can be calculated as

$$p_T \left[\frac{\text{GeV}}{c}\right] = 0.2998 \cdot r[\text{m}] \cdot B[\text{T}] \tag{3.1}$$

The layout of the CMS tracking detector is shown in Figure 3.5. Tracking is available up to $|\eta| = 2.5$ and is done using the pixel tracker with an extremely high granularity close to the beam axis and silicon strip detectors at larger radii.

The pixel detector currently consists of three barrel layers at radii of 4.4 cm, 7.3 cm and 10.2 cm, each 53 cm long. Two endcap disks on either side of the interaction point complement the barrel layers. The modules have a pixel size of $100 \times 150\,\mu\text{m}^2$ resulting

Radius (cm)	**Flux of fast hadrons ($10^{14}\,\mathrm{cm}^{-2}$)**	**Dose (kGy)**	**Charged Particle Flux ($\mathrm{cm}^{-2}s^{-1}$)**
4	32	840	10^8
11	4.6	190	
22	1.6	70	$6 \cdot 10^6$
75	0.3	7	
115	0.2	1.8	$3 \cdot 10^5$

Table 3.1.: Particle flux and radiation dose in the barrel part of CMS for $\int \mathcal{L}dt = 500 fb^{-1}$ [96]

in 65.9 million pixels in total. During collisions in the 2011 and 2012 data-taking period, more than 95% of the pixel channels were active and the single hit resolution was between 10–20 µm [98].

However, the pixel detector is exposed to the highest radiation dose (compare Table 3.1 for expected radiation doses at different radii) and is already suffering from significant radiation damage. The high amount of pileup due to the 50 ns bunch spacing in 2011 and 2012 data-taking already lead to a reduced efficiency due to data losses in the readout buffers. Such data losses would severely affect the performance at even higher pileup.

In [98], the phase-1 upgrade of the pixel detector is presented in detail. Key improvements with respect to the current detector are improved readout chips with larger buffers to cope with higher instantaneous luminosities/pileup and the addition of a fourth outer layer.

At larger radii, from r = 0.2 m to r = 1.1 m, the silicon strip detector with a total length of 5.5 m is installed. It consists of the tracker inner barrel (TIB), the tracker outer barrel (TOB), the tracker inner disks (TID), and the tracker endcaps (TEC). In the inner region ($r < 55$ cm), the modules have a minimum cell size of 10 cm × 80 µm, in the outer region ($r > 55$ cm) the maximum cell size is 25 cm × 180 µm. The TIB consists of 4 layers of silicon sensors with a thickness of 320 µm. The TOB consists of 6 layers of 500 µm thick sensors.

In [99], the tracking and primary vertex performance in 7 TeV collision data is discussed. The excellent hit position resolution of the pixel vector leads to a very efficient reconstruction of vertices with a spatial resolution between 20-25 µm. The reconstruction of primary vertices caused by *pp* collisions and the reconstruction of displaced secondary vertices is crucial for the identification of pileup and b-tagging.

The momentum resolution of the CMS inner tracking system is excellent. As an example, the expected momentum resolution for muons is depicted in Figure 3.6. In the central detector region, using the inner detector alone, the momentum resolution is well below 1% below 50 GeV. At high p_T the resolution degrades linearly, roughly

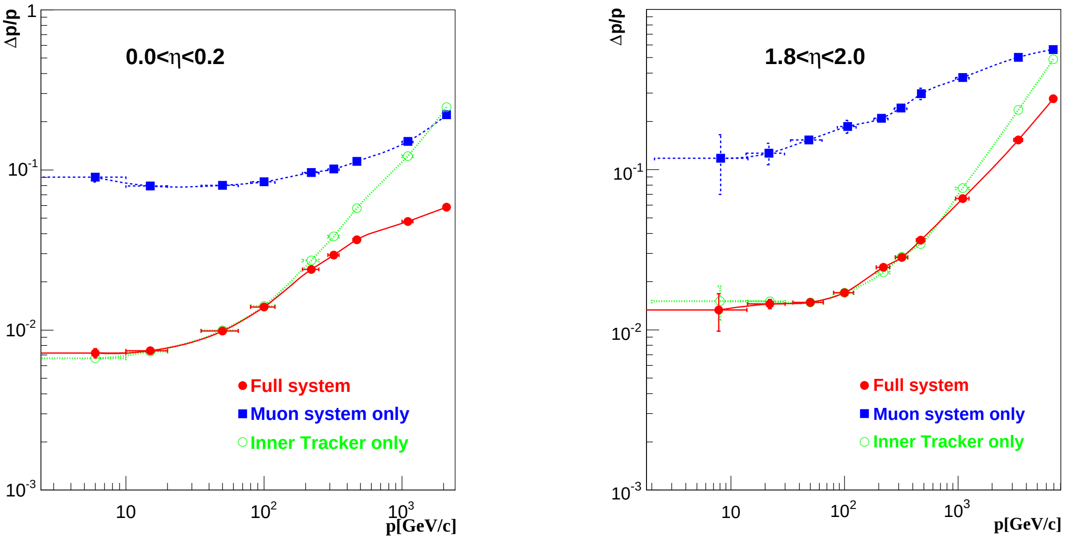

Figure 3.6.: The muon momentum resolution versus p using the muon system only, the inner tracker only, or both ("full system"). a) barrel, $|\eta| < 0.2$; b) endcap, $1.8 < |\eta| < 2.0$. [96]

proportional to the hit resolution, but is still ≈ 6% for a 500 GeV muon. At high momenta, the actual momentum measurement of muons is significantly improved by the muon chambers.

3.3.2. Electromagnetic calorimeter

The electromagnetic calorimeter (ECAL) is located around the inner tracking system. Its sensitive components are 61200 lead tungstate ($PbWO_4$) crystals in the barrel region and 7324 crystals in the endcap region. Lead tungstate has a high density ($8.3\,g/cm^3$), a short radiation length (0.89 cm), and a small Molière radius (2.2 cm). Lead tungstate is relatively radiation hard, but during 2011 and 2012 data-taking the transparency was already significantly reduced leading to a degradation of the response as discussed in Section 5.5.5. The scintillation process in lead tungstate is very fast, 80 % of the photons are emitted within the nominal LHC bunch spacing of 25 ns. However, the light yield is very low at about 30 photons per MeV. Silicon avalanche photodiodes in the barrel and vacuum phototriodes in the endcaps amplify this signal. As both, the light yield and the photodetector performance, depend significantly on the temperature, the temperature needs to be stabilized within 0.1% in order to avoid degrading the energy resolution.

The ECAL barrel (EB) has an inner radius of 1.3 m and covers the pseudorapidity range of $0 < |\eta| < 1.479$. The crystals are mounted in a quasi-projective geometry covering 0.0174 in $\Delta\varphi$ and $\Delta\eta$. The crystals have a length of 23 cm, corresponding to $25.8\,X_0$. At the inner side of the detector, the front area is $\approx 22 \times 22\,\mathrm{mm}^2$.

The ECAL endcap disks (EE) extend the pseudorapidity range to $1.479 < |\eta| < 3.0$. The crystals in the endcap region have a length of 22 cm, corresponding to $24.7\,X_0$, and a front area of $\approx 28.6 \times 28.6\,\text{mm}^2$. In front of the ECAL endcaps, a preshower detector is installed, covering $1.653 < |\eta| < 2.6$. It has a very high granularity and is used to identify photons originating from the decay of neutral pions.

The energy resolution of the electromagnetic calorimeter for electrons with energy E has been evaluated in test beam data [96] yielding

$$\left(\frac{\sigma}{E_{\text{electron}}}\right) = \left(\frac{3.63 \pm 0.1\%}{\sqrt{E_{\text{electron}}/\,\text{GeV}}}\right) \oplus \left(\frac{12.4\%}{E_{\text{electron}}/\,\text{GeV}}\right) \oplus (0.26 \pm 0.01\%) \qquad (3.2)$$

In [100], the challenges of operating and calibrating the ECAL in 7 TeV pp collisions are discussed in detail. The requirements on e.g. the temperature stability have been fulfilled and a laser monitoring system was used to correct for response degradation due to radiation damage. Single-channel intercalibrations were done with an accuracy as good as 0.4% for $|\eta| < 1$ using $\pi^0 \to \gamma\gamma$ events, isolated electrons from W and Z boson decays (comparing to the track measurement), and exploiting large samples of minimum bias events for which a φ-symmetry of all crystals in a particular η ring is assumed.

The energy resolution in data has been found to be worse than anticipated from the simulation which is - at least partially - attributed to the significant amount of material in front of the calorimeter due to the tracking system (compare Figure 3.7 for a sketch of the material budget of tracker and calorimeters). Nevertheless, an excellent energy resolution was achieved: For photons with $E_{\text{T}} \approx 60$ GeV from 125 GeV Higgs boson decays, the resolution was found to vary from 1.1% to 2.6% in the barrel and from 2.2% to 5% in the endcaps. For electrons from Z boson decays with $E_{\text{T}} \approx 45$ GeV, the energy resolution is better than 2% in $|\eta| < 0.8$ and between 2% and 5% elsewhere.

3.3.3. Hadronic calorimeter

The hadronic calorimeter aims at containing the full shower of hadrons entering the calorimeter system. In comparison to the characteristic length unit of electromagnetic interactions, the radiation length X_0, the nuclear interaction length λ_I governing hadronic showers is much longer. This was a great challenge for the design of the CMS HCAL as the solenoid magnet at radius of 3 m limits the size of the calorimeter system.

The material budget of the tracker and calorimeter systems is depicted in Figure 3.7. In order to maximize the depth in units of interaction lengths, a sampling calorimeter with brass ($\lambda_I = 16.42\,\text{cm}$) as absorber material and thin slices of plastic scintillators has been constructed for the central detector region. It is supplemented by the hadron outer system outside of the solenoid to catch tails of the hadronic showers and extended to high pseudorapidities with a hadron forward calorimeter using a different technique.

The Hadron Barrel (HB) covers the pseudorapidity range of $0 < |\eta| < 1.305$ with a segmentation of 0.087 in $\Delta\varphi$ and $\Delta\eta$, which corresponds to 2304 towers in total. A single HCAL tower covers 5x5 ECAL crystals and is composed of two steel plates at both ends and 14 brass plates ($\approx$ 5cm thick). The brass used as absorber material has a density of $8.83\,\mathrm{g/cm^3}$, a radiation length of $X_0 = 1.49\,\mathrm{cm}$ and an interaction length $\lambda_I = 16.42\,\mathrm{cm}$. The total absorber thickness is $5.82\,\lambda_I$ at $\eta = 0$, increasing to $10.6\ \lambda_I$ at $|\eta| = 1.3$. The ECAL adds $\approx 1.1\lambda_I$ to the effective thickness. It is described in detail in [101].

In order to enhance the effective thickness of the hadronic calorimeter to more than 10 interaction lengths and fully contain highly energetic hadronic showers, the Hadronic Outer (HO) has been added as a tail catcher outside of the solenoid magnet, covering $0 < |\eta| < 1.26$. It is currently undergoing an upgrade with silicon photomultipliers to be fully operational for LHC Run II, starting in 2015 [102, 103].

The Hadron Endcap (HE) covers the pseudorapidity range of $1.3 < |\eta| < 3.0$ with another 2304 towers in total. The segmentation in $\Delta\varphi$ and $\Delta\eta$ is coarser than in the barrel region above $|\eta| = 1.7$ and corresponds to 0.350x0.175 at $|\eta| = 3$.

The Hadron Forward (HF) completes the almost hermetic detector coverage up to $|\eta| < 5$ and is needed for a good resolution of the missing transverse energy and forward jet physics. The HF is situated $11.2\,\mathrm{m}$ from the interaction region and has a depth of $1.65\,\mathrm{m}$ or $\approx 10\lambda_I$. The HF calorimeter is based on steel absorber with embedded fused-silica-core (quartz) optical fibers of different lengths in which Cherenkov radiation forms the basis of signal generation. The readout bundles the fibers in towers with a segmentation of 0.175x0.175 in $\Delta\varphi$ and $\Delta\eta$. The design, performance, and calibration of the HF is described in [104].

The combined ECAL/HCAL barrel system performance for pion test beam momenta ranging between 2 and 300 GeV [105] can be parameterized as

$$\frac{\sigma(E)}{E} = \left(\frac{115.3\%}{\sqrt{E/\,\mathrm{GeV}}}\right) \oplus 5.5\% \tag{3.3}$$

As discussed in detail in [106], several upgrades of the HCAL are foreseen. For example, the SiPM technology now being used in the HO is going to be installed in the HB and HE and a readout with more channels will be implemented for the HF. These measures are needed to sustain or improve the performance in the upcoming high luminosity LHC runs.

3.3.4. Muon System

The muon system is located outside of the solenoid magnet and uses the iron magnetic flux return yokes as absorber material. It has a coverage up to $|\eta| = 2.4$ and uses gaseous tracking detectors, covering a total sensitive area of 25000 m^2. The muon system has

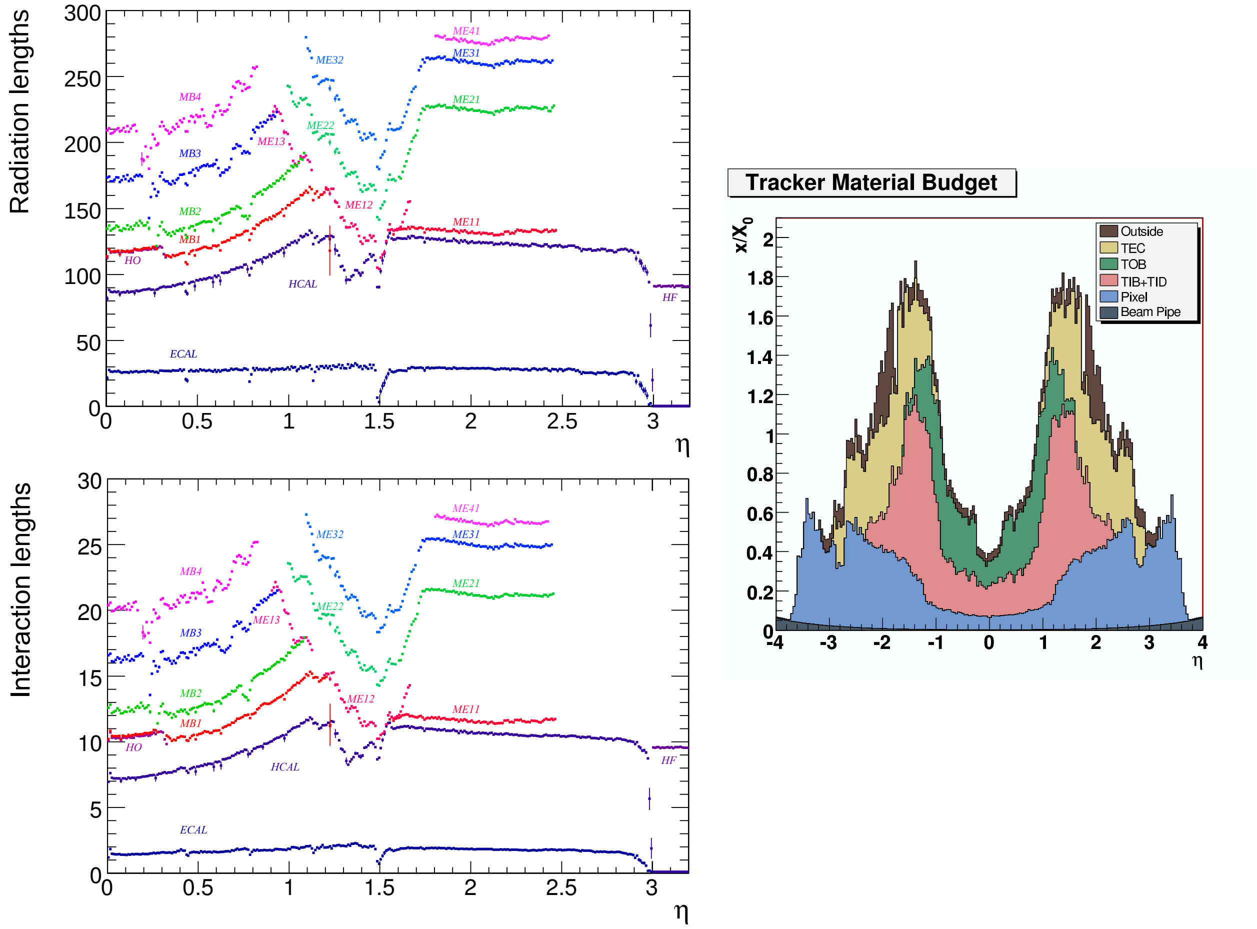

Figure 3.7.: Top left: material budget in terms of the radiation length as a function of the pseudorapidity after the ECAL, HCAL and at different muon stations; Lower left: material budget in units of interaction length as a function of the pseudorapidity after the ECAL, HCAL and at different muon stations; Right plot: material budget in units of the radiation length as a function of η for the inner detector (tracker); [96] and [95]

three functions: muon identification, improvement of the inner tracking momentum measurement, and fast triggering.

The barrel drift tube (DT) chambers cover the pseudorapidity region $|\eta| < 1.2$ with four layers (stations). In this region, the muon rate is relatively low and the magnetic flux is mostly contained in the return yokes, enabling the use of this detector type.

Cathode strip chambers (CSC) extend the coverage up to $|\eta| < 2.4$ where the particle flux and neutron-induced background is higher. In the detector region up to $|\eta| = 1.6$, resistive plate chambers (RPC) complement the two other detector types. They are characterized by a good time resolution and a very fast response and are primarily used for the trigger system.

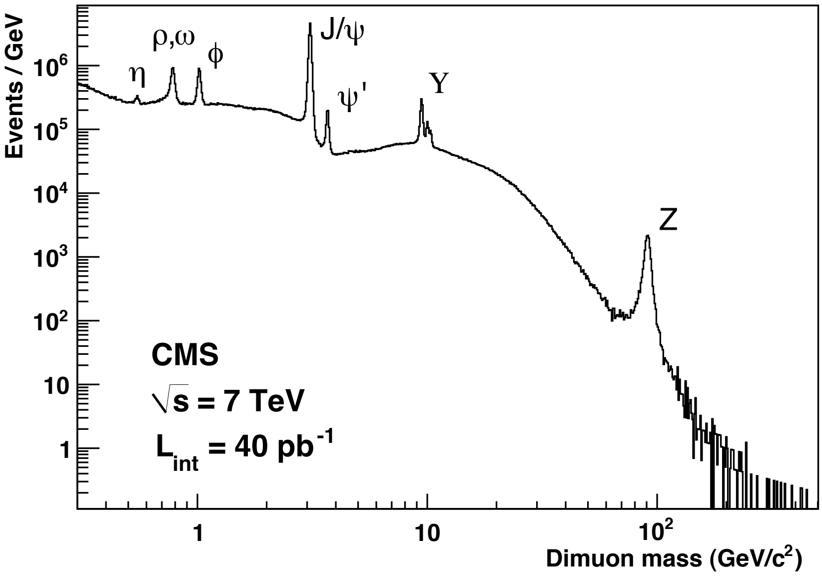

Figure 3.8.: Invariant mass spectrum of dimuons in events collected with the loose double-muon trigger in 2010. [107]

The momentum resolution of the muon system and the combined muon and inner tracking system is shown in Figure 3.6. At high momenta, the long lever arm of the muon system significantly improves the resolution to well below 10% at 1 TeV. The performance in *pp* collisions has been studied in detail in [107] and agrees well with the MC expectations. The muon reconstruction and identification efficiency is above 95% at any $|\eta| < 2.4$ with a p_T larger than a few GeV. The probability to misidentify a hadron penetrating the massive amount of material in front of the muon system as a muon is well below 1%. The impressive muon reconstruction performance is condensed in a plot of the dimuon mass spectrum in 2010 data shown in Figure 3.8. Due to the relatively low instantaneous luminosity in 2010 it could be recorded with a loose dimuon trigger without p_T thresholds and resolves resonances with masses from below 1 GeV up to the Z boson at 90 GeV without the need for any sophisticated analysis.

3.3.5. Trigger system

With the nominal bunch crossing rate of the LHC of 40 MHz and an average event size at CMS of ≈ 1 MB, the amount of data continuously recorded by the experiment can not be stored permanently.

However, this does not limit the physics reach of CMS as most interactions have a low momentum transfer and have been studied before. As indicated in Figure 3.3, the cross sections of processes of particular interest, such as with very high p_T jets or the production of Higgs bosons, is of the order of a few events per second. In 2012 data-taking, the “core” proton-proton physics program was recorded at a rate of $\approx 300 - 350$ events per second and available for physics analyses after ≈ 48 hours. At an additional rate of

$\approx 300 - 350$ events per second, data was "parked" for later reconstruction [108]. This parked dataset extends the physics program and became available during the shutdown. Trigger paths with the highest average rate included in the dataset were a generic trigger for vector boson fusion final states and a four-jet trigger with a lowered p_{T} threshold in comparison to the core dataset.

The necessary reduction of the event rate by a factor of $\approx 10^5$ is done by the two-fold CMS trigger system: A custom hardware Level-1 (L1) trigger and a high-level trigger (HLT) on commodity PC hardware, discussed in detail in [109, 110]. This is in contrast to most other general purpose high energy physics experiment. For example, ATLAS, the Tevatron, and HERA experiments use more trigger levels. This concept was chosen as it provides the highest flexibility given the (up to the present) exponentially evolving memory size, memory speed, processor speed, and network capacities and avoids the ambiguity of many subsequent trigger levels. The disadvantage of this two-fold approach is that the single HLT-step on PC hardware must cope with a much higher event input rate, requiring more CPU resources.

The Level-1 trigger is based on a simplified event reconstruction, employing reduced-granularity and reduced-resolution data from the calorimeters and muon system. The decision whether to keep an event or discard it has to be taken very fast ($\approx 3\,\mu$s) as the full resolution data can only be kept in pipelined memories on the detector for such a short time. The hardware-based trigger logic uses p_{T}-thresholds and cuts on global event variables like the sum of E_{T} and the missing transverse energy $E_{\mathrm{T}}^{\mathrm{miss}}$ to reduce the event rate by a factor of 1000 to a maximum of 100 kHz.

After a positive L1-decision, the data held in the pipeline buffers is readout and the full event data is transferred to the HLT computing farm. Here, the events are fully reconstructed considering information from all subdetector systems. The reconstruction algorithms used are already very close to the offline reconstruction software and fully adaptable during operation. For example, a simplified variant of the Particle Flow event reconstruction discussed in Section 4.3 has been adopted at HLT level for the 2012 data-taking and the HLT-trigger is based on the same CMSSW framework used for offline analyses. The time allowed for the HLT trigger decision is $\approx$ 50ms. After a positive HLT decision, the data is either directly transferred to prompt reconstruction or saved for later analysis as "parked" data.

Chapter 4

Event reconstruction and jet-energy corrections at CMS

The goal of the event reconstruction is to identify and measure the actual particles traversing the detector, starting from the raw detector signals. In general, these are the particles either directly produced in the pp collisions at the interaction point or decay products formed e.g. in the hadronization process of quarks and gluons and subsequent decays.

The true identity of the particles traversing the detectors after hadronization is only known in simulations. This is referred to as the particle or "generator level". A hypothetical ideal detector with perfect particle identification and momentum measurement capabilities would be able to reconstruct the event at this level. For example, this generator level is the reference to which the jet-energy corrections discussed in Section 4.5 aim to correct reconstructed jets on average. In Feynman diagrams, the graphical representations of particle physics interactions, the outgoing entities are often quarks or gluons (not jets). Even with an ideal detector the level of quarks and gluons, referred to as "parton level", is not accessible and the full event interpretation all the way from detector deposits up to the parton level is only accessible in simulation.

The procedure how to arrive at a suitable event interpretation is ambiguous as many of the particles leave signals in various subdetectors and this information has to be combined. The reconstruction is generally split into three steps: local reconstruction within a subdetector module, global reconstruction within the full subdetector, and the subsequent combination to high-level objects.

The local reconstruction takes digitized electronic detector signals as input. From this level onwards, simulation and data are treated in the same way. The digitized signals are either taken directly from the data acquisition system of the detector or formed from simulated energy deposits. The output of this local reconstruction is a collection of reconstructed hits with details specific to the subdetector, but always containing position, time, and reconstructed energy deposition information.

In the global reconstruction, these reconstructed hits are combined to form either tracks (separately in the inner tracking and the muon system) or calorimetric towers in the calorimeter system. Higher-level objects are then formed by combining the collections resulting from the global reconstruction. The detector performance and reconstruction techniques are described in detail in [96].

Here, the track and vertex finding is briefly discussed in Section 4.1 and typical signatures of particles traversing the detector are described in Section 4.2.

For most practical purposes, the reconstruction of high-level objects at CMS is currently done with the Particle Flow algorithm, described in Section 4.3. It aims at identifying and reconstructing all particles in an event by combining optimally the information of all subdetectors. The resulting "PF candidates" are charged hadrons, photons, neutral hadrons, electrons, and muons and can then be treated like generator level particles in further analysis steps, e.g. the jet clustering or the calculation of missing transverse energy $\vec{E}_{\mathrm{T}}^{\mathrm{miss}}$.

The practical formation of jets at generator level or from PF objects is discussed in Section 4.4, the calibration of reconstructed jets to that of generator level jets is discussed in Section 4.5.

4.1. Tracks and vertices

The reconstruction of charged particle trajectories and the vertex reconstruction in the dense LHC environment is very demanding. However, the very high granularity inner tracking system of CMS is suited particularly well for this task. The procedures are described in detail in [96] and the performance in collisions is analyzed in [99, 111–113].

The track finding procedure is subdivided into several steps. First, individual hits of particles in the sensitive layers are clustered, then two or three clusters are combined as seeds to find trajectories, matching clusters in neighboring more outward sensitive layers.

The clustering process starts with pixel seeds (requiring a signal-to-noise ratio of $S/N > 6$) in the pixel detector or strip seeds ($S/N > 3$) in the strip detector. Adjacent pixels or strips are added to the cluster if they meet similar signal-to-noise requirements (pixel: $S/N > 5$; strip: $S/N > 2$) and the final cluster is retained if the total S/N-ratio exceeds 10.1 in the pixel and 5 in the strip detector. The position resolution is enhanced when charge sharing across several strips or pixels occurs, resulting in typical resolutions of 4-15 µm in the pixel detector (pixel size $100 \times 150\,\mu\mathrm{m}^2$ as described in Section 3.3.1).

The seeding step to get initial track estimates is done using triplets of hits in the pixel tracker or pairs of hits additionally constrained by the beamspot or a reconstructed vertex. The pixel detector is well suited for the seed finding as it has a high granularity, providing three-dimensional space points, and (as a result of the granularity) a low occupancy. The initial track estimate is extrapolated to more outward sensitive layers to find compatible hits. If one or more compatible hits are found, they are added to track candidates with correspondingly updated track parameters and uncertainties. Even if no hit is found in the next layer, a track candidate with an "invalid hit" can be kept. To limit the combinatorial complexity, the number of track candidates at each extrapolation step is limited (default: 5). Only the best candidates ordered by their track fit's normalized χ^2 are retained. This process is repeated until the boundary of the tracker is reached, no more compatible hits can be found or another stopping criterion is fulfilled.

At the end of each track finding iteration, the reconstructed tracks are filtered to remove likely fake tracks and retain good-quality tracks. Hits that are unambiguously assigned to good-quality-tracks are removed and the combinatorial track finding (CTF) outlined above is repeated with the remaining hits. A total of six iterations [112] is done with more relaxed requirements in later iterations to find low-momentum tracks and displaced tracks seeded by pixel/strip or strip seeds. This "iterative tracking" guarantees a high efficiency and low fake rates.

Due to the large amount of tracker material in terms of radiation/interaction lengths (about one radiation length at $|\eta| \approx 0.9$), there is a high probability for photons to convert to $\mathrm{e}^-\ \mathrm{e}^+$ pairs and a non-negligible probability for hadrons to undergo nuclear interactions producing multiple hadrons. However, this detection efficiency loss can be partially recovered by identifying the production vertices and are taken into account in the reconstruction of particles.

The vertex reconstruction is generally performed using tracks, but the vertex-finding algorithm and applicable tracks differ depending on the physics case, e.g. primary or secondary vertex fitting or reconstruction of photon conversions. During a typical bunch crossing in 2012 data-taking, about 20 *pp* collisions took place. It is important to identify the primary vertices linked to the hard interaction (which generally fired the trigger and is of physics interest), but also the primary vertices of the simultaneous pileup interactions.

For the primary vertex reconstruction, the tracks are clustered using a deterministic annealing (DA) algorithm described in [113]. This was introduced for 2011 and 2012 data-taking as the relatively high number of pileup interactions lead to the merging of all vertices with a distance of less than 2 mm in the "gap clustering" used in 2010, described in [96]. Using this refined approach, it is possible to resolve primary vertices even in the harsh high-luminosity environment in 2012. The resulting vertex candidates containing at least two tracks are fit using the "adaptive vertex fitter" in which each track associated with the vertex is assigned a weight between 0 and 1, indicating the likelihood of belonging to the vertex. Genuine tracks belonging to the vertex have a weight close to 1 while outliers are weighted down. The number of degrees of freedom is defined as $n_{dof} = \sum_{i=1}^{nTracks} w_i - 3$. For valid offline vertices it is required that $n_{dof} > 4$. The vertex with the highest $\sum p_\mathrm{T}^2$ of all tracks is likely to be the hard interaction vertex while other vertices are usually regarded as pileup vertices.

The reconstruction of secondary vertices is extremely important for the b-tagging of jets described in Section 4.4.4. In the case of the production of B-hadrons or charm hadrons having a measurable average lifetime, it is often possible to reconstruct a secondary vertex (and eventually a tertiary vertex in the case of a b-c-decay chain). For this specific secondary vertex reconstruction, high purity tracks within a cone of

$\Delta R = 0.3$ around the jet axis are selected and an adaptive vertex fitting as done for primary vertices is performed. Well-fitting tracks are removed and several secondary vertices may be reconstructed iteratively. For b-tagging only secondary vertices which meet certain criteria are considered. They are e.g. required to be significantly different from the primary vertex and share less than 65% of their tracks with it. The radial distance may not exceed 2.5 cm and the mass is required to be less than 6.5 GeV.

4.2. Typical signatures of particles

For the reconstruction of events, only a relatively small number of different particle species can be distinguished in the detector. Here, typical signatures of these particles are summarized. These "ideal signatures" in the detector are also depicted in Figure 4.1.

Muons: In the p_{T}-range usually probed by CMS, muons deposit only small amounts of energy by ionization in the detector and pass through the full detector (the critical energy, at which radiative losses start to dominate, is several hundred GeV for muons in iron [40]). This leads to an extremely efficient identification with low fake rates as they traverse the muon system. The momentum of high-quality "global" muons is measured by combining the inner tracking and the muon system.

Photons: Electromagnetic showers initiated and contained in the electromagnetic calorimeter are the typical signature of photons. A typical electromagnetic shower is contained in 3x3 ECAL crystals. However, due to the large material budget in front of the calorimeter system it can occur relatively often that conversions take place in the tracker material.

Electrons: Electrons will also induce electromagnetic showers in the ECAL, but can be distinguished from photons due the tracks pointing to the calorimeter cluster. In order to reconstruct the full energy, bremsstrahlung photons are also considered.

Hadrons: Hadrons typically produce hadronic showers in the calorimeter system. A shower start in the HCAL having the largest depth in nuclear interaction lengths is a clean signature. However, nuclear interactions in the tracker or a shower start in the ECAL can also occur. While neutral hadrons will usually only leave a signal in the calorimeter, charged hadrons will leave a track in the inner tracking system. Most hadrons in a typical jet will be pions, but kaons, protons, and neutrons may also reach the calorimeters.

Invisible particles: Neutrinos and other weakly interacting particles, e.g. some proposed supersymmetric particles such as LSPs (lightest supersymmetric particles) in R-parity preserving models, typically do not leave a signal in the detector. However, this "non-signature" can still be inferred by imposing transverse momentum balance on the full event. Due to the (almost) hermetic coverage of general purpose detectors like CMS, the reconstructed missing transverse energy ($\vec{E}_{\mathrm{T}}^{\mathrm{miss}}$) can be used to obtain a signature of "invisible" particles.

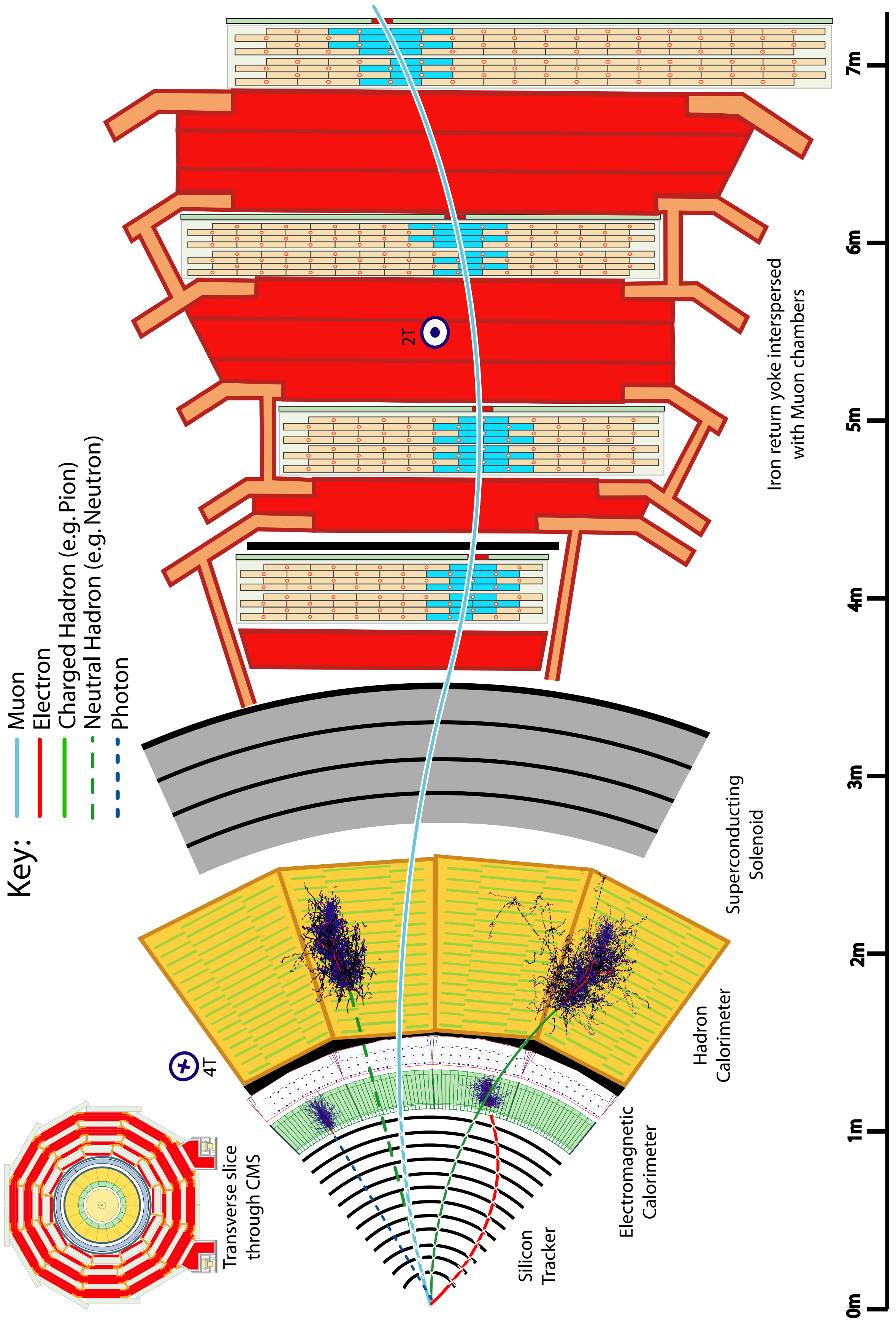

Figure 4.1.: Transverse slice through the CMS detector indicating the different onion-like particle detection layers. Indicated trajectories of particles show typical interactions and signal depositions in the detector [114]

4.3. Particle Flow event reconstruction

The Particle Flow (PF) event reconstruction is a cornerstone of most CMS physics analyses. The goal of this approach is to get an optimal detailed representation of the full event avoiding ambiguities. This is achieved by deriving a consistent list of “particle/PF candidates” that avoids doublecounting of detector signals by reconstructing PF candidates in a stringent order following a fixed algorithm.

A detailed description of the procedure is given in [115], the performance in early LHC data for jets and taus is discussed in [116, 117]. The iterative tracking as discussed in Section 4.1 and a PF-specific calorimeter clustering described in Section 4.3.1 are prerequisites of the linking and particle identification procedure which leads to a list of PF candidates, described in Section 4.3.2, that can be used to e.g. calculate $\vec{E}_{\mathrm{T}}^{\mathrm{miss}}$ (see Section 4.6) or cluster jets as described in Section 4.4.

4.3.1. Clustering and linking

Excellent tracking capabilities are an important prerequisite for the PF event reconstruction. In addition, a finely segmented calorimeter system is needed to distinguish the energy deposits of separate particles and help in the identification of particle types.

A specific calorimeter clustering algorithm has been developed for PF at CMS [115] to optimize the detection efficiency of low-energy particles and the separation of close-by energy deposits. The clustering is performed separately in the barrel and endcap parts of the ECAL and the HCAL as well as in the two layers of the preshower detector. A cluster calibration is performed to correct for the non-linear response of ECAL and HCAL to incident hadrons.

Cluster seeds are found as calorimeter cells surpassing a given threshold. Starting from these seeds, neighboring cells passing noise thresholds (ECAL barrel: 80 MeV; ECAL endcap: 300 MeV; HCAL: 800 MeV) are iteratively added to grow “topological clusters”. The energy in these topological clusters is then split up and shared among as many PF clusters as there were cluster seeds in the topological cluster.

Particles like charged hadrons or electrons will usually leave a signal in more than one subdetector as outlined in Section 4.2. In order to connect the signals in the different subdetectors, a procedure is performed to link tracks and clusters in the different subdetectors to “blocks”. Due to the high resolution of the tracker and the high granularity of the ECAL, these blocks usually contain only a small number of elements so that the particle identification is oriented along the lines of the typical signatures in Section 4.2.

The linking procedure is done outwards from the tracking detector: Extrapolating the charged particle tracks, any clusters in the preshower, the ECAL, and the HCAL along this trajectory are linked to the track. The strength of such a link (link distance) is given by the distance in ΔR between the trajectory and the cluster. The potential emission of bremsstrahlung photons is checked by looking for ECAL deposits tangential to the track when passing a detector layer.

In descending order of granularity, preshower clusters are linked to ECAL clusters, and ECAL clusters to HCAL clusters. Finally, links are formed between tracks from the inner tracker and tracks from the muon system to form “global muons”. In case of ambiguities in the matching of a muon system track to tracks in the inner tracker, only the global muon candidate with the smallest χ^2 is kept.

4.3.2. Particle identification

The blocks resulting from the linking algorithm are subject to the PF particle identification algorithm. Guiding principle of the algorithm is to identify particles with the clearest signature first, remove their signature from the event record (i.e. the list of blocks), and repeat this procedure for all considered particle types.

PF candidates in this sense can be charged or neutral hadrons, electrons, muons and photons. Most muons can easily be identified due to their signal in the muon system. The global muons reconstructed in the linking procedure give rise to PF muons. The tracks are removed and the typical energy deposition in the ECAL (0.5 GeV) and HCAL (3 GeV) is subtracted from the calorimeter clusters at a later stage.

Electron candidates are formed in the next step, refitting the track taking into account bremsstrahlung energy losses and energy depositions due to bremsstrahlung photons in the ECAL. The identification as an electron is decided upon by a number of tracking and calorimetric variables. If an electron candidate is identified and kept, the corresponding track and ECAL energy deposits are removed from the block.

For the next step, only those tracks with a relative uncertainty on the measured p_T smaller than the expected relative uncertainty of charged hadrons in the calorimeter are kept (a rejection rate of 0.2% is found in typical jets). If the calorimetric energy in a block is smaller than the sum of the momenta of the tracks linked to the block, the compatibility of both is required to be within three standard deviations. In the rare case that both measurements are incompatible, a relaxed search for muons is performed. Subsequently, tracks with the highest p_T uncertainties are removed to reduce fakes until the calorimetric energy is compatible.

The remaining tracks give rise to charged hadrons. Initially, they are assigned the track momentum and pion mass. In case the calorimetric energy is compatible with the track momentum, both measurements are combined. This is particularly relevant at high energies where the calorimeter energy resolution improves while the tracker momentum resolution degrades.

If the calorimetric energy in a block is significantly larger than the charged-particle momentum, i.e. more different than the calorimeter energy resolution would suggest, a different procedure is followed: In this case the expected calorimetric energy deposition is removed and the excess energy is distributed to either photons or neutral hadrons. In case the excess is larger than the total ECAL energy, the ECAL energy is attributed to photons, the calibrated HCAL energy to neutral hadrons. Otherwise only photon candidates are formed.

From the remaining ECAL and HCAL clusters not linked to any tracks, more photons (ECAL energy) and neutral hadrons (HCAL energy) are formed. The high granularity of most CMS detector components is a key to the success of the Particle Flow approach at CMS. The impact of the relatively poor HCAL energy resolution is reduced to the PF neutral hadrons. This leads to large improvements, especially in the jet reconstruction as discussed in Section 4.4.

4.4. Jets

Even though the concept of jets is not unique, it is useful to define a fixed procedure how jets are formed. This procedure is given by a choice how to combine the momenta of jet constituents and a choice of a jet algorithm as described in Section 4.4.1.

This recipe to reconstruct jets can be applied at the generator level to form generator jets or Particle Flow jets as described in Section 4.4.2 and 4.4.3, respectively.

It is often useful to know the flavor of a jet, defined by the parton that initiated the jet. This can be defined on the generator level, but there are also means to reconstruct the flavor of a jet using reconstructed quantities. This is pursued in the form of b-tagging and quark/gluon discrimination, briefly described in Section 4.4.4 and 4.4.5. An efficient b-tagging is of extraordinary value to select event topologies which feature b-jets, such as top-quark pair events, and suppress backgrounds.

In the high-luminosity environment of the LHC, soft jets from pileup interactions can overlay and fake high p_{T} jets. In order to identify such jets, a pileup jet identification method has been developed by CMS and is briefly described in Section 4.4.6.

4.4.1. Jet algorithms

If there is little activity in addition to the hard scattering in the detector, jets are objectx which ban be identified easily. As an example, the CMS event with the highest reconstructed dijet mass during the 2010 data-taking is shown in Figure 4.2 with two high p_{T} back-to-back jets. In order to get reproducible and well defined jets it is necessary to follow a fixed algorithm, applicable to both generator level particles and reconstructed objects. An extensive discussion of currently used jet-finding algorithms is given in [118]. In CMS, the jet-finding is performed using a number of different algorithms, which are implemented in FastJet framework [119]. The recombination scheme adopted by CMS for merging jet constituents to jets is the four-momentum sum of all constituents.

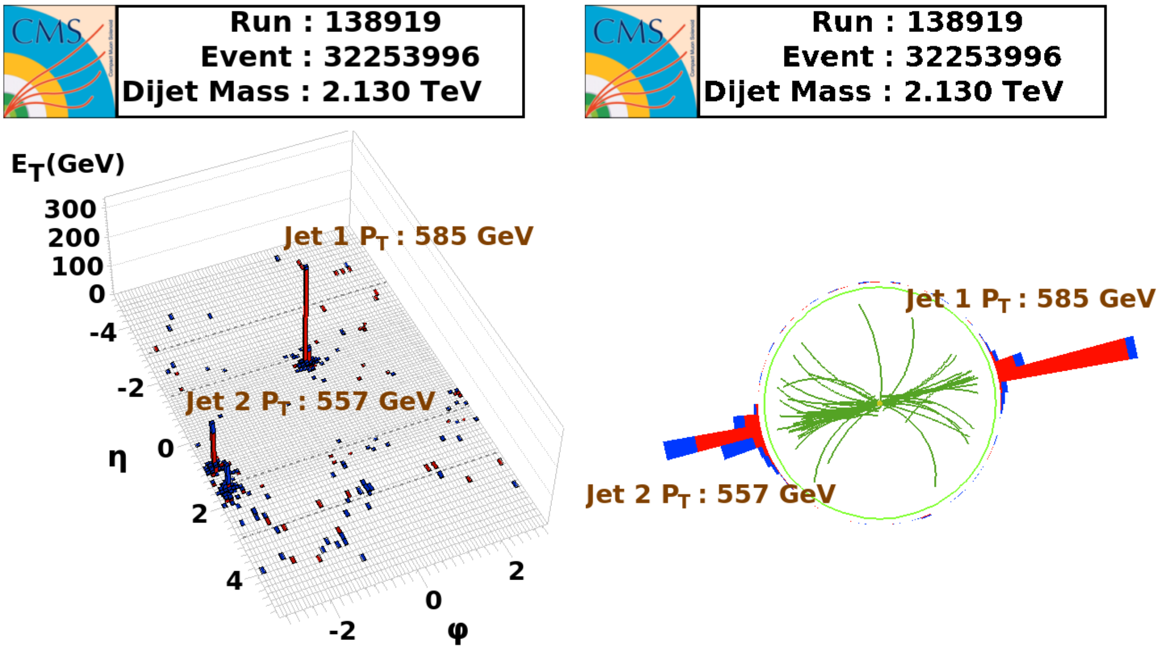

Figure 4.2.: Display of the 2010 event with the highest reconstructed dijet mass in η/φ coordinates and in an r/φ view of the transverse plane. Tracks are shown in green, calorimeter energy deposits in red and blue. [120]

Theoretical considerations dictate that jet-finding algorithms should be insensitive to the addition of soft radiation (infrared safe) and to the splitting of constituents (collinear safe). Simple cone-type algorithms (first proposed in [35]) often fail to meet these requirements. The seedless infrared save cone algorithm (SIScone [121]), developed to meet the requirements and at the same time result in regularly-shaped cone jets, is not used in the current data-taking as the computing time for the jet-finding scales $\propto N^2 \ln(N)$, where N is the number of constituents in the event. That is much slower than that of sequential-clustering algorithms being the current standard for LHC physics.

There is a family of three closely-related sequential-clustering algorithms: The k_t, the anti-k_t, and the Cambridge/Aachen algorithm. They all iteratively cluster objects according to the minimum of a distance measure. The distance measures d_{ij} and d_{iB} are commonly defined as

$$d_{ij} = min(p_{T,i}^{2k}, p_{T,j}^{2k}) \frac{\Delta_{ij}^2}{R^2} \tag{4.1}$$

$$d_{iB} = p_{T,i}^{2k} \tag{4.2}$$

where R is the distance parameter, i and j are indices of all objects in the event, $k = 1$ for the k_t-algorithm, $k = -1$ for the anti-k_t algorithm, and $k = 0$ for the Cambridge/Aachen-algorithm. Δ_{ij} denotes the distance in η-φ space as

$$\Delta_{ij}^2 = (\eta_i - \eta_j)^2 + (\varphi_i - \varphi_j)^2 \tag{4.3}$$

All distances d_{ij} and d_{iB} are calculated and the smallest of all d_{ij} and d_{iB} is determined. In case the minimum is d_{ij}, the objects i and j are recombined into a single new object by addition of their four-momenta and all distances are recalculated. In case the minimum distance is d_iB, the object i is regarded as a jet and removed from the input list. This procedure is repeated until all input objects are clustered.

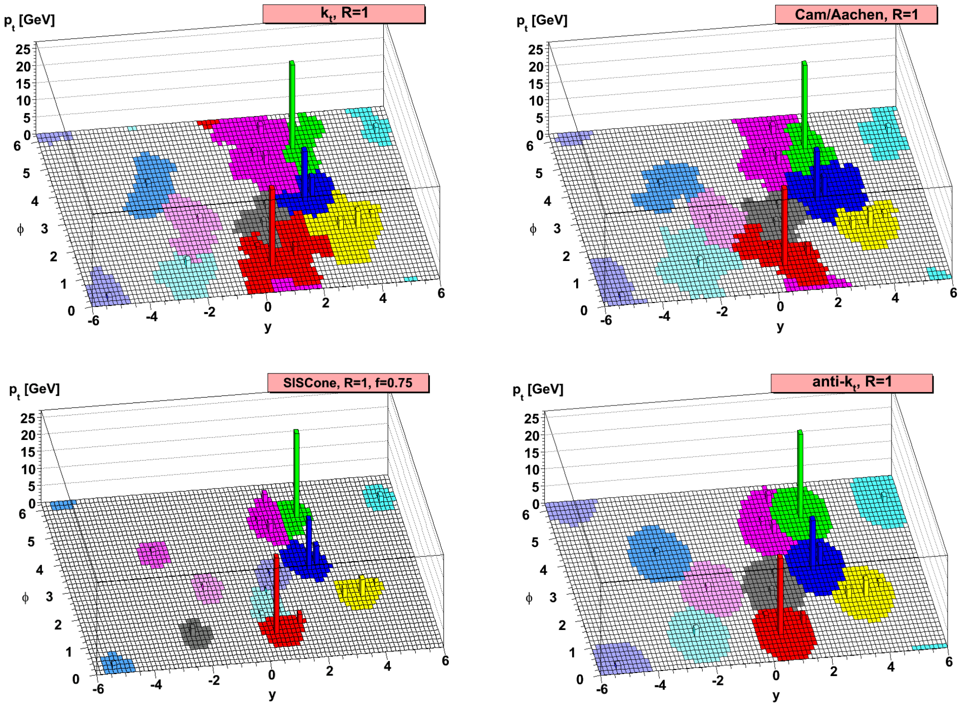

Figure 4.3.: A sample of particle-level jets generated with HERWIG++, clustered with the k_t, Cambridge/Aachen, anti-k_t, and SIScone algorithms. Many random soft “ghosts” have been added to illustrate the “active area” of the jets [122]

All three algorithms are infrared and collinear safe, but the clustering order and resulting jet shapes differ a lot. The clustering in an example event is shown in Figure 4.3, comparing the sequential-clustering algorithms with SIScone jets. The anti-k_t algorithm produces almost cone-type jets with a very regular shape. It is regarded as an infrared and collinear safe replacement of the iterative cone algorithm (previous standard jet-finding algorithm at CMS) and is the standard jet-finding algorithm at CMS. It is discussed in detail in [122]. In the following analysis, jets reconstructed with the anti-k_t algorithm and a distance parameter of $R = 0.5$ (short: AK5) are used if not otherwise stated.

4.4.2. Generator level jets

An important reference for many physics analyses are particle-level or generator jets. They are clustered using the jet-finding algorithms discussed in Section 4.4.1. Input objects to the jet formation are the four-momenta of “(semi-)stable” particles being the output of MC event generators like PYTHIA or HERWIG++. The decay of particles with a very short lifetime, e.g. π^0, is handled directly by the event generators.

Typical objects at this particle level are charged hadrons (mainly π^+/π^- and K^+/K^-), photons (mainly from π^0 decays) and neutral hadrons. At this particle level stage no propagation through or interaction with the detector has happened. The jets clustered from these particles (excluding neutrinos) are considered as reference objects for jet-energy corrections as their energy is independent of the detector response. Kinematic quantities of these jets are usually denoted with the superscript “gen”, e.g. p_T^{gen}.

4.4.3. Particle Flow jets

PF jets are clustered from the four-momenta of the particle candidates resulting from the identification process in Section 4.3.2. In comparison to classical calorimeter jets which only consider the energy deposits in (often coarse) calorimeter towers for clustering, the PF jets as depicted in Figure 4.4 try to closely resemble the particle level.

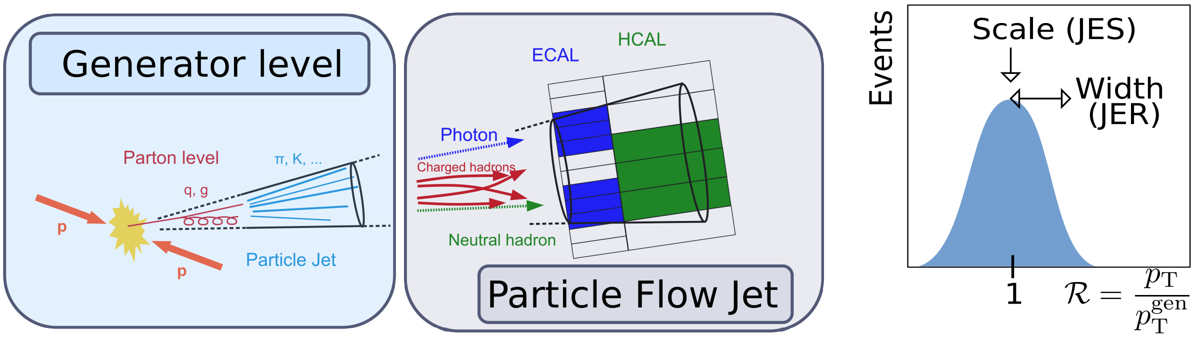

Figure 4.4.: Left: Visualization of a particle-level or generator jet and a PF jet which tries to resemble the particle-level as close as possible by reconstructing individual particle candidates. Sketch based on [123]; Right: Illustration of the jet-energy response distribution, indicating the average response (jet-energy scale (JES)) and the width (jet-energy resolution (JER)).

In general, the energy deposited in and reconstructed from the detector is not equal to the energy of the particle-level jet. This effect is quantified by the jet response, often referred to as jet-energy response or - more precisely - as jet transverse-momentum response. It is defined as the ratio $\mathcal{R}$ of the reconstructed transverse momentum p_T and the transverse momentum at the particle or generator level p_T^{gen}

$$\mathcal{R} = \frac{p_\mathrm{T}}{p_T^{gen}} \tag{4.4}$$

The average response is referred to as the jet-energy scale (JES) and is expected to be equal to one after applying the jet-energy corrections discussed in Section 4.5. The width of the response distribution is referred to as the jet-energy resolution or - more precisely - the jet transverse-momentum resolution. A detailed, yet concise, discussion of the jet-energy response at CMS can be found in [124]. Even though also systematically limited by the detector resolution and secondary interactions of the particles traversing the detector, the PF jets have a superior performance in comparison to calorimeter jets in terms of the jet-energy response and jet-energy resolution.

Particle Flow composition studies

As jets using PF objects have become the standard jet type for physics analyses at CMS, they are subject to the most detailed studies in the context of JEC as well. As the PF-jets are formed from individual PF-particle candidates, the understanding of the PF composition is a good handle on the quality of the MC-modelling. Energy scale differences observed for example as a function of $|\eta|$ in the form of relative residual corrections as discussed in Chapter 5 can be understood when deviations in the PF-energy composition are observed and vice versa. The PF compositions shown here are evaluated after the dijet event selection and analysis cuts detailed in Chapter 5. Some examples of these results are shown in Figure 4.5, where the fraction of jet p_T carried by PF components is depicted as a function of p_T and $|\eta|$. While the description is very accurate in the central detector region, some deviations at the %-level are observed in the endcap and forward regions.

A difference in the observed photon energy fraction f_photons could be linked to an ECAL scale different from one. This can roughly be approximated from

$$f_\mathrm{photons} = \frac{f^{true}_\mathrm{photons} \cdot R_\mathrm{photons}}{f^{true}_\mathrm{photons} \cdot R_\mathrm{photons} + f^{true}_\mathrm{remainder} \cdot R_\mathrm{remainder}} \tag{4.5}$$

where R_photons ($R_\mathrm{remainder}$) is the response for the photons (remaining components) respectively. Solving for R_photons yields

$$R_\mathrm{photons} = \frac{f^{true}_\mathrm{remainder} \cdot R_\mathrm{remainder} \cdot f_\mathrm{photons}}{f^{true}_\mathrm{photons} \cdot (1 - f_\mathrm{photons})} \tag{4.6}$$

The jet-energy response R_Jet can be calculated as

$$R_\mathrm{Jet} = R_\mathrm{photons} \cdot f^{true}_\mathrm{photons} + f^{true}_\mathrm{remainder} \cdot R_\mathrm{remainder} \tag{4.7}$$

Assuming $f_\mathrm{photons} = 23\%$ with $f^{true}_\mathrm{photons} = 25\%$ (implying $f^{true}_\mathrm{remainder} = 75\%$) and $R_\mathrm{remainder} = 1$ would then yield $R_\mathrm{Jet} \approx 0.974$, i.e. an energy scale difference of 2.6%. The detailed study of the differences of the relative energy scale in data and MC in the following will determine whether these modelling imperfections indeed become observable in the form of relative residual corrections. The powerful tool of PF composition study is used in Section 5.5.5 in parallel, to monitor the time stability of the jet-energy scale and to get hints at what is causing any observed time instability.

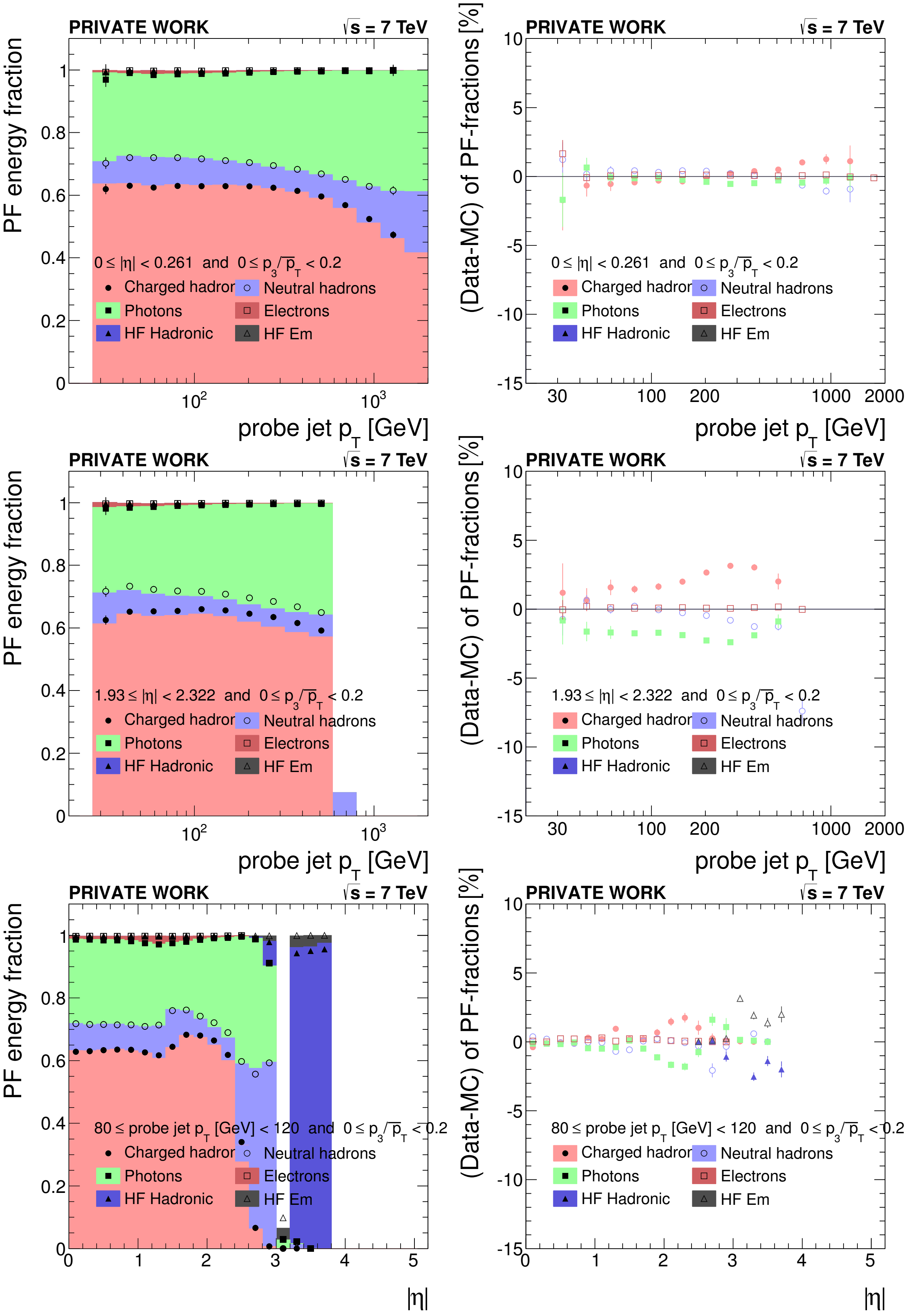

Figure 4.5.: PF-composition as a function of p_T and η, evaluated for the probe jet at arbitrary η (the other jet in the dijet system is required to be in the barrel region). “HF Em” and “HF Hadronic” denote the energy depositions in the hadronic forward calorimeter without tracker coverage. Electromagnetic and hadronic depositions are distinguished by the depth at which they leave a signal.

4.4.4. B-jet identification

The efficient identification of jets that were initiated by b-quarks is of great importance. These jets are present in many physics processes under study at the LHC, such as in decays of top quarks, the Higgs boson, and yet undiscovered particles predicted by supersymmetric models. Tools to identify b-jets allow to suppress otherwise overwhelming background processes.

B-hadrons are characterized by their long lifetimes, relatively large masses, and by a sizable fraction of semileptonic decays. Detailed descriptions and studies of the b-tagging performance at 7 and 8 TeV can be found in [125, 126].

Properties of reconstructed objects like tracks, (secondary) vertices, and identified leptons are used in a number of algorithms of varying complexity to identify b-jets. Different working points are available for each of the algorithms, indicating a misidentification probability of light quark jets of 10% (loose), 1% (medium), or 0.1% (tight).

The most efficient b-tagging algorithm in a wide variety of applications is the combined secondary vertex algorithm (CSV), based on likelihood ratios. If available, it mainly relies on secondary vertex information, but even without reconstructed secondary vertices it provides discrimination power using track-based lifetime information. As depicted in Figure 4.6, the b-jet efficiency is as high as $\approx 65\%$ at a misidentification probability for light quark and gluon jets of 1% and the discriminator is well modeled by simulation in 8 TeV data. Performance differences between data and simulation are taken into account in the form of scale factors and associated systematic uncertainties.

4.4.5. Quark/gluon-jet discrimination

It is known from direct experimental measurements [127–130] and expected from theoretical considerations that jets initiated by either light quarks or gluons have different properties.

Most notably, the gluon-initiated jets have been measured to be wider and to have higher particle multiplicities. These properties have been exploited in [131] to construct a discriminator applicable to reconstructed jet properties. It relies on the PF reconstruction to calculate discriminating observables and has been validated in Z+jets and dijet events. The performance achieved allows to select quark jets with an efficiency of up to 80% for a gluon rejection rate of $\approx 60\%$ as depicted in Figure 4.7.

4.4.6. Pileup-jet identification

In the high-luminosity environment of recent and future LHC runs, the impact of additional interactions on the reconstruction of the hard interaction of interest is twofold: First, the energy depositions due to pileup will often overlap with reconstructed jets

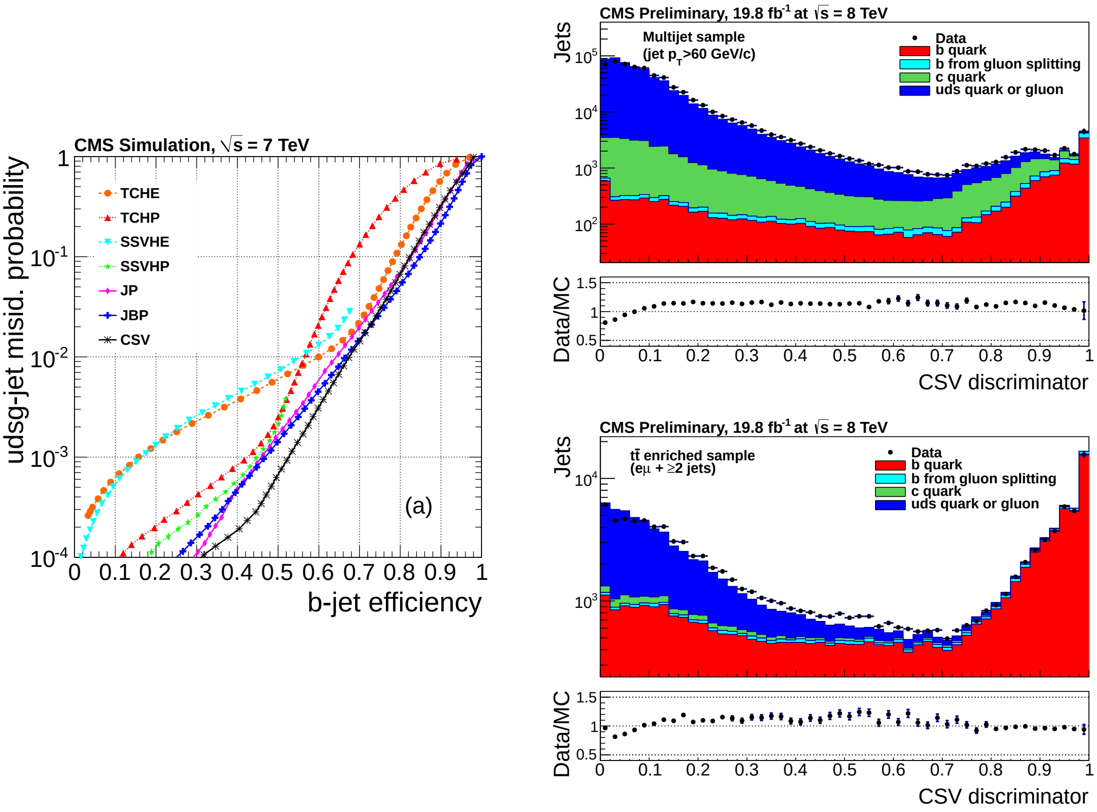

Figure 4.6.: Left: Bottom-jet tagging discriminator performance from simulation: Misidentification probability of light-quark or gluon initiated jets as a function of the b-jet efficiency [126]; Right: 8 TeV control distributions of the combined secondary vertex (CSV) discriminator value in multijet and $t\bar{t}$-enriched events [125].

leading to energy offsets that have to be subtracted, at least on average. Second, the energy depositions of multiple pileup events may overlay to form “pileup jets“ with sizable reconstructed p_T but no equivalent in the hard interaction. The rate of such pileup jets increases quadratically as a function of pileup as shown in Figure 4.8 for Z+jet events and can severely impede the selection of physics processes of interest. The largest fraction of jets with $p_T < 25\,\text{GeV}$ in the 2012 data-taking period is made up of pileup jets and even at higher p_T they contribute significantly to the observed jet rate.

Within CMS, a pileup jet identification algorithm has been developed [132] exploiting vertexing and shape related variables to distinguish the pileup jets from real jets. For example, the fraction of tracks in a jet associated with pileup vertices or a diffuse and wide energy distribution are hints for the occurrence of pileup jets. A large number of observables has been defined for the pileup jet identification. Their discrimination power is exploited in boosted decision trees and results in a performance of e.g. $\approx 99\%$ signal efficiency at a rejection rate of 86% for $20 < p_T < 30\,\text{GeV}$ in the tracker-covered detector region as depicted in Figure 4.8.

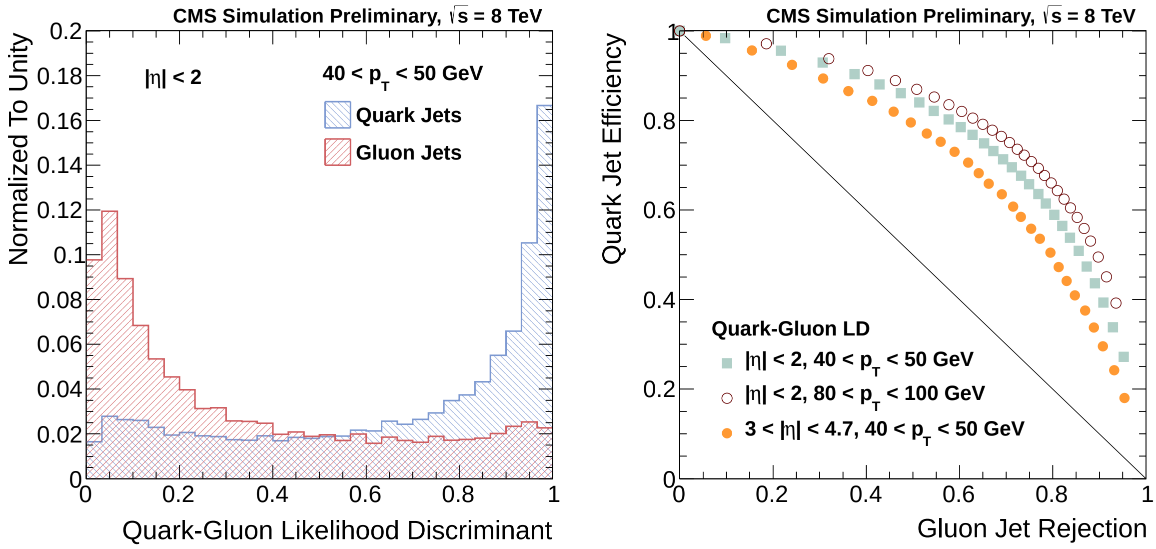

Figure 4.7.: Left: Shape of the quark-gluon likelihood discriminator for jets with $40 < p_{\mathrm{T}} < 50\,\mathrm{GeV}$; Right: Efficiency and rejection performance in the central (equipped with tracking) and forward region. [131].

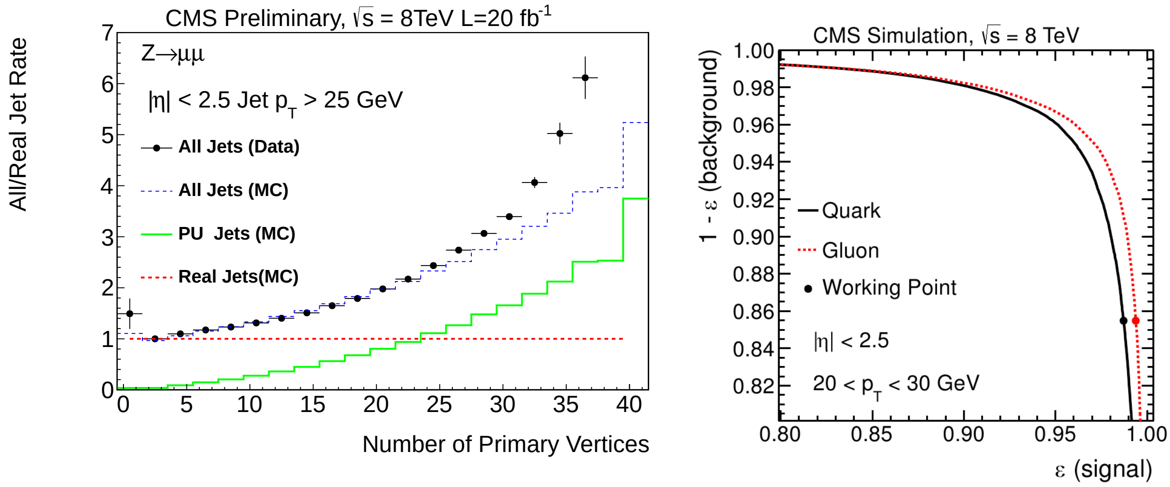

Figure 4.8.: Left: The rate of pileup jets relative to the real jet rate increases quadratically as a function of the number of primary vertices; Right: Efficiency and rejection performance of the pileup jet identification in the central detector region. [132].

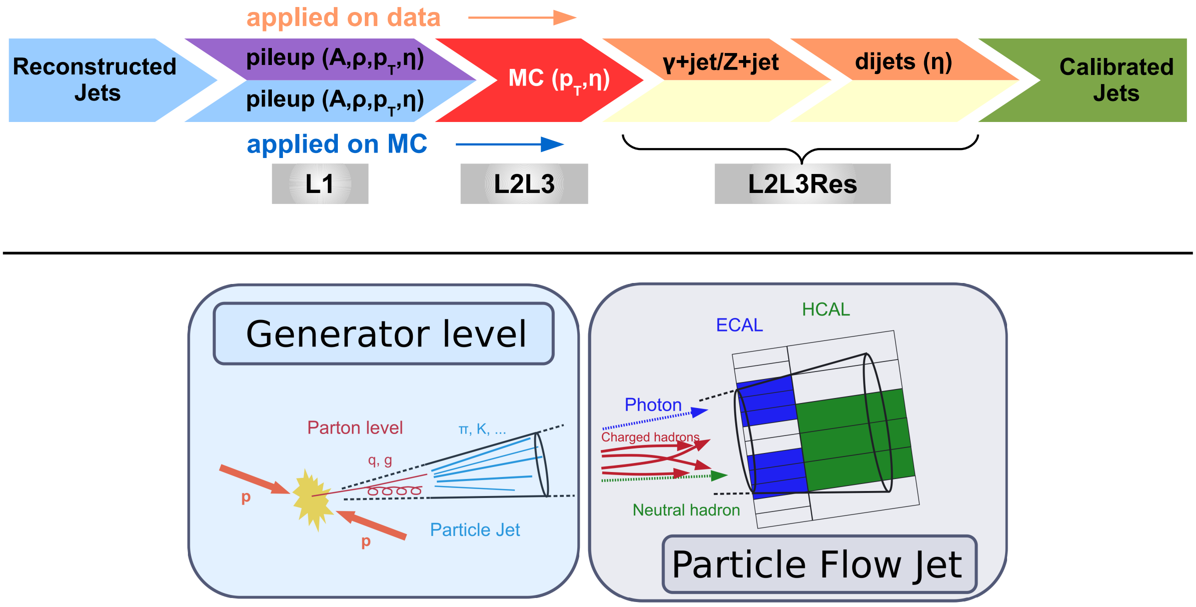

Figure 4.9.: Top: Sketch of the factorized approach to jet-energy corrections adopted by CMS, subsequently correcting for offset energy due to pileup, response dependencies as a function of p_{T}/η derived from simulations, and residual corrections from data-driven methods. Bottom: Sketch of a generator level jet used as reference level for JEC and a PF jet as an example of a reconstructed jet.

4.5. Jet-energy corrections at CMS

It is the goal of jet-energy corrections at CMS to correct the energy of reconstructed jets on average to an observable that is independent of the response of the CMS detector. This is achieved by relating the energy of reconstructed jets – on average – to that of particle level or generator jets. Following a factorized approach of successively correcting for pileup offset, non-linearity in p_{T}, and non-uniformity in η depicted in Figure 4.9, the average value of the response as defined in equation (4.4) is expected to be equal to one.

Residual Data/MC-differences are corrected according to the results of data-driven response studies in dijet, Z+jet, and γ+jet event topologies. A detailed account of the CMS jet energy calibration strategy at $\sqrt{s} = 7$ TeV is given in [133], performance plots for the final 2011 calibration are available in [134]. The jet-energy correction and jet-energy resolution results including a detailed account of the refined techniques used at $\sqrt{s} = 8$ TeV will be published in [135], performance plots are available in [136–138]. Differences between the jet-energy corrections at $\sqrt{s} = 7$ TeV and $\sqrt{s} = 8$ TeV are pointed out.

4.5.1. L1 - Pileup corrections

Corrections for pileup effects have become increasingly important during the LHC Run I. The mean number of primary vertices in 2011 data was $\langle N_{PV} \rangle \approx 7$ and increased to more than 20 in 2012. Both, in-time and out-of-time pileup from previous or following bunch crossings contribute to the energy offset amounting on average to $\Delta p_{\mathrm{T}} = 0.72\,\mathrm{GeV}/N_{PV}$ for central AK5 PF jets. This means that approximately one quarter of the energy of a 60 GeV jet is – on average – due to pileup. In the 2012 data-taking period PF-jets with charged hadron subtration (CHS) have become the default. PFCHS jets are clustered from a reduced list of PF candidates: Charged hadrons that can unambiguously be linked to pileup vertices are removed. This significantly mitigates the pileup effects and consequently reduces the size of JEC pileup corrections. A more generalized approach to pileup mitigation is currently under study to be adopted by CMS in the next data-taking period: The "pileup per particle identification" (`PUPPI`) [139] assigns weights for each reconstructed particle (PF candidate in the case of CMS) corresponding to its probability to stem from pileup.

CMS derives a pileup correction that depends on the jet area A, the median p_{T} density ρ per unit area, p_{T}, and η. The jet area A is defined as the catchment area of the jet and is practically determined by adding soft ghost particles prior to jet clustering as depicted in Figure 4.3. Pileup subtraction based on the jet area and ρ has been proposed in [119, 140]. ρ characterizes the soft jet activity being the sum of underlying event, electronics noise, and pileup activity. At CMS, it is calculated on an event-per-event basis from jets clustered with the k_t-algorithm with radius parameter $R = 0.6$ as the median of the distribution of ratios of the clustered jets' $p_{T,j}$ and jet area A_j:

$$\rho = \text{median}\left[\frac{p_{T,j}}{A_j}\right] \tag{4.8}$$

The choice of the median ensures that the result is not biased significantly by high p_{T} jets from the hard interaction and approximates the diffuse offset energy.

The parameters of the correction are mostly determined by comparing two MC samples with exactly the same hard events, one with and one without pileup overlay. In addition, the random cone method [133] applicable to data and MC is used to correct for the non-uniformity of the detector response in η.

In 2011, the correction was exactly the same in data and MC and contained no explicit p_{T}-dependence. Data/MC differences and the observed p_{T}-dependence were considered as systematic uncertainties. In 2012, a logarithmic p_{T}-dependence is explicitly corrected for and the slightly different dependence of the offset on ρ in data and MC at very high ρ is taken into account by providing two different sets of pileup corrections.

4.5.2. L2L3 - MC truth corrections

The L2L3-corrections are based on simulation and correct the energy of the reconstructed jets such that it equals - on average - the energy of the jets at particle level. Simulated jet events, generated with PYTHIA [49], tune Z2 (tune Z2* in 2012) and processed through the full, GEANT-based [141] detector simulation are used for the determination of these corrections. The generated and reconstructed jets are matched in space by requiring a separation of $\Delta R < 0.1$. For these pairs, the transverse momentum of the reconstructed jet p_{T}^{reco} and the response $p_{\mathrm{T}}^{reco}/p_{T}^{gen}$ are determined in fine bins of p_{T}^{gen} and η^{gen}. The correction factor is then determined as the inverse of the mean response as a function of p_{T}^{reco} in fine η-bins.

The use of MC for deriving the central part of JEC has many advantages: It is possible to cover corners of the phase space difficult to access in data, e.g. at very low or high p_{T} and at low or high pileup. In contrast to data-driven techniques, any biases in deriving corrections, e.g. due to the detector resolution, are avoided. In addition, with the knowledge of the MC truth one can define the jet flavor without relying on tagging techniques in order to evaluate uncertainties related to the jet flavor or derive flavor corrections.

The reliability of simulation is not to be taken for granted at HEP experiments. A good description of jet properties in data is mandatory to be able to make use of the simulation for the central part of JEC. Fortunately, the long set-up time of CMS has been used for the development of a very accurate detector simulation, tuned to testbeam data [142]. The validation in collision data confirmed the success of these elaborate preparations [143].

4.5.3. L2L3Res - Residual corrections from data-driven techniques

The corrections from simulated data (MC) are the basis of the jet-energy correction chain in CMS. These corrections are applied to data and MC in order to measure and compare the jet-energy scale. Response estimators from the p_{T} balance and the missing transverse energy projection fraction (MPF) method are used to determine the mean response in data and MC. The p_{T} balance and MPF-method will be covered in more detail in the context of the determination of residual corrections from dijet events in Section 5.1.

Absolute scale from Z+jet and γ+jet: Z+jet and γ+jet events provide a very clean signature with a well understood and precisely measured reference object balancing the jet. The jets are selected to be in the barrel region ($|\eta| < 1.3$) and back to back to the reference object.

The response estimators are defined as

$$\mathcal{R}_{\text{balance}} = \frac{p_{\mathrm{T}}^{jet}}{p_{\mathrm{T}}^{\gamma,Z}} \tag{4.9}$$

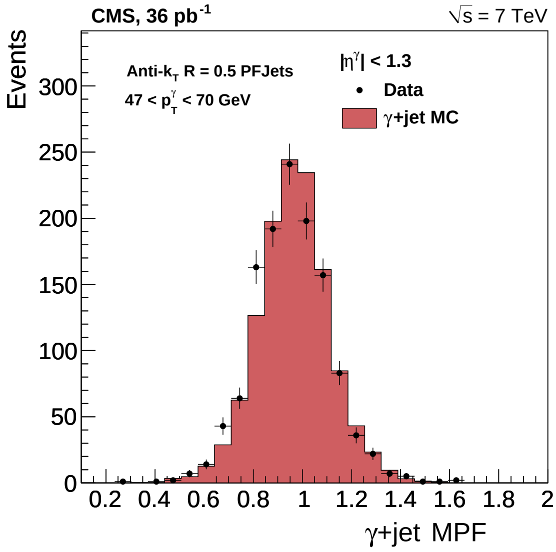

Figure 4.10.: Sample MPF-distribution for γ+jet events, [133]

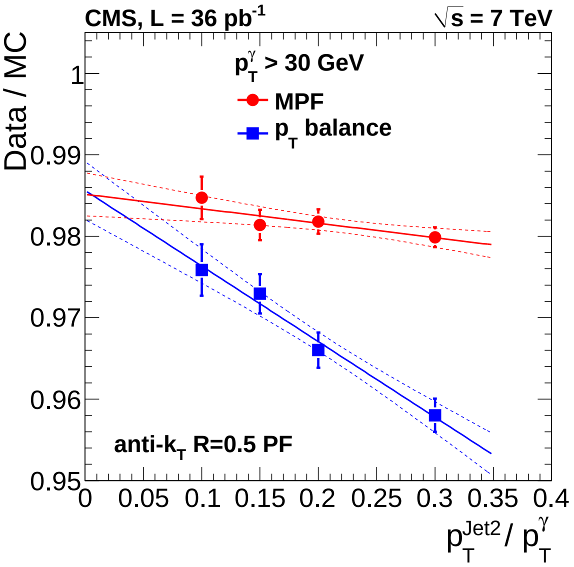

Figure 4.11.: Extrapolation to zero additional event activity for γ+jet, [133]

for the p_T-balance method and as

$$\mathcal{R}_\mathrm{recoil} = \mathcal{R}_{\gamma,\mathrm{Z}} + \frac{\vec{E}_\mathrm{T}^\mathrm{miss} \cdot \vec{p}_\mathrm{T}^{\,\gamma,\mathrm{Z}}}{(\vec{p}_\mathrm{T}^{\,\gamma,\mathrm{Z}})^2} \equiv R_\mathrm{MPF} \equiv \mathcal{R}_\mathrm{probe} \tag{4.10}$$

for the MPF-method, where $\vec{E}_\mathrm{T}^\mathrm{miss}$ is the missing transverse energy and $\mathcal{R}_{\gamma,\mathrm{Z}}$ the response of the reference photon or Z-boson. The idea underlying the MPF response estimator is that there is no intrinsic $\vec{E}_\mathrm{T}^\mathrm{miss}$ in such events and that the measured $\vec{E}_\mathrm{T}^\mathrm{miss}$ is instead induced by mismeasurements of the hadronic recoil. The projection of $\vec{E}_\mathrm{T}^\mathrm{miss}$ along the reference object axis can then be used to yield a MPF response estimator.

In order to determine the energy scale as a function of p_T, the distributions of the previously defined response estimators $\mathcal{R}_\mathrm{balance}$ and $\mathcal{R}_\mathrm{MPF}$ are evaluated. An example distribution is shown in Figure 4.10. The mean of the estimated response is determined in bins of p_T for different thresholds of p_T^{Jet2}/p_T^γ. The ratio of data to simulation of $\mathcal{R}_\mathrm{balance}$ and $\mathcal{R}_\mathrm{MPF}$ is extrapolated to zero additional event activity (corresponding to $p_T^{Jet2}/p_T^\gamma = 0$) to suppress the influence of soft radiation on the results. An example of such an extrapolation is shown in Figure 4.11 and illustrates the significantly reduced dependence of $\mathcal{R}_\mathrm{MPF}$ on the radiation modeling in simulation with respect to the p_T balance method. The resulting ratio of data to simulation as a function of p_T is depicted in Figure 4.12. A deviation of ≈ 1% is observed in the central detector region.

In 2010 and 2011, no evidence for a p_T-dependence of the Data/MC ratios of the response in Z+jet and γ+jet events is observed and the uncertainty on the p_T-dependence of the response is estimated from MC. In the 2012 data-taking period, given the much higher number of events in those channels, it is possible to further constrain a possible

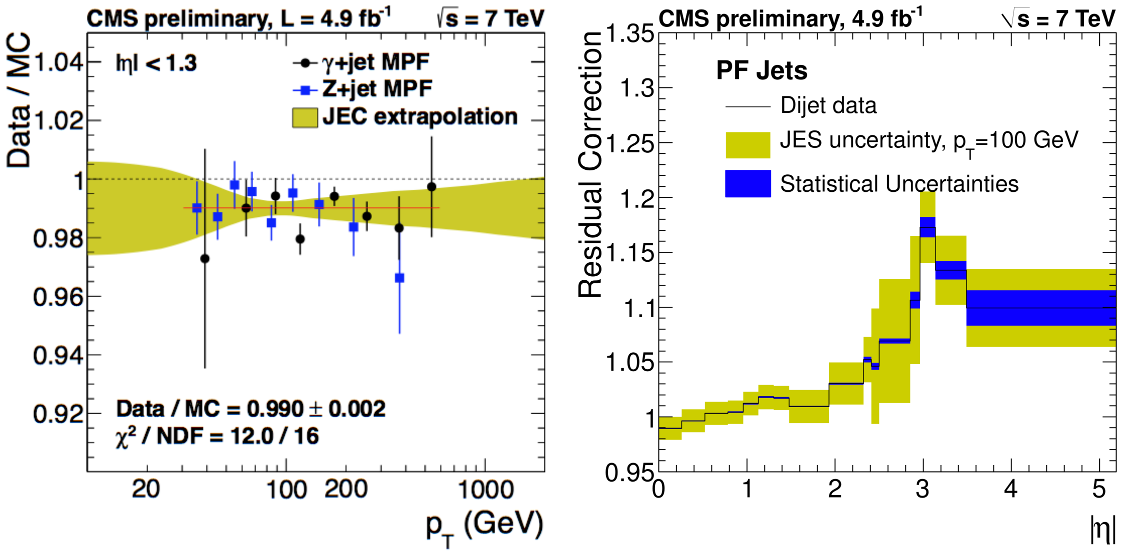

Figure 4.12.: Absolute scale determined from Z+jet and γ+jet in 2011 and the relative residual correction factor determined from dijet data in 2011 [134]

p_T-dependence from data and it is being considered to explicitly correct for any observed dependence.

Relative scale from dijet events: With the absolute scale accurately determined in the central detector region, the missing component is the relative scale. This is determined from dijet events and the used techniques are explained in detail in Chapter 5. As depicted in Figure 4.12, these relative differences are very small in the central detector region and below 5% in the region up to $|\eta| < 2.5$.

The remaining differences observed in Z/γ+jet and dijet events are explicitly corrected for in data in the L2L3Residual correction step which completes the previously discussed jet energy correction chain. A significant advantage of this approach is that biases inherent to data-driven methods are canceled to first order by determining only the ratio of data to simulation.

4.5.4. Jet-energy scale uncertainties for 2011 data

Starting with the 2011 dataset, the systematic uncertainties associated with the calibration are provided in the form of mutually uncorrelated signed sources from which a correlation matrix can be calculated easily. Each source is parameterized as a function of p_T and η. If appropriate, decorrelations are achieved by coarsely splitting sources into regions in p_T and η. The quadratic sum of all individual sources adds up to the total JES uncertainty.

The JES uncertainties are classified in four broad categories: pileup offset, relative calibration of the jet energy scale versus η, absolute energy scale versus p_T, and jet flavor dependent differences. As an extra uncertainty, the residual time dependence of the JES is considered.

There are five sources being considered for the pileup offset, most relevant at low p_{T}: The *PileUpDataMC* source encodes observed Data/MC differences in the offset measurement using the random cone method, *PileUpPt* covers the observed offset dependence on jet p_{T} in the random cone method, *PileUpBias* covers the difference between the MC truth offset and the offset measured in MC using the random cone method. *PileUpOOT* estimates the residual out-of-time pileup for prescaled triggers and *PileUpJetRate* covers for observed jet rate variations as a function of the number of reconstructed primary vertices in 2011 single jet triggers after applying pileup-corrections.

For the relative jet calibration, variations of the jet energy resolution (*RelativeJER*), statistical uncertainties in the forward region (*RelativeStat*), and an uncertainty related to the corrections for final-state radiation (*RelativeFSR*) are considered. A more detailed account of systematic uncertainties related to the derivation of residual corrections from dijet events is given in Chapter 5.

The absolute scale uncertainties cover for the uncertainties related to the in-situ measurements and uncertainties related to the MC extrapolation to high and low p_{T} outside of the p_{T}-range directly accessible using Z+jet and γ+jet events. Statistical uncertainties of the measurements are propagated as *AbsoluteStatistical*, uncertainties on the ECAL and the tracking scale as *AbsoluteScale*, MPF-method biases as *AbsoluteMPFBias*, and the difference in flavor mixture between the nominal QCD mixture and the Z+jet/γ+jet composition is covered by *AbsoluteFlavorMapping*. *SinglePion* and *HighPtExtra* account for a variation of the single particle response within uncertainties indicated by direct measurements and response differences due to different fragmentation and underlying event modeling in PYTHIA and HERWIG++.

Differences in the detector response of light, charm, and bottom quark as well as gluon-initiated jets relative to the nominal QCD mixture are evaluated by comparing PYTHIA and HERWIG++ as *Flavor* uncertainty source, taking the largest observed difference as uncertainty. Observed time-dependent variations of the detector response not fully compensated in the prompt reconstruction in the endcap regions are considered as *Time* uncertainty.

The individual uncertainty sources available for 2011 analyses are listed in Table 4.1. In the central detector region, the systematic uncertainties are dominated by uncertainties related to pileup at low p_{T}. For extremely high transverse momenta, not accessible by Z+jet and γ+jet events, MC and single particle response extrapolation uncertainties become dominant. The total systematic jet-energy scale uncertainty is as low as about 1% at 200 GeV for central jets. In the endcap region, the *Time* uncertainty dominates. At high $|\eta|$, the uncertainties related to the relaive intercalibration using dijet events give the largest contributions to the total uncertainty.

In spite of the much harsher pileup conditions for analyses of 2012 data, the jet-energy scale uncertainties could be kept at a comparable level for 8 TeV analyses. The total

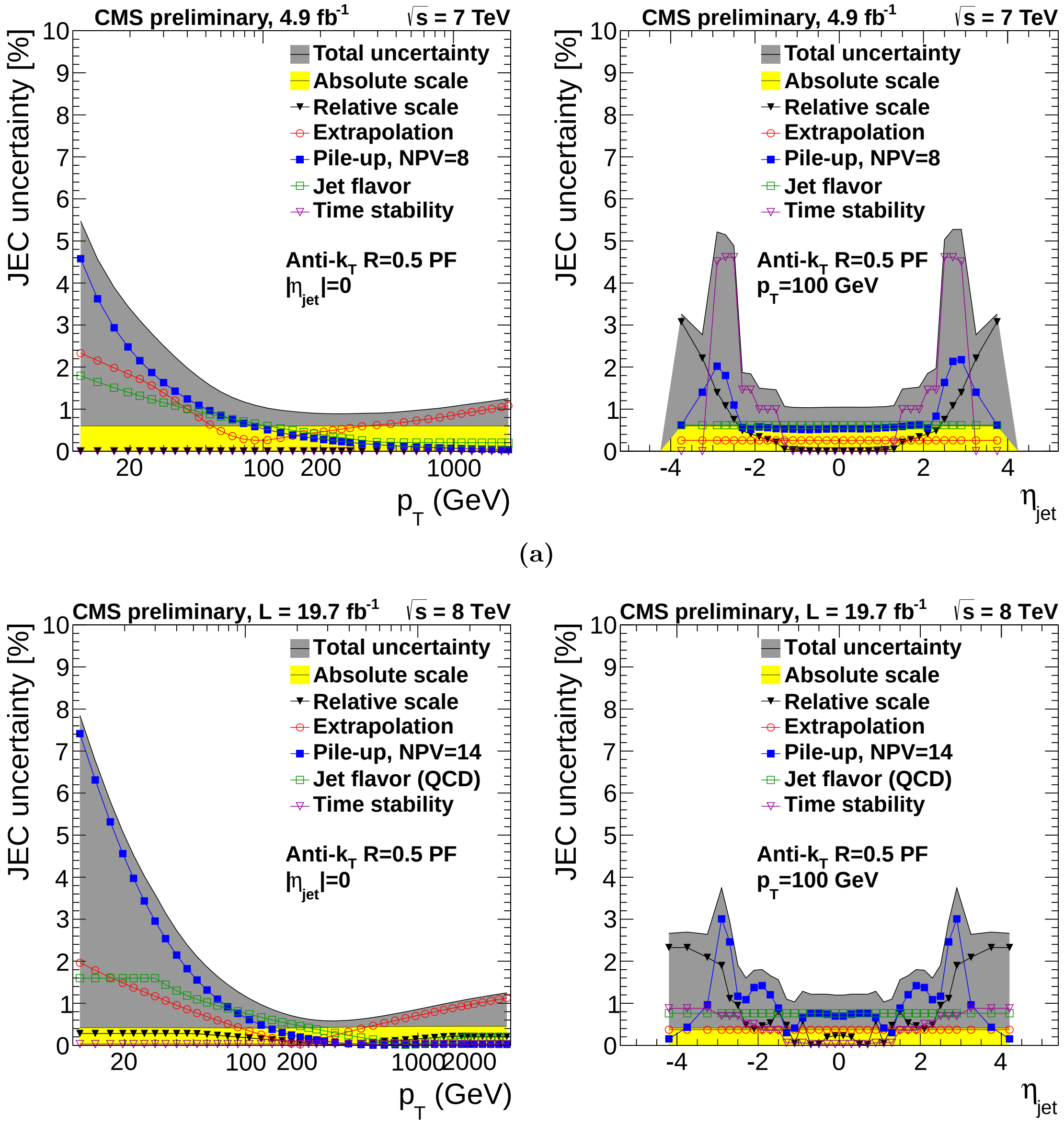

(a)

(b)

Figure 4.13.: (a): 2011 jet-energy scale uncertainties as a function of p_T and η [134]; (b): 2012 jet-energy scale uncertainties as a function of p_T and η [136]

jet-energy scale uncertainty is below 1% for central jets with a p_T between 200 and 500 GeV. Changes in the determination of the flavor response uncertainties in the 2012 data-taking period are discussed in Section 4.5.5. Plots summarizing the jet-energy scale uncertainties in 2011 and 2012 are shown in Figure 4.13.

For analyses like the top-quark mass measurements with simultaneous JSF-fit, which are sensitive to the differences in the response between light quark and gluon originated jets to b-quark originated jets, it is recommended to apply an additional b-JES uncertainty. In 2011 analyses, the response of b-jets is varied by the full flavor-dependent JES uncertainty

Table 4.1.: List of CMS JEC uncertainty sources with range of validity in $|\eta|$ indicated as suffix BB($|\eta| < 1.3$); EC1($1.3 < |\eta| < 2.5$); EC2($2.5 < |\eta| < 3.0$); EC($1.3 < |\eta| < 3.0$); HF($3.0 < |\eta| < 5.2$)

Category	Sources
Pileup offset	PileUpDataMC, PileUpBias PileUpOOT, PileUpJetRate PileUpPtBB, PileUpPtEC, PileUpPtHF
η-dependent calibration	RelativeStatEC2, RelativeStatHF, RelativeFSR RelativeJEREC1, RelativeJEREC2, RelativeJERHF
p_{T}-dependent calibration	AbsoluteStat, AbsoluteScale AbsoluteMPFBias, AbsoluteFlavorMapping HighPtExtra, SinglePion
Other	Flavor, Time

as defined above to get a conservative estimate. Cross-checks varying the b-fragmentation and semileptonic b-hadron decays as well as comparing PYTHIA and HERWIG directly in $t\bar{t}$ events yield uncertainties of comparable size. This more detailed determination of b-JES specific systematic uncertainties in 2012 analyses is discussed in detail in Chapter 7.

4.5.5. Flavor response uncertainties in 2012

The flavor response uncertainty in 2010 and 2011 was estimated as the envelope of the light quark and gluon flavor[1] response differences defined as

$$\frac{\frac{\mathcal{R}^{\text{Flavor}}_{\text{Herwig}}}{\mathcal{R}^{\text{Inclusive}}_{\text{Herwig}}}}{\frac{\mathcal{R}^{\text{Flavor}}_{\text{PYTHIA}}}{\mathcal{R}^{\text{Inclusive}}_{\text{PYTHIA}}}} \tag{4.11}$$

where $\mathcal{R}^{\text{Flavor}}$ is the response of jets of a particular flavor and $\mathcal{R}^{\text{Inclusive}}$ is the inclusive response of all jets in the standard QCD MC sample used for determining the jet-energy corrections. The 2010 results are depicted in Figure 4.14.(a), published in [133] and considered as valid for the 2011 data-taking period. Bottom and charm quark responses were not included in the plot, but were found to be covered by the envelope between light quarks and gluons.

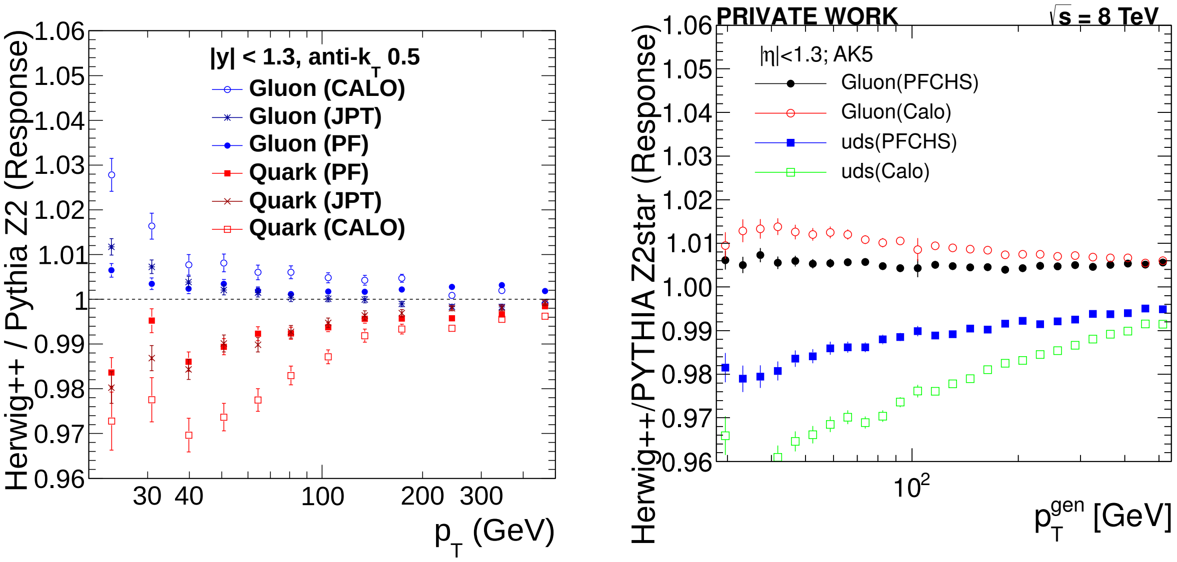

(a) (b)

Figure 4.14.: (a): Flavor response difference in PYTHIA/HERWIG++ in 2010 MC samples for different jet types: calorimeter jets (CALO), jet-plus-track jets (JPT), and Particle Flow jets (PF). Published by CMS in [133]; (b): Flavor response differences determined in the same way in 2012 MC samples for calorimeter jets (Calo) and PF-jets with charged hadron subtraction (CHS) as discussed in Section 4.5.1.

For the 2012 data-taking period, the flavor responses were re-evaluated and the corresponding plot is shown in Figure 4.14.(b). Similarly to the evaluation at 7 TeV, the observed differences are significantly reduced for the PF event reconstruction in

---

[1] For simplicity, flavor is used to denote both, quarks and gluons, in the context of flavor response uncertainties

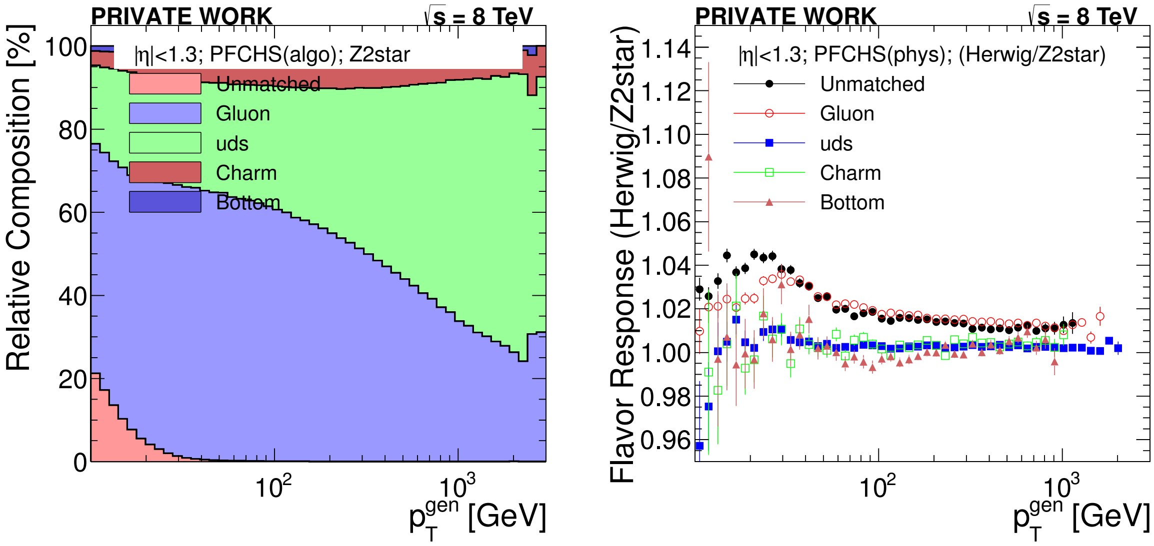

(a) (b)

Figure 4.15.: (a): Flavor composition in the barrel region for QCD MC sample (unmatched means that no parton could be matched within $\Delta R < 0.3$ with respect to the reconstructed jet axis); (b): Individual flavor response differences between PYTHIA and HERWIG++ in 2012 MC samples

comparison to calorimeter jets. However, the envelope of flavor response differences is much larger than that found for 7 TeV due to the large deviation of the light quark response in the double-ratio leading to an increased systematic uncertainty. Further studies showed that the response differences between PYTHIA and HERWIG++ in the 8 TeV MC production (which uses different software versions of HERWIG++ and PYTHIA for the event generation in comparison to the 2010 7 TeV production) are limited to the description of gluons which are the dominant partons produced in QCD events. This is illustrated in Figure 4.15 showing the jet composition of the QCD MC sample and the response differences between PYTHIA and HERWIG++ for each flavor without normalizing to the inclusive response (which is dominated by the gluon response). The reasons for the relatively large difference in the gluon (inclusive) response between PYTHIA and HERWIG++ is not fully understood. The most viable solution to resolve the difference seems to be to use tunes, as consistent as posssible, for both generators.

Reapplying the 7 TeV method to estimate systematic uncertainties related to the flavor response suggests that the modeling of light and heavy quarks is doubtful. As only the description of the gluon response is different between PYTHIA and HERWIG++, a more sophisticated scheme to determine flavor uncertainties was developed by the JEC group for the 2012 JEC uncertainties: As the jet-energy response can directly be probed in-situ using Z+jet/γ+jet and dijet events with great precision, no additional flavor uncertainty is needed in case the flavor composition exactly matches the reference flavor composition used for the derivation of residual corrections. For flavor compositions which differ from this reference composition, the response differences of the individual flavors relative to the reference composition are propagated. This means that for gluon-dominated samples the flavor-related uncertainties are relatively large. As a default, the flavor composition of QCD events, also used for deriving the MC truth jet-energy corrections, is assumed to provide a generic flavor composition assumption conservative enough for most analyses. If the gluon fraction in the examined sample is significantly lower (higher), it is possible to derive an analysis-specific flavor uncertainty which is reduced (increased) depending on the gluon fraction. For a number of predefined sample compositions, the corresponding uncertainties are shown in Figure 4.16

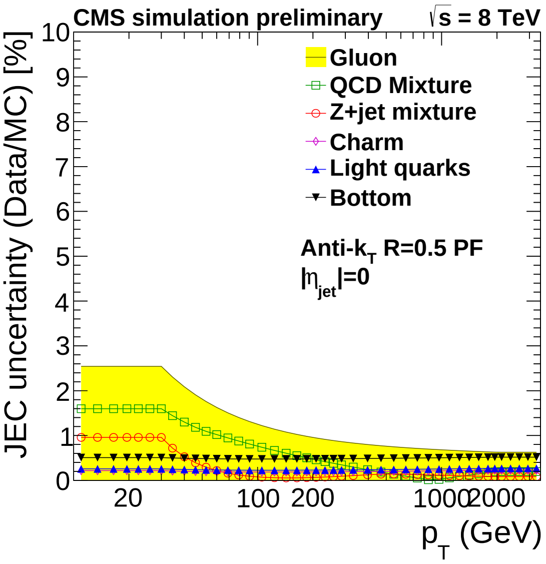

Figure 4.16.: Flavor uncertainty for different predefined sample compositions directly provided in the form of uncertainty sources. As conservative estimate, the QCD mixture is assumed as default flavor composition in the total JES uncertainties.

4.6. Missing Transverse Energy

As discussed in Section 4.2, most particles traversing the detector leave typical signatures. Notable exceptions are neutrinos and hypothetical weakly interacting neutral particles.

If no such particles are present in an event, the vectorial sum of all transverse momenta cancels. This momentum balance does not strictly hold true for reconstructed events due to the finite resolution of the detector. It is useful to define the missing transverse energy $\vec{E}_{\mathrm{T}}^{\mathrm{miss}}$ as the imbalance of all "visible" particles interacting with the detector. The negative vectorial sum of all visible particles, $\vec{E}_{\mathrm{T}}^{\mathrm{miss}}$, is then an estimator of the transverse momentum sum of the invisible particles.

This definition is also used for reconstructed quantities and a large number of $\vec{E}_{\mathrm{T}}^{\mathrm{miss}}$ reconstruction methods exist in CMS. A detailed account of the $\vec{E}_{\mathrm{T}}^{\mathrm{miss}}$-reconstruction and performance at 7 and 8 TeV is given in [144, 145].

The most widely used $\vec{E}_{\mathrm{T}}^{\mathrm{miss}}$ is called PF-$\vec{E}_{\mathrm{T}}^{\mathrm{miss}}$ and calculated as the negative vectorial sum over all PF particle transverse momenta. A precise calibration of all physics objects is crucial as the $\vec{E}_{\mathrm{T}}^{\mathrm{miss}}$ reconstruction is sensitive to mismeasurements and detector malfunctions in the whole detector coverage.

In order to reduce the impact of various possible misreconstructions, most often fake high amplitude signals in the calorimeters, a number of filters have been developed and are applied when using $\vec{E}_{\mathrm{T}}^{\mathrm{miss}}$ for physics analyses.

Biases due to remaining miscalibration are largely reduced by using type-I-corrected $\vec{E}_{\mathrm{T}}^{\mathrm{miss}}$. For this, the jet-energy corrections are propagated as

$$\vec{E}_{\mathrm{T}}^{\mathrm{miss,corr}} = \vec{E}_{\mathrm{T}}^{\mathrm{miss}} - \sum_{\mathrm{jets}} \left(\vec{p}_{\mathrm{T,jet}}^{\,\mathrm{L1L2L3}} - \vec{p}_{\mathrm{T,jet}} \right) \tag{4.12}$$

where only PF jets with $p_{\mathrm{T,jet}}^{\mathrm{L1L2L3}} > 10\,\mathrm{GeV}$ are considered.

The studies in [144, 145] show an excellent understanding of $\vec{E}_{\mathrm{T}}^{\mathrm{miss}}$ in data. Specialized reconstruction techniques using the association of PF candidates to primary vertices or multivariate techniques have been commissioned and help to maintain an excellent $\vec{E}_{\mathrm{T}}^{\mathrm{miss}}$ resolution, even in harsh pileup conditions.

Chapter 5

Relative residual corrections determined from dijet events

In the factorized approach to jet energy corrections at CMS, the pileup (L1) and MC truth corrections (L2L3) are the fundamental components as described in Section 4.5. If the simulation fully describes the data, no additional corrections are needed to relate the energy scale of reconstructed jets – on average – to that of generator jets. Data-driven analyses are used to compare the jet-energy response between simulation and data. Slight differences are in the jet-energy response are observed. Thus, (small) residual corrections are determined to correct for these differences. Biases, that would have to be taken care of explicitly when determining the scale directly using data-driven techniques, are drastically reduced by correcting only for the differences.

In this chapter, studies on the determination of relative residual corrections using dijet events are presented. These correct the response differences between data and simulation as a function of η and p_{T} relative to the well calibrated central detector region. Dijet events are well suited for this purpose, as a dataset covering a large phase space at high jet momenta can easily be obtained due to the high QCD jet production cross section. The limiting factor of the size of the dataset is the employed set of triggers which limits the number of available events, especially at low p_{T}.

Previous detailed studies of the determination of the relative jet-energy scale and relative residual correction in CMS are documented in [146, 147]. The final calibration obtained for 2010 data and the p_{T}-balance technique is documented in [133]. Public CMS results based on work performed in the context of this thesis include cross-checks of the relative scale in 2010 in [133] and the final calibration results for 2011 data as documented in [134, 148]. For the 2012 results documented in [135–138], the setup originally developed for 2010 and 2011 data has been developed further and used for the determination of residual corrections. The setup is based upon and extends the University of Hamburg calibration framework Kalibri [149].

In the following, the techniques for the determination of the relative residual corrections are summarized. Section 5.1 describes the p_{T} balance and the missing transverse energy projection fraction (MPF) method. In this analysis, the MPF-method is introduced to CMS for the response determination in dijet events for the first time. Section 5.2

introduces the definition of the relative residual correction which can be determined using either the response from the MPF or the p_{T} balance methods as input. Technicalities, like the used samples, the determination of trigger thresholds, applied jet-energy corrections, the event selection, and mandatory reweightings of the simulation, are discussed in Section 5.3.

As an example of the determination of residual corrections, the derivation of the correction on the full 2011 dataset, re-reconstructed using improved detector calibration constants, and the corresponding evaluation of systematic uncertainties are discussed in detail in Section 5.4. Several additional studies, which were performed either on 2011 or on 2012 data samples, are discussed in Section 5.5. These include a study of the time stability of the response, tests regarding the optimal choice of the binning variables and trigger strategy, a study of jet-energy resolution scale factors using the dijet asymmetry method, the φ and PU-dependence of the response as well as an evaluation of the impact of close-by jets on the measured jet-energy response. The tool of Particle Flow composition studies introduced in Section 4.4.3 is used as a cross-check for the study of the time stability.

5.1. Methodology

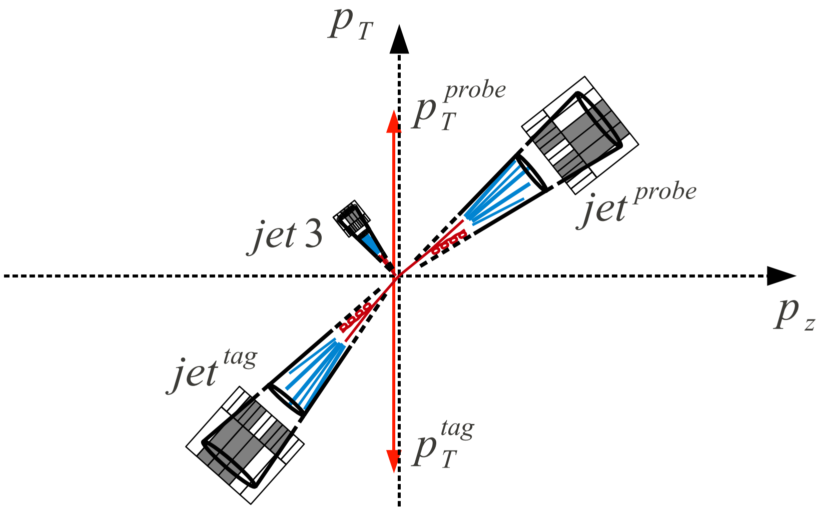

Figure 5.1.: Dijet topology: The momenta of the two back-to-back jets are projected to the transverse plane. The ideal dijet topology is degraded by additional jets.

The basic event topology of dijet events is depicted in Figure 5.1. While an ideal dijet event would manifest itself as two jets with exactly balanced transverse momenta, back-to-back in φ, the radiation of further hard partons can lead to additional jets distorting the momentum balance of the leading two jets. In order to select events closely resembling the ideal topology, the two jets in the event leading in p_{T} are required to be separated by

$$\Delta\varphi(j_1, j_2) = \min(|\varphi_1 - \varphi_2|, 2\pi - |\varphi_2 - \varphi_1|) > 2.7 \tag{5.1}$$

Additionally, cuts on the relative transverse momentum of the third jet

$$p_{\mathrm{T}}^{\mathrm{rel}} = \frac{p_{\mathrm{T,j_3}}}{0.5 \cdot (p_{\mathrm{T,j_1}} + p_{\mathrm{T,j_2}})} \tag{5.2}$$

are made, where $p_{\mathrm{T,j}_i}$ refers to the p_{T} of the ith jet.

For the determination of the relative residual corrections in η, one of the two leading jets is required to be in the barrel region ($|\eta| < 1.3$). p_{T}^{barrel} refers to the p_{T} of this jet in the central detector region, and p_{T}^{probe} refers to the p_{T} of the other of the two leading jets at arbitrary η.

The average transverse momentum of the two leading jets is defined as

$$\overline{p}_{\mathrm{T}} = p_{\mathrm{T}}^{\mathrm{ave}} = \frac{p_{\mathrm{T}}^{barrel} + p_{\mathrm{T}}^{probe}}{2} \tag{5.3}$$

5.1.1. Definition of the asymmetry and the relative response (RR)

The p_{T}-balance method uses momentum conservation to determine the energy response of probe jets at arbitrary values of the pseudorapidity η relative to jets in a control region (here: barrel jets in the region $|\eta| < 1.3$). The method has first been used at the UA2-experiment [150], and is used at both Tevatron experiments [151–153] and as central method for the 2010 CMS jet-energy corrections [133]. Here, the method is utilized to determine a residual correction from the comparison of data and simulation.

The following quantities are needed for its application: The asymmetry $\mathcal{A}$ for events with at least two jets is defined as

$$\mathcal{A} = \frac{p_{\mathrm{T}}^{probe} - p_{\mathrm{T}}^{barrel}}{p_{\mathrm{T}}^{probe} + p_{\mathrm{T}}^{barrel}} \tag{5.4}$$

The asymmetry distributions are determined as a function of $\overline{p}_{\mathrm{T}}$ and η^{probe}. The average value of the $\mathcal{A}$ distribution, $\langle\mathcal{A}\rangle$, is used to define the relative response $\mathcal{R}_{\mathrm{rel}}$ (RR)[1] of the probe jet with respect to the barrel jet

$$\mathcal{R}_{\mathrm{rel}}(\eta^{probe}, \overline{p}_{\mathrm{T}}) = \frac{1 + \langle\mathcal{A}\rangle}{1 - \langle\mathcal{A}\rangle} \tag{5.5}$$

---

[1] Relative response (RR) will in the following always refer to the response estimator from the asymmetry/p_{T} balance method

With a sufficiently fine binning in $\overline{p}_{\mathrm{T}}$, this reduces to $\mathcal{R}_{\mathrm{rel}} \approx \langle p_{\mathrm{T}}^{probe}\rangle / \langle p_{\mathrm{T}}^{barrel}\rangle$ (and $p_{\mathrm{T}}^{probe}/p_{\mathrm{T}}^{barrel}$ for a single event).

The resolution bias is an effect inherent to the p_{T}-balance method in dijet events. This bias is caused by the fact that the resolution of both, the probe jet and the barrel jet, is of comparable size. Due to the steeply falling p_{T} spectrum of QCD dijet events, the response is biased towards higher values when recording $\mathcal{R}_{\mathrm{rel}}$ as a function of reconstructed p_{T}. For jets with slightly different resolutions, the response is biased in favor of the jet with the worse response, reducing $\mathcal{R}_{\mathrm{rel}}$ at high $|\eta|$.

The binning in $\overline{p}_{\mathrm{T}}$ and the definition of $\mathcal{R}_{\mathrm{rel}}$ assure that the resolution bias, described in more detail in [133, 154], is minimized. For the determination of residual corrections from the MC/Data ratio of $\mathcal{R}_{\mathrm{rel}}$, it is assumed that the effect of the resolution bias is the same in data and simulation after considering resolution differences in data and simulation.

Asymmetry and jet-energy resolution

Another possible application of the asymmetry of the dijet system is the determination of the jet-energy resolution (JER). In a more generic formulation of the asymmetry for the two leading jets, it is given as

$$\mathcal{A} = \frac{p_{T,j_2} - p_{T,j_1}}{p_{T,j_2} + p_{T,j_1}}. \tag{5.6}$$

The variance of the asymmetry $\mathcal{A}$ is then given by

$$\sigma_{\mathcal{A}}^2 = \left|\frac{\partial\mathcal{A}}{\partial p_{T,j_2}}\right|^2 \cdot \sigma(p_{T,j_2})^2 + \left|\frac{\partial\mathcal{A}}{\partial p_{T,j_1}}\right|^2 \cdot \sigma(p_{T,j_1})^2 \tag{5.7}$$

The most straightforward approach to extract the JER from the variance of the asymmetry distribution is to select such events that $p_{\mathrm{T}} \approx p_{T,j_2} \approx p_{T,j_1}$ and $\sigma(p_T) \approx \sigma(p_{T,j_2}) \approx \sigma(p_{T,j_1})$. In this case, equation (5.7) simplifies to

$$\frac{\sigma(p_T)}{p_T} \approx \sqrt{2}\sigma_{\mathcal{A}} \tag{5.8}$$

and $\sigma_{\mathcal{A}}$ is proportional to the jet-energy resolution. As the jet-energy resolution is known to depend on the pseudorapidity η, an event selection with both leading jets in the same $|\eta|$-region is pursued, assuming $|\eta|/\eta$ symmetry. Additional jets and the underlying event distort the perfect balance, even on the particle level. In Section 5.5.4, a study on the agreement of the modeling of the JER in MC and data based on the asymmetry method is performed.

5.1.2. Definition of the Missing Transverse Energy Projection Fraction (MPF)

The missing transverse energy projection fraction (MPF) method was pioneered by [155] and used for the derivation of jet-energy corrections at both Tevatron experiments [151–154]. At the LHC experiments, it has been used for energy calibrations in Z+jet and γ+jet topologies.

The MPF method is based on the property of dijet events having either of the jets (the barrel jet for the analysis of the response) perfectly balanced by its hadronic recoil in the transverse plane:

$$\vec{p}_{\mathrm{T,true}}^{\,\mathrm{barrel}} + \vec{p}_{\mathrm{T,true}}^{\,\mathrm{recoil}} = 0 \tag{5.9}$$

As dijet events have no intrinsic missing transverse energy ($\vec{E}_{\mathrm{T}}^{\mathrm{miss}}$), the measured $\vec{E}_{\mathrm{T}}^{\mathrm{miss}}$ is caused by mismeasurements of the jets and hadronic recoil:

$$\mathcal{R}_{\mathrm{barrel}} \cdot \vec{p}_{\mathrm{T,true}}^{\,\mathrm{barrel}} + \mathcal{R}_{\mathrm{recoil}} \cdot \vec{p}_{\mathrm{T,true}}^{\,\mathrm{recoil}} = -\vec{E}_{\mathrm{T}}^{\mathrm{miss}} \tag{5.10}$$

The recoil denotes any event activity other than the barrel jet potentially showing up in $\vec{E}_{\mathrm{T}}^{\mathrm{miss}}$. This is primarily the probe jet, but contributions from initial and final state radiation (additional soft jets in the event), underlying event, out-of-cone energy depositions or undetected particles like neutrinos will generally also occur. Solving these equations for $\mathcal{R}_{\mathrm{recoil}}$ gives:

$$\mathcal{R}_{\mathrm{recoil}} = \mathcal{R}_{\mathrm{barrel}} + \frac{\vec{E}_{\mathrm{T}}^{\mathrm{miss}} \cdot \vec{p}_{\mathrm{T,true}}^{\,\mathrm{barrel}}}{(\vec{p}_{\mathrm{T,true}}^{\,\mathrm{barrel}})^2} \tag{5.11}$$

As the calibration is done relative to the central detector part, whose absolute scale is separately determined using γ and Z+jet-events, $\mathcal{R}_{\mathrm{barrel}}$ can be set equal to one (and $p_{\mathrm{T}}^{barrel} = \vec{p}_{\mathrm{T,true}}^{\,\mathrm{barrel}}$) to determine the approximate scale relative to the one in the barrel region. In order to identify $\mathcal{R}_{\mathrm{probe}}$with $\mathcal{R}_{\mathrm{recoil}}$, the other contributions to the recoil have to be small. Even though most contributions are expected to cancel on average, it should be ensured that most of the recoil is indeed clustered in the probe jet and the influence of initial and final state radiation (ISR and FSR) is reduced as much as possible. For this purpose, any further jets in the selected back-to-back dijet events need to be suppressed by cutting on $p_{\mathrm{T}}^{\mathrm{rel}}$ as defined in equation (5.2). Once this suppression is applied the response simplifies to

$$\mathcal{R}_{\mathrm{probe}} \approx \mathcal{R}_{\mathrm{MPF}} = 1 + \frac{\vec{E}_{\mathrm{T}}^{\mathrm{miss}} \cdot \vec{p}_{T}^{\,\mathrm{barrel}}}{(\vec{p}_{T}^{\,\mathrm{barrel}})^2}. \tag{5.12}$$

Utilizing $\vec{E}_{\mathrm{T}}^{\mathrm{miss}}$ in a response estimator in such a way allows to reduce the influence of an exact modeling of radiation in the simulation. Other biases such as the resolution bias known from the relative response are also expected to have a reduced influence

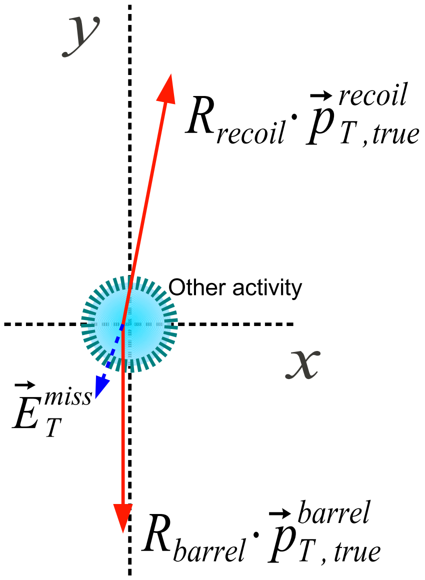

Figure 5.2.: MPF sketch: Projection of the $\vec{E}_{\mathrm{T}}^{\mathrm{miss}}$ along the reference axis gives an estimator for the response of the recoil (and thus the probe jet).

on the MPF response. This way, the systematic uncertainties can be assessed in a complementary way.

For most parts of this study, the “raw” $\vec{E}_{\mathrm{T}}^{\mathrm{miss}}$ definition as described in [156] is used. Jet energy corrections are not propagated to the “raw” $\vec{E}_{\mathrm{T}}^{\mathrm{miss}}$. Due to the small response inhomogeneities of PF candidates (in contrast to large correction factors needed for calorimeter towers), the “raw” $\vec{E}_{\mathrm{T}}^{\mathrm{miss}}$ and the thereby defined MPF response is expected to perform already very well for PF-jets.

However, in order to run a full closure test of the correction procedure on the p_{T}-balance as well as the MPF method, “type-1 corrected” $\vec{E}_{\mathrm{T}}^{\mathrm{miss}}$ to which the jet-energy corrections are propagated has been used in this particular case.

5.2. Determination of the relative residual correction

In order to determine the energy scale as a function of η and p_{T}, the distributions of the previously defined response estimators (relative response $\mathcal{R}_{\mathrm{rel}}$ via asymmetry distribution and MPF response $\mathcal{R}_{\mathrm{MPF}}$) in data and simulation are evaluated in bins of $\overline{p}_{\mathrm{T}}$ and η^{probe}.

The amount of additional event activity is estimated utilising the fraction $p_{\mathrm{T}}^{\mathrm{rel}}$ of the transverse momentum of the third jet and the average p_{T} of the two leading jets as defined in equation (5.2).

The nominal working point is chosen to be a cut of

$$p_{\mathrm{T}}^{\mathrm{rel}} < 0.2 \tag{5.13}$$

on the third jet. The cut on $p_{\mathrm{T}}^{\mathrm{rel}}$ ensures that the p_{T}-balance of the two leading jets is not affected too strongly while keeping enough events to perform the determination of the response estimators with high statistics in a fine η-binning.

The arithmetic mean of the response distributions is computed to determine deviations of the response in data and simulation. The essential ingredient for the residual correction is the response ratio

$$\mathcal{Q} = \langle \frac{\mathcal{R}^{\mathrm{MC}}}{\mathcal{R}^{\mathrm{data}}} \rangle_{p_{\mathrm{T}}^{\mathrm{rel}}<0.2} \tag{5.14}$$

where $\mathcal{R}$ stands either for $\mathcal{R}_{\mathrm{MPF}}$ as defined in equation (5.11) or for $\mathcal{R}_{\mathrm{rel}}$ as defined in equation (5.5) and is evaluated at the working point defined in equation (5.13). This response ratio can generally depend on the transverse momenta at which it is evaluated, but only a weak dependence was observed and is considered in the systematic uncertainties.

The residual correction factor is defined as

$$\mathcal{C}(\eta^{probe}) = \langle \frac{\mathcal{R}^{\mathrm{MC}}}{\mathcal{R}^{\mathrm{data}}} \rangle_{p_{\mathrm{T}}^{\mathrm{rel}}<0.2} \cdot k_{rad} = \mathcal{Q} \cdot k_{rad} \tag{5.15}$$

where the k_{rad} correction is introduced to correct for the remaining bias due to the radiation of additional jets as

$$k_{rad} = \lim_{p_{\mathrm{T,eval}}^{\mathrm{rel}} \to 0} \left(\frac{\langle \frac{\mathcal{R}^{\mathrm{MC}}}{\mathcal{R}^{\mathrm{data}}} \rangle_{p_{\mathrm{T}}^{\mathrm{rel}}<p_{\mathrm{T,eval}}^{\mathrm{rel}}}}{\langle \frac{\mathcal{R}^{\mathrm{MC}}}{\mathcal{R}^{\mathrm{data}}} \rangle_{p_{\mathrm{T}}^{\mathrm{rel}}<0.2}} \right) \tag{5.16}$$

The k_{rad} correction transforms the response-ratio $\mathcal{Q}$ from the working point with soft radiation in the form of additional jets to an ideal dijet event topology without any additional radiation.

As discussed in Section 5.4.2, no significant $|\eta|/\eta$-asymmetry is observed in the 7 TeV data and the correction factor is thus determined in bins of $|\eta|$. A possible p_T-dependence of $\mathcal{Q}$ and k_{rad} will be discussed in more detail in Section 5.5.1. For the actual determination of the residual correction factors, the jet-energy resolution of the jets in the MC sample has been smeared in such a way that the resolutions in MC and in data are equal. The application of dijet events to determine the JER is discussed in Section 5.5.4.

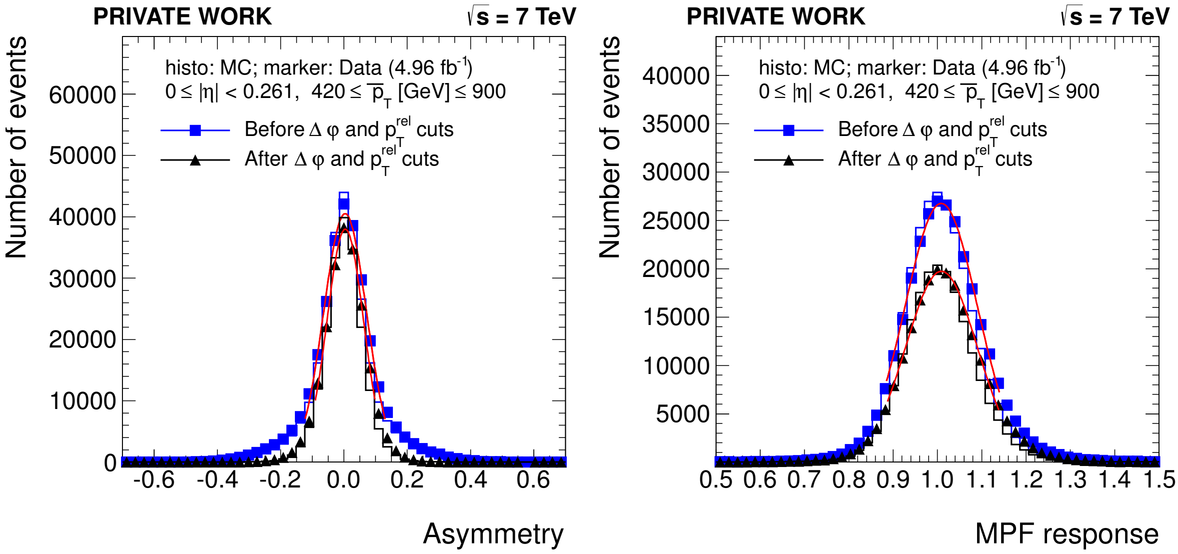

Figure 5.3.: The asymmetry $\mathcal{A}$ and MPF response $\mathcal{R}_\mathrm{MPF}$ distributions before and after the cuts on $\Delta\varphi(j_1, j_2)$ and $p_\mathrm{T}^\mathrm{rel}$ described in equation (5.1) and equation (5.13). The result of an iterative Gaussian fit of the core region ($\pm 1.5\sigma$ around the mean) is shown in red.

Example distributions

For illustration purposes, example distributions of $\mathcal{A}$ (from which $\mathcal{R}_\mathrm{rel}$ is calculated) and $\mathcal{R}_\mathrm{MPF}$ are shown in Figure 5.3. An iterative Gaussian fit of the distribution ($\pm 1.5\sigma$ around the mean) describes the core region reasonably well as is expected for well-behaved response estimators.

The CMS convention is to consider the arithmetic mean of response distributions. Other conventions, such as to consider the mean of Gaussian fits, would also be possible. For most practical purposes the difference is negligible, because neutrinos which would produce low response tails are not considered at the reference level to which the CMS jet-energy corrections aim to correct to.

In Figure 5.4, the mean value of the MPF response is shown as a function of $|\eta|$ for various p_T ranges corresponding to trigger thresholds of the final analysis. The left plot shows results from data and from simulation separately. Significant deviations are

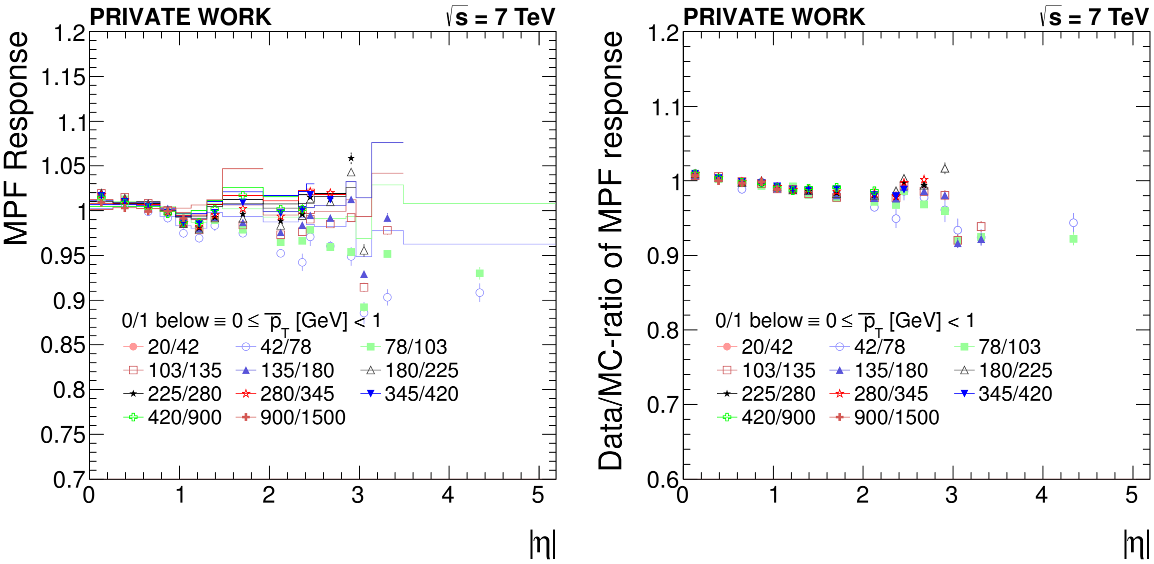

Figure 5.4.: $|\eta|$-dependence of MPF response (left plot) and MC/Data ratio (right plot) in different bins of $\overline{p}_{\mathrm{T}}$ (bin boundaries given in the legend next to the markers) for the MPF response at the nominal working point given in equation (5.13). In the left plot, lines indicate the MPF response in MC and markers indicate the MPF response in data.

observed between data and MC, but also the mean values of the response estimators in different p_{T} ranges vary significantly. In the plot showing the Data/MC ratio, the markers of different p_{T} ranges overlap, the p_{T} dependence is mostly canceled in the ratio. The remaining Data/MC differences correspond to the corrections determined in equation (5.15).

Example extrapolations to zero additional event activity as used for deriving the k_{rad} correction are shown in Figure 5.5 for both, the MC/Data ratio and the separate MC and data response estimators. The dependence of the response estimators on $p_{\mathrm{T}}^{\mathrm{rel}}$ is relatively strong for the relative response, the k_{rad} correction amounts to about 2% at $|\eta| = 3$. Directly extrapolating the double-normalized MC/Data-ratio (corresponding to equation (5.16) before taking the limit) cancels to first order this effect. For the MPF response, the dependence on the cut on $p_{\mathrm{T}}^{\mathrm{rel}}$ is negligible, no matter whether it is extrapolated separately or as MC/Data-ratio. As discussed in Section 5.4.1, a full closure between residual corrections using either MPF or the relative response is only observed, if the extrapolation to zero additional event activity is done (for the relative response).

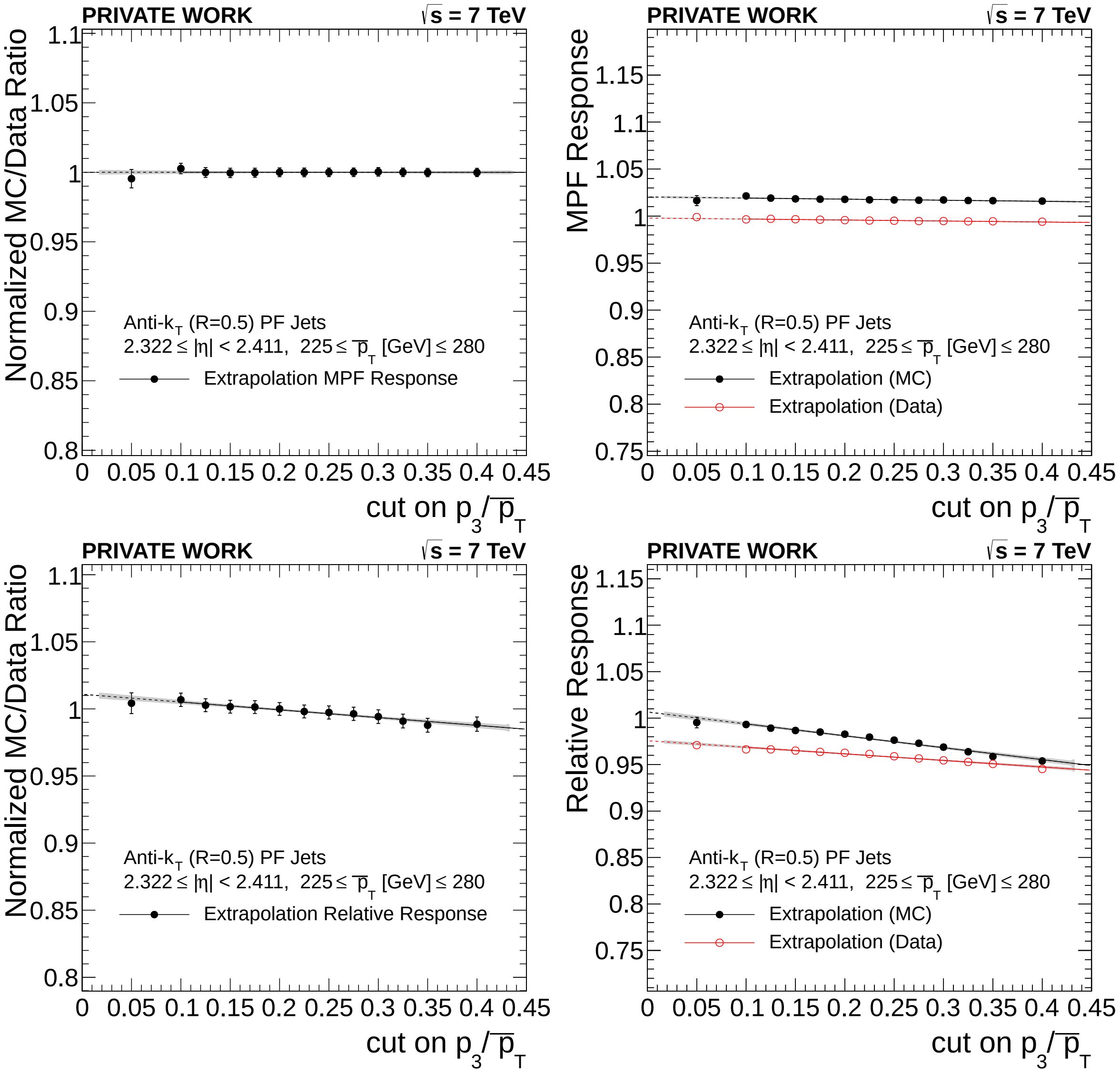

Figure 5.5.: Left: k_{rad}-example extrapolations as a function of p_T^{rel} for MPF (upper row) and relative response(lower row), showing the results of equation (5.16) before taking the limit of $p_T^{\mathrm{rel}} = 0$. Right: Separate MC/Data extrapolation of the mean values of $\mathcal{R}_{\mathrm{MPF}}$ (upper row) and $\mathcal{R}_{\mathrm{rel}}$ (lower row) for comparison.

5.3. Samples and event selection

In this section, the samples used for the analysis, the event selection, and the necessary event reweightings of the simulated samples are summarized. While the main part of the analysis focuses on the determination of the 2011 relative residual jet-energy corrections, some supplementary studies are presented using 2012 data, for which the presented analysis methods have been used without substantial changes for the determination of the corrections.

5.3.1. Datasets 2011

The data samples used in the main part of the analysis are listed in Table A.1. The data samples have been reprocessed in 2012 (ReReco data using CMSSW44) to use the latest reconstruction software as well as updated detector calibration constants.

The residual correction used for most 2011 data analyses is based on an older reconstruction version (mostly PromptReco using CMSSW42) and data taken directly from the prompt reconstruction. These results are documented in [134] and compared to the improved analysis based on the ReReco data in Section 5.5.5. Data samples used in this context are listed in Table A.2.

Trigger thresholds

The dijet balance analysis utilizes dedicated dijet triggers. These triggers are specifically tailored to acquire an unbiased dataset for the analysis. They are therefore based on $\overline{p}_{\mathrm{T}}$ as trigger variable instead of the p_{T} of single jets. At an early stage of data-taking in 2011, the triggers were reconfigured and since then use $\overline{p}_{\mathrm{T}}$ of JEC-corrected jets as trigger variable (no jet-energy corrections were applied to jets on the trigger level before). The dataset used in this analysis contains all events taken with these triggers, starting from run 163337. The preceding runs had to be omitted because of a faulty trigger configuration and correspond to an integrated luminosity of $85.4\,\mathrm{pb}^{-1}$.

The trigger thresholds used for the analysis have been determined on the 2011 dataset, starting from run 163337, corresponding to a nominal integrated luminosity of $5.013\,\mathrm{fb}^{-1}$. As the dijet triggers are heavily prescaled due to the high instantaneous luminosity, the trigger-turn on function cannot be determined by a simple tag-and-probe approach using a low-threshold trigger to monitor a high-threshold trigger. The number of events firing both triggers simultaneously is too low.

Table 5.1.: Trigger thresholds of $\overline{p}_\mathrm{T}$ triggers used for the analysis in 2011 and 2012

Trigger (2011)	threshold (GeV)	Trigger (2012)	Threshold (GeV)
`HLT_DiJetAve30`	42	`HLT_DiPFJetAve40`	62
`HLT_DiJetAve60`	78	`HLT_DiPFJetAve80`	107
`HLT_DiJetAve80`	103	`HLT_DiPFJetAve140`	175
`HLT_DiJetAve110`	135	`HLT_DiPFJetAve200`	242
`HLT_DiJetAve150`	180	`HLT_DiPFJetAve260`	310
`HLT_DiJetAve190`	225	`HLT_DiPFJetAve320`	379
`HLT_DiJetAve240`	280	`HLT_DiPFJetAve400`	467
`HLT_DiJetAve300`	345		
`HLT_DiJetAve370`	420		

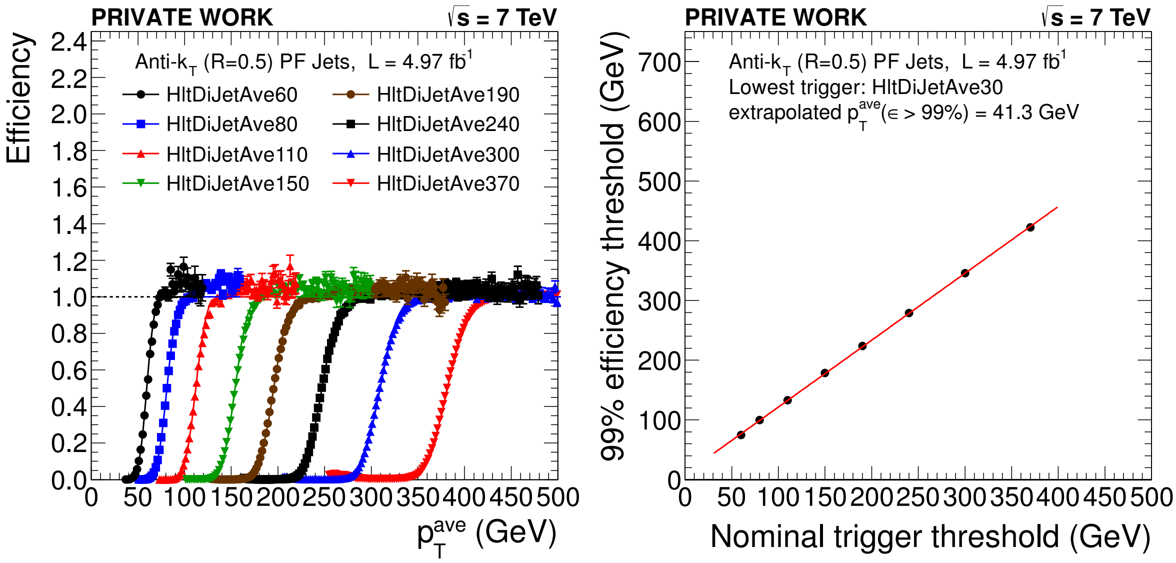

Figure 5.6.: Left: Turn on curves determined for PF-jets in 2011 data; Right: Linear extrapolation of the threshold of the lowest p_T-trigger

Instead, the determination of trigger-turn on functions was performed as documented in [124, 157]. Following this approach, the efficiency is defined as:

$$\epsilon = \frac{N(\text{passing } A)}{N(\text{passing } B)} \tag{5.17}$$

where A and B are two triggers. In this case, $0 \leq \epsilon \leq 1$ does not hold true since the turn-on curve of A is convoluted with the turn-on curve of B. As these are monotonic functions, the trigger threshold $p^\mathrm{ave}_{\mathrm{T},99}(A)$ can still be precisely computed as the value of $\overline{p}_\mathrm{T}$ where the efficiency ϵ equals 99% of the plateau-value $\epsilon(\overline{p}_\mathrm{T} \to \infty)$. The absolute value of the plateau depends on the prescales of the triggers.

Figure 5.6 depicts the efficiencies $\epsilon(\overline{p}_\mathrm{T})$ of the different triggers used in this analysis. In almost all cases, ϵ has been computed from equation (5.17) using the trigger with the next lower threshold as a reference and has been normalized such that the plateau $\epsilon(\overline{p}_\mathrm{T} \rightarrow \infty)$ lies at one. ϵ is fitted with the smooth function

$$f(\overline{p}_\mathrm{T}) = \frac{1}{2}\left[\mathrm{erf}\left(p_0 \cdot (\overline{p}_\mathrm{T} - p_1)\right) + 1\right] \ ,$$

which is used to determine the threshold $p^\mathrm{ave}_{\mathrm{T},99}$ from

$$f(p^\mathrm{ave}_{\mathrm{T},99}) = 0.99$$

All relevant dijet trigger paths, together with their $p^\mathrm{ave}_{\mathrm{T},99}$ thresholds, are listed in Table 5.1. The turn on of the lowest trigger has been determined differently by using a linear extrapolation of all higher-threshold triggers, also shown in Figure 5.6. In order to evaluate the stability, the thresholds are varied by ± 5 GeV as a cross-check of the analysis in Section 5.4.2. The influence of the varied thresholds on the final result is found to be negligible.

5.3.2. Datasets 2012

The 2012 data were recorded at a center-of-mass energy of $\sqrt{s} = 8\,\mathrm{TeV}$. The larger integrated luminosity of the 2012 data enabled more detailed analyses of the time dependence, the φ dependence, and the dependence on close-by jets of the response. The 2012 datasets used for the analysis are listed in Table A.3. Trigger thresholds have been determined in the same fashion as for 2011 data and are listed in Table 5.1.

5.3.3. Corrections

Following the factorized jet-energy correction approach discussed in detail in Section 4.5, the L1Fastjet and L2L3 MC truth corrections were applied to the jets used in this analysis. The corresponding corrections for the 2011 data are included in the global tag START44_V13. It should be noted, that these corrections were determined on datasets and MC samples reconstructed with CMSSW42X. Results for the CMSSW42X dataset are documented in [134]. For the determination of residual corrections, which are only sensitive to Data/MC differences, the fact that the reconstruction software has changed is expected to play a minor role. However, the updated calibration constants in the re-reconstructed dataset are expected to impact the resulting residual corrections. In particular, the time dependence observed in the previous analysis of datasets reconstructed with CMSSW42X is expected to be reduced. This is discussed in detail in Section 5.5.5.

5.3.4. Dijet event selection

In order to select suitable dijet events, the $\overline{p}_{\mathrm{T}}$-triggered datasets are an ideal starting point. At least two reconstructed jets are required to pass loose jet identification criteria [158] and their $\overline{p}_{\mathrm{T}}$ has to be above the trigger thresholds listed in Table 5.1. In order to serve as reference, at least one of the two jets leading in p_{T} has to lie in the control region $|\eta_{tag}| < 1.3$. In order to enrich the sample with events closely resembling the ideal dijet topology, the two leading jets are required to be back-to-back in the transverse plane, i.e. $\Delta\varphi(j_1, j_2) > 2.7$, and extreme asymmetry values are rejected, requiring $|\mathcal{A}| < 0.70$.

If more than two jets are present in the event, the relative third jet fraction $p_{\mathrm{T}}^{\mathrm{rel}}$ as defined in equation (5.2) is evaluated. A default working point of $p_{\mathrm{T,max}}^{\mathrm{rel}} = 0.2$ has been chosen to suppress additional jet activity in the event. In order to extrapolate to zero additional event activity with the k_{rad} correction as discussed in Section 5.2, all relevant quantities are recorded for a number of different $p_{\mathrm{T}}^{\mathrm{rel}}$ cuts, namely 0.050, .100, .125, .150, .175, .200, .225, .250, .275, .300, .325, .350, and .400.

The effect of these selections is illustrated in Figure 5.7 and an extensive collection of control plots is provided in Appendix B.1. The selection for simulated data follows the same procedure. [2]

In 2011 data, the total yield in data after applying the selection is 8724943 events. 23491 events are collected in the fully efficient p_{T} range of the lowest $\overline{p}_{\mathrm{T}}$ trigger ($42 < \overline{p}_{\mathrm{T}}[\,\mathrm{GeV}] < 78$), 989735 events are selected above the threshold of 420 GeV of the unprescaled highest $\overline{p}_{\mathrm{T}}$ trigger.

In 2012, 17892129 events survive the basic event selection. The threshold of the lowest $\overline{p}_{\mathrm{T}}$ trigger is as high as 62 GeV, severely limiting the statistical sensitivity at high $|\eta|$. 77527 events are collected in the p_{T} range below the next trigger threshold of 107 GeV. 3471559 events are selected above 467 GeV, the threshold of the unprescaled highest $\overline{p}_{\mathrm{T}}$ trigger.

---

[2] Due to a slightly inconsistent handling of mixed-in pileup events in the QCD MC samples used for the analysis, an additional cut on the events has to be performed to avoid the migration of events with very high event weights as discussed in [159]. If the leading jet p_{T} is larger than $2.0 \cdot \hat{p_{\mathrm{T}}}$, where $\hat{p_{\mathrm{T}}}$ is the energy scale associated with the hard event, simulated events are rejected.

This selection ensures that events containing additional mixed-in pileup events with $p_{\mathrm{T}} \gg \hat{p_{\mathrm{T}}}$ are disregarded and not considered further in the analysis. These (few) events would otherwise distort response distributions due to artificially high event weights.

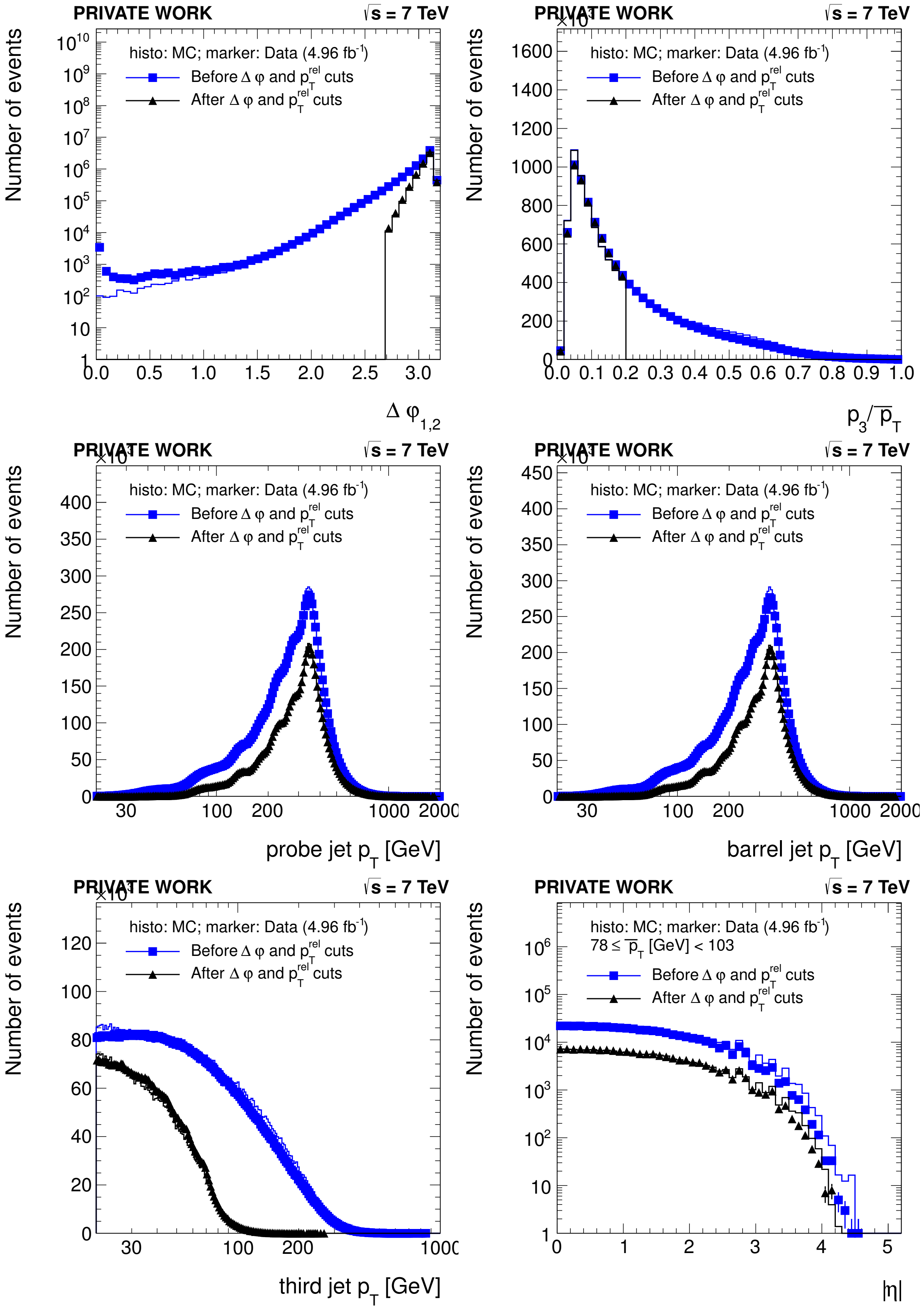

Figure 5.7.: Illustration of topological cuts on $\Delta\varphi$ and $p_{\mathrm{T}}^{\mathrm{rel}}$: Distribution of $\Delta\varphi$ (upper left) and $p_{\mathrm{T}}^{\mathrm{rel}}$ (upper right) before and after applying cuts on both variables. p_{T}^{probe} (middle left), p_{T}^{barrel} (middle right), third jet p_{T} (lower left), and probe jet $|\eta|$ (lower right) distributions before and after these cuts.

5.3.5. Event reweighting in simulation

In order to take into account the prescaled triggers and the p_T-dependent pileup distributions in data, two event reweightings are performed for the simulated events before the final analysis.

Pileup reweighting

The distribution of the number of pileup interactions in the collected data depends strongly on the instantaneous luminosity. As the prescales of the used triggers have not been static during the 2011 data-taking, the dependence is also largely different for the individual trigger paths. As the simulated data only contains a single p_T-independent scenario for the pileup distribution, a trigger dependent reweighting procedure has been carried out in order to match the pileup distribution in simulation to that observed in data.

In current MC samples, the number of pileup events mixed into the QCD-events is directly accessible. The collision data is separated into small portions (lumi sections) for which the integrated luminosity, the average per bunch instantaneous luminosity, and the uncertainty on the per bunch luminosity are provided in a central database. This information is modified to take into account the average prescales of the triggers in each lumi section.

Starting from these numbers and assuming a certain total inelastic cross section ($68\,\mathrm{mb} \pm 5\%$ for 2011 determined from $Z \rightarrow \mu\mu$ events [160]), the expected number of events for each lumi section can be calculated directly. Examples of the different distributions in MC and calculated for the individual trigger paths are depicted in Figure 5.8. In comparison, the pileup distribution of the unprescaled `HLT_DiJetAve370` trigger is biased towards higher numbers of pileup events, because the prescales of the lower $\overline{p}_\mathrm{T}$ triggers were increased during the data-taking as the instantaneous luminosity reached higher values.

The impact of the reweighting procedure on the distribution of the number of reconstructed vertices in two p_T ranges populated by different triggers is depicted in Figure 5.9. Only minor deviations are observed after the reweighting procedure. The influence of pileup and the corresponding corrections on the results for the residual correction are discussed in Section 5.5.3.

Dijet event weighting

The MC events in each p_T-region defined by the trigger thresholds determined for the `HLT_DiJetAveXX` triggers are weighted such that the number of events in MC and in data is equal (for the working point $p_\mathrm{T}^\mathrm{rel} < 0.2$). In this way, the prescales of the individual triggers are taken into account and the number of events in the different distributions is

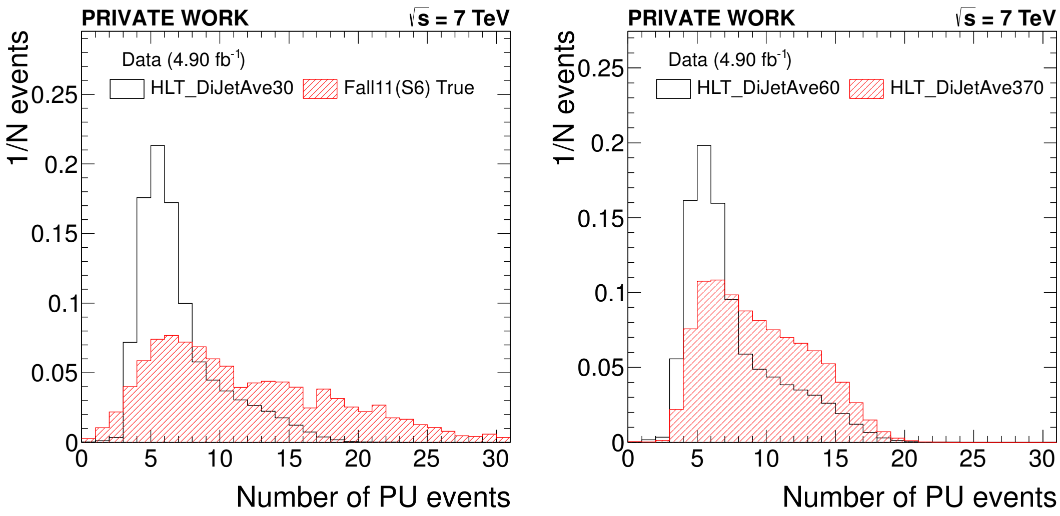

Figure 5.8.: Left: Pileup distribution used for MC-event generation (in the Fall11 or S6 scenario) compared to the distribution calculated for data from measurements of the instantaneous per bunch luminosity for the `HLT_DiJetAve30` trigger (taking into account the evolving prescales); Right: Pileup distributions calculated for data for the `HLT_DiJetAve60` and `HLT_DiJetAve370` trigger.

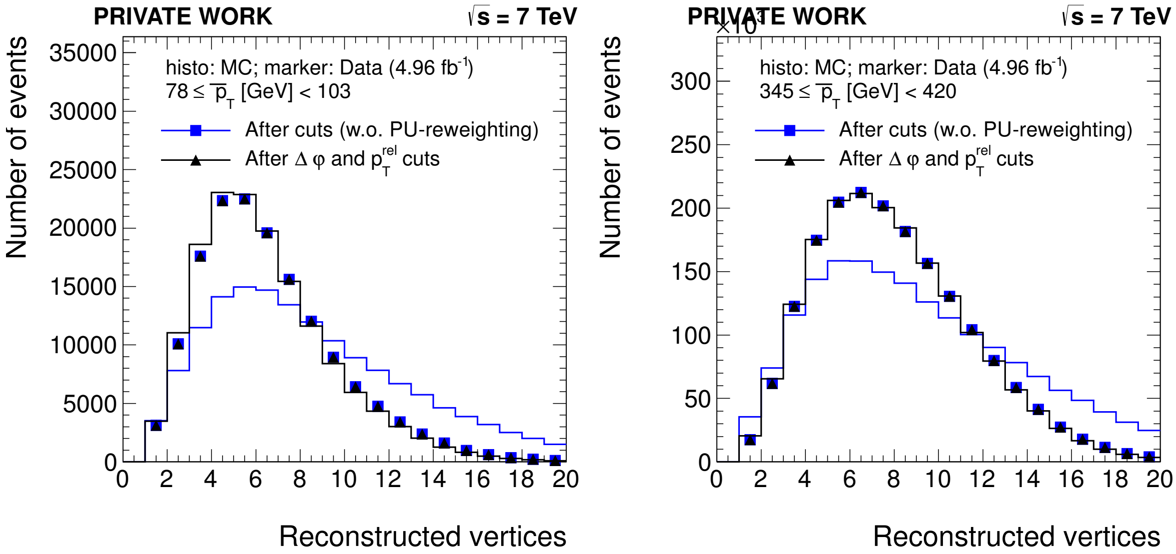

Figure 5.9.: Number of reconstructed vertices distribution for individual triggers (Left: `HLT_DiJetAve30`; Right: `HLT_DiJetAve300`) before and after pileup reweighting. The data is not reweighted. Therefore, the markers indicating data are overlaying each other in the plots.

comparable. The effect of this reweighting procedure and the resulting p_{T}-spectrum is illustrated in Figure 5.10, showing a good agreement of the spectra after reweighting in different $|\eta|$-regions. The nominal MC event weights are extremely low, but the number of MC events is sufficient to perform the reweighting, even at high $\overline{p}_{\mathrm{T}}$. This is enabled

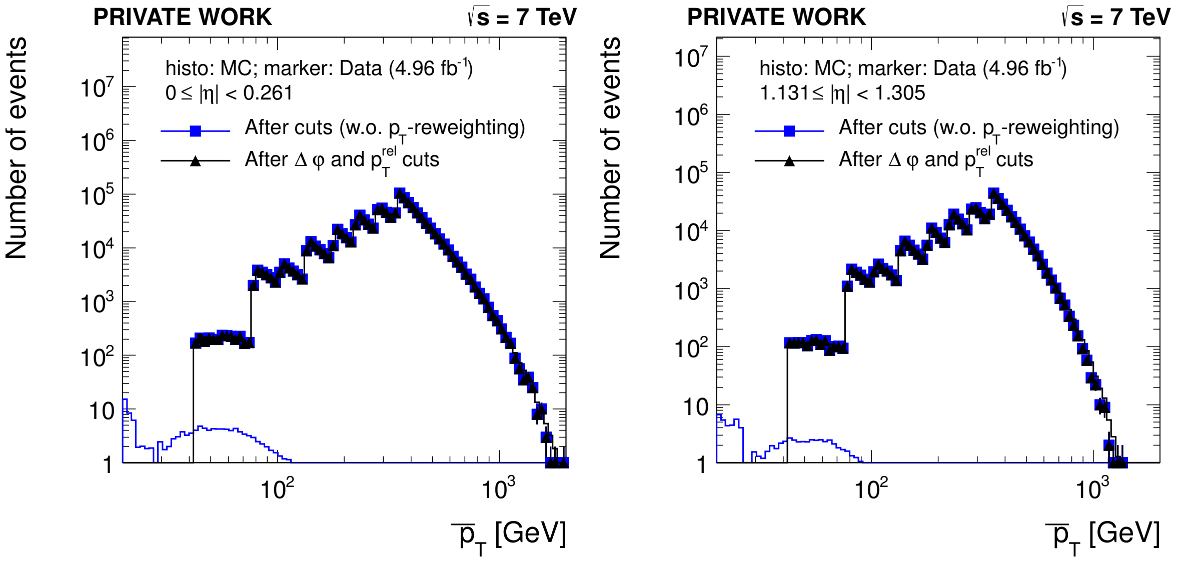

Figure 5.10.: $\overline{p}_{\mathrm{T}}$ distribution (sum of weights) in data (markers) and in simulation (histogram) with and without the p_{T}-reweighting procedure (MC event weights are extremely low before the reweighting, events not surpassing the trigger thresholds are disregarded in the reweighting process).

by the the particular setup of the sample by artificially flattening the p_{T} spectrum in the event generation process, increasing the number of MC events at high p_{T}. The events visible for MC in the plots below the lowest $\overline{p}_{\mathrm{T}}$ threshold are disregarded in the reweighting procedure.

5.4. Results for the 2011 data-taking period (re-reconstructed with CMSSW44)

In Figure 5.11, the resulting k_{rad} correction and relative residual correction factors of the 2011 data re-reconstructed with CMSSW44 are shown as a function of $|\eta|$.

The values for the k_{rad} correction are found to be of the order of 1-2% for the relative response (RR) and almost negligible for the MPF response. The size of the k_{rad} correction for the RR method depends on the used MC sample (e.g. the correction factor is below 1 when using the available HERWIG++ MC sample as reference and is expected to vanish if the radiation of additional jets is accurately described by the simulation). The shape of the k_{rad} correction is found to be described well by a fit function that includes terms $cosh(\eta)^3$ as illustrated in Figure 5.12.

The resulting relative residual correction factors are below 3% for $|\eta| < 3$ and can be as high as 10% in the HF-region ($|\eta| > 3$). The largest changes of the correction factor are observed in the transition region between the endcap and forward calorimeters at $|\eta| = 3$.

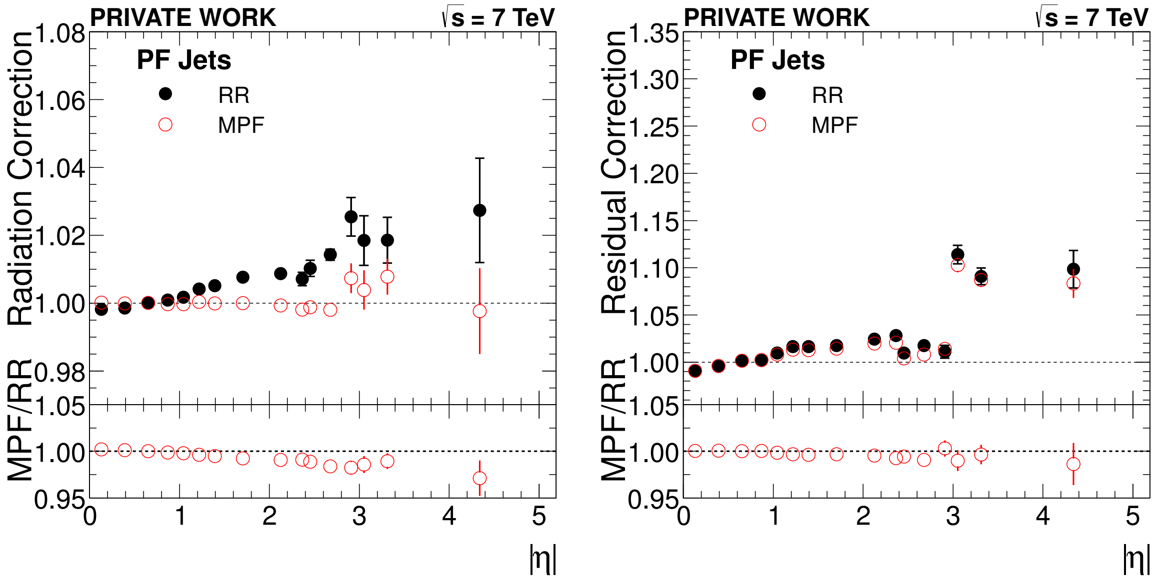

Figure 5.11.: Left: k_{rad} correction factors for MPF and relative response; Right: k_{rad}-corrected resulting relative residual correction. Both are determined for the CMSSW44 ReReco data with PYTHIA as reference MC, listed in Table A.1

---

[3] The energy of jets relates to the transverse energy as $E = E_{\mathrm{T}} \cdot cosh(\eta)$.

5.4.1. Systematic uncertainties

In order to test the stability and evaluate systematic uncertainties, the whole analysis is repeated using slightly modified conditions. To estimate the systematic uncertainties resulting from these variations, the difference of the nominal result and the result with a variation is taken.

For the central result, the correction factor defined in equation (5.15) does not depend on p_{T}. It is determined by fitting a constant to the MC/Data ratio of the response estimators, recorded in bins of $\overline{p}_{\mathrm{T}}$:

$$\mathcal{Q}_{\mathrm{const}}(\eta^{probe}) = const(\eta) \tag{5.18}$$

This is refered to as the "constant fit" in the following. Alternatively, a possible p_{T} dependence is taken into account by fitting the following function to the MC/Data-ratio:

$$\mathcal{Q}_{\text{log-lin}}(\eta^{probe}, \overline{p}_{\mathrm{T}}) = a_{\eta} + b_{\eta} \cdot log(\overline{p}_{\mathrm{T}}) \tag{5.19}$$

This is refered to as the "log-linear fit" in the following.

For up/down variations, the average deviation of the up/down variations is considered. If not otherwise stated, this is taken as the larger difference of either the constant fits $\mathcal{Q}_{\mathrm{const}}$ or the log-linear fits $\mathcal{Q}_{\text{log-lin}}$ for variations with the same generated event sample (JER, k_{rad}, MPF/RR-closure) or the difference of the constant fit result $\mathcal{Q}_{\mathrm{const}}$ for different MC samples (model dependence) in order to suppress statistical fluctuations. In the following, the analysis variations are described.

p_{T}-dependence: It has been assumed that the relative residual correction is constant as a function of p_{T}. This assumption is valid for most $|\eta|$-regions. In order to take into account a possible p_{T}-dependence, half of the difference between the residual corrections, as determined from $\mathcal{Q}_{\mathrm{const}}$ and from $\mathcal{Q}_{\text{log-lin}}$, is assigned as systematic uncertainty. In the endcaps and more forward regions, where the p_{T}-range tested by dijet events is relatively small, this can become a relatively large effect. However, its significance is limited by the amount of data available for the determination. The p_{T} dependence of the residual corretion is discussed in more detail in Section 5.5.1.

Jet-energy resolution: In order to correct for the slight disagreement of the JER in data and MC (about 10%), also observed in this analysis, the jet-energy resolution is smeared in the simulation such that the resolutions match the ones in data. This way it is ensured that the resolution bias in MC and in data for the determination of residual corrections is described in a consistent way. The resolution of the jets is broadened by the scaling factor $\mathcal{S}$ as derived in [124, 161]. The systematic variations are propagated to the analysis and the average deviation observed from the up/down variation is considered as a systematic uncertainty.

k_{rad} correction: In order to evaluate the stability of the k_{rad} correction and estimate an uncertainty of the extrapolation procedure, the analysis is repeated with varied $p_{\mathrm{T}}^{\mathrm{rel}}$

ranges. While for the nominal corrections, thresholds of $p_\mathrm{T}^\mathrm{rel}$ in the range of $0.05\ldots0.40$ are considered for the extrapolation, the range is limited to $0.15\ldots0.40$ or $0.05\ldots0.30$ respectively for these variations.

Model dependence: Closely related to the k_{rad} correction, the model dependence of the residual correction is evaluated by comparing the resulting corrections either using MC samples generated using PYTHIA or HERWIG++ as reference. As depicted in Figure 5.12.(a), the k_{rad} correction is observed to differ by up to 5% for the relative response between PYTHIA and HERWIG++. However, this difference precisely corresponds to the deviation that would be observed at the nominal working point ($p_\mathrm{T}^\mathrm{rel} < 0.2$) before applying the k_{rad} correction. When performing the extrapolation, the differences are largely reduced as illustrated for a single $|\eta|$-bin in Figure 5.12.(b). Corresponding plots for all $|\eta|$-bins, comparing the p_T-inclusive extrapolation of the MC/Data ratios for PYTHIA and HERWIG++, both for MPF and the relative response, are listed in Appendix B.4.

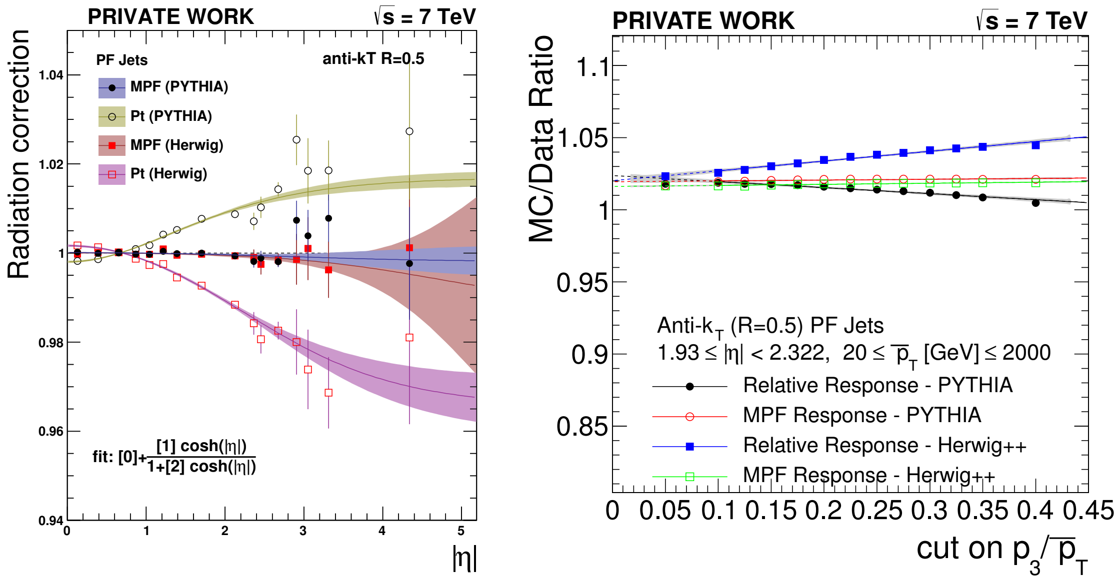

(a) (b)

Figure 5.12.: Left: Resulting k_{rad} corrections for PYTHIA/HERWIG++, both for MPF and relative response. The colored regions indicate the fit uncertainty when approximating k_{rad} with the function indicated in the lower left corner of the plot; Right: Effect of extrapolation to zero additional event activity on the resulting residual correction (either using PYTHIA or HERWIG++ as reference MC), both for MPF and relative response in one example $|\eta|$-bin.

MPF/RR-closure: For the determination of the residual corrections, the RR and MPF method have both been considered. The MPF method is more resilient against biases due to additional jet activity in the event, as indicated by its negligible k_{rad} correction. However, for the usage of the composite object $\vec{E}_\mathrm{T}^\mathrm{miss}$ for jet calibration purposes, special care has to be taken. As an estimate of the stability and consistency of both methods, the full difference between the results from the RR and MPF method is considered as a systematic uncertainty.

The differences observed due to the evaluation of the considered systematic uncertainties have been integrated into the existing CMS framework for the determination of JES uncertainty sources. Corresponding plots showing the resulting uncertainties for both, the MPF method and relative response method, are shown in Figure 5.13. Up to around $|\eta| < 2.2$, the uncertainties related to the relative residual corrections are below 1% and well below 0.5% in the central detector region ($|\eta| < 1.3$). In the endcap and forward detector regions, where the amount of data available for the analysis is decreasing due to the relatively high thresholds in $\overline{p}_{\mathrm{T}}$ and the reduced reach to high p_{T} due to kinematic constraints, the uncertainties grow. The p_{T}-dependence accounts for sizable contributions to the uncertainty for very high and low p_{T}. The MPF/RR difference contributes significantly at high $|\eta|$.

Other effects like the extrapolation uncertainty and JER variations are relatively small and even the impact of the chosen MC event generator, the modeling uncertainty, is very small due to the extrapolation to zero additional event activity. In the iterations of this analysis performed on 2012 data, the closure between the MPF and RR-method could be improved further by using the Type-1-corrected $\vec{E}_{\mathrm{T}}^{\mathrm{miss}}$ for MPF, which also allows for precise closure tests of the derived residual corrections.

5.4.2. Analysis cross-checks

In the dijet event selection in Section 5.3.4, several choices regarding the cut on $\Delta\varphi$, the cut on the asymmetry, and the trigger thresholds had to be taken. Even though not considered directly as systematic uncertainties, variations of these selections have been done and the same evaluation as for the systematic uncertainties has been performed to ensure the stability of the analysis with regard to these choices.

Asymmetry-cut variation: In order to suppress the extreme tails of the asymmetry distribution, a cut on the asymmetry of $|\mathcal{A}| < 0.70$ is imposed for both, MPF and p_{T} balance. This cut is varied by ± 0.1 and differences are evaluated.

$\Delta\varphi$-cut variation: In order to select a clean sample of back-to-back dijet events, a standard cut of $\Delta\varphi(j_1, j_2) > 2.7$ is used. This cut is varied by ± 0.2 in order to evaluate whether a dependence on the cut would bias the analysis significantly.

Trigger-threshold variation: The influence of the trigger thresholds given in Table 5.1 on the result is estimated by varying the thresholds by $\pm 5\,\mathrm{GeV}$.

In Figure 5.14, the resulting variations are shown. As expected, the modest variation of cut parameters has negligible influence on the results after the extrapolation to zero additional event activity. Only at very high $|\eta|$ where the systematics determination is affected by a lack of events, slight deviations are observed.

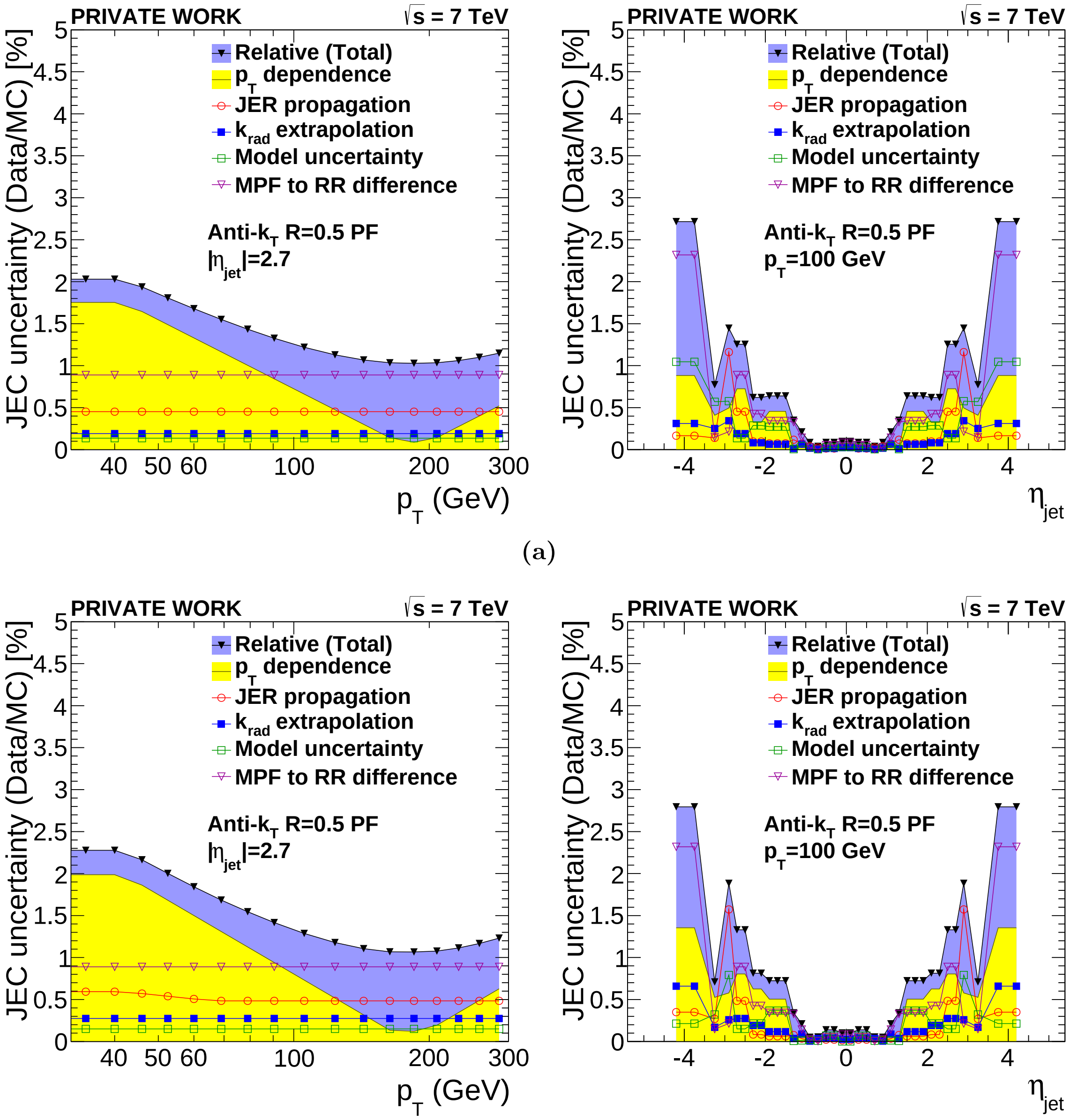

(a)

(b)

Figure 5.13.: (a): Systematic uncertainties when using the MPF method for the determination of relative residual corrections for a fixed η as a function of p_T (left) and for a fixed p_T as a function of η (right). Relative (Total) denotes the quadratic sum of the individual uncertainty components; (b): Same when using the relative response method for the determination of residual corrections.

$|\eta|/\eta$ asymmetry: The residual correction has been determined as a function of $|\eta|$, but miscalibrations as a function of η would also lead to a response asymmetric in η. In Figure 5.15, the results are overlayed for the MPF and relative response methods. Only in the transition region between the endcaps and the HF, a significant η-asymmetry is

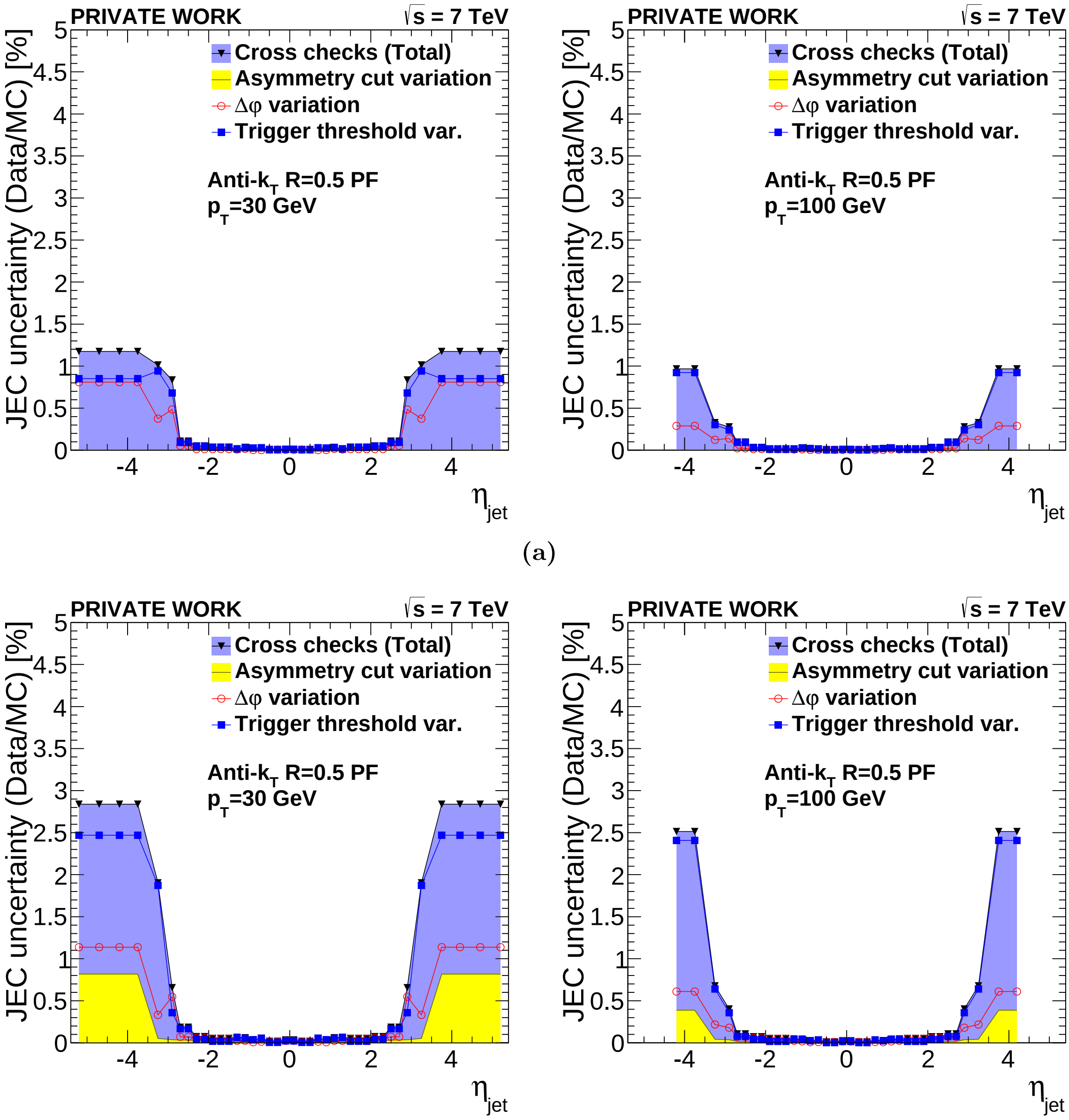

(a)

(b)

Figure 5.14.: (a): Summary of cross checks performed by varying a number of analysis cuts when using the MPF method for the determination of relative residual corrections for a fixed η as a function of p_{T} (left) and for a fixed p_{T} as a function of η (right). Cross checkse (Total) denotes the quadratic sum of the listed analysis cut variations; (b): Same when using the relative response method for the determination of residual corrections

observed. This asymmetry is taken care of by explicitly using the resulting correction factors at $\pm\eta$ in this region. In all other regions, the $|\eta|$-correction factor is used.

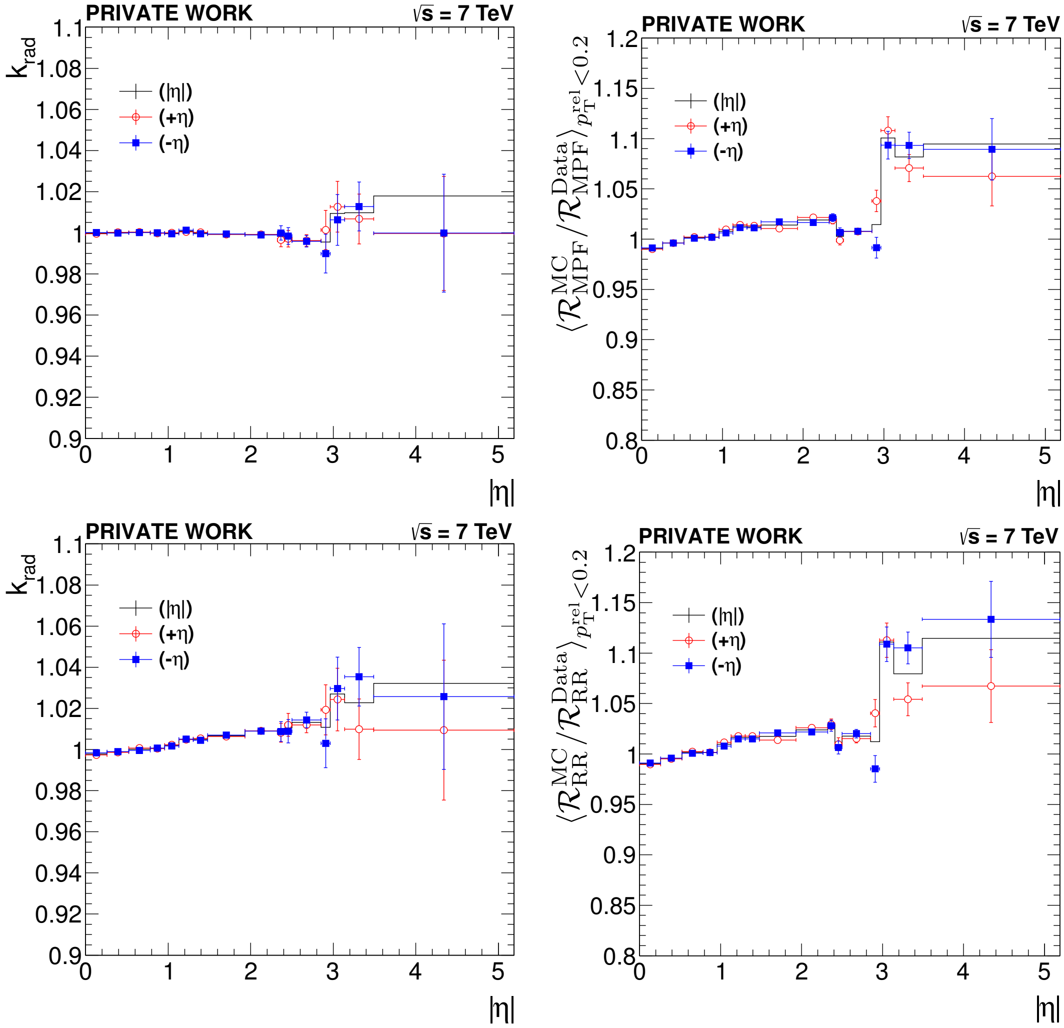

Figure 5.15.: η-asymmetry for k_{rad} and residual correction, comparing the results at $\pm\eta$ with those at $|\eta|$. Upper left: MPF k_{rad}; Upper right: MPF residual correction factor; Lower left: relative response k_{rad}; Lower right: relative response residual correction factor

5.5. More detailed studies

In this section, a number of supplementary studies are presented, which have been performed in order to test the techniques used in Section 5.4 in more detail. The p_T-dependence of the two individual parts of the residual correction, the MC/Data-ratios at the nominal working point and the p_T-dependence of the k_{rad} correction, are discussed in Section 5.5.1. A MC-study of the closure of the MPF and RR methods and the optimal p_T-binning and triggering is presented in Section 5.5.2. The dependence of the correction on the amount of pileup in the event and the interplay with the pileup-reweighting and the L1-corrections applied before deriving the residual corrections are discussed in Section 5.5.3. A preliminary study utilizing the asymmetry method to cross-check the jet-energy resolution scale factors is discussed in Section 5.5.4. The time stability of the response during the 2011 and 2012 data-taking periods is discussed in Section 5.5.5, a study to use dijet events to map the jet-energy response on a granularity corresponding to single calorimeter cells is presented in Section 5.5.6. The dependence of the jet-energy response on closeby jets is discussed in Section 5.5.7.

5.5.1. p_T dependence of the MC/Data-ratios of the response estimators

As the residual correction is based on the MC/Data-ratio of the response estimators, the p_T-dependence of the jet-energy response is expected to cancel to first order for the residual correction. This will be checked for the MC/Data-ratios at the nominal working point and for the k_{rad} correction determined in the same p_T-binning.

p_T dependence of MC/Data-ratios at nominal working point: In Figure 5.16, the Data/MC-ratios of the response estimators are shown as a function of $\overline{p}_\mathrm{T}$ for two representative $|\eta|$-regions at the nominal working point. No significant p_T-dependence is observed for the relative response and MPF ratio in almost all $|\eta|$-regions (compare Appendix B.2.3 and B.3.3 for all plots). A remaining slope in the resulting Data/MC-ratios is a hint at a jet-energy resolution being different in MC and in data. Indeed, this has been observed and will be discussed in more detail in Section 5.5.4. This “artificial” p_T-dependence is drastically reduced when the response estimators are determined as a function of $\overline{p}_\mathrm{T}$, reducing the resolution bias as discussed in previous studies [133].

Only in $|\eta|$ regions with a narrow accessible p_T range, the fir of the MC/Data ratio hints at a p_T-dependence. As observed in the plots in Appendix B.2.3 and B.3.3, the log-linear fit of the p_T-dependence is compatible to the constant fit within its uncertainties in most cases. Thus, the a-priori assumption of a p_T-independent MC/Data-ratio is kept and only part of the difference between the constant fit and the p_T-dependent fit is assigned as systematic uncertainty.

Even though the results indicate that no strong p_T-dependence is observed, it should be noted that this does not hold true if the response estimators are examined before

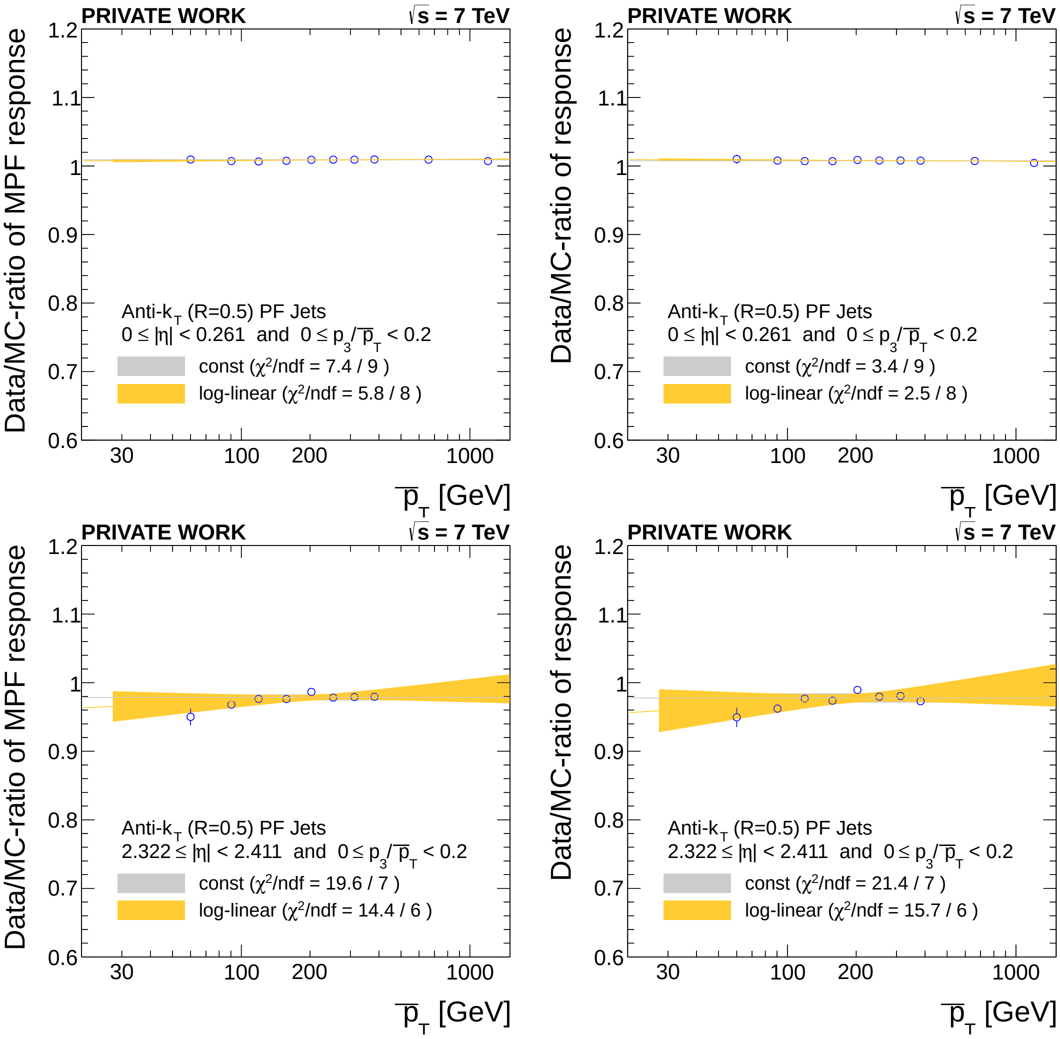

Figure 5.16.: p_T-dependence of the Data/MC-ratios of $\mathcal{R}_\mathrm{MPF}$ (left column) and $\mathcal{R}_\mathrm{rel}$ (right column) in two $|\eta|$ regions. Fits as defined in equation (5.18) and equation (5.19) are also shown. The grey and yellow bands indicate the 95% confidence intervals of the fit (the uncertainty of the log-linear fit is usually larger and covers the grey band of the fit of a constant).

taking the Data/MC-ratio. This has already been illustrated in Figure 5.4, which shows the MPF response as a function of $|\eta|$ in various $\bar{p}_\mathrm{T}$-bins separately for Data and MC and the respective ratios. In the ratio, the p_T-dependence is canceled to a very large extent as indicated by the overlapping markers.

p_T dependence of the k_{rad} correction: The k_{rad} correction is a non-negligible correction for the p_T-balance method. Even though its size is slightly smaller than in 2010 (2010 results are documented in [133]), it remains to be checked whether there is any p_T-dependence in the radiation modeling imperfections of the used generators. In order to do this, the determination of the radiation correction factor is performed separately in bins of p_T and $|\eta|$ for both, MPF and the relative response.

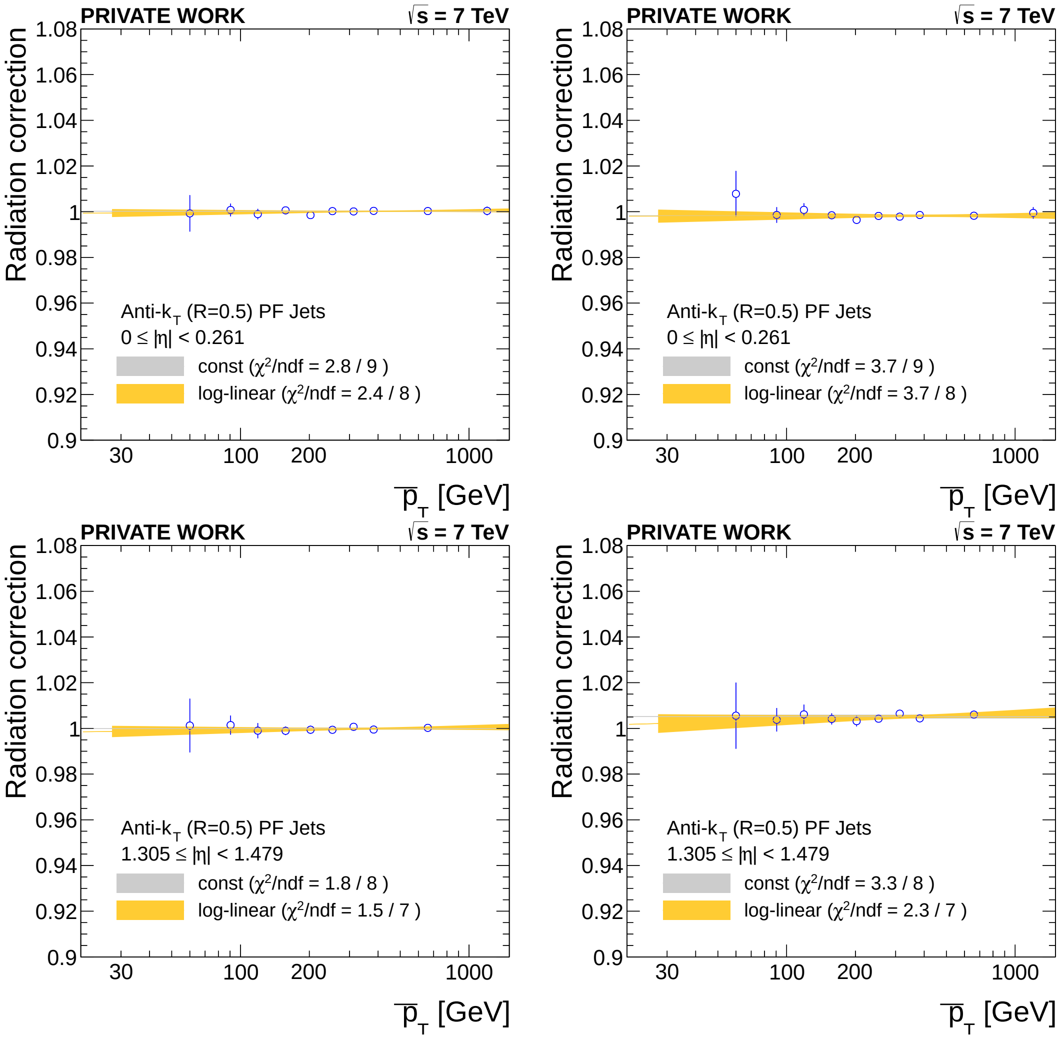

Figure 5.17.: p_{T}-dependence of the the radiation correction k_{rad} in two $|\eta|$-regions for the MPF method (left column) and the RR method (right column). As the correlations are not explicitly accounted for in the extrapolation procedure, the χ^2/ndf values are not to be taken as reliable estimates in these plots.

The extrapolation results for two representative $|\eta|$-regions are shown in Figure 5.17. The full set of plots is shown in Appendix B.2.3 and B.3.3. The extrapolation to zero additional event activity is done by varying the cuts on the relative third jet p_{T} and normalizing the results to the MC/Data-ratio at the nominal working point as defined in equation (5.16). As the samples with a looser cut also contain the events with a tighter cut, the samples with different α-thresholds are correlated (see Appendix B.1 for control distributions of α showing the falling α spectrum). For the extrapolation point at the nominal working point, the events are 100% correlated with the results to which the normalization is done.

However, this correlation is not explicitly accounted for and thus the errors from the extrapolation are only approximate. This is also confirmed by the systematically low

χ^2/ndf in all $|\eta|$-regions. For the determination of the relative residual corrections, this is not relevant as the extrapolation to zero additional event activity, the p_{T}-independent k_{rad} correction, is only applied as a multiplicative factor to the MC/Data-ratios determined at the working point and is not even needed for the MPF method.

Nevertheless, a strong p_{T}-dependence should become visible and would necessitate an alteration of the procedure outlined in Section 5.2. As no clear p_{T}-dependence becomes evident, the p_{T}-independent assumption is kept in the following.

A correct treatment of the errors in these kind of extrapolations is particularly important if the extrapolated results are used further, e.g. if directly aiming at determining the jet-energy resolution. Indeed, newer studies on 2012 data include a correct treatment of these extrapolations and are expected to become public in the context of the 8 TeV CMS jet-energy correction and resolution publication [135]. Biases that are linked to the extrapolation to zero additional event activity are explicitly considered in the systematic uncertainties. Related uncertainties are the extrapolation range variation, the model exchange (PYTHIA vs. HERWIG++), and the residual non-closure uncertainty (from the comparison of the results obtained by the MPF method and the relative response method).

5.5.2. MC studies on the closure of the correction and the choice of triggers and p_{T} observables

In order to validate the p_{T} balance and MPF methods described before, a full closure test using simulated data has been performed. In parallel, slight variations of the methods with respect to the p_{T}-dependence are evaluated and different choices for the triggering are discussed. This is of particular interest for the MPF-method, as p_{T}^{barrel} is part of the definition of $\mathcal{R}_{\mathrm{MPF}}$ in equation (5.12). This would indicate that the usage of single-jet triggers or a p_{T} binning e.g. in p_{T}^{barrel} could have advantages over the dijet triggers and $\bar{p}_{\mathrm{T}}$-binning used for the nominal analysis.

To allow a full validation of the MPF-corrections, type-I corrected $\vec{E}_{\mathrm{T}}^{\mathrm{miss}}$ has been used in this analysis in contrast to the 2011 analysis in Section 5.4. In this $\vec{E}_{\mathrm{T}}^{\mathrm{miss}}$-type, the jet-energy corrections have been propagated to the $\vec{E}_{\mathrm{T}}^{\mathrm{miss}}$-object. For a closure study, the PYTHIA sample is used twice: Once with the nominal MC-corrections applied to the $\vec{E}_{\mathrm{T}}^{\mathrm{miss}}$ distribution and once as pseudo-data with the residual corrections as shown in Figure 5.18 propagated as additional correction to the $\vec{E}_{\mathrm{T}}^{\mathrm{miss}}$. In order to apply the residual correction to the $\vec{E}_{\mathrm{T}}^{\mathrm{miss}}$ for the pseudo-data, the method of [156] has been followed:

$$\vec{C}_{\mathrm{T}}^{\text{type1 - Residual}} = - \sum_{\substack{\text{jet} \\ \vec{p}_{\mathrm{T,\,jet}}^{\,\mathrm{L123}} > 10\mathrm{GeV}}} \left(\vec{p}_{\mathrm{T,\,jet}}^{\,\mathrm{L123Res}} - \vec{p}_{\mathrm{T,\,jet}}^{\,\mathrm{L123}} \right) \tag{5.20}$$

This way, it can be tested whether such a superimposed response deviation can be retrieved to good precision by determining the residual corrections. All other basic event selection criteria listed in Section 5.3.4 remain the same. The 2012 MC samples listed in Table A.3 are used for the analysis.

Closure test: In Figure 5.18, the closure of the central methods used for the data analysis is shown. As an input, the correction as published in [138] is used to mimic a realistic scenario of residual corrections. The shape of this input correction is reproduced very precisely. Only for the most forward region, where the method is limited by statistics, minor deviations of the order of 0.5% are observed. However, these are always compatible with the central input value within statistical uncertainties.

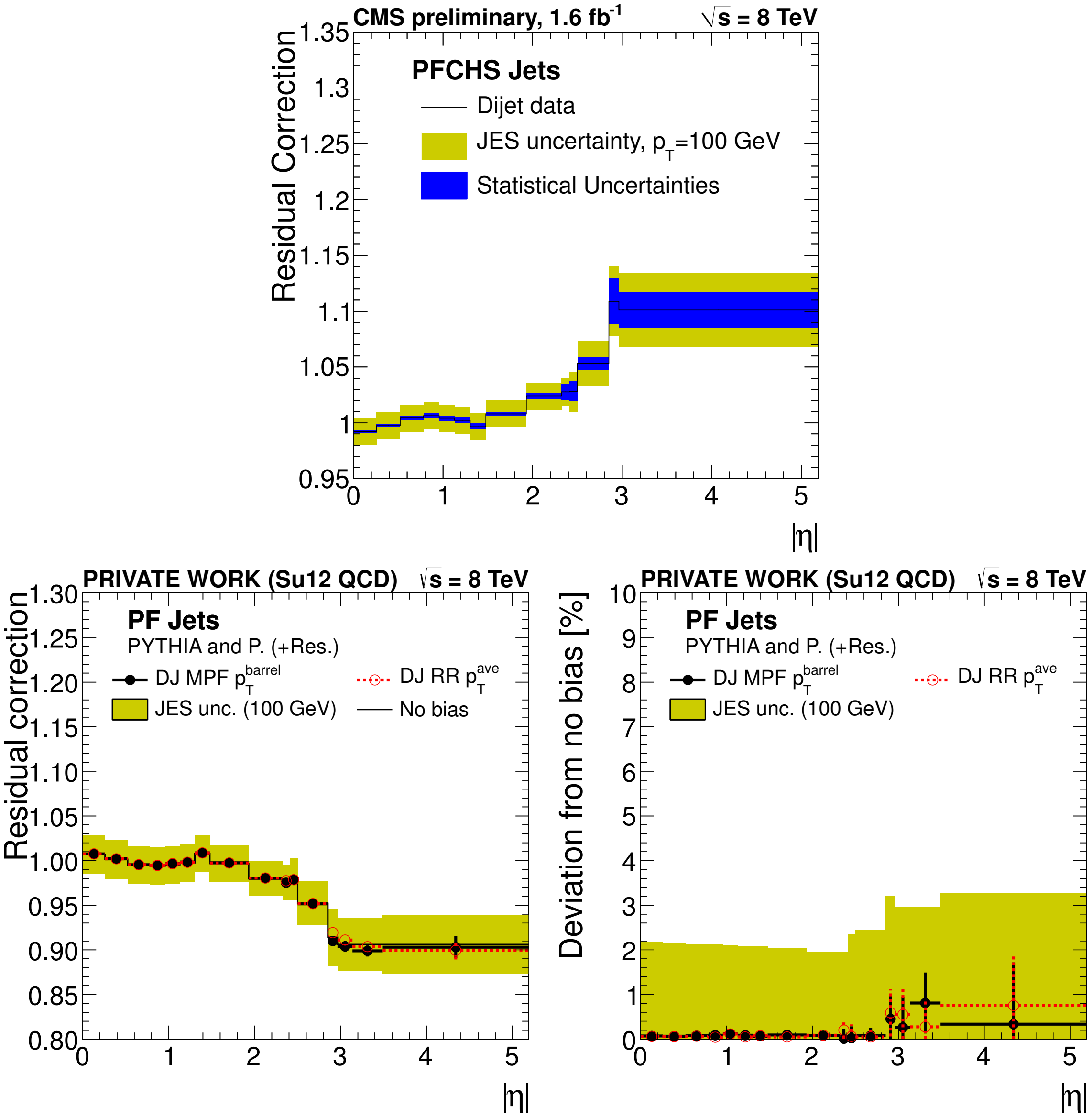

Figure 5.18.: Top: Residual correction as made public in [138]; Bottom: Method closure for MPF and relative response central method using dijet triggers and the Summer 2012 residuals as input (the lower right plot summarizes the observed deviations from reproducing the original input).

Choice of trigger path and p_T-binning variables: As an extension to the previous evaluation, different trigger paths and the resulting dependence of the response estimators on various p_T-variables have been examined. This was considered useful, as, in contrast to the long-established dijet balance method using the relative response, the optimal trigger configuration and appropriate p_T-variable for the MPF-response had not been finally determined.

Two different trigger paths are compared: One using all available DiJetAve-triggers, which are specifically tailored for the dijet balance method, the other one using all available SingleJet-triggers. For the SingleJet-triggers, the p_T of the leading barrel jet is used for evaluating trigger thresholds. The reweighting of the p_T and pileup distributions are performed in the same way as described in Section 5.3.

The p_T-dependence of the response estimators and their Data/MC-ratio are determined for both trigger configurations for various p_T-variables: the average p_T of the two leading jets, $\overline{p}_\mathrm{T}$, the p_T of the jet with the highest p_T, $p_\mathrm{T}^\mathrm{lead}$, and the p_T of the jet with the highest p_T in the barrel ($|\eta| < 1.3$) region, $p_\mathrm{T}^\mathrm{lead,\ barrel}$.

In Figure 5.20 and 5.19, the p_T-dependence of the response estimators of the nominal MC and the MC with superimposed response deviation as well as the corresponding ratios are shown in the $2.322 < |\eta| < 2.411$ region. To summarize the p_T-dependence, Figure 5.21 depicts the "weighted standard deviation" calculated from the histograms of the response estimators and ratios as a function of $|\eta|$. For this context, the weighted standard deviation is defined as

$$\sigma^2 = \frac{\sum_{i=1}^{N} w_i x_i^2 \cdot \sum_{i=1}^{N} w_i - (\sum_{i=1}^{N} w_i x_i)^2}{(\sum_{i=1}^{N} w_i)^2} \tag{5.21}$$

where the weight w_i is taken as the inverse of the uncertainty on the individual histogram entries. In the last column, the deviation from reproducing the input correction as illustrated in Figure 5.18 is shown for the various p_T and trigger configurations.

While the response estimators are almost constant as a function of $\overline{p}_\mathrm{T}$ for both trigger configurations, significant biases are observed when evaluated in bins of p_T^{barrel}. This can be understood as a selection bias: For a fixed $\overline{p}_\mathrm{T}$, the response of the probe jet will be high for $p_\mathrm{T}^{barrel} < \overline{p}_\mathrm{T}$ and low for $p_\mathrm{T}^{barrel} > \overline{p}_\mathrm{T}$. This slope cancels to first order when the ratio, relevant for the determination of the residual corrections, is determined. The standard deviation of the response estimators and the PYTHIA/PYTHIA(+residual correction) ratios, determined as a function of the different p_T-variables, depicted in Figure 5.21, supports this expectation. As a function of p_T^{barrel}, the largest deviations are observed, no matter which method. For MPF, the lowest deviations are observed for $\overline{p}_\mathrm{T}$ and $p_\mathrm{T}^\mathrm{lead,\ barrel}$. For the relative response, $\overline{p}_\mathrm{T}$ exhibits the most stable behavior.

Even though the impact on the final determination of the residual corrections by varying the configurations is fairly small, the stability of the response estimators before taking any ratios can be quite different. Determining the response estimators as a function of p_T^{barrel} yielded an artificial slope in the barrel which can be remedied by evaluating

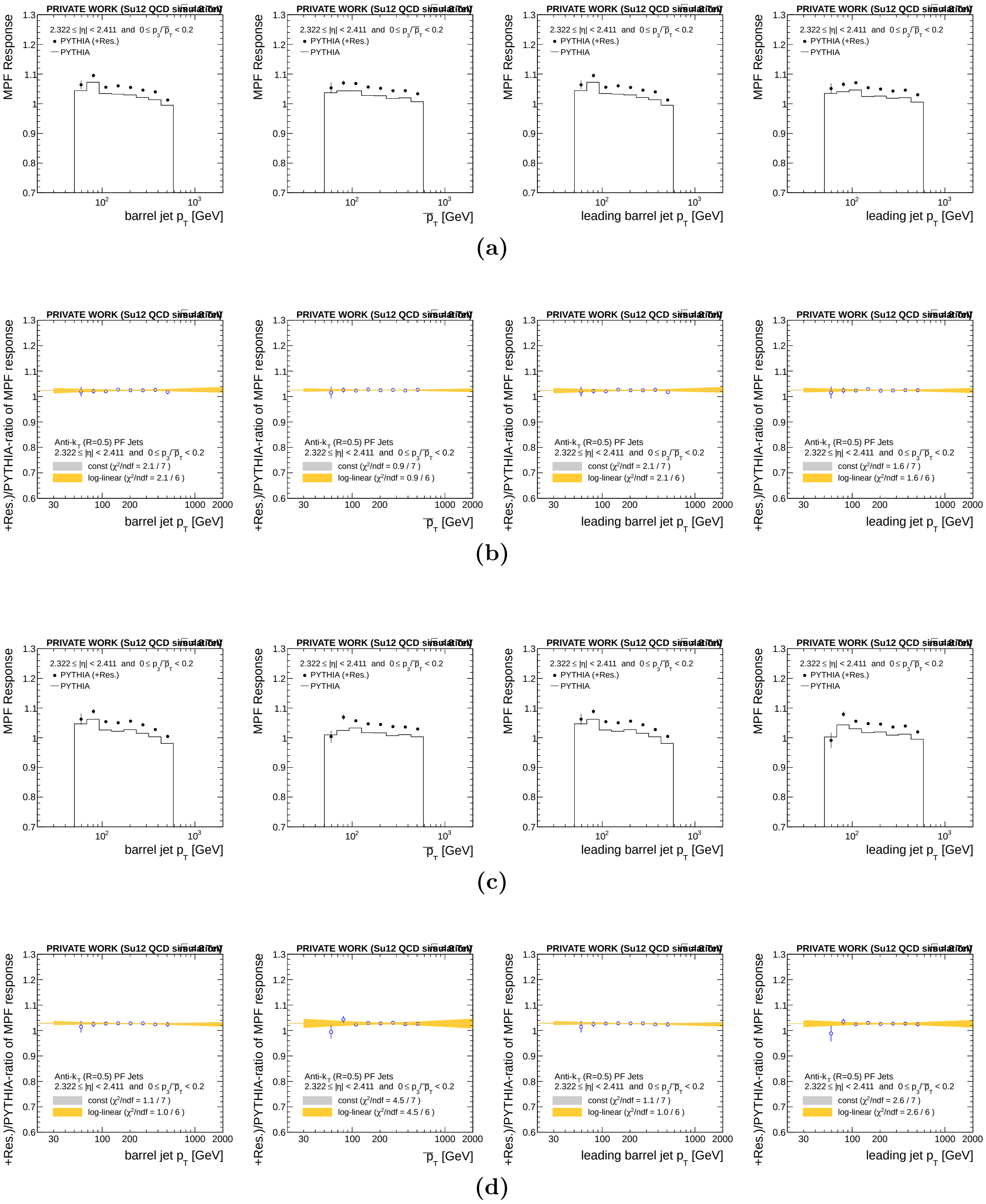

(a)

(b)

(c)

(d)

Figure 5.19.: p_T-dependence of the MPF response estimator and the PYTHIA+Residual/PYTHIA-ratios in the $2.322 < |\eta| < 2.411$ region for different configurations of triggers and binning in p_T. (a) MPF response estimator for different p_T-binning variables using dijet triggers. (b) PYTHIA+Residual/PYTHIA-ratios of MPF response using dijet triggers. (c) same as (a) but for single jet triggers. (d) same as (b) but for single jet triggers

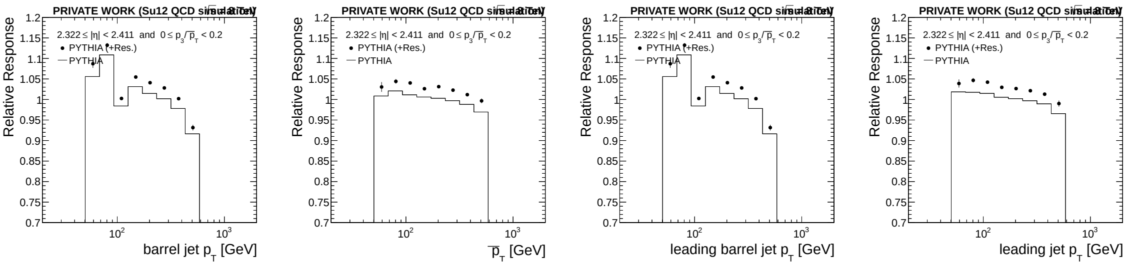

(a)

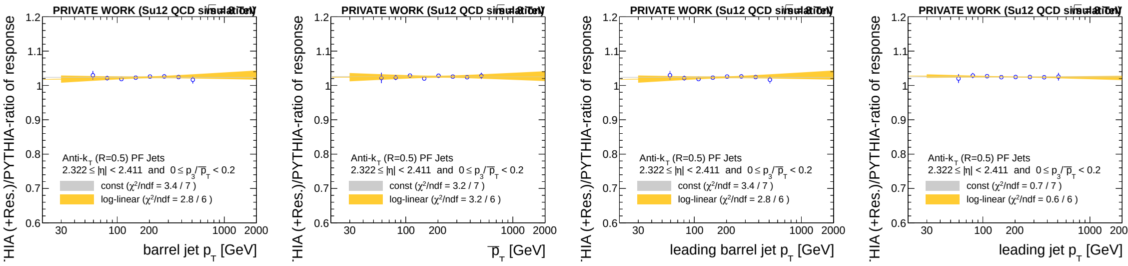

(b)

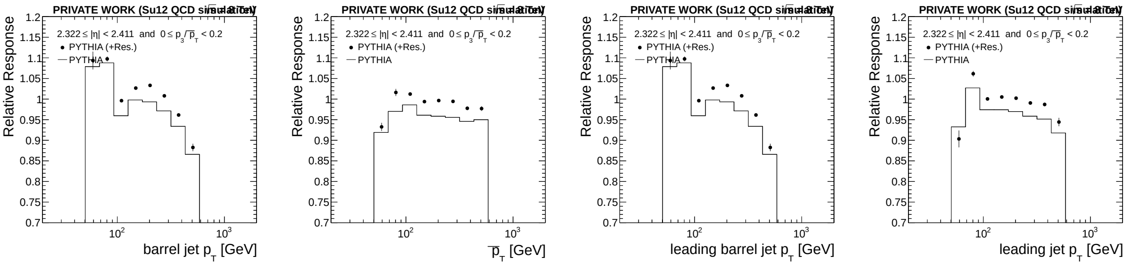

(c)

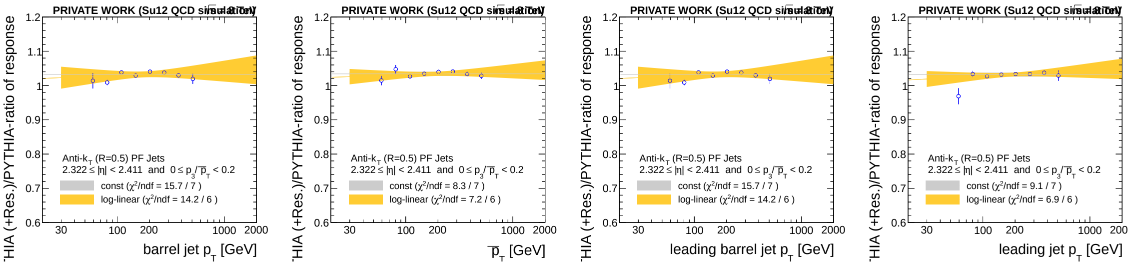

(d)

Figure 5.20.: p_T-dependence of the relative response estimator and the PYTHIA+Residual/PYTHIA-ratios in the $2.322 < |\eta| < 2.411$ region for different configurations of triggers and binning in p_T. (a) Relative response estimator for different p_T-binning variables using dijet triggers. (b) PYTHIA+Residual/PYTHIA-ratios of Relative response using dijet triggers. (c) same as (a) but for single jet triggers. (d) same as (b) but for single jet triggers

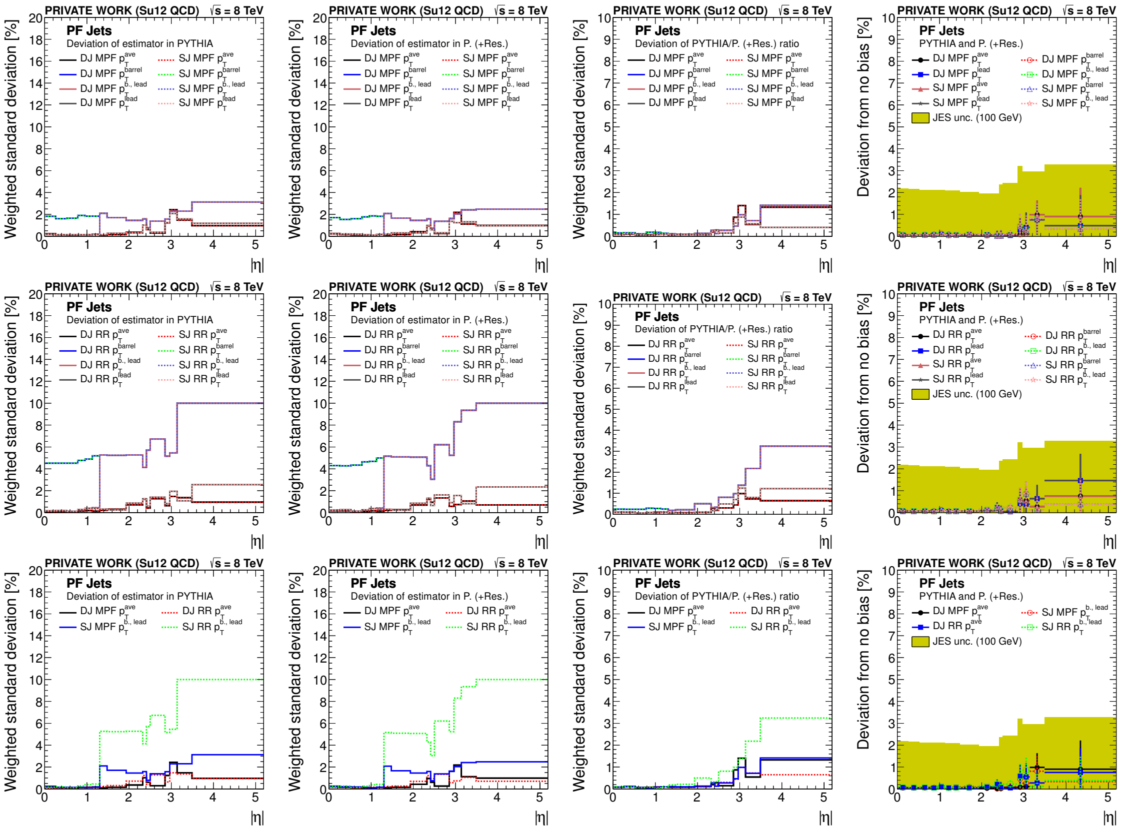

Figure 5.21.: Standard deviation of the p_T-dependence of the response estimators in PYTHIA (first column), PYTHIA+Residual (second column) and the respective ratios (third column) as a function of $|\eta|$. The rightmost (fourth) column shows the deviation from reproducing the input correction as depicted in Figure 5.18. The top row shows the different MPF-variants, the middle row all relative response variants, and the bottom row the most relevant trigger/p_T configurations for MPF and relative response.

the same estimator as a function of $p_\mathrm{T}^{\text{lead, barrel}}$ or $\bar{p}_\mathrm{T}$. The determination of the residual corrections using the dijet trigger paths and binning in $\bar{p}_\mathrm{T}$ gives the most reliable results in this closure test. This configuration continues to be the standard for current studies of the MPF and relative respons methods.

5.5.3. Pileup dependence

It is useful to check if there is a dependence of the residual corrections on the number of reconstructed vertices in order to validate the simulation of pileup. In addition, this is valuable as a cross-check of the previous jet-energy correction steps in which the L1-correction explicitly corrects the pileup influence on the jet-energy response. As the MC/Data ratios of the MPF and relative response have been found to be largely p_{T}-independent, the direct p_{T}-inclusive dependence of the response estimators on the number of reconstructed vertices has been evaluated in different $|\eta|$-regions. It can be observed in Figure 5.22 that neither the MPF-response nor the relative response exhibit a significant dependence on the number of reconstructed vertices. The same holds true for the Data/MC-ratios. This can at least partly be attributed to the relatively high p_{T} of the jets used in the analysis (see e.g. Figure 5.10), which are by definition less affected by the low p_{T} PU effects.

In order to further evaluate the stability of the residual correction results against pileup, several cross-checks determined in the same way as the systematic uncertainties are shown in Figure 5.23.

In order to evaluate systematic uncertainties due to the pileup modeling and pileup reweighting process, it is standard procedure at CMS to vary the cross section assumed for minimum bias events by 5% [160]. This procedure leads to negligible effects for the determination of the residual correction and is not considered as systematic uncertainty for the residual correction alone. Instead systematic uncertainties regarding the pileup JEC corrections are part of the total jet-energy scale uncertainties.

The extreme case without any PU-reweighting has also been tested. Even in this case the resulting deviations are very small and the method can be regarded as robust to PU-influence. More control plots of relevant distributions when not applying the PU-reweighting at all are shown in Appendix B.1.

The L1-corrections is needed to subtract the offset energy added to the hard jets in the event by pileup activity. The cross-check of not applying the L1-correction leads to only minor deviations of the determined residual correction. Only in the endcap-region, where the influence of out-of-time (OOT) pileup was strongest during 2011 data-taking, some small deviations are observed.

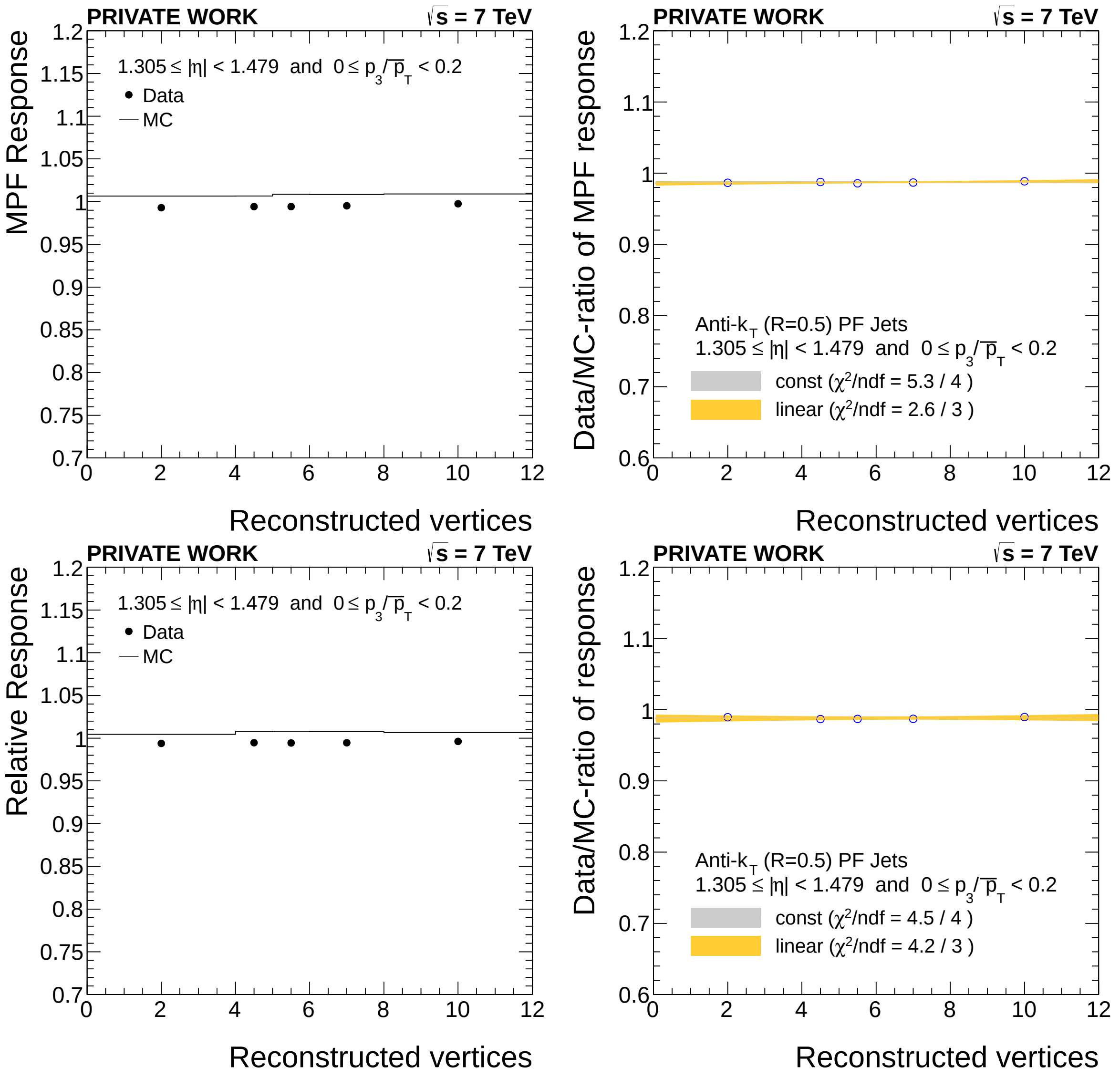

Figure 5.22.: Response in data and MC (left colum) and their ratio (right column) as a function of the number of reconstructed vertices in the region of $1.305 < |\eta| < 1.479$. The top row shows the MPF results, the bottom row shows the relative response results.

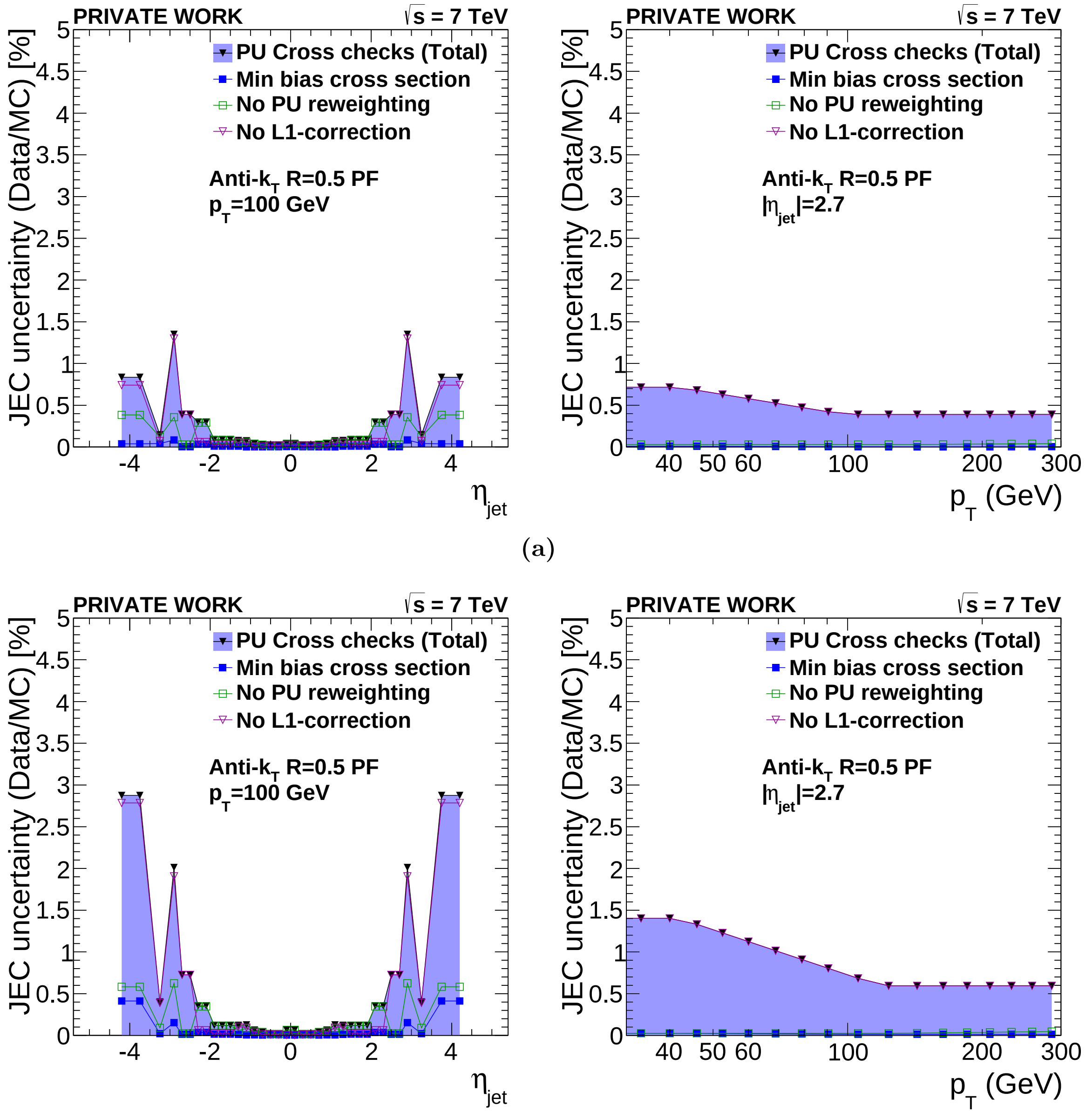

(a)

(b)

Figure 5.23.: Results of the cross-checks related to pileup modeling at $p_\mathrm{T} = 100\,\mathrm{GeV}$ and $|\eta| = 2.7$. (a): MPF method; (b): relative response method. “PU Cross Checks (Total)” denotes the quadratic sum of the individual listed cross-checks.

5.5.4. Jet energy resolution

The jet-energy resolution and jet-energy scale are closely related and the uncertainties on both measurements influence each other. For example, the systematic uncertainty on the jet-energy resolution in data has been propagated to the residual correction results described in Section 5.4. Dijet events are commonly used to study both, the jet-energy resolution and the jet-energy scale, as described e.g. in [133].

Here, an analysis based on the dijet asymmetry method is performed to extract new JER-scaling factors as a cross-check to previous findings. Requiring the jets to be in the same $|\eta|$ bin limits (drastically) the number of events in the forward regions, but is the best understood method.

Following the generalized asymmetry definition in Section 5.1.1, the events are selected to be in the same $|\eta|$-bin and the resolution is related to the width of the asymmetry by

$$\frac{\sigma(p_T)}{p_T} \approx \sqrt{2} \cdot \sigma_A \tag{5.22}$$

An iterative Gaussian fit of the core of the asymmetry distribution (fitted in the range $\pm 1.5\sigma$ of the first iteration) is performed and the Gaussian widths of the asymmetry are determined as a function of $\overline{p}_{\mathrm{T}}$ in various $|\eta|$-regions. The results are shown in Figure 5.24 and show a slight difference of the width between simulation and data. In order to extrapolate to the ideal dijet event topology, the cut on the relative third jet p_{T} is varied as described above (compare e.g. equation (5.16)).

Some examples of these extrapolations are depicted in Figure 5.25. For more detailed JER-studies, the goal is to determine the full resolution behavior. As the only scope of this analysis is to spot MC/Data differences, the extrapolation has in the following been performed for MC/Data-ratios. In comparison to the residual correction study, slightly larger non-linearities are observed in the extrapolation which are reduced by limiting the used α-range to a maximum of $0.2 - 0.25$, e.g. in [124, 162].

As a result of the extrapolations, the MC/Data-ratio of the asymmetry width is determined as a function of p_{T}. The results are shown in Figure 5.26 and are fitted with a constant. Presumably due to the non-linearity of some of the extrapolations, a relatively strong p_{T}-dependence of the scale factors is observed with this simple approach.

The results for the JER-scaling factors when fitting a constant are shown as a function of $|\eta|$ in the lower right plot in Figure 5.26. As observed in previous studies on 2011 data, a deviation of the order of 10% is observed in most parts of the detector. As no systematic uncertainties have been evaluated for this study and the extrapolation technique is not optimal as it neglects the correlations of the asymmetry widths measured for different α thresholds, the officially recommended scaling factors [161] and associated uncertainties have been used for adapting the jet-energy resolution in the simulation. The numerical values of the results presented here and the commonly used scaling factors are covered by the systematic uncertainties determined for the official numbers.

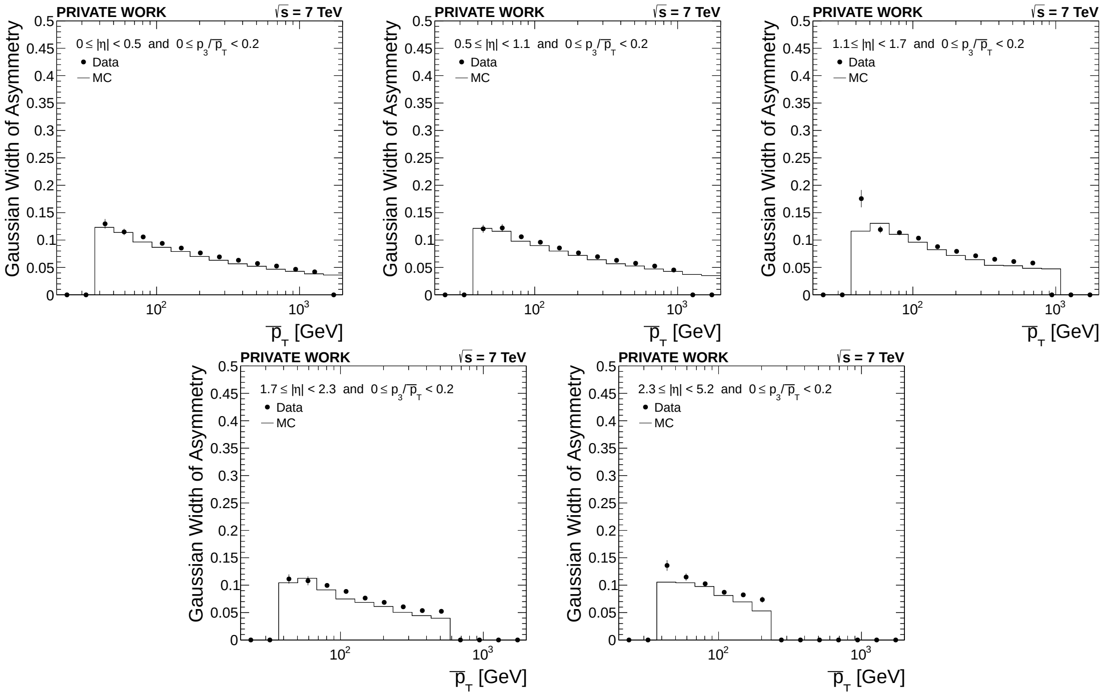

Figure 5.24.: p_{T}-dependence of the width of the asymmetry, determined by an iterative Gaussian fit to the core of the asymmetry distribution, at the working point $\alpha < 0.2$ in various $|\eta|$ regions.

Due to the interplay between the resolution and scale it would be highly beneficial for future studies on dijet events to measure both at the same time in a consistent way.

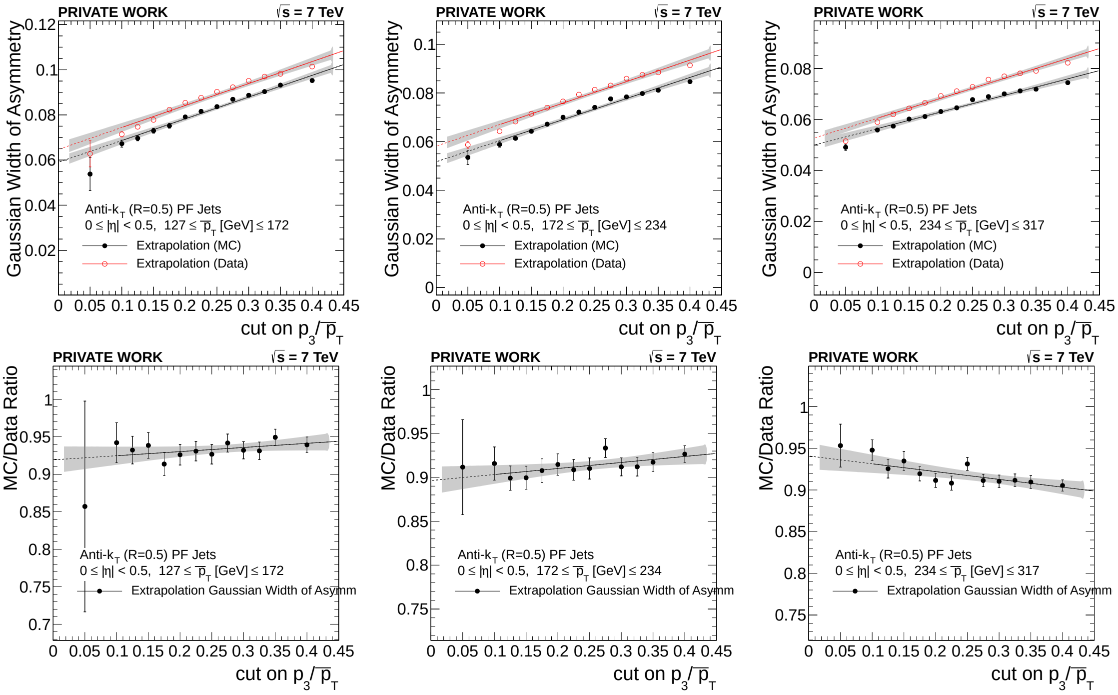

Figure 5.25.: Extrapolation of resolution in MC and data (upper row) and their ratio (lower row) to zero additional event activity for three consecutive $\overline{p}_{\mathrm{T}}$-ranges in the central detector region.

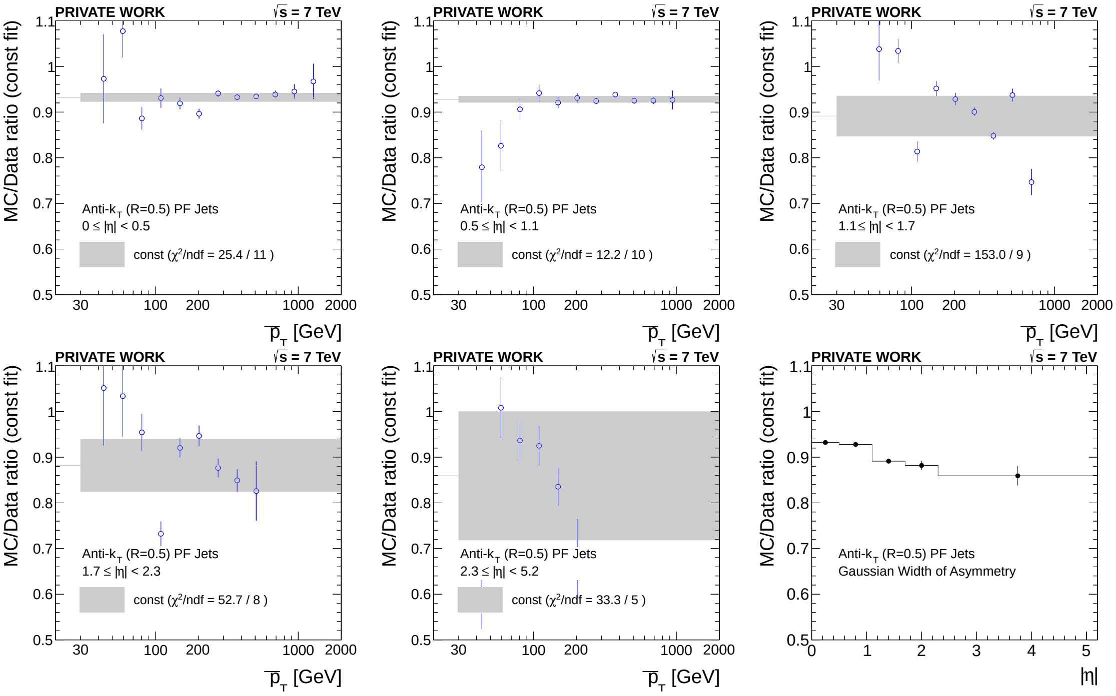

Figure 5.26.: p_{T}-dependence of the MC/Data ratios determined from the extrapolation to $\alpha = 0$ in the considered $|\eta|$-regions and summary of the resulting JER scaling factors as a function of $|\eta|$ (lower right plot)

5.5.5. Time dependence

During 2011 and 2012, a significant time dependence of the response in the endcap region has been observed. This has been attributed to gain-drifts in the calorimeter readout that could not be corrected for fully in the prompt reconstruction of data (see Figure 5.27 for the time stability of the ECAL response).

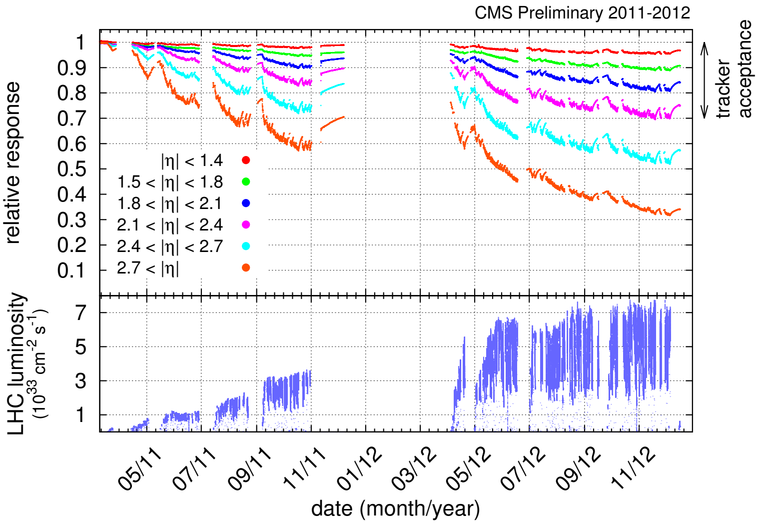

Figure 5.27.: Relative response to laser light (440 nm in 2011 and 447 nm in 2012) measured by the ECAL laser monitoring system, averaged over all crystals in bins of pseudorapidity, for the 2011 and 2012 data-taking periods. The response change observed in the ECAL channels is up to 6% in the barrel and it reaches up to 30% at $\eta \approx 2.5$, the limit of the tracker acceptance. The response change is up to 70% in the region closest to the beam pipe. These measurements are used to correct the physics data. Taken from [163]

Most published CMS physics analyses of the 2011 data have used a prompt reconstruction dataset ("PromptReco" in CMSSW42X). Due to the sub-optimal calibration constants used in the propt reconstruction, this has had a major impact on the systematic uncertainties of the jet-energy scale. The time dependence mainly affected the endcap region, in which the response losses were largest due to high radiation doses. The systematic uncertainty on the JES assigned due to the drifting response was estimated from the relative residuals measured for different run periods. These results are summarized in Figure 5.28.

In the meantime, the full 2011 dataset has been reprocessed and this analysis shows mainly results from the re-reconstructed dataset ("ReReco" using software version CMSSW44X and updated detector calibration constants), in which the time dependence is expected to decrease. In order to assess the time-dependence more closely, the dataset has been divided such that run-ranges with a roughly equal number of events were selected. In bins of $|\eta|$, the drift of the mean value of the response estimators can explicitly be

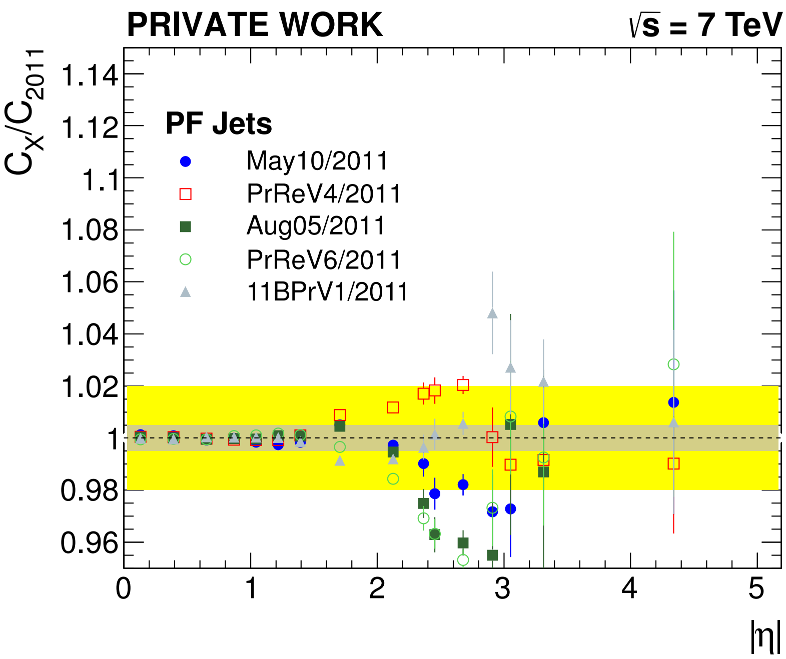

Figure 5.28.: Time dependence in the 2011 dataset reconstructed with CMSSW42. A large fraction of the dataset was only available as PromptReconstruction. C_x/C_{2011} refers to the deviation of the residuals determined for individual run periods from those determined on the full 2011 dataset.

examined. As the p_T-spectrum evolves with time (due to the changing trigger prescales) and the response estimators themselves (in contrast to the MC/Data ratio, which is used to extract the residual corrections) show some p_T-dependence, a slight bias of this p_T-inclusive evaluation can not be excluded. However, an additional evaluation in p_T-bins did not show any significant qualitative differences. Larger drifts and the difference between the PromptReco and ReReco datasets are therefore examined without additional p_T-binning in order to maximize the statistical precision. A selection of these time dependence monitoring plots is shown in Figure 5.29. Here, the PF composition as well as the relative and MPF response are shown in bins of the run number for two different $|\eta|$-regions.

In the endcap region, a very strong drift is observed for 42X in the PrReV4-period, with the response decreasing with time. This could be explained by a drift in the ECAL response that is also indicated by the decrease of the photon fraction over time. The ECAL-response is indeed deteriorating with integrated radiation fluence (i.e. time) as depicted in Figure 5.27 and this loss has not been completely compensated for in the promptly reconstructed datasets. In the forward $|\eta|$-region, the difference between the maximum measured MPF-response and the minimum measured MPF response is as high as 10% for promptly reconstructed data, while the differences for the re-reconstructed dataset do not exceed 4%. The time dependence seems to have decreased significantly due to the re-reconstruction, but has not vanished completely. In the PrRe2011B-period, the same drift in the photon fraction is observed for 44X-re-reconstructed data. It is possible that another re-reconstruction of the full 2011 dataset with final calibration constants of the different detector components could further stabilize the behavior as a function of time. The current status of time stability is summarized in Figure 5.30 showing the weighted standard deviation of the MC/Data ratios for the different datasets.

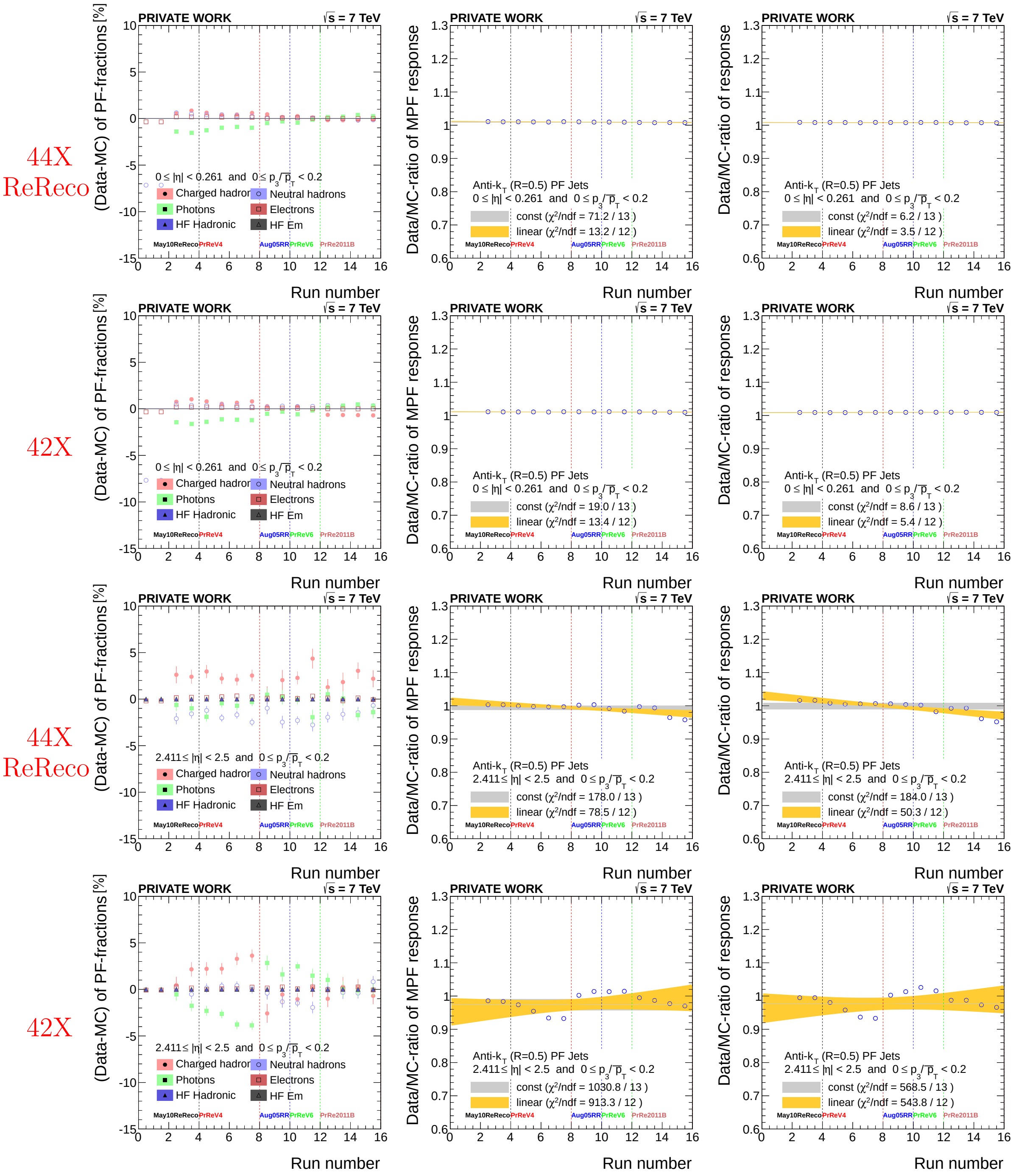

Figure 5.29.: Time dependence of the PF-composition modelling (left column) and the Data/MC ratios of $\mathcal{R}_{\mathrm{MPF}}$ (center column) and $\mathcal{R}_{\mathrm{rel}}$ (right column) for two $|\eta|$-regions ($0 < |\eta| < 0.261$ in the upper two rows, $2.411 < |\eta| < 2.5$ in the lower two rows) and the 44X/42X data sample as an example.

Table 5.2.: Run ranges of the different PrReco/ReReco data-taking periods in 2011. Binning used for the run numbers in the histogram: 160329 163062 163471 163869 165955 166642 167042 168437 171573 172619 173103 175770 176851 177648 178611 180296

Data-taking period	from Run	to Run	bins in histogram
May10 ReReco	160329	163869	3
PromptReco Run2011A v4	165071	168437	4
Aug5 Rereco	170053	172619	2
PromptReco Run2011A v6	172620	175770	2
PromptReco Run2011B v1	175832	180296	4

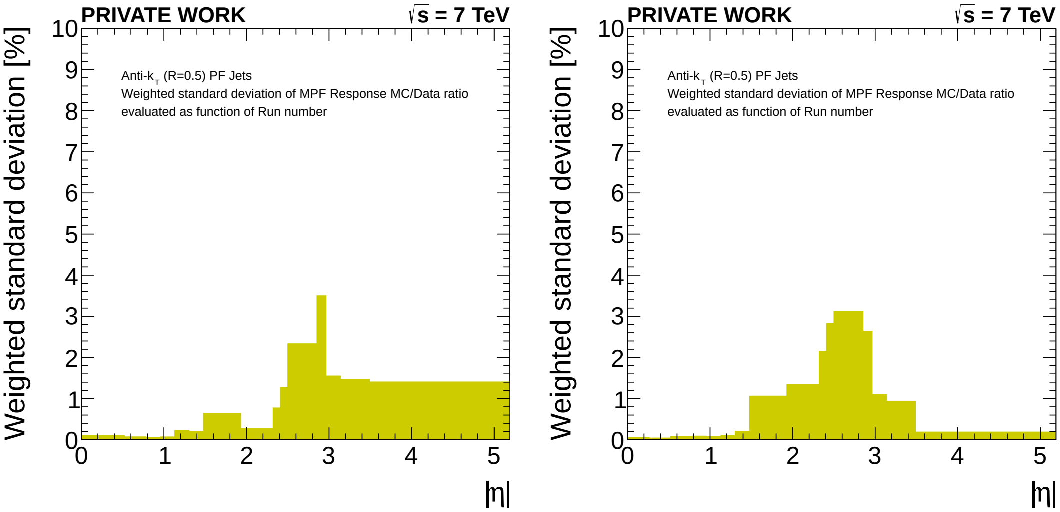

Figure 5.30.: Time dependence in 44X (left) and 42X (right) as a function of $|\eta|$, quantified by the weighted standard deviation (compare equation (5.21) for definition) of the MC/Data ratios evaluated as a function of the run number in bins of $|\eta|$. The difference in the most forward $|\eta|$ bin is an unphysical artefact caused by an insufficient number of events for the adopted run number subdivision.

Time dependence in 2012 data: The same technique has been used to monitor the time stability in the 2012 datasets. The 2012 dataset have been re-reconstructed using the same reconstruction software version as used for the prompt reconstruction so that differences in the time stability are only due to updated calibration constants. The subdivision of the dataset into run periods and the corresponding bin edges are given in Table 5.3. Plots showing the time stability in two example $|\eta|$-bins are shown in Figure 5.31, and the $|\eta|$-summary is given in Figure 5.32.

Similarly to the behavior in 2011, the response is degrading with time. In contrast to the 2011 dataset which already included partially re-reconstructed data, the response is degrading linearly as a function of accumulated events. In the re-reconstructed dataset, this slope is fully corrected for in the endcap region. In the more forward region no significant conclusion can be drawn as the amount of data is not sufficient to determine the responses in the fine run number binning.

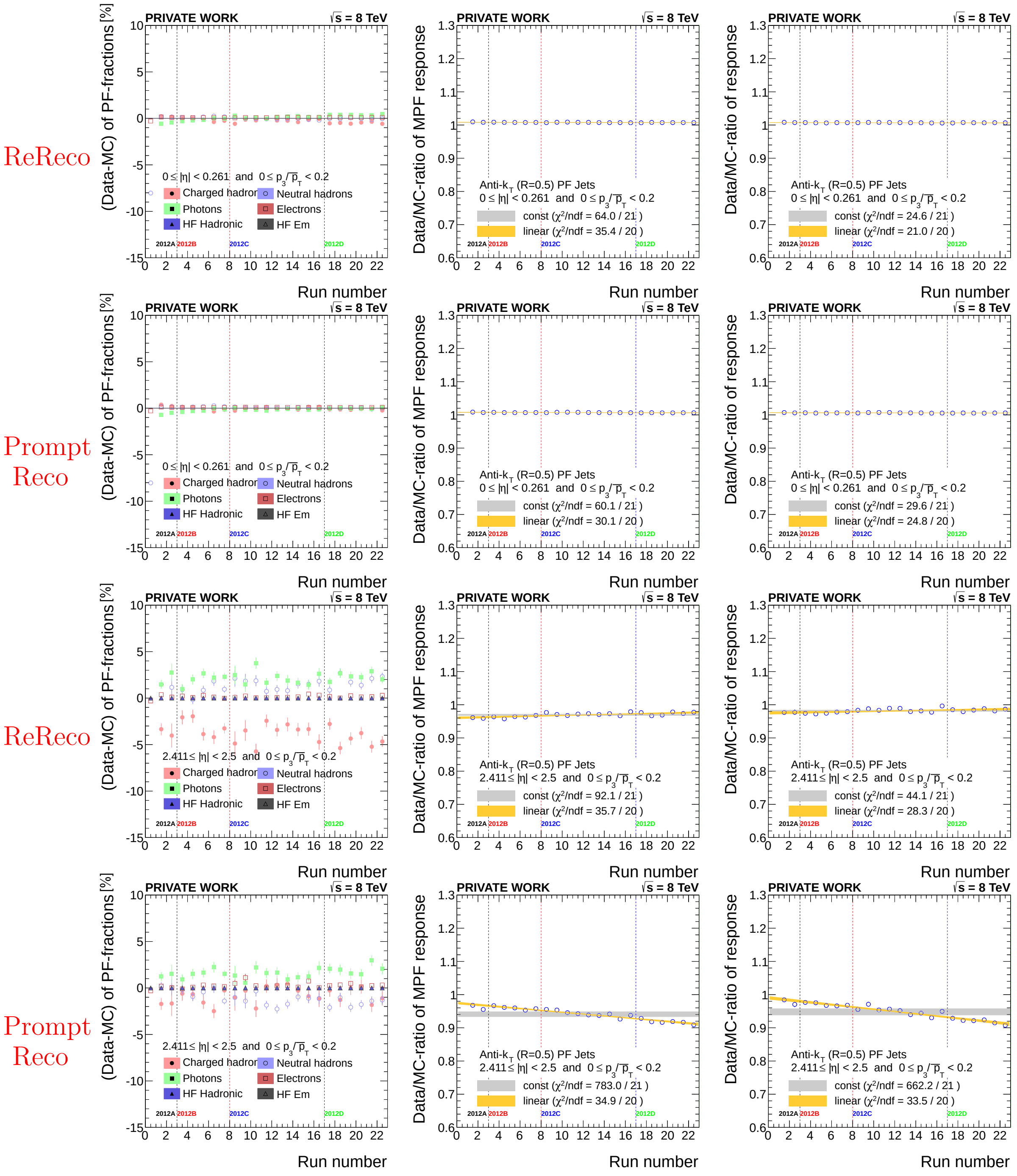

Figure 5.31.: Time dependence of the PF-composition modelling (left column) and the Data/MC ratios of $\mathcal{R}_{\mathrm{MPF}}$ (center column) and $\mathcal{R}_{\mathrm{rel}}$ (right column) for two $|\eta|$-regions and the 2012 PromptReco/ReReco dataset.

Table 5.3.: Run ranges of the different PrReco/ReReco data-taking periods in 2012. Binning used for the run numbers in the histogram: 190641 193124 193621 194198 194630 195108 195552 196531 198231 198913 199408 199834 200473 201196 202016 202327 203746 205216 205832 206448 206905 207455 208684

Data-taking period	from Run	to Run	bins in histogram
2012A	190641	193621	2
2012B	193621	196531	5
2012C	196531	203746	9
2012D	203746	208684	6

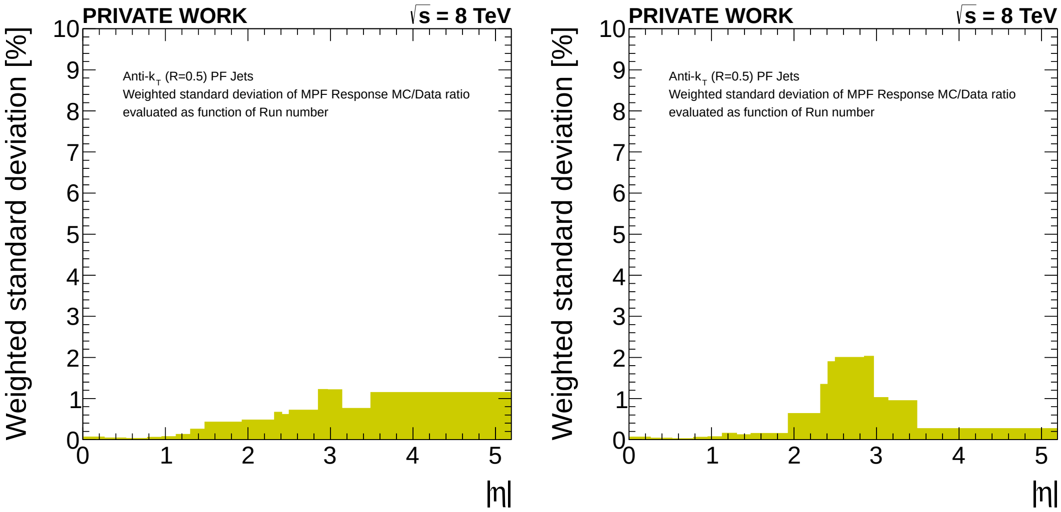

Figure 5.32.: Time dependence in ReReco(left) and PromptReco (right) 2012 datasets as a function of $|\eta|$, quantified by the weighted standard deviation (compare equation (5.21) for definition) of the MC/Data ratios evaluated as a function of the run number in bins of $|\eta|$.

5.5.6. φ dependence of the jet-energy scale determined from dijet events

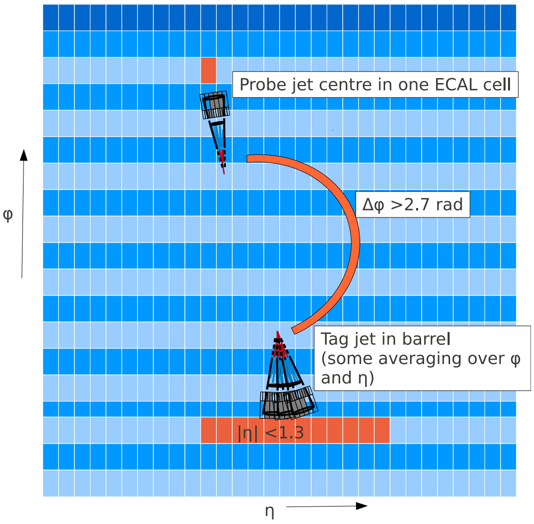

Figure 5.33.: Illustration of using the machinery used for the derivation of relative residual corrections to test for a φ dependence of the jet-energy response: The response of the probe jet is tested in single ECAL-cell segmentation (72 cells in φ in barrel) relative to the tag jet in the barrel ($\Delta\varphi > 2.7$). The η binning corresponds to the calorimeter tower edges.

In the barrel region, the number of available dijet events is very high and it is possible to check the response in a very fine granularity. This has been used to perform a scan of response inhomogeneities on the granularity level of single calorimeter cells. The response of the probe jets is determined in bins of η corresponding to the calorimeter tower edges and bins of φ corresponding to the single ECAL-cell segmentation (72 cells in φ in the barrel). The reference object is the tag jet which is required to be in the barrel and separated from the probe jet by $\Delta\varphi > 2.7$. This means that no absolute response calibrations can be done this way in a single iteration. Instead, the calibration is relative to some η/φ slice. Nevertheless, differences in the description of the response in the simulation and data can be detected.

This study was performed after a modulation of the reconstructed $\vec{E}_{\mathrm{T}}^{\mathrm{miss}}$ in φ was observed. This modulation and corresponding corrections are discussed in [144], but the cause for this modulation has not yet been identified unambiguously. Possible causes are a φ-dependence of the detector response, a displacement of the beam spot or detector misalignment. An anisotropic detector response in φ could also be one of the possible causes of the differences of the measured jet-energy resolution in data and simulation.

Before building higher level objects like $\vec{E}_{\mathrm{T}}^{\mathrm{miss}}$ or jets, the individual detector components are intercalibrated separately. For example, the ECAL crystal response is calibrated using various techniques including the analysis of photons from π^0-events and exploiting the expected isotropic distribution of energy depositions by minimum bias events in the calorimeter as explained in [100].

In Figure 5.34, the dependence of the Particle Flow energy fractions, the MPF and relative response are shown for one examplary η-bin for the 2012 re-reconstructed dataset. While some spikes in the response, caused by non-functioning ECAL-cells registered as such in the simulation, are described well by the simulation, e.g. around $\varphi_{probe} \approx 0$ in the selected η-region, significant variations in the MC/Data-ratio remain at other values of φ_{probe}.

It should be checked whether these response variations observed in high level objects like jets can be used to either calibrate the detector components in a top-down approach or whether these remaining inhomogeneities can be resolved by further improving the detector-level calibrations. Resolving these Data/MC-differences could help to improve the jet-energy resolution in the data.

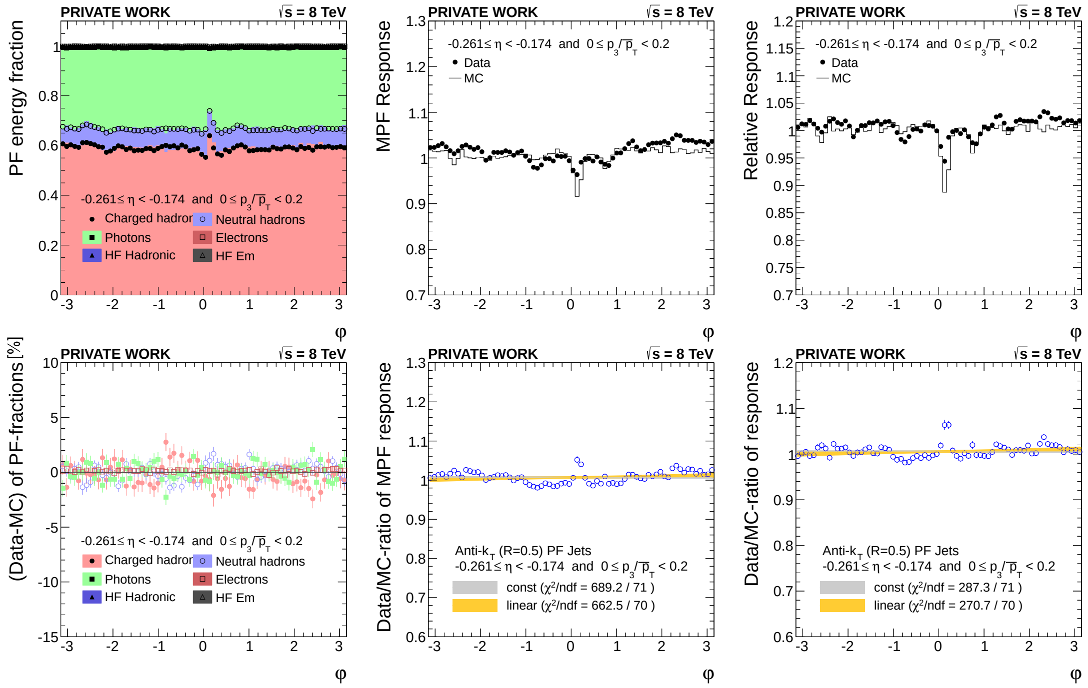

Figure 5.34.: Dependence of the PF composition, the MPF and the relative response on φ_{probe} in an example η-region. Absolute values are shown in the upper row, percentage differences of the PF composition and Data/MC ratios of the response estimators in the lower row.

5.5.7. Response behavior of close-by jets

In the discussions between ATLAS and CMS on the correlation of the jet-energy scale uncertainties of both experiments, which is explained in more detail in Chapter 6, one of the ATLAS jet-energy scale uncertainties could not be matched with a CMS equivalent systematic uncertainty. As explained in [164, 165], ATLAS considers a systematic uncertainty due to close-by jets, estimated by comparing the ratio of jets built out of tracks and calorimeter jets as a function of the distance between the two jets in data and Monte Carlo. For jets clustered from calorimeter entries which is the default jet reconstruction method at the ATLAS experiment, the response can differ significantly if close-by jets are present, i.e. the jets are non-isolated. The response (relative to generator jets) has been found to be significantly decreased, especially for low p_{T} jets with close-by jets directly outside of the cone.

At CMS, the Particle Flow event reconstruction uses tracking information for the largest energy fraction of average jets (charged hadrons make up ≈ 60% of a typical jet) and is thus expected to be less susceptible to such effects. Indeed, the dependence of the jet-energy response has been found to show only a small dependence for PF jets. This is illustrated in Figure 5.35, where a MC/Data comparison using $\mathcal{R}_{\mathrm{MPF}}$ to determine residual corrections shows a good description of the data by the simulation. For these cross-checks, no specific requirements regarding the p_{T} of the close-by jets were made.

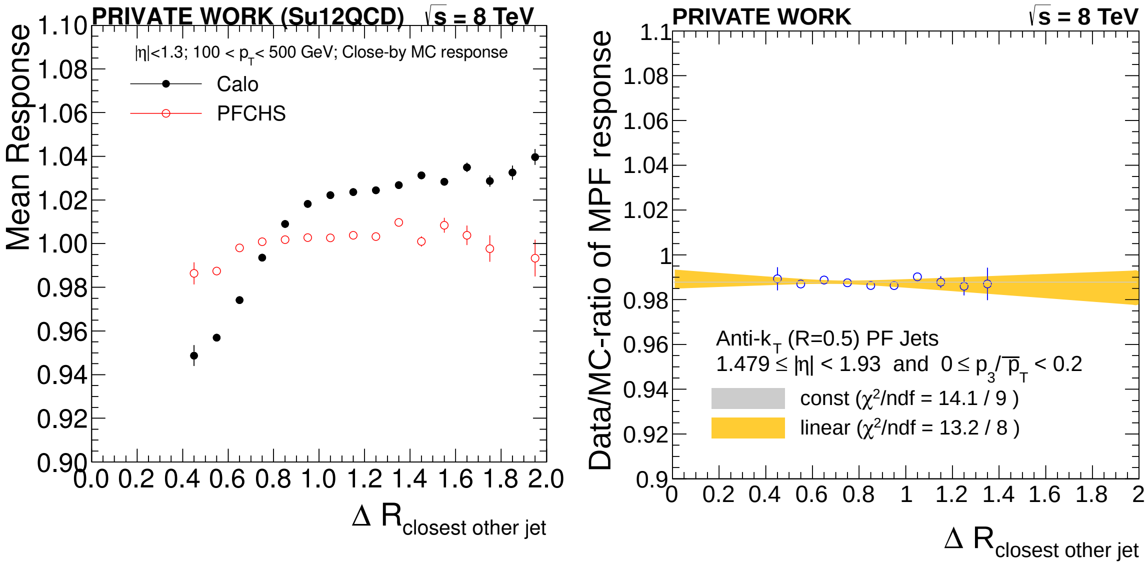

(a) (b)

Figure 5.35.: Dependence of the jet response on the distance to the next jet. (a): MC truth response for calorimeter and PF jets; (b): MC/Data ratio of MPF response estimators as a function of the distance in ΔR to the next jet

Similarly to the Tevatron experiments, no additional close-by jet uncertainty has been assigned at 7 or 8 TeV in the context of CMS jet-energy scale uncertainties. Nevertheless, it would be useful to continue studies on the effect of close-by jets on the jet-energy scale, possibly in the context of the extensive study and commissioning of techniques for boosted topologies, e.g. W and top tagging [166, 167].

5.6. Summary

The MPF response was introduced for determining the residual corrections from dijet events in CMS for the first time and a very promising agreement of the resulting corrections could be achieved for the MPF and the relative response method. Systematic studies on the closure of both methods, the choice of the trigger and p_{T}-variables were presented in Section 5.5.2. They show that the default method of using dijet triggers and a binning in $\overline{p}_{\mathrm{T}}$ is giving the most reliable results.

The MPF response is more robust in terms of radiation modelling. This way, the radiation correction k_{rad} is basically negligible, potentially allowing for a looser working point (cut on third jet p_{T}) in the future. It has to be emphasized that a good closure is observed between MPF and relative response both for HERWIG++ and PYTHIA as refernce MC as illustrated in an example $|\eta|$-region in Figure 5.12, in spite of their different showering models. The MPF-method is now the default method to determine relative residual corrections at CMS.

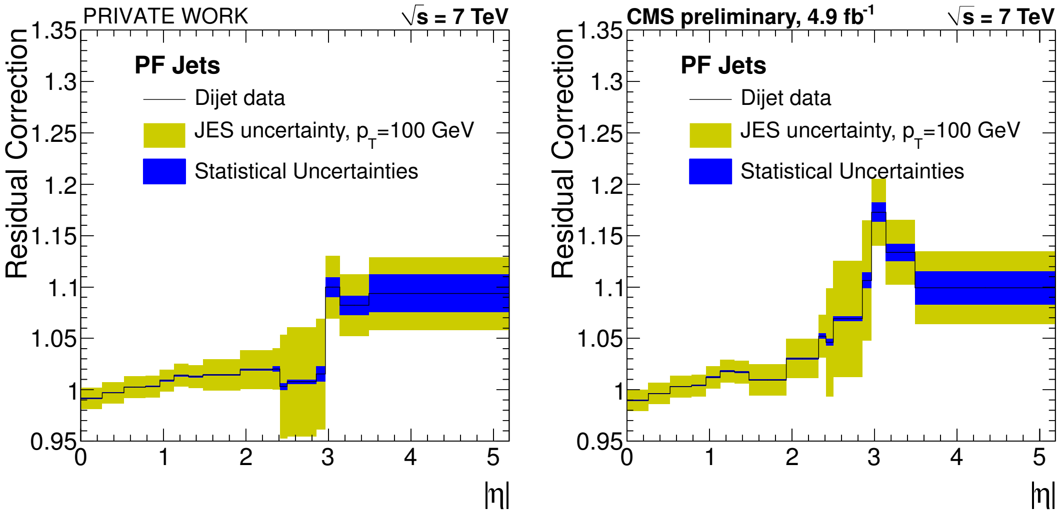

Figure 5.36.: Left: 2011 ReReco (using CMSSW44X) residual corrections as presented in detail in this chapter; Right:Residual corrections determined on the 2011 PromptReco dataset (using CMSSW42X). Both plots show the JES systematic uncertainties as yellow band and statistical uncertainties as blue band. The latter plot is made public by CMS in [134].

In Figure 5.36, the final residual corrections for the fully re-reconstructed dataset as discussed in Section 5.4 and the public residual corrections for the 2011 dataset used by most analyses (using datasets promptly reconstructed using CMSSW42X) are shown as a function of $|\eta|$. For the fully re-reconstructed dataset, the needed residual corrections are slightly smaller than for the PromptReco dataset. This can be attributed to the large reduction of the time dependence behavior in the re-reconstructed dataset.

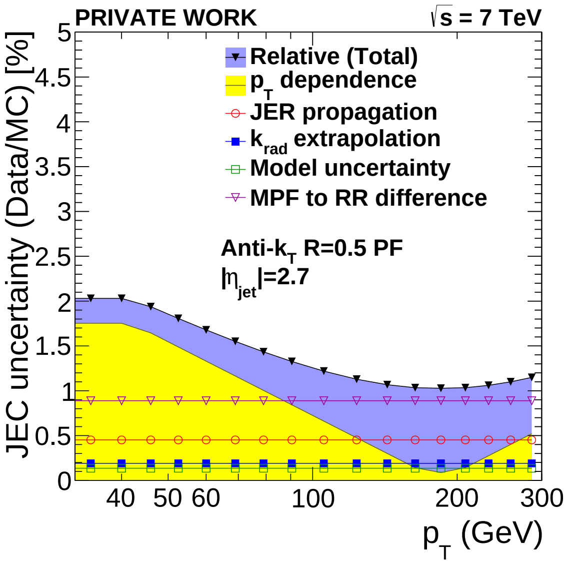

Figure 5.37.: Systematic uncertainties when using the MPF method for the determination of relative residual corrections for a fixed η as a function of p_{T} (left) and for a fixed p_{T} as a function of η (right). Relative (Total) denotes the quadratic sum of the individual uncertainty components.

As shown in Figure 5.37, the systematic uncertainties evaluated in the re-reconstructed 2011 data are below 1% in the detector region up to $|\eta| < 2.2$ and close to zero in the central detector region $|\eta| < 1.3$. In the tracker-covered detector region, the high precision of the relative residual correction has a very small impact on the total systematic uncertainty of the jet-energy scale.

The forward detector regions outside of tracker coverage remain problematic in terms of statistical precision. Due to the lack of events in the forward region, the correction factor can only determined in coarse bins of $|\eta|$. This is related to the steeply falling spectrum in η, the high trigger thresholds, and large prescales, especially for the triggers with relatively low nominal $\overline{p}_{\mathrm{T}}$. The lack of statistical sensitivity at high $|\eta|$ leads to the fact that the systematic uncertainties on the jet-energy scale at high $|\eta|$ are dominated by the relative residual corrections from dijet events. Some dedicated forward triggers for dijets or complementary studies using Z/γ+jet events are expected to greatly improve the precision here. A slight improvement could also be gained by adopting the matrix method proposed by ATLAS and discussed briefly in Section 6.1. Currently, the contributions from the difference in the results between the MPF and the RR method, together with the model uncertainty, add up to uncertainties of about 3 % in the forward detector region.

It would be beneficial to further improve studies of the jet-energy resolution as outlined in Section 5.5.4 in order to reduce the size of resulting systematic uncertainties even further. The powerful tool of PF-composition studies can help to track down the cause of residual non-closure and helps in monitoring the time stability of the jet-energy response.

The relative residual correction from dijet events will continue to help scrutinize the jet-energy scale as a function of η and is an important and powerful tool to test the understanding of the detector. However, it is crucial to overcome the statistical limitations at high $|\eta|$ in order to further improve the precision in the forward detector region. With the abundance of available events in the central detector region, even more differential studies, such as e.g. the study of the φ dependence of the response modelling, have become possible. This is an interesting field for further studies in its own right.

Chapter 6

Correlation of jet-energy scale uncertainties between ATLAS and CMS

The precise understanding of jet-energy corrections and the associated jet-energy scale uncertainties is a key requirement for all physics analyses with jets in the final state. In a large number of physics measurements and searches for new phenomena, jet cross section [168, 169] measurements are a classical example, the systematic uncertainties are dominated by uncertainties related to the jet-energy scale. The jet-energy measurement and associated systematic uncertainties in pp and $p\bar{p}$ collisions are documented for many HEP experiments [133, 135, 150, 151, 153, 164, 170].

In order to improve the precision of measurements it is often useful to combine the results of different experiments. Especially for measurements in which the jet-energy scale uncertainties are among the dominating sources, the precise knowledge of the correlations between the JES uncertainty sources of the different experiments is crucial.

For the two LHC experiments ATLAS and CMS, such an effort has been undertaken in the context of the TOPLHCWG (working group on top physics at the LHC) to understand the level of correlation between similar uncertainty sources for the 2011 data-taking period. Measurements of top-quark properties like e.g. the measurement of its mass are often systematically dominated by jet-energy scale uncertainties and the understanding of correlations is considered a prerequisite to perform combinations of those measurements.

While the CMS approach to jet-energy corrections has been discussed in detail in Section 4.5, a short account of the techniques used and the uncertainties considered by ATLAS is given in Section 6.1. In Section 6.2, the so-called "correlation groups" are explained, which were agreed upon in discussions between ATLAS and CMS. These correlation groups are used for the combination of precision measurements including the LHC and World combinations of the top-quark mass and are publicly documented in [171, 172].

6.1. ATLAS jet-energy scale (in comparison to CMS)

ATLAS has performed extensive studies of jet-energy scale measurements as presented in [170] for the 2010 data-taking and in [173] for the 2011 data-taking. ATLAS considers "truth jets" reconstructed from generated particles, track jets reconstructed from tracks, and calorimeter jets reconstructed from calorimeter clusters in the context of jet energy measurements as summarized in Figure 6.1. The standard jet clustering algorithm is anti-k_t with a distance parameter of 0.4 or 0.6 (default at CMS in 2010/2011/2012: 0.5).

The truth jets correspond to the particle-level or generator jets at CMS and are independent of the detector response. They are used as the reference level to which the reconstructed jets are calibrated, just as in CMS. The treatment differs in that muons are not considered as part of the truth jets in ATLAS, i.e. muons and neutrinos are excluded. This is a useful definition for ATLAS as mostly calorimeter jets are used by the experiment and muons usually leave only a small fraction of their energy in the calorimeter system.

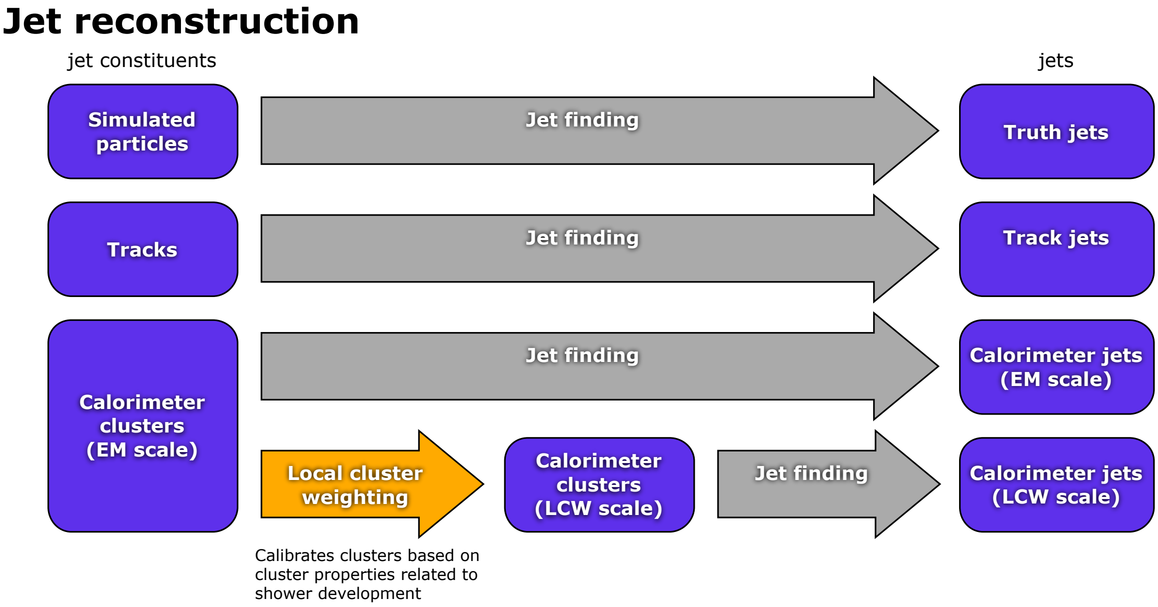

Figure 6.1.: ATLAS jet reconstruction scheme illustrating the different types of jets and calorimeter scales. Taken from [164]

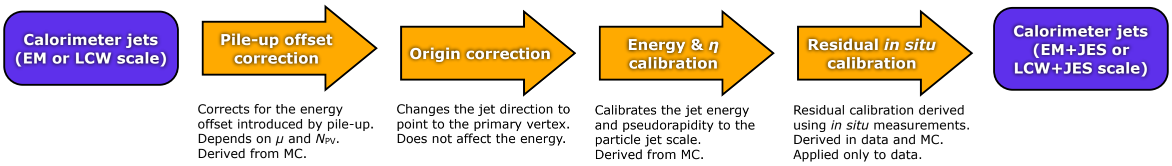

Figure 6.2.: ATLAS jet energy calibration scheme, taken from [164]

Two different variants of calorimeter jets are considered by ATLAS: Those which are formed directly from calorimeter topological clusters ("topo-cluster") calibrated for electromagnetic showers (EM scale) and those formed from topo-clusters after a local cell signal weighting (LCW scale). The LCW technique classifies clusters as either of hadronic or electromagnetic type, depending on the measured energy density and longitudinal shower profile. Energy corrections derived from simulation are applied according to the classification, but also to reduce the impact of detector effects like calorimeter non-compensation, noise, and non-instrumented regions in the vicinity of the topo-clusters.

The jet-energy response is much closer to one at the LCW scale in comparison to the EM scale and the jet-energy resolution is found to be improved by $\approx 10\%$ at low p_{T} and up to 30% at 300 GeV if using LCW scale calorimeter jets [174]. The ATLAS LCW scale calorimeter jets and CMS Particle-Flow jets are comparable with a value of the jet-energy resolution for both experiments of about 10% at 100 GeV.

Similarly to CMS, ATLAS has adopted a factorized approach to calibrate the calorimeter jets to the level of particle jets. The scheme is outlined in Figure 6.2 and consists of corrections for offset energy due to pileup, an origin correction, a MC truth p_{T}/η-calibration, and residual corrections from data-driven methods only applied to data.

The pileup correction employed by ATLAS is not based on the jet area approach adopted by CMS. It is derived from MC as a function of the pseudorapidity η, the number of reconstructed primary vertices N_{PV} correlated with in-time pileup, and μ, the average number of interactions per bunch crossing(averaged over many bunch crossings at the time of recording the data), correlated with out-of-time pileup. A linear expansion around the reference points $\mu^{\mathrm{ref}} = 5.4$ and $N_{PV}^{\mathrm{ref}} = 4.9$ is performed to obtain the expected pileup offset energy to be subtracted from the jets. A systematic shift in jet p_{T} is applied in case N_{PV} or μ differ from the chosen reference values for which the JES calibration is optimized. The systematic shift is estimated from the difference between the offset observed in data and simulation.

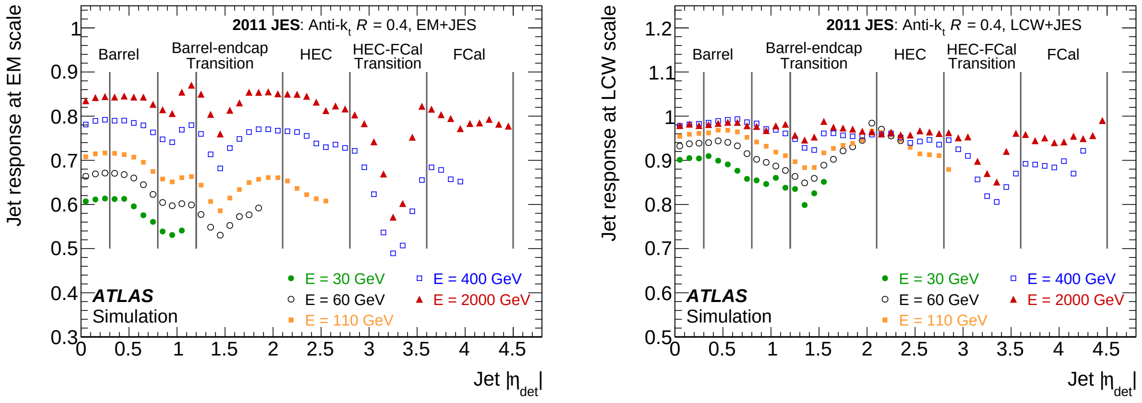

Figure 6.3.: Jet energy scale before application of p_{T} and η-dependent calibration for EM scale (left) and LCW scale jets (right), taken from [164].

An origin correction is applied that alters the jet direction to point to the primary vertex associated with the hard collision, but does not alter its energy. After the origin correction, a MC truth calibration is performed to correct the jet energy - on average - to that of the associated truth level jet. The size of the corrections that has to be applied to the jets is depicted in Figure 6.3. It is significantly reduced in the LCW calibration scheme in comparison to the EM scale.

This MC-derived calibration is applied to all jets, regardless of whether they are reconstructed from simulation or data. In order to validate the jet-energy scale in data, several topologies are exploited to derive small residual corrections only applicable to data. Jets in the central region are calibrated using Z+jet and γ+jet events up to $p_{\mathrm{T}} \approx 800\,\mathrm{GeV}$. The high p_{T}-region is probed using a multijet balance technique in which a system of low-p_{T} jets recoils against a high-p_{T} jet. A p_{T}-dependent combination of these calibration results is performed to derive a p_{T}-dependent residual correction in the central detector region, covering the p_{T}-range from as low as 20 GeV up to 1 TeV. Resulting correction factors range between 3% at very low p_{T} and 1% at 1 TeV.

The forward-jet calibration is done using dijet events, i.e. the same topology used by CMS and discussed in detail in Chapter 5. ATLAS considers two intercalibration techniques: Either the classical p_{T}-balance method termed "central reference method" or a matrix method. The matrix method is used to increase the number of events used for the intercalibration by not only considering central-forward jet pairs. Instead, the full number of events is considered by recording the asymmetry distributions for "left" and "right" jets with $\eta_{\mathrm{det}}^{\mathrm{left}} < \eta_{\mathrm{det}}^{\mathrm{right}}$ instead of central "reference" jets and forward "probe" jets. The asymmetry distribution is recorded in bins of $\eta_{\mathrm{det}}^{\mathrm{left}}$, bins of $\eta_{\mathrm{det}}^{\mathrm{right}}$, and bins of $\overline{p}_{\mathrm{T}}$. A minimization procedure is performed to obtain correction factors for a jet with a given η in a specific $\overline{p}_{\mathrm{T}}$-bin.

In comparison to the CMS analysis for 2011, the statistical precision for ATLAS is higher. One reason is the higher statistics of the matrix method, the second reason seems to be linked to a better tuning of the prescales of the jet triggers in ATLAS: While for CMS, the low $\overline{p}_{\mathrm{T}}$ events are scaled down much stronger than the high $\overline{p}_{\mathrm{T}}$ events due to the suboptimal prescale configuration as shown in Figure 5.10, the number of available events for the ATLAS analysis at low $\overline{p}_{\mathrm{T}}$ (and high $|\eta|$) is much higher. Significant advantages of the CMS analysis of dijet events are the complementary use of the MPF method and the extrapolation to zero additional event activity not pursued by the ATLAS analysis. The MC modeling uncertainty (a PYTHIA/HERWIG comparison) yields the largest systematic uncertainties for ATLAS. For CMS significant deviations are observed at the nominal working point with only partially suppressed additional event activity, but disappear after the extrapolation to zero additional event activity. At high $|\eta|$, the uncertainties related to the η intercalibration dominate the systematic uncertainties of both, CMS and ATLAS.

A summary of the resulting jet-energy scale uncertainties is given in Figure 6.4 for ATLAS LCW scale jets and CMS PF jets. In comparison to the corresponding CMS uncertainties, the impact of pileup on the uncertainties is slightly reduced (despite the long charge collection times in the ATLAS calorimeters) while the overall uncertainties are of comparable size, only slightly larger at $\approx 100 - 500\,\mathrm{GeV}$ in the central detector region

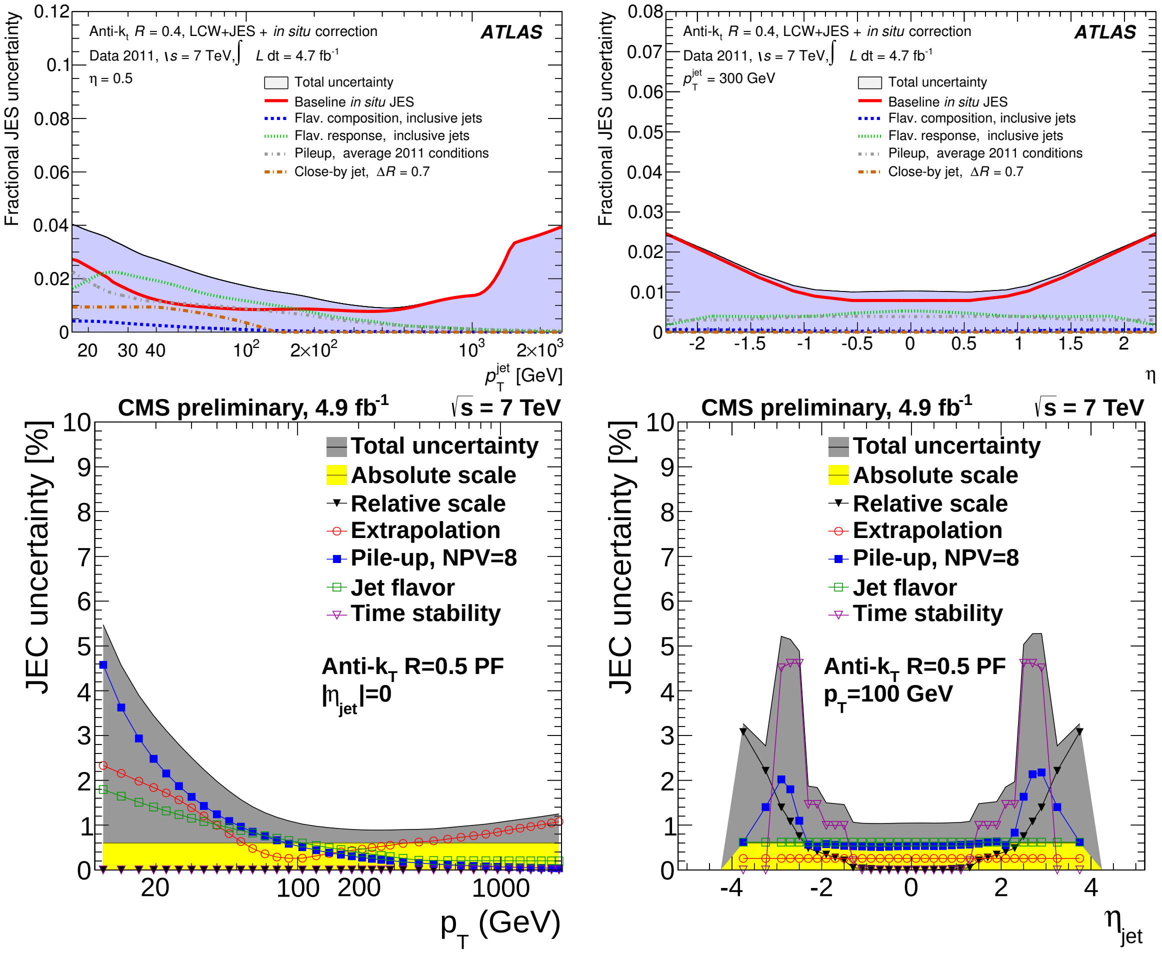

Figure 6.4.: Top: Summary of jet-energy scale uncertainties considered by ATLAS for 2011 analyses with a flavor composition corresponding of that in the inclusive jets analysis, taken from [164]. Bottom: Summary of jet-energy scale uncertainties considered by CMS for the 2011 data-taking period.

due to the ATLAS flavor and in situ JES uncertainties. In the CMS endcap regions, the uncertainties related to pileup effects and the time stability of the response significantly increase the total systematic uncertainty. The extensive studies by both collaborations have already lead to remarkably low systematic uncertainties, only a short time after the LHC commenced operations. In comparison, the systematic uncertainties on the JES at D0 have recently been found to be about 1-2% for central jets with transverse momenta of about 100 GeV [152]. This means that the total systematic uncertainties in the central detector regions of ATLAS and CMS are already of comparable size or superior to those achieved at the Tevatron experiments.

6.2. Correlation of JES uncertainties betwen ATLAS and CMS

The dedicated effort performed to gain an understanding of the jet-energy scale uncertainty correlations among the two experiments lead to the definition of five correlation groups:

1. **Uncorrelated uncertainties:** Statistical and detector-based components of the jet-energy scale uncertainties are considered as uncorrelated due to the physically different detectors and statistically independent MC and data samples. As there is no direct equivalent at CMS, the close-by jet uncertainty of ATLAS is considered as uncorrelated (compare Section 5.5.7 for cross-checks of the effect using dijet events). Uncertainties due to pileup activity are also considered as uncorrelated, because different techniques are used by both experiments. Even though both experiments rely on MC-extrapolations to very high/low p_{T}, the derivation of uncertainties is different and no correlation is assumed.
    - **Correlation range:** 0%
    - **CMS uncertainties considered:** [1] *PileUpDataMC, PileUpBias, PileUpOOT, PileUpJetRate, PileUpPtBB, PileUpPtEC, PileUpPtHF, RelativeStatEC2, RelativeStatHF, RelativeJEREC1, RelativeJEREC2, RelativeJERHF, AbsoluteStat, AbsoluteScale, HighPtExtra, SinglePion, Time*
2. **Modelling uncertainties in the in-situ techniques:** Both experiments rely on the MPF method to derive corrections from Z+jet and γ+jet events and consider similar systematic uncertainties in the individual analyses. However, the different treatment in the combination of individual channels as well as differences in the actual derivations (e.g. an extrapolation in $\Delta\phi$ in the case of ATLAS) are expected to mostly decorrelate the uncertainties.
    - **Correlation range:** 0% - 50%
    - **CMS uncertainties considered:** *AbsoluteMPFBias*
3. **Model dependence of the relative intercalibration:** Both experiments observe differences in the relative calibration due to radiation modeling when comparing to either PYTHIA or HERWIG++ as reference MC and assign systematic uncertainties. This is reflected in the uncertainty related to the difference at the nominal working point with partially suppressed additional event activity for ATLAS and in the uncertainty related to the extrapolation to zero additional event activity for CMS (compare Section 5.4.1 for more details on the extrapolation).
    - **Correlation range:** 50% - 100%
    - **CMS uncertainties considered:** *RelativeFSR*

---

[1] The following abbreviations have been explained in Section 4.5.4.

4. **Flavor uncertainties:** Both experiments use comparisons of the jet response in PYTHIA and HERWIG++ to derive flavor-related jet-energy scale uncertainties. As a consequence, a correlation of the uncertainties is expected.
   - **Correlation range:** 0% - 100%
   - **CMS uncertainties considered:** *Flavor, AbsoluteFlavorMapping*
5. **b-JES uncertainties:** While ATLAS provides an explicit b-JES uncertainty that considers a PYTHIA and HERWIG++ response comparison and e.g. a systematic variation of the fragmentation, replacing the nominal flavor uncertainty, b-JES related uncertainties at CMS are expected to be covered by the inclusive flavor uncertainty. For analyses in which a jet-energy scale factor is determined simultaneously, CMS recommends to scale the response of b-jets additionally by the flavor uncertainty to cover any residual differences between the jet-energy scale of light quark or b-jets.
   - **Correlation range:** 50% - 100%
   - **CMS uncertainties considered:** *Flavor* (as additional uncertainty separately applied to b-jets)

This effort to understand the correlations of jet-energy scale uncertainties in both experiments has been used for combinations of precision measurements, e.g. the LHC combination of top-quark mass measurements [69]. As an outcome of the discussions, several possibilities for a more coherent treatment of systematic uncertainties in both experiments were proposed. This includes e.g. the extrapolation to zero additional event activity in the ATLAS dijet analysis and a combination of the direct measurements of the absolute scale for the p_T-dependent residual correction in the case of CMS. It will be useful to repeat the exercise in future iterations in order to scrutinize the techniques used by both experiments and foster improvements.

Chapter 7

B-jet energy regression

Jets induced by high p_{T} b-quark production (b-jets) play an important role in a wide variety of interesting processes, among them are the $H \rightarrow b\bar{b}$ decay channel and top-quarks, which almost always decay into b-quarks due to $V_{tb} \approx 1$ in the CKM-matrix or the . In the top-quark mass measurements pursued at the Tevatron and LHC [70] and more specifically the top-quark mass measurements performed at 7 TeV by the University of Hamburg CMS group [6, 175], the uncertainty on the b-jet energy scale has been found to be one of the dominant systematic uncertainties.

For the ongoing measurements using the dataset collected during the 2012 run, two refinements regarding flavor response uncertainties have been pursued: In Section 4.5.5, the determination of the flavor uncertainties of individual flavors and flavor mixtures based on a PYTHIA/HERWIG++ comparison in QCD events is discussed. In this chapter, b-jets and uncertainties on the b-jet response are examined in detail directly in $\mathrm{t\bar{t}}$-events with lepton+jets final states.

This includes a study of the description of b-jet properties and the derivation of a dedicated b-jet energy regression (BJER) in order to optimally exploit the knowledge of a number of b-jet properties to improve the jet-energy scale of b-jets. In the standard CMS jet energy corrections, the reference scale is that of generator jets without neutrinos as discussed in Section 4.5.2. For b-jets, this is not optimal because of the different internal properties of b-jets and because a significant fraction of the produced B-hadrons decays semileptonically. In these decays, the part of the energy taken by the neutrino is invisible to the detector. This results in missing energy and a low jet-energy response tail of reconstructed b-jets.

Building up on the standard jet energy calibration which corrects the jet energy as a function of p_{T}, η, the jet area A, and the median event energy density ρ, an additional jet-energy correction specifically tailored for b-jets is developed. For this b-jet energy regression (BJER), the correlation of jet properties with the b-jet response is exploited.

A number of analyses have adopted such a BJER after the successful usage of such an approach in $H \rightarrow b\bar{b}$ searches at CDF [176]. For example, the CDF top-quark mass measurement [177] uses such a regression correction. CMS has developed a similar regression for the search in the channel of $H \to b\bar{b}$ in association with a W or a Z boson [178] and similar studies are ongoing in the ATLAS collaboration [179].

In the following, the systematic uncertainty on the b-jet energy scale is estimated by evaluating the differences of the b-jet response comparing PYTHIA and Herwig directly in $\mathrm{t\bar{t}}$-events, varying the semileptonic branching fraction of B-hadrons and the b-fragmentation function. It is studied how the systematic uncertainty on the b-jet response changes when the BJER, which is supposed to improve the reconstruction of b-jets, is applied.

A number of b-jet specifics which distinguish them e.g. from light quark or gluon jets are discussed in Section 7.1. The description of b-jet properties in lepton+jets $\mathrm{t\bar{t}}$-events is discussed in Section 7.2. The regression technique which exploits the correlation of b-jet properties with the jet-energy response to improve the b-jet reconstruction as well as the derivation and performance of the BJER are discussed in Section 7.3. Systematic uncertainties related to the b-jet response are evaluated and compared with and without applying the BJER in Section 7.4. Biases that could be introduced by applying the BJER are discussed in Section 7.5 and possible improvements are outlined in Section 7.6.

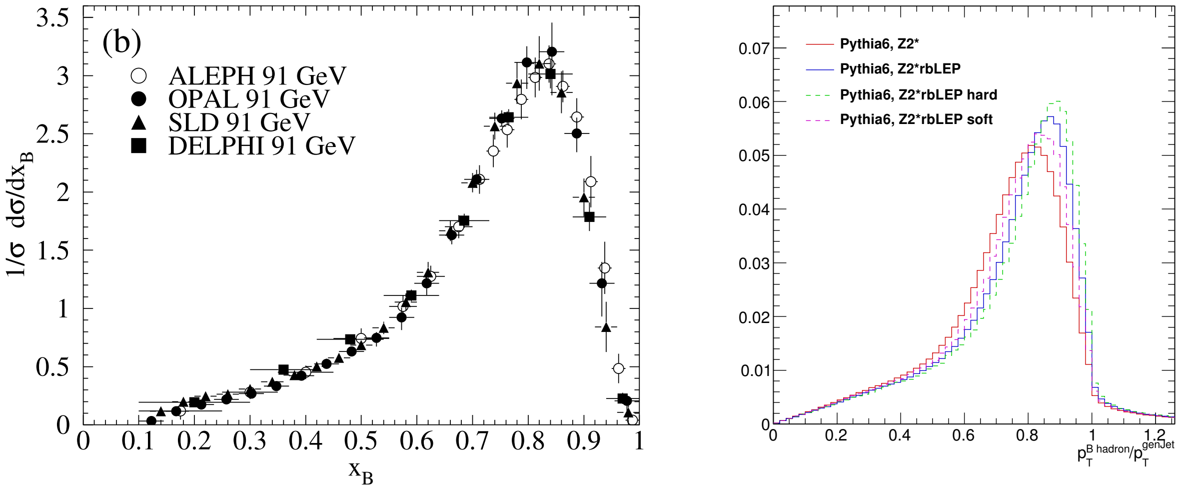

(a) **(b)**

Figure 7.1.: (a): Fraction of energy x_B taken by B-hadrons in the fragmentation process. Taken from [40]; (b): Fraction of energy taken by B-hadrons relative to the p_T^{gen}in $t\bar{t}$ events using the default PYTHIA tune or a custom tuning to ALEPH and DELPHI data (and hard/soft variations of the tuning) as described in [185].

7.1. Specifics of jets initiated by bottom quarks

Bottom quarks are the heaviest quarks in the Standard Model which form hadrons as bound states. In most cases excited B-hadrons are produced which decay immediately into ground state B-hadrons via the electromagnetic or strong interaction. A combination of available measurements summarized in Table 7.1 yields a fraction of ≈ 91% of ground-state B-mesons and ≈ 9% B-baryons produced out of the fragmentation of a b-quark. These ground-state B-hadrons have typically a high mass of the order of 5 GeV and undergo weak decays, leading to a relatively long average lifetime of 1.566 ± 0.009 ps [180].

The fragmentation of b-quarks into B-hadrons has been studied in detail at e^- e^+ machines [181–184]. The B-hadron resulting from the fragmentation process carries - on average - a very high energy fraction of the initial quark as depicted in Figure 7.1.(a). In the top-quark mass analysis that this study of a b-jet energy regression is supposed to supplement, the CMS default PYTHIA Tune Z2* has been compared to the x_B measurements in Figure 7.1.(a). It has been observed that the fragmentation in the CMS default tune is softer than the measurements indicate. A retuning has been done as described in [185], resulting in a modified tune, Z2*rbLEP as depicted in Figure 7.1.(b). The harder fragmentation of this tune can be achieved by reweighting the standard $t\bar{t}$ MC samples. In order to evaluate systematic uncertainties of the b-jet response in Section 7.4, the full difference between the standard MC sample and the reweighting is considered.

Semileptonic B-Decays: Due to their direct impact on the measurable response, the

Table 7.1.: Fractions of weakly decaying B-hadron species in $Z \to b\bar{b}$ (LEP), in $\bar{p}p$ collisions at $\sqrt{s} = 1.8\,\text{TeV}$ (Tevatron), and pp-collisions (LHCb), adapted from [180]

B-hadron	**Combined fraction from $e^+e^-, \bar{p}p, pp$**
$B^+ or B^0$	$40.1 \pm 0.7\%$
B_s	$10.7 \pm 0.5\%$
B-baryons	$9.1 \pm 1.5\%$

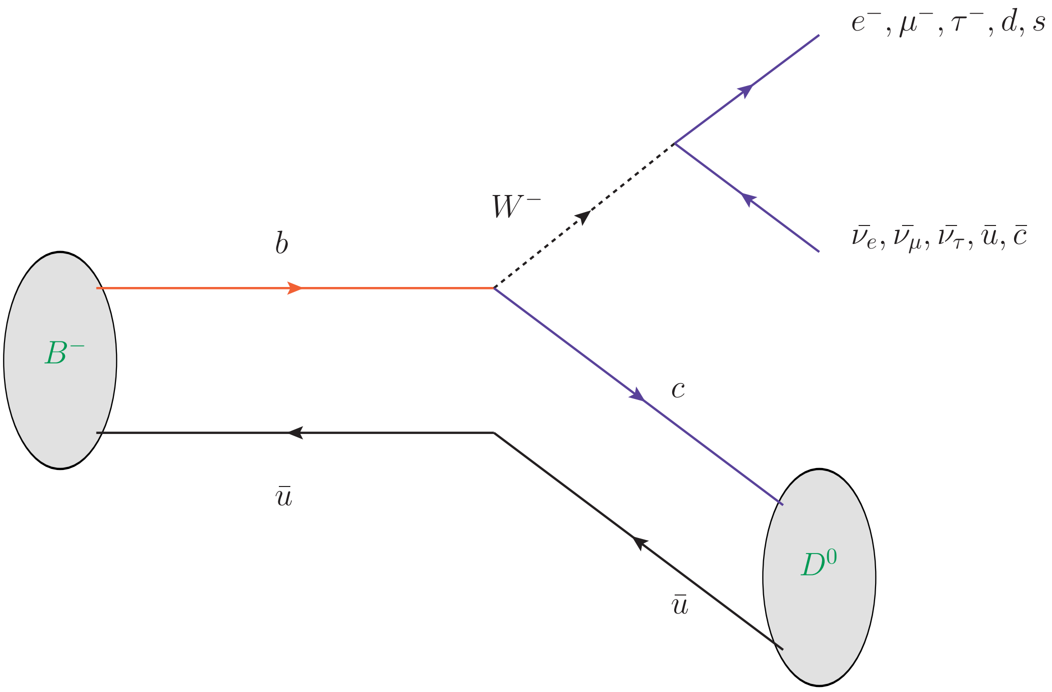

Figure 7.2.: Sketch of the (spectator model) decay of $B^- \to D^0 + (W \to X)$. Leptonic decays of the W boson result in neutrino production, thus lowering the energy visible to the detector.

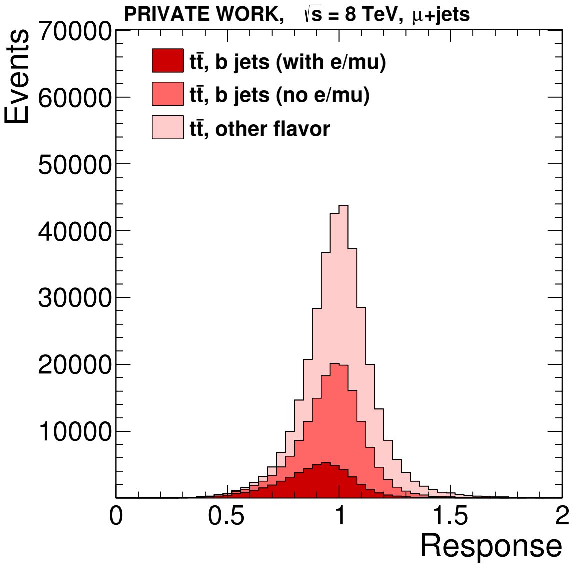

Figure 7.3.: Simulated response distribution of all jets with $p_{\mathrm{T}} > 30$ GeV after the top event selection in the muon+jets channel, split up into b-jets with electrons/muons in the jet, other b-jets, other flavor.

semileptonic decays of B-hadrons are of particular relevance to the development of a b-jet energy regression. As an example, the decay of a B^- meson is depicted in Figure 7.2. In case the W boson decays leptonically, energy is "lost" to neutrinos as they will leave the detector without a signal. With decay fractions of

$$\Gamma\left(B^{\pm} \to l^{\pm}\nu_l + \mathrm{X}\right)/\Gamma \approx 10.99 \pm 0.28\% \tag{7.1}$$

$$\Gamma\left(B^{0} \to l^{\pm}\nu_l + \mathrm{X}\right)/\Gamma \approx 10.33 \pm 0.28\% \tag{7.2}$$

where l can be an electron, muon or tau [40], the $\approx 30\%$ fraction of semileptonic decays contributes significantly to the low response tail specific to b-jets. This is illustrated in Figure 7.3, which shows the response distribution of all jets with $p_{\mathrm{T}} > 30$ GeV after the top event selection in the muon+jets channel. The low response tail is dominated by b-jets containing electrons or muons, hinting at semileptonic B-hadron decays.

7.2. Description of b-jet properties in data

Before discussing the b-jet energy regression, i.e. the correction of observed correlations between the jet-energy response and b-jet properties in order to improve the b-jet reconstruction, the description of various b-jet properties in data by simulation is examined.

This is done adopting the same selection as used for the measurement of the top-quark mass, described in detail in [7]. Events are selected containing exactly one isolated muon, with $p_{\mathrm{T}} > 33\,\mathrm{GeV}$ and $|\eta| < 2.1$, and at least four jets with $p_{\mathrm{T}}^{L1L2L3} > 30\,\mathrm{GeV}$ and $|\eta| < 2.4$. Two of the four leading jets are required to pass a cut on the combined secondary vertex (CSV) b-tagging discriminator at the medium working point. Only events which pass a cut on the kinematic fit probability (compare Section 8.1 for a description of the kinematic fit) of $P_{gof} > 0.2$ are considered.

Owing to the Particle Flow reconstruction, jet properties can be studied in great detail: These include the energy fractions of the different PF constituent types, jet shape observables computed from the PF candidates, but also b-tagging related and basic kinematic quantities. These need to be described adequately by the MC simulation if a MC-trained b-jet energy regression utilizing exactly these quantities is foreseen to be applied to data.

For the distributions discussed in the following, the MC samples are scaled to match the integrated luminosity in data. The hatched uncertainty bands take into account $\mathrm{t\bar{t}}$ modeling uncertainties (variations of the ME-PS matching scale, the $\mathcal{Q}^2$ scale, $p_{\mathrm{T}}^{\mathrm{top}}$ reweighting, a hadronization uncertainty (comparing to POWHEG +HERWIG)), experimental uncertainties (JES and JER uncertainties), and uncertainties on the background normalization.

7.2.1. Basic kinematic and pileup-correction related quantities

Basic kinematic quantities as well as quantities related to the pileup jet energy corrections should be described well by the simulation. In Figure 7.4, the distributions of these quantities are shown after the event selection outlined above.

"Raw p_{T}" refers to the jet p_{T} before applying the jet-energy corrections, "corr. p_{T}" to the jet p_{T} after applying L1L2L3 (+L2L3Res for data) corrections. m_{T} is defined as $\sqrt{(|E^2 - p_z^2|)}$ after application of jet-energy corrections. η is the pseudorapidity of the PF-jet 4-vector. The jet area A and median energy density ρ are essential ingredients for the L1-correction explained in Section 4.5.1, ρ_{25} used here is obtained by limiting the determination of ρ to the well-understood tracker-covered detector region up to $|\eta| < 2.5$. In the majority of selected events, the b-jets are in the central detector region ($|\eta| < 1.3$) and have a p_{T} in the range of 30-100 GeV.

While the η and jet area distributions are perfectly matched by the MC, the description of the other observables is not quite as good: The corrected jet p_{T} and m_{T} distributions show a deficit of data events in the region of $150\,\mathrm{GeV} < p_{\mathrm{T}} < 250\,\mathrm{GeV}$. A slope in jet p_{T} observables has been observed in many top analyses and the Data/MC agreement is known to be improved by a top p_{T} reweighting derived from differential $\mathrm{t\bar{t}}$ cross section measurements [186, 187]. However, due to the unclear origin of the observed difference, this p_{T} reweighting is not applied here.

The slope in raw p_{T} is expected as the jet-energy corrections, which are applied before the p_{T}-cuts, differ in MC and simulation at the pileup-correction level (L1) and in the L2L3Residual-correction step. The difference in ρ_{25} is taken into account by the different L1-jet-energy corrections for MC and data.

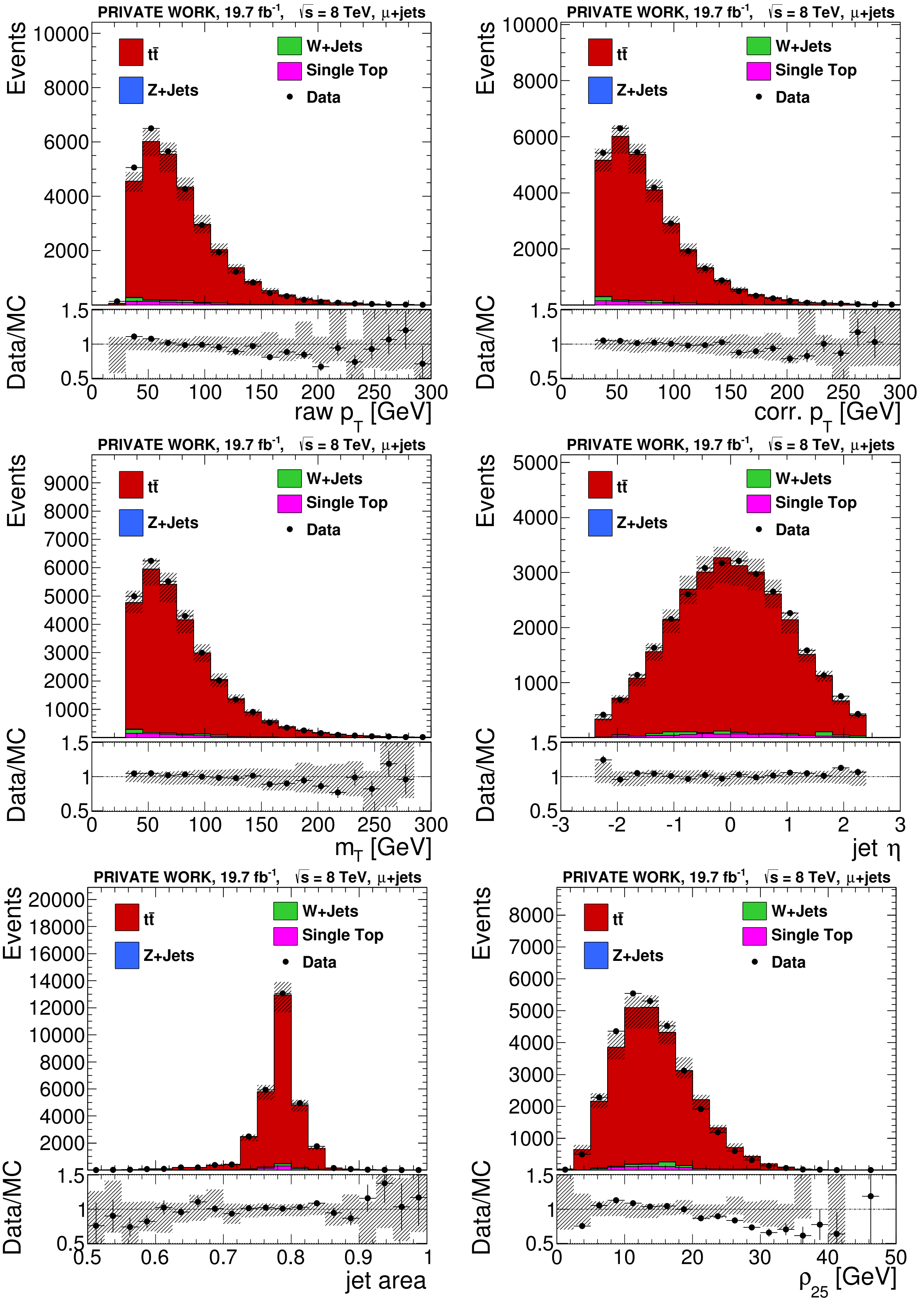

Figure 7.4.: Distribution of basic kinematic and pileup-correction related quantities of b-jets after the selection used in the top-quark mass analysis. The hatched uncertainty bands take into account $t\bar{t}$ modeling uncertainties (variations of the ME-PS matching scale, the $\mathcal{Q}^2$ scale, p_T^{top} reweighting, a hadronization uncertainty (comparing to POWHEG +HERWIG)), experimental uncertainties (JES and JER uncertainties), and uncertainties on the background normalization.

7.2.2. Particle Flow energy fractions and particle multiplicities

As discussed in Section 4.3, PF-jets are clustered from individual electron, muon, charged/neutral hadron, and photon candidates. The distributions of the associated energy fractions for electrons, muons, charged hadrons (CHF), the charged hadron and overall candidate multiplicity are shown in Figure 7.5. In addition, the jet width in φ calculated from the PF candidates is shown:

$$\sigma_{\varphi\varphi} = \sqrt{\frac{\sum p^i_{T,\text{PF cand.}} \cdot (\varphi_i - \varphi_{\text{PF jet}})^2}{\sum p^i_{T,\text{PF cand.}}}}, \text{ where } \varphi_{\text{PF jet}} = \frac{\sum p^i_{T,\text{PF cand.}} \cdot \varphi^i}{\sum p^i_{T,\text{PF cand.}}} \tag{7.3}$$

This observable was studied for calorimeter jets in [32] and showed a strong correlation with the jet-energy response. In this $\mathrm{t\bar{t}}$ event selection, $\sigma_{\varphi\varphi}$ is described by the simulation within uncertainties.

Due to semileptonically decaying B-hadrons, which themselves often carry a high fraction of the jet energy due to the hard b-fragmentation, there is an extra source of relatively high energetic non-isolated leptons specific to b-jets. In about 30% of the b-jets in the $\mathrm{t\bar{t}}$ sample, the PF algorithm reconstructs electrons or muons in the jet. For light quark jets, this occurs in only 8% of such jets. In jets containing reconstructed electrons or muons, an average of 20% of the reconstructed jet energy is carried by the leptons. This is reflected in both, the simulation and collision data.

For most jets, charged hadrons constitute the largest energy fraction (on average $\approx 2/3$). Slightly more events are observed in the data than in MC for very high and very low values of the charged hadron fraction. The overall PF candidate multiplicity increases - on average - from about 20 at $p_{\mathrm{T}} \approx 30$ GeV to about 40 at 200 GeV for b-jets. For light quark jets, the average multiplicity is $\approx 15\%$ lower indicating a harder constituent energy spectrum. The charged hadron and overall PF candidate multiplicity description exhibits a slight slope but is described within $\pm 20\%$ in the bulk of the distribution.

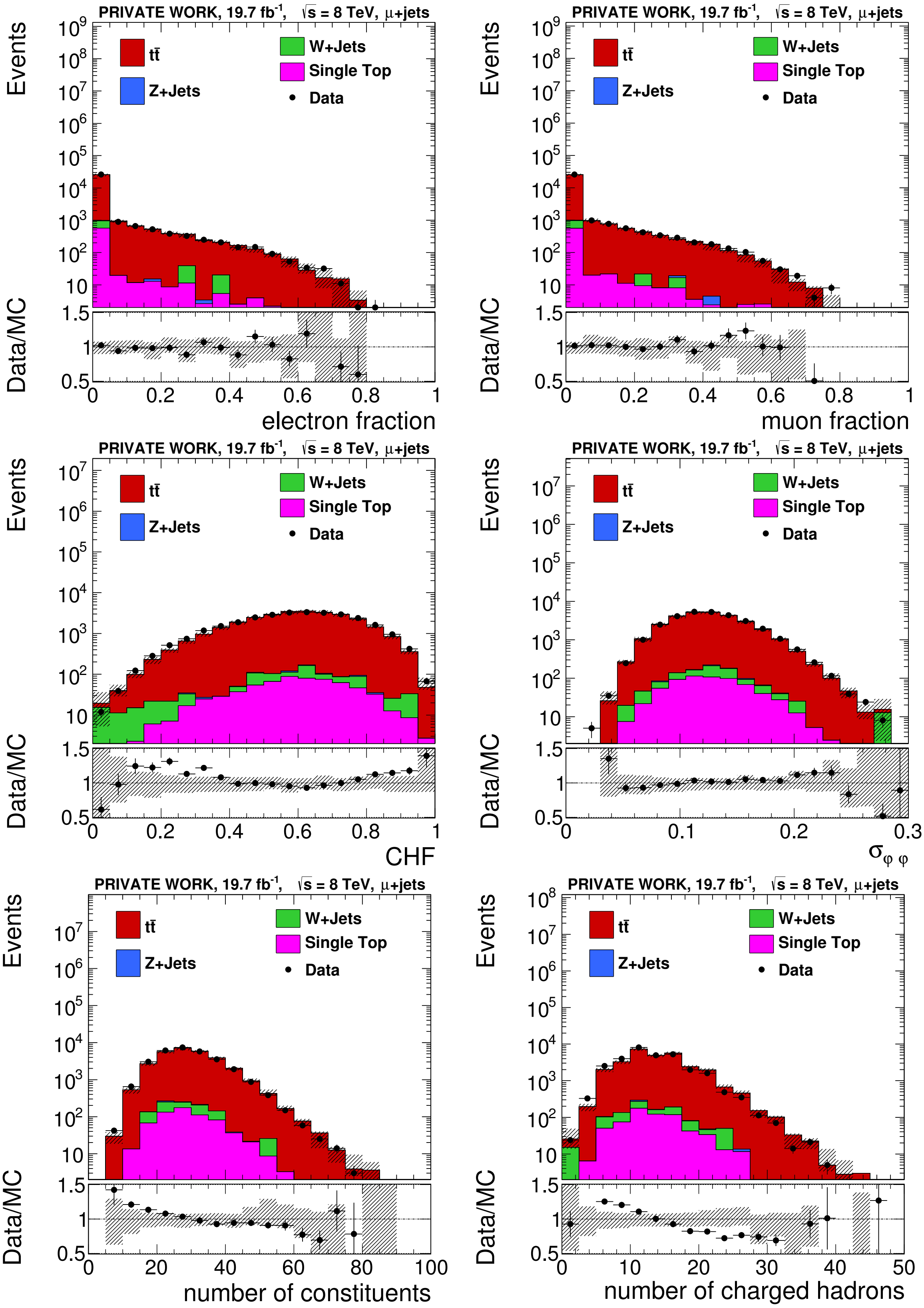

Figure 7.5.: Distributions of muon, electron, and charged hadron energy fractions, the jet width in φ, the multiplicity of PF constituents, and the charged hadron multiplicity for b-jets after the selection used in the top-quark mass analysis.

7.2.3. B-tag discriminator and secondary vertex information

In order to distinguish b-jets from jets initiated by other partons, extensive studies on b-tagging have been performed in CMS as described in Section 4.4.4 and [125, 126]. Crucial observables for this identification are secondary vertex (SV) and track-based observables exploiting the long lifetime of B-hadrons. The combined secondary vertex (CSV) discriminator, largely based on SV criteria, is the most-widely used b-tagging algorithm.

In Figure 7.6, the distributions of the SV flight length (+uncertainty), the SV mass, SV p_{T} (relative fraction), and the CSV value are depicted. The SV flight length and its uncertainty are described within the given uncertainties. The CSV value is modeled with a comparable accuracy as in [125] while the slopes observed for the SV p_{T} and mass appear slightly enhanced in comparison to the validation plots in [125]. The fraction of the SV p_{T} relative to the jet p_{T} is well modeled by the simulation.

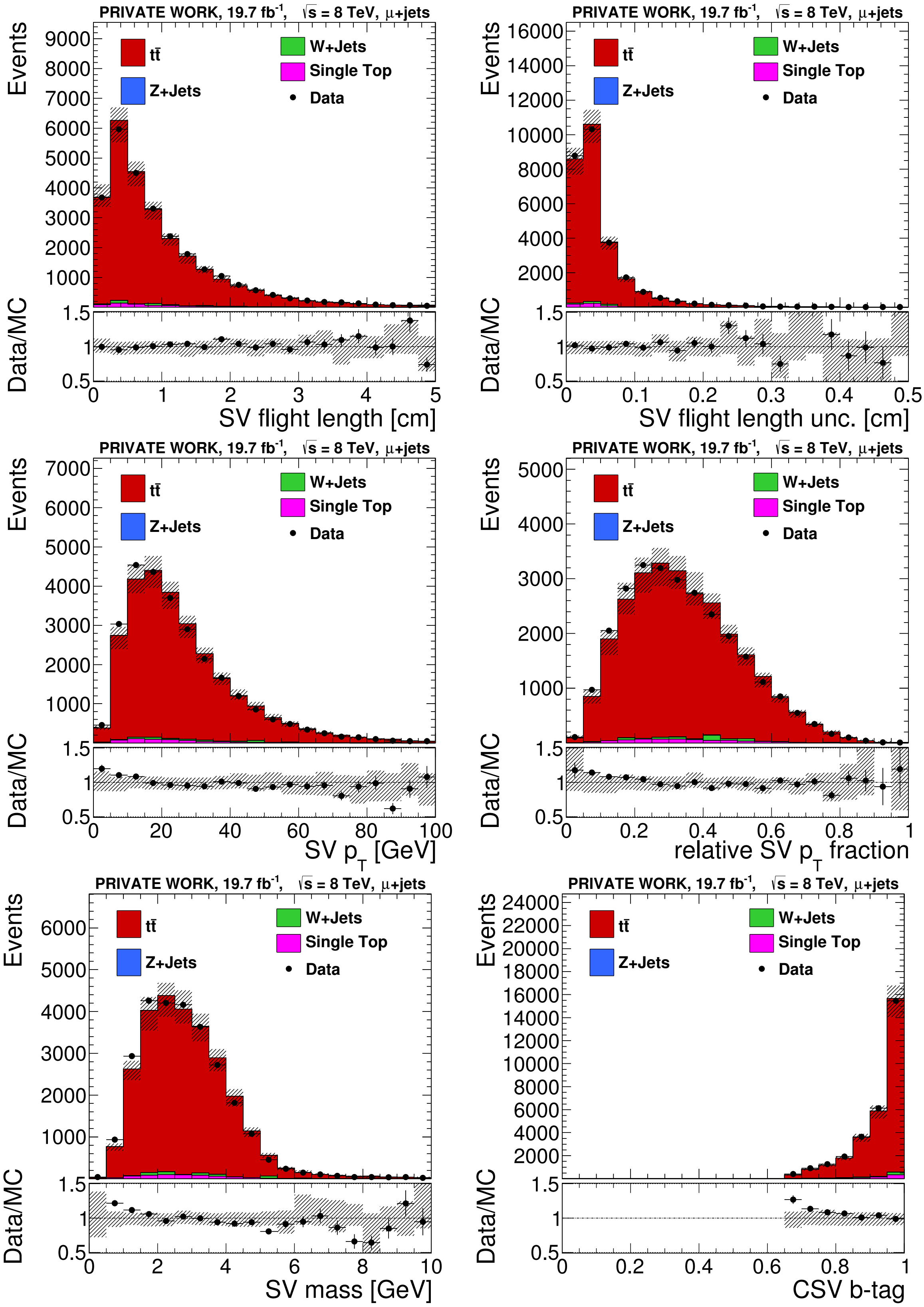

Figure 7.6.: Distributions of the secondary vertex (SV) flight length, its uncertainty, the SV p_T, the fraction of the SV p_T relative to the jet p_T, the SV mass, and the b-tag discriminator value (combined secondary vertex), evaluated for b-jets after the selection used in the top-quark mass analysis.

7.2.4. Soft lepton information

As discussed in Section 7.2.2, about 30% of the b-jets are characterized by at least one reconstructed PF muon or electron in the jet cone. In order to perform b-tagging efficiency studies, such soft leptons are required in the jets to enrich the heavy flavor content.

The semileptonic decays producing leptons and neutrinos are the major cause of the low jet-energy response tails of b-jets and are therefore of particular interest for the study of a b-jet energy regression. In Figure 7.7, observables used for the b-tagging studies are shown. The p_{T} of the leading soft electron/muon reconstructed within $\Delta R < 0.4$ of the jet axis, the p_{T} fraction relative to the jet p_{T}, and the distance in ΔR relative to the jet axis are described by the simulation within the uncertainties.

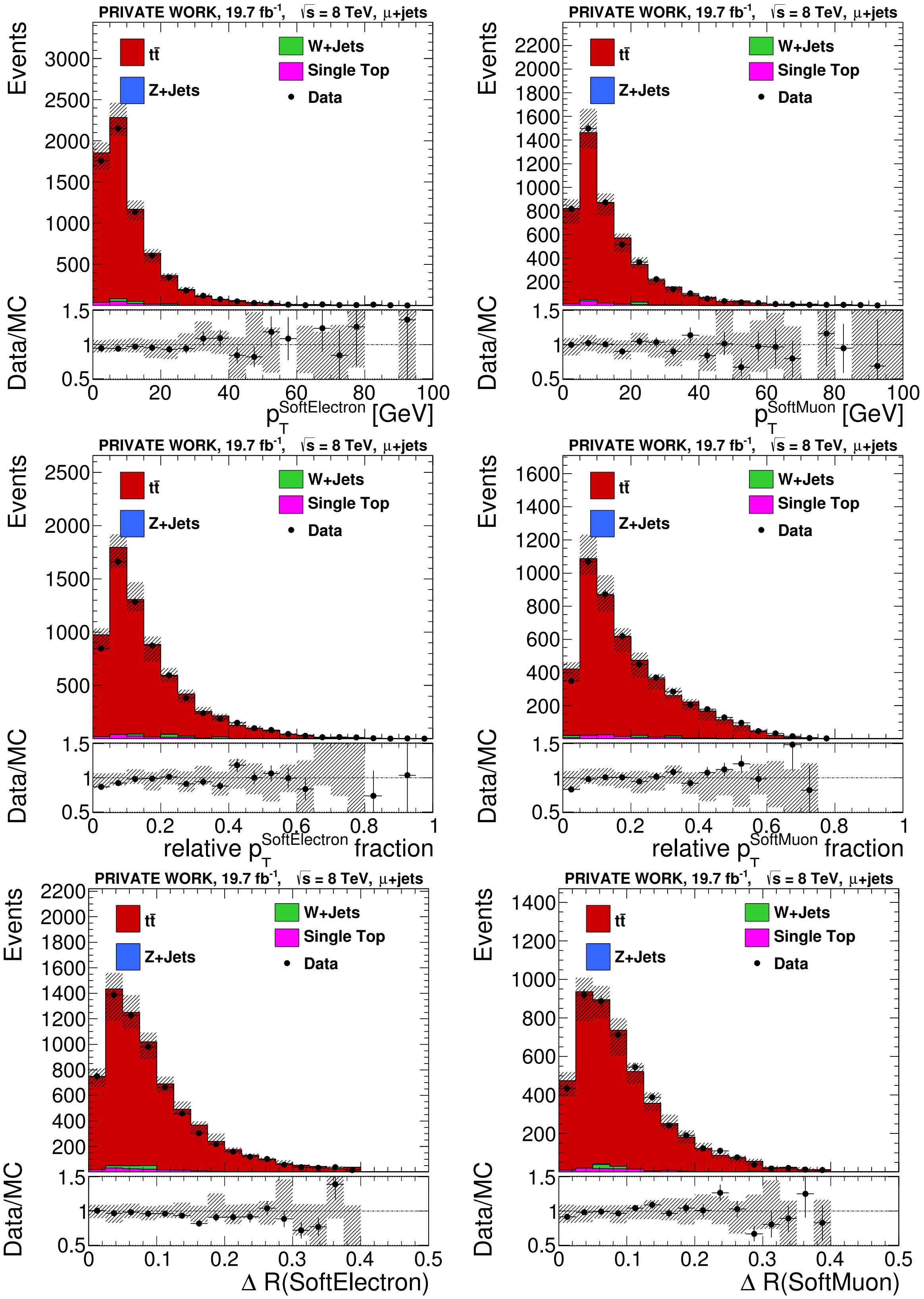

Figure 7.7.: Distribution of soft lepton observables originally used in the context of b-tagging, evaluated for b-jets after the selection used in the top-quark mass analysis. ΔR is the distance of the soft lepton with respect to the jet axis, $p_T^{\text{soft lepton}}$ the p_{T} of the leading soft lepton, and the relative $p_T^{\text{soft lepton}}$ fraction is normalized to the jet p_{T}.

7.2.5. Other observables

A large number of observables has been considered in the context of a pileup jet identification scheme, briefly described in Section 4.4.6. For example, a number of jet shape observables are defined by the energy fraction taken by PF candidates in annuli of a width of 0.1 in ΔR:

$$A < (\Delta R) < A + 0.1 = \frac{1}{p_T^{jet}} \sum_{i \in A < (\Delta R) < A+0.1} p_{Ti} \tag{7.4}$$

where A can take values of 0.0, 0.1, 0.2, 0.3, and 0.4 for the standard jets usd by, clustered with a radius parameter of $R = 0.5$. These observables help to identify whether energy is largely deposited in the central region of the jet or in peripheral regions. Diffuse energy deposits are typical for pileup jets.

In order to distinguish quarks and gluons on a jet-by-jet basis complementary to b-tagging, studies on a quark-gluon discriminator have been carried out in CMS, briefly described in Section 4.4.5. A number of jet-shape observables were introduced in this context to gain discrimination power. Among them are width observables similar to the one defined in equation (7.3), PF candidate multiplicities, and $p_T D$ which aims at quantifying the hardness of the fragmentation and is defined as

$$p_T D = \frac{\sqrt{\sum_i p_{T,i}^2}}{\sum_i p_{T,i}} \tag{7.5}$$

where the sum runs over the constituents (PF candidates) of the jet.

In the 3-dimensional template fit of the top-quark mass lepton+jets $\mathrm{t}\bar{\mathrm{t}}$ events by ATLAS [188], the observable

$$R_{lb}^{\mathrm{reco,2b}} = \frac{p_T^{b_{had}} + p_T^{b_{lep}}}{p_T^{W_{jet1}} + p_T^{W_{jet2}}} \tag{7.6}$$

is introduced as the ratio of the scalar sum of the two b-jet p_{T} relative to the p_{T} sum of the two jets from the hadronic W-decay. In [188], this observable is used to simultaneously fit a b-jet energy scale factor.

The distributions of these observables are depicted in Figure 7.8. No significant deviations are observed for the annulus energy fraction observables. They show the expected behavior that the energy is concentrated close to the jet axis for most jets. The distribution of $p_T D$ is slightly shifted to higher values in data. The $R_{lb}^{\mathrm{reco,2b}}$ observable is described by the simulation within uncertainties and has a similar shape to the results shown in [188].

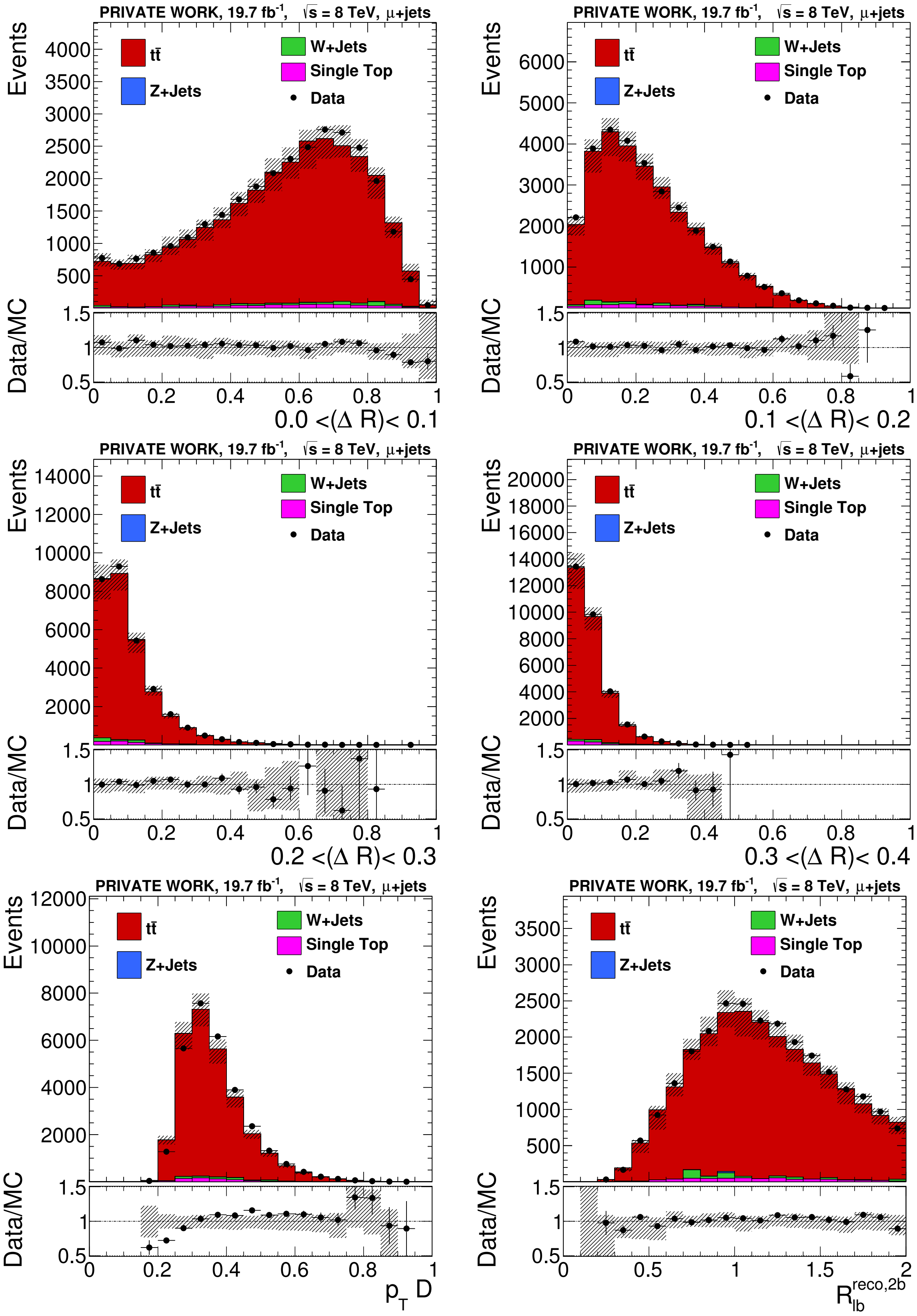

Figure 7.8.: Distribution of the energy fraction taken by PF candidates in annuli of a thickness of 0.1 in ΔR, the fragmentation sensitive observable $p_T D$, and $R_{lb}^{\text{reco,2b}}$ for b-jets after the selection used in the top-quark mass analysis.. The definitions of these observables are given in Section 7.2.5

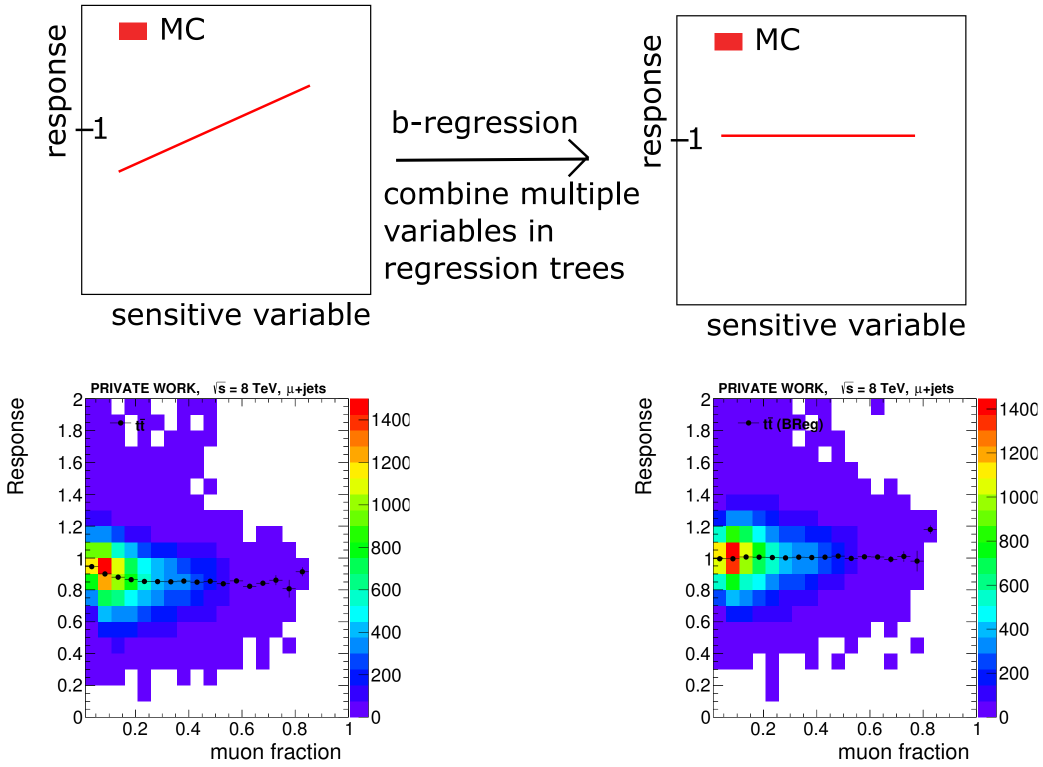

Figure 7.9.: Top: Basic idea of the b-jet energy regression: Find (many) jet properties sensitive to the jet-energy response and correct for the observed correlation using a multivariate regression technique like boosted regression trees. Adapted from [189]; Bottom: Correlation of jet-energy response and muon fraction before (left) and after (right) applying the actual regression correction discussed in Section 7.3.3.

7.3. Derivation and discussion of the b-jet energy regression

As most of the b-jet properties are reasonably well described by the standard simulation, it appears feasible to examine an additional jet-energy correction for b-jets. This approach was pursued previously in [176, 178].

The basic idea is illustrated in Figure 7.9: Whenever a b-jet property is correlated with the jet-energy response, correcting for the observed correlation will lead to an overall improved jet-energy response distribution, i.e. an improved jet-energy resolution.

In order to include a multitude of properties in this correction, gradient boosted regression trees [191] have been chosen. They are considered as robust to the addition of only mildly discriminating variables, yet exhibit a good regression performance.

Single classification and regression trees on which the boosted variants build as basic elements are discussed in detail in [192]. Classification trees are used to distinguish

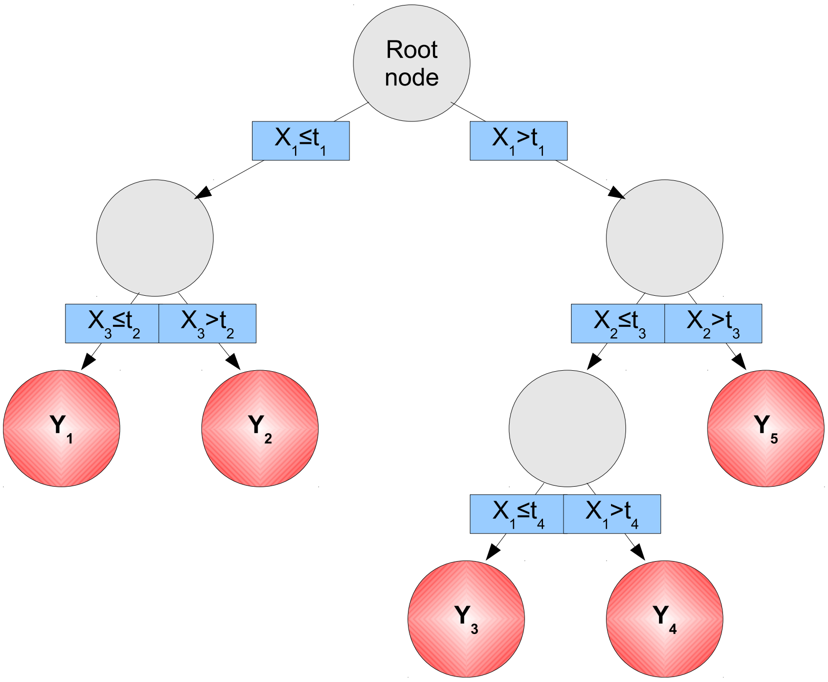

Figure 7.10.: Sketch of a single regression tree, modelling an output variable Y depending on a set of input variables X_i and cut thresholds t_i splitting up the phasespace. Based on the classification tree schematic in [190].

different categories of input data. In high energy physics they are often used to distinguish signal from background events.

Instead of separating signal and background, regression trees model numerical values. Such a single regression tree is depicted in Figure 7.10: The target variable Y is modeled as a single number for a small part of the phase space after a number of binary splits of the sample. These splits separate the sample into a part with values of the input variable X_i smaller or larger than the cut threshold t_i. When a certain cutoff-criterion is fulfilled, no more splittings are tried and a single number Y_i is assigned as terminal node minimizing the deviation of Y_i from the true value Y_{true} in this phasespace region.

As single regression trees are known to be sensitive to statistical fluctuations, the extension of this basic idea to "boosting" [191] is pursued for most practical purposes. Instead of a single tree (weak learner), a large number of trees is trained that specialize on those events that the previous trees could not model well, i.e. where the deviation of the regression output Y from the true value Y_{true} is large. These events are weighted up such that the next training will result in different splits and consequently a different tree than the previous one.

The implementation adopted in this analysis has been used within CMS to determine corrections for photons and electrons with a high number of input parameters [193, 194]. In comparison to the standard TMVA-implementation [190], it has been optimized to be more robust against outliers and multi-thread compatible, resulting in a greatly reduced training time (about a factor of 20, [193]). In this implementation a configurable tree-growth cutoff mechanism is used to minimize overtraining. For this cutoff, the significance of a split is given by the difference in mean target values on both sides of the split (left: $\bar{Y}_L$; right: $\bar{Y}_R$) divided by the statistical uncertainty on the difference defined as

$$S = \frac{\bar{Y}_R - \bar{Y}_L}{\delta\left(\bar{Y}_R - \bar{Y}_L\right)} \tag{7.7}$$

For the trainings in this thesis, a significance cut-off of 3 and a minimum number of 250 events were required for a split if not otherwise stated. The resulting forest for the main result consists of 64 trees. Target of the regression is the correction factor

$$C_{Reg} = \frac{p_T^{gen}}{p_{\mathrm{T}}^{L1L2L3}} \tag{7.8}$$

that is necessary to correct the p_{T} of the jet after the standard jet-energy corrections - on average - to the p_{T} of generator jets including neutrinos.

7.3.1. Training Samples

In order to have a large number of b-jets available for training and as the BJER is intended to supplement the top-quark mass measurement, the training is performed on b-jets in all available $\mathrm{t\bar{t}}$ MC samples with various generated top-quark masses. These samples are listed in Appendix A.2. Events are selected to have exactly one isolated muon, with $p_{\mathrm{T}} > 33\,\mathrm{GeV}$ and $|\eta| < 2.1$ and at least four jets with $p_{\mathrm{T}}^{L1L2L3} > 30\,\mathrm{GeV}$ and $|\eta| < 2.4$. In these preselected events, all b-jets are considered for the training (in contrast to Section 7.2 where a cut on the fit-probability is applied). The falling b-jet p_{T} spectrum is reweighted to be flat in order to avoid a bias of the training on the low p_{T}-region.

7.3.2. Bottom-jet properties considered for the training

The selection of a reasonable set of input observables is crucial for the derivation of a BJER. For example, high electron/muon energy fractions are signatures of semileptonically decaying B-hadrons, lowering the jet-energy response due to the energy loss to neutrinos. Other jet properties known to be correlated with the response and b-jet tagging specific observables are also considered for the regression in order to improve the performance. As the distribution of many of these jet properties vary for different jet kinematics, basic jet kinematic quantities like p_{T}, η, and pileup related quantities like the jet area A and the median energy density ρ_{25} are part of the regression.

Table 7.2.: List of input observables considered for the b-jet energy regression

categories	**observables**
jet kinematics	raw / JEC-corrected p_{T}, η, m_T
jet properties	energy fractions e/μ/charged hadrons, number of (charged) constituents, width (in φ)
b-tag	CSV discriminator
(b-tag) secondary vertices	p_{T}, m, flight length (+uncertainty)
(b-tag) soft lepton	p_{T} of the leading lepton, relative p_{T}-fraction, ΔR
pileup-correction related	jet area A, $\rho_{25}(\rho\,\text{in}\ |\eta| < 2.5)$

A list of observables considered for the main result is given in Table 7.2. It is very similar to the selection of observables in the CMS $H \to b\bar{b}$ analysis [178] and contains most of the properties discussed in Section 7.2. Many variations of the observable selection were tested and the performance of single observables was evaluated. This is discussed in Section 7.3.3 in the context of the performance of the main training result.

A selection of the observables used in the nominal training is discussed in the following in more detail showing the correlation of the b-jet properties before and after applying the b-jet energy regression. If the training was successful, the correlation of all b-jet properties with the jet-energy response should be largely reduced or in the best case vanish completely.

In Appendix C, a collection of control plots for all observables studied in the context of the regression training is given. These show how well the simulation describes the data (including systematic variations discussed in Section 7.4), but also the correlation before and after applying the nominal BJER.

Lepton fractions: In Figure 7.11, the correlation of the lepton fractions with the jet-energy response is shown. When a jet has a significant energy fraction taken by electrons or muons, the jet-energy response is on average too low, saturating at $\approx -15\%$ for electron/muon fractions above 20%. Even though only $\approx 30\%$ of the b-jets in the training sample contain reconstructed leptons, a significant improvement can be expected by exploiting this correlation. As expected, the trained b-jet energy regression fully compensates for the observed correlation.

Other PF-properties: For the particle multiplicity as well as e.g. the jet width distribution, a correlation with the response is observed as shown in Figure 7.12. For jets with a low constituent multiplicity (usually low p_{T} jets), the response is systematically too low. This correlation is compensated for by applying the BJER. More PF-related observables have been used for the training of the regression. Corresponding control distributions for

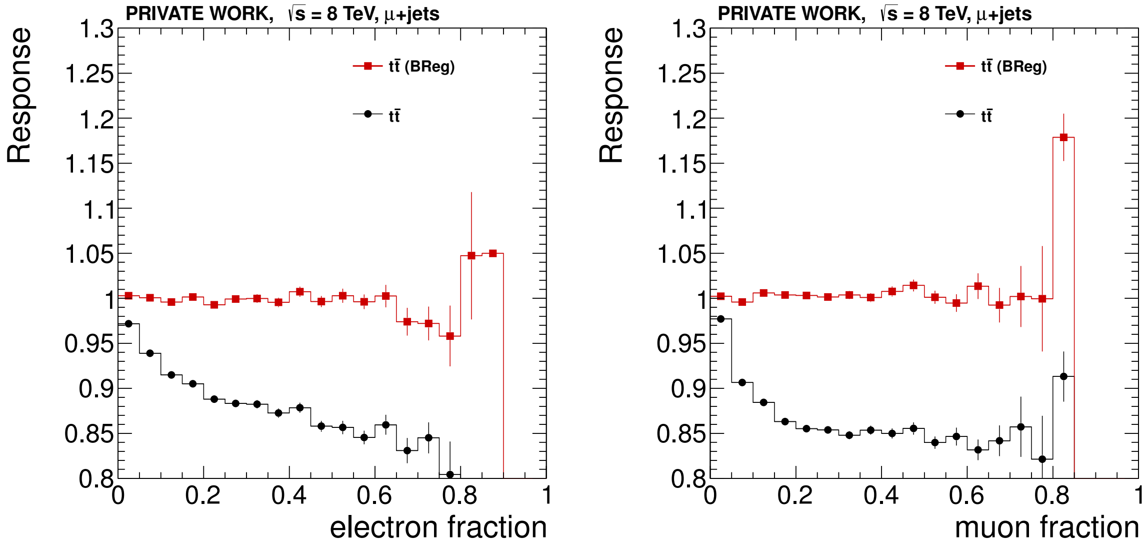

Figure 7.11.: Correlation of the mean jet-energy response with the lepton fractions before and after applying the regression correction for all (true) b-jets. The correlation is expected to be be significantly reduced after application of the BJER.

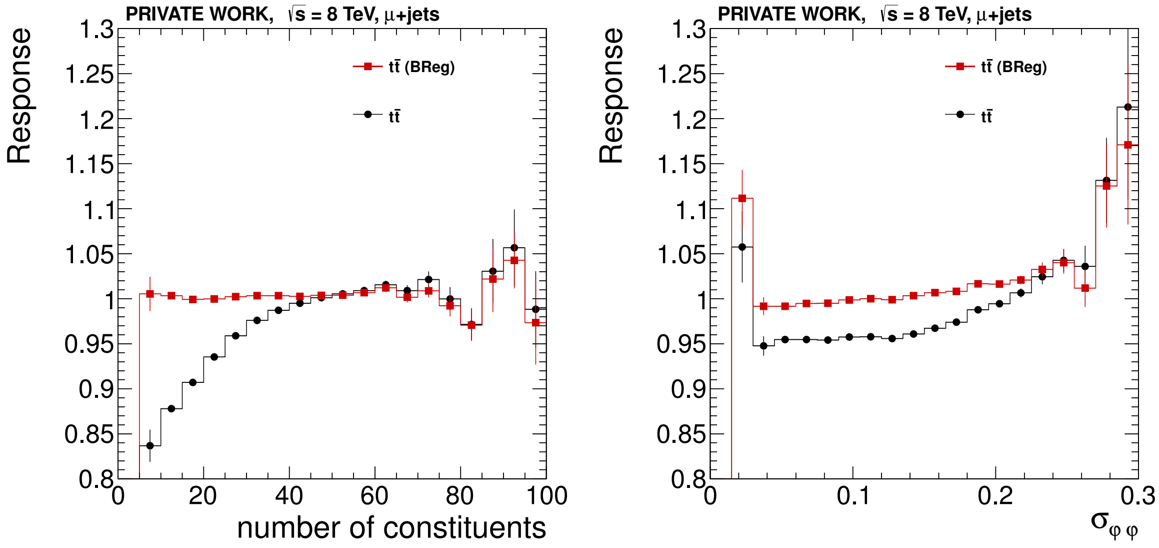

Figure 7.12.: Correlation of the jet-energy response with the PF candidate multiplicity and jet width $\sigma_{\varphi\varphi}$ before and after applying the regression correction for all (true) b-jets.

the number of charged hadrons, the number of charged PF candidates, and the charged hadron fraction (CHF) are listed in Appendix C.1.2.

B-tagging related quantities: The observables most relevant to b-tagging have also been considered for the b-jet energy regression. Exemplary, the correlation of the distance in ΔR of the leading soft muon with respect to the jet axis and the secondary vertex flight length with the jet response are shown in Figure 7.13. A small ΔR goes - on average -

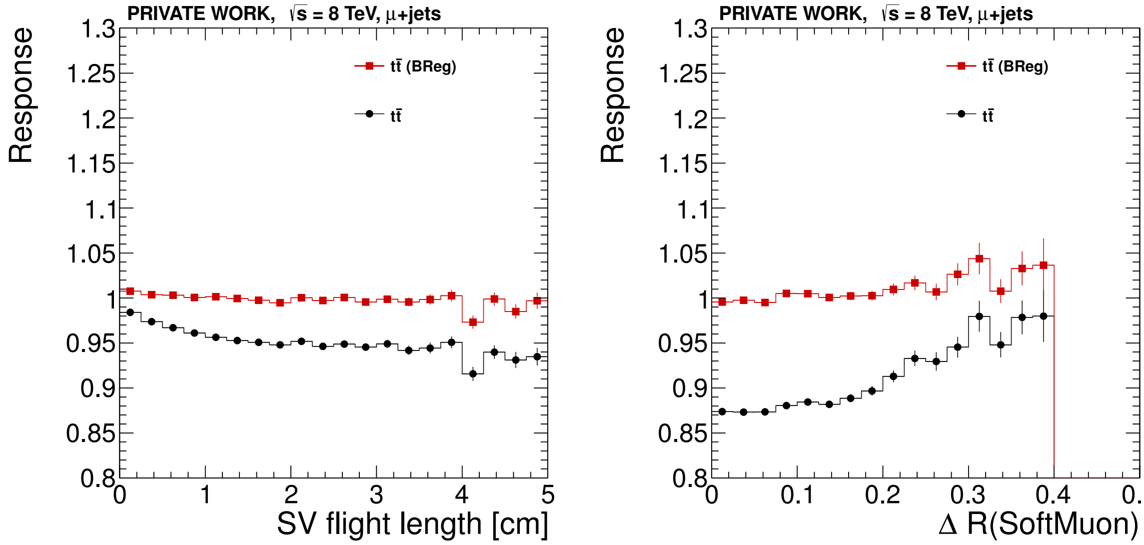

Figure 7.13.: Correlation of the jet-energy response with the secondary vertex flight length and the distance in ΔR between the leading soft muon and the jet axis before and after applying the regression correction for all (true) b-jets.

along with a relatively high energy fraction of the jet taken by this muon indicating a low jet energy response. More b-tagging-related observables have been used for the training of the regression. Corresponding control distributions for the CSV discriminator value, the soft lepton relative p_T fraction, the soft lepton p_T, the distance of reconstructed leptons ΔR with respect to the jet axis, as well as the secondary vertex mass and p_T are shown in Appendix C.1.3.

Kinematic observables: In order to allow the b-regression to take into account the kinematic dependence of sensitive jet properties on the kinematic region, but also in order to take into account the specific analysis selection later used for the top-quark mass measurement and any resulting response biases, observables like the corrected jet p_T and η are included in the training.

For most of these basic quantities no clear correlation is observed and the b-jet energy regression leads to a constant offset of the response. This is shown for η in Figure 7.14. For the jet p_T, a significant correlation is observed in Figure 7.14 and being corrected for. This can be understood when taking into account the b-jet p_T spectrum specific to the preselection of at least four jets with $p_T > 30$ GeV as shown in Figure 7.4. The b-jet p_T spectrum peaks at around 70 GeV where the jet-energy resolution has a value of about 13%. As the spectrum is steeply falling left and right of the peak, the relatively poor jet-energy resolution leads to a shift of the observed mean jet-energy response down (left of the peak) and up (right of the peak) for a given p_T, an effect observed for many jet response measurements and known as resolution bias. This is discussed in more detail using a toy MC in Section 7.5.3.

The b-jet energy regression learns this feature and uses it to correct the jets. However, this p_T spectrum is highly analysis-specific and leads to the fact that the b-jet energy

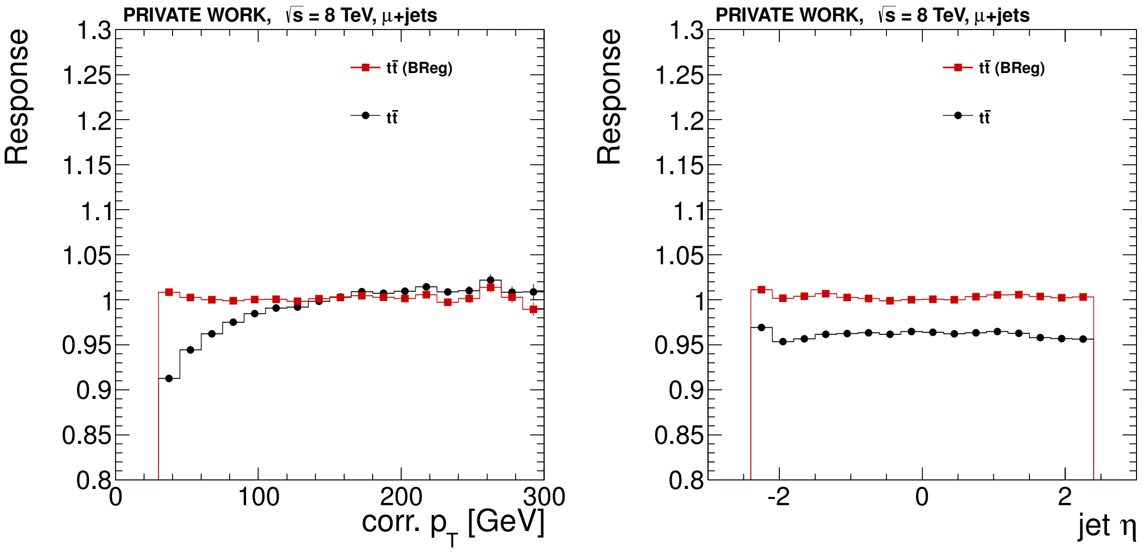

Figure 7.14.: Correlation of the jet-energy response with the corrected jet p_{T} and η before and after application of the regression correction for all (true) b-jets.

regression in the current form is not applicable to other topologies with different p_{T}-spectra. Possible improvements to the b-jet energy regression are discussed in Section 7.6. Control distributions for other kinematic and pileup-related quantities like the jet transverse mass, the uncorrected jet p_{T}, the jet area A, and the average energy density in the tracker covered region ρ_{25} are shown in Appendix C.1.4.

7.3.3. Performance in MC

For all observables considered for the nominal training, the correlation with the jet-energy response is compensated for when applying the BJER. Even for many of the observables not considered in the nominal training, the correlation with the jet-energy response is reduced after applying the BJER as illustrated in Appendix C.1.5. Only adding observables to the training showing a correlation with the response after applying the BJER would promise further improvements.

In order to evaluate the resolution and scale improvements due to the application of the b-regression, the response distributions before and after applying the regression correction have been compared. In Figure 7.15.(a), the response distribution is shown for all b-jets in the MC sample with the response $R_{\mathrm{noBReg}} < 2$ in a logarithmic view before and after applying the b-jet energy regression. Both distributions have been scaled such that the mean response is exactly equal to 1 in order to allow the comparison of the tails. The low response tail is significantly reduced by applying the b-jet energy regression and the overall resolution is slightly improved.

The response distributions before and after applying the BJER are shown for different p_{T}-ranges and in different detector regions in Figure 7.15(b)-(g). The labels indicate the arithmetic mean (m), the mean of an iterative Gaussian fit[1] to the core of the distribution (μ), and the relative resolution as given by the Gaussian fit (σ/μ). In all p_{T}-ranges, the average response is moved closer to unity and the energy resolution is improved slightly. In the central detector region, the core resolution is improved by $\approx 16\%$ for jets with $30 < p_{\mathrm{T}} < 50$ GeV and by $\approx 6\%$ for jets with $p_{\mathrm{T}} > 70$ GeV.

The average deviation of the jet response from the true jet response before/after applying the b-regression is shown in Figure 7.16. It is lowered by approximately the same amount across $|\eta|$ with the largest improvements of 20% at $p_{\mathrm{T}} \approx 30\,\mathrm{GeV}$ and about 6% at $p_{\mathrm{T}} \approx 200\,\mathrm{GeV}$

Training variations

In order to test the stability of the regression technique, but also in order to evaluate the strength of individual observables for the regression, a number of different trainings have been prepared and tested. For the single observable trainings and the cumulative training, in which more and more jet properties are added to the regression training, the cut on the significance has been increased to $8\,\sigma$ and the minimum number of events for each node is required to be 2000 events in order to keep the training times at an acceptable level.

Cumulative training: The selection of suitable input observables is crucial to the success of the regression. Adding more observables to the training can help to improve the performance of the regression. Fortunately, regression trees are known to be fairly resilient to adding correlated observables or observables with a relatively small separation power. They are simply not considered for the node-splitting if other observables provide better separation.

However, the stability of the nominal regression to adding/removing observables should be checked. This has been examined by subsequently adding more and more observables to individual trainings, starting with basic kinematic quantities, then adding width, lepton fractions, and subsequently all observables considered for the regression. Evaluating the observed relative resolution for the nominal MC sample and the tree growth observed in the training yields Figure 7.17.(a). Adding the first b-jet properties to the training yields a significant improvement of the relative resolution. Only very small resolution improvements are observed after adding the first 15 input observables. The size of the regression forest also remains approximately the same after adding the first 15 input observables.

Some additional improvement seems possible by adding observables used for the quark gluon discriminator [131] or pileup jet identification [132]. However, these observables have not been examined in detail and further follow-up studies would be needed to quantify possible gains.

---

[1] This refers to the same iterative fit of a Gauss function as in Chapter 5: After an initial fit with a Gauss function, the second fit is limited to the range $\pm 1.5\,\sigma$ around the mean of the initial fit.

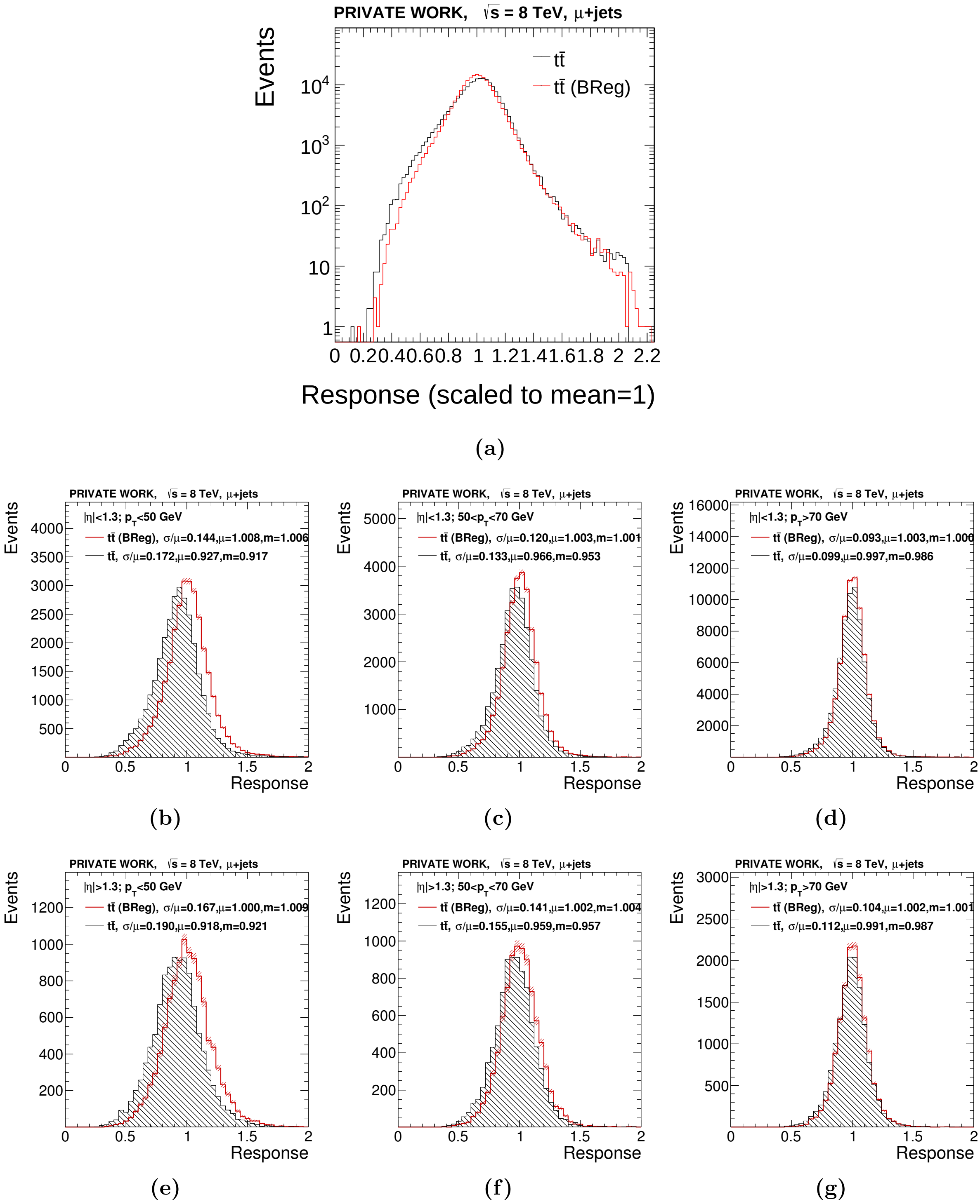

(a)

(b) (c) (d)

(e) (f) (g)

Figure 7.15.: (a): Logarithmic view of the response distribution before/after applying the b-jet energy regression (mean response scaled to 1 in both cases); (b-d): Response distributions of true b-jets before/after applying the b-regression in the barrel region for different p_T (a: $p_T < 50$ GeV; b: $50 < p_T < 70$ GeV; c: $p_T > 70$ GeV) (e-g): Response distributions in the endcap region (d: $p_T < 50$ GeV; e: $50 < p_T < 70$ GeV; f: $p_T > 70$ GeV)

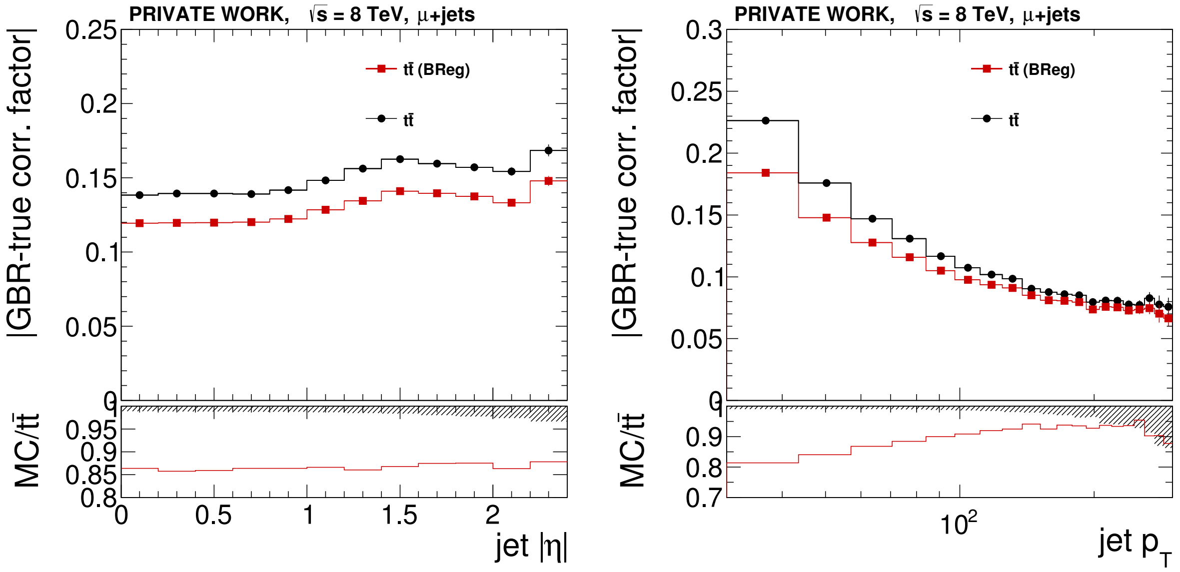

(a) (b)

Figure 7.16.: Mean deviation of jet response from the jet response at the particle level (including neutrinos) as a function of a.) $|\eta|$ and b.) p_T for true b-jets. The lower pads in both plots show the ratio of the mean deviation when applying the residual correction and when not applying the residual correction, i.e. the percentage improvement of the mean deviation.

Single observable trainings: Complementary to the cumulative training, for each individual observable in question for the BJER, a "single observable" training has been performed. For these trainings, the observable in question, the jet η, and the nominal JEC-corrected p_T of the jet (3 observables) are included in the training.

In Figure 7.17.(b), the results of these single observable checks are summarized: The lepton fractions, other lepton (especially muon) related observables and secondary vertex observables lead to the largest improvements for these single observable trainings and are also included in the nominal training.

Reduced number of input observables: The major part of improvement is expected by adding a relatively small number of highly sensitive jet properties to the training. A dedicated training with the same technical regression parameters as for the nominal training has been performed, considering only 12 input observables: the jet width in φ, lepton energy fractions, PF constituent multiplicity, secondary vertex decay length/mass and kinematic observables. In Figure 7.18, the response distributions for both variations are shown. Indeed, the differences between both trainings are only small and for future iterations of such a regression correction, the best compromise between optimizing the resolution improvement and minimizing the complexity by reducing the number of input observables has to be determined.

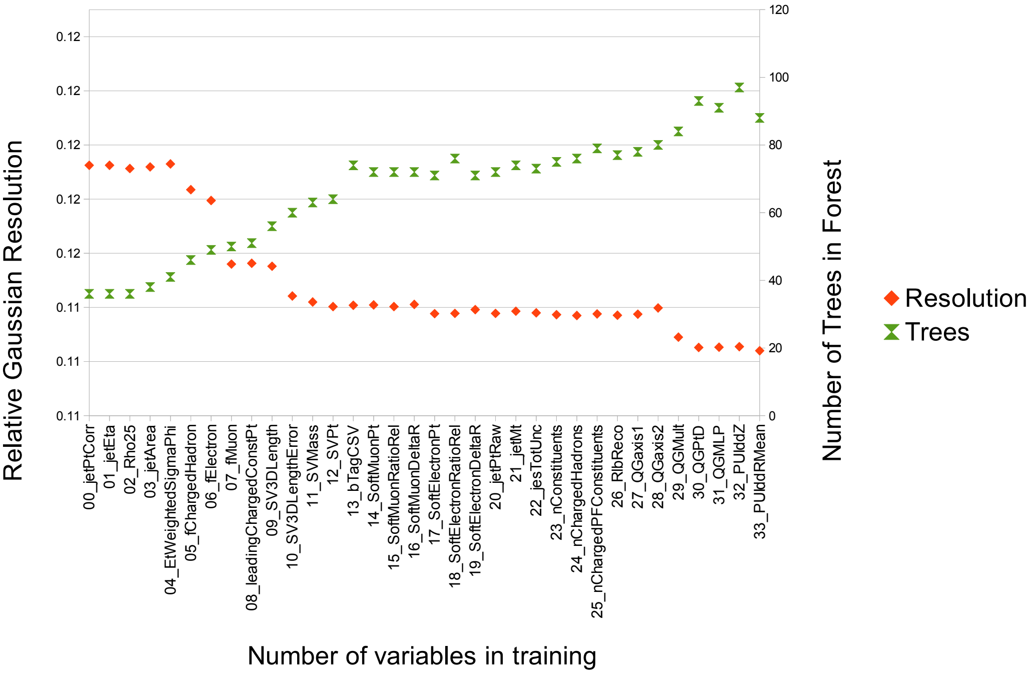

(a)

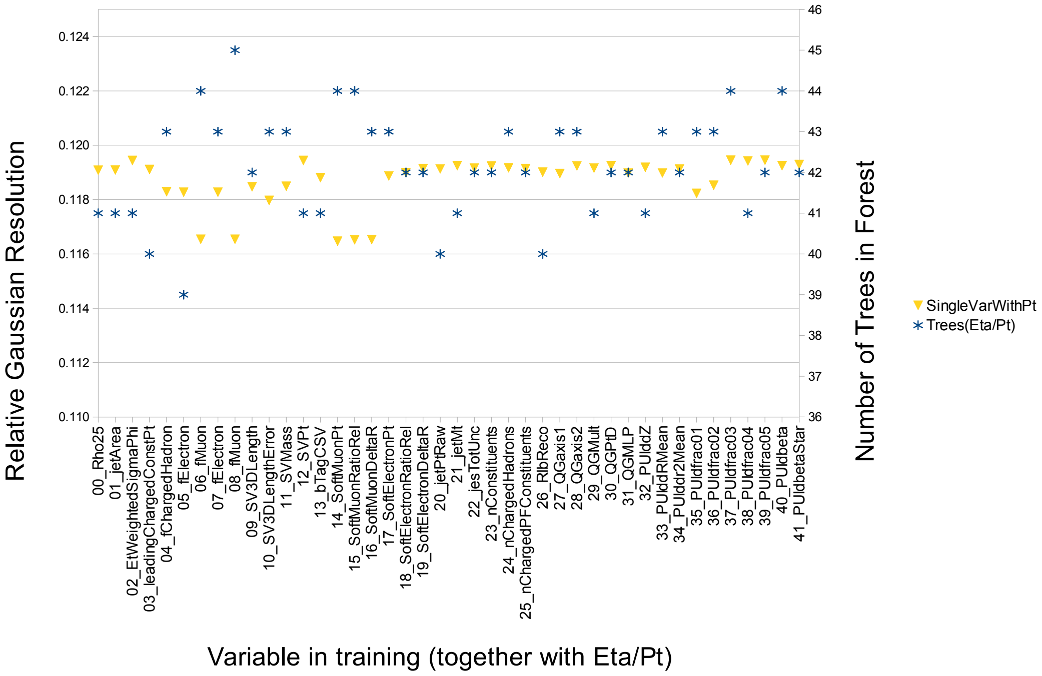

(b)

Figure 7.17.: (a): Relative resolution and number of trees in forest when adding subsequently more and more observables to the training. Starting with basic kinematics (p_{T}, η, ρ, jet area A), jet width, energy fractions, secondary vertex info. (b): Relative resolution and number of trees in forest for trainings considering only three input observables: jet η, p_{T}, and the observable in question.

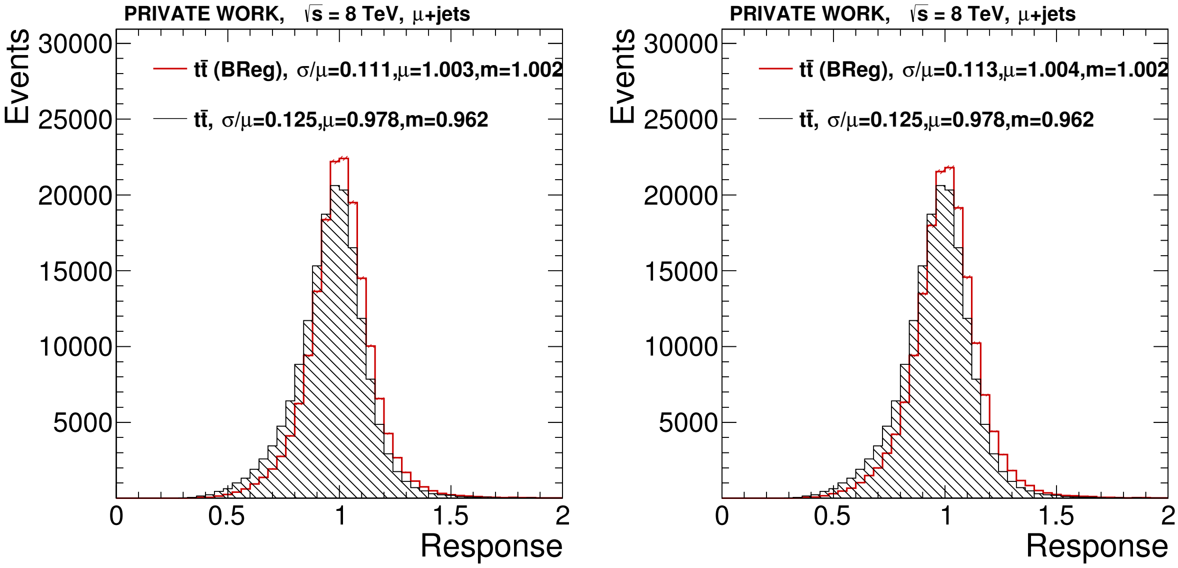

(a) (b)

Figure 7.18.: Response distributions of true b-jets (a) nominal training; (b) reduced set of input observables (12 instead of 24)

7.4. Systematic uncertainties on the b-jet response in $\mathrm{t\bar{t}}$-events

In order to determine the systematic uncertainties on the b-jet response, the response is evaluated as a function of p_T both with and without applying the b-regression correction for true b-jets in the nominal MC sample.

Several systematic variations are applied and the deviation from the nominal response as a function of p_T for the variation is considered as systematic uncertainty on the b-jet response. In the context of the JES uncertainties described in Section 4.5.5, a PYTHIA/HERWIG++ comparison in QCD multijet events is used to determine flavor uncertainties. This approach is adopted here using $\mathrm{t\bar{t}}$ MC samples. In addition, following the evaluation of b-JES specific systematic uncertainties at Tevatron experiments [195], the b-fragmentation in the MC is reweighted to fit to the expectation from previous direct measurements (compare Section 7.1) and the neutrino decay fractions are varied within uncertainties of previous measurements as described in [7].

PYTHIA/Herwig differences

In the context of jet-energy scale uncertainties, the study of biases due to the choice of a specific default Monte Carlo event generator are important. For example, the different hadronization models of PYTHIA with respect to HERWIG (string vs. cluster fragmentation) can have a large influence on the observed soft particles as discussed in the context of the relative residual jet energy corrections in Section 5.4.1. Such PYTHIA to Herwig comparisons have also been used to model the flavor response uncertainties in CMS as discussed in Section 4.5.5.

In addition to the default CMS MADGRAPH $\mathrm{t\bar{t}}$ samples, $\mathrm{t\bar{t}}$ events have been produced using POWHEG [196] interfaced with either PYTHIA or HERWIG for showering. [2] In these samples, the difference in the b-jet response is determined directly in the top analysis environment. It should be noted that these top samples use HERWIG instead of HERWIG++. HERWIG++ is used for the production of QCD datasets usually considered in the context of jet-energy scale uncertainties.

In Figure 7.19.(a), the impact of exchanging PYTHIA and HERWIG in the interface with POWHEG is shown. The nominal response is taken as the response in the POWHEG +PYTHIA sample. The b-jet response in the POWHEG +HERWIG sample is lower in comparison to POWHEG +PYTHIA. However, when comparing the observed response differences before and after applying the regression correction, the differences are reduced by $\approx 50\%$ when applying the regression correction.

---

[2] The samples used for this comparison are:
`/TT_CT10_TuneZ2star_8TeV-powheg-tauola/Summer12_DR53X-PU_S10_START53_V7A-v2/AODSIM`
`/TT_CT10_AUET2_8TeV-powheg-herwig/Summer12_DR53X-PU_S10_START53_V19-v1/AODSIM`

b-fragmentation

The description of the B-hadron fragmentation function in the default MC samples is not optimally tuned to direct measurements as discussed in Section 7.1. A reweighting to the retuned fragmentation has been applied in order to take into account these differences. It is observed for the b-regression correction in its current implementation that it does not reduce the impact of the varied b-fragmentation. This is shown in the comparison in Figure 7.19.(b) in which the response differences are $\approx 50\%$ larger for the case that the b-regression is applied.

Neutrino fraction

In semileptonic decays a certain fraction of the jet energy is lost to neutrinos which escape the fiducial volume of CMS undetected as discussed in Section 7.1. In order to estimate the size of the effect, the uncertainty attributed to the semileptonic branching ratio of $B^{\pm}/B^0$-mesons is propagated. For this, the branching ratio is reweighted as in [7] to correspond to an envelope that takes into account the measured branching ratios and uncertainties of both, $B^{\pm}$ and B^0 (-0.45%/+0.77%, [40]). As observed in Figure 7.19.(c), the already small effect on the response is reduced further by applying the b-regression.

Comparison of resulting b-JES uncertainty with/without applying the regression

In Figure 7.19.(d), the systematic uncertainties resulting from the direct PYTHIA/HERWIG comparison, the fragmentation reweighting, and the variation of the neutrino fraction are summarized: When adding up quadratically the three effects, the resulting total uncertainty is slightly reduced when applying the b-jet energy regression. If the influence of the fragmentation could be reduced further, the total gain could be increased significantly.

7.5. Systematic biases of the b-jet energy regression

As illustrated in Figure 7.19.(d), the application of the BJER to b-jets could help to decrease the size of systematic uncertainties related to the b-JES. However, it was observed that the resulting response variation for the fragmentation variation is larger in case the BJER is applied.

A possible cause discussed in Section 7.5.1 would be that input observable distributions influenced strongly by the fragmentation reweighting lead to shifts in the overall response. It could also be beneficial to more directly target the fragmentation in a dedicated BJER training as discussed in Section 7.5.2.

In the currently examined forms of b-jet energy regressions, the training is analysis-specific: It is trained using the same preselection applicable to the further analysis.

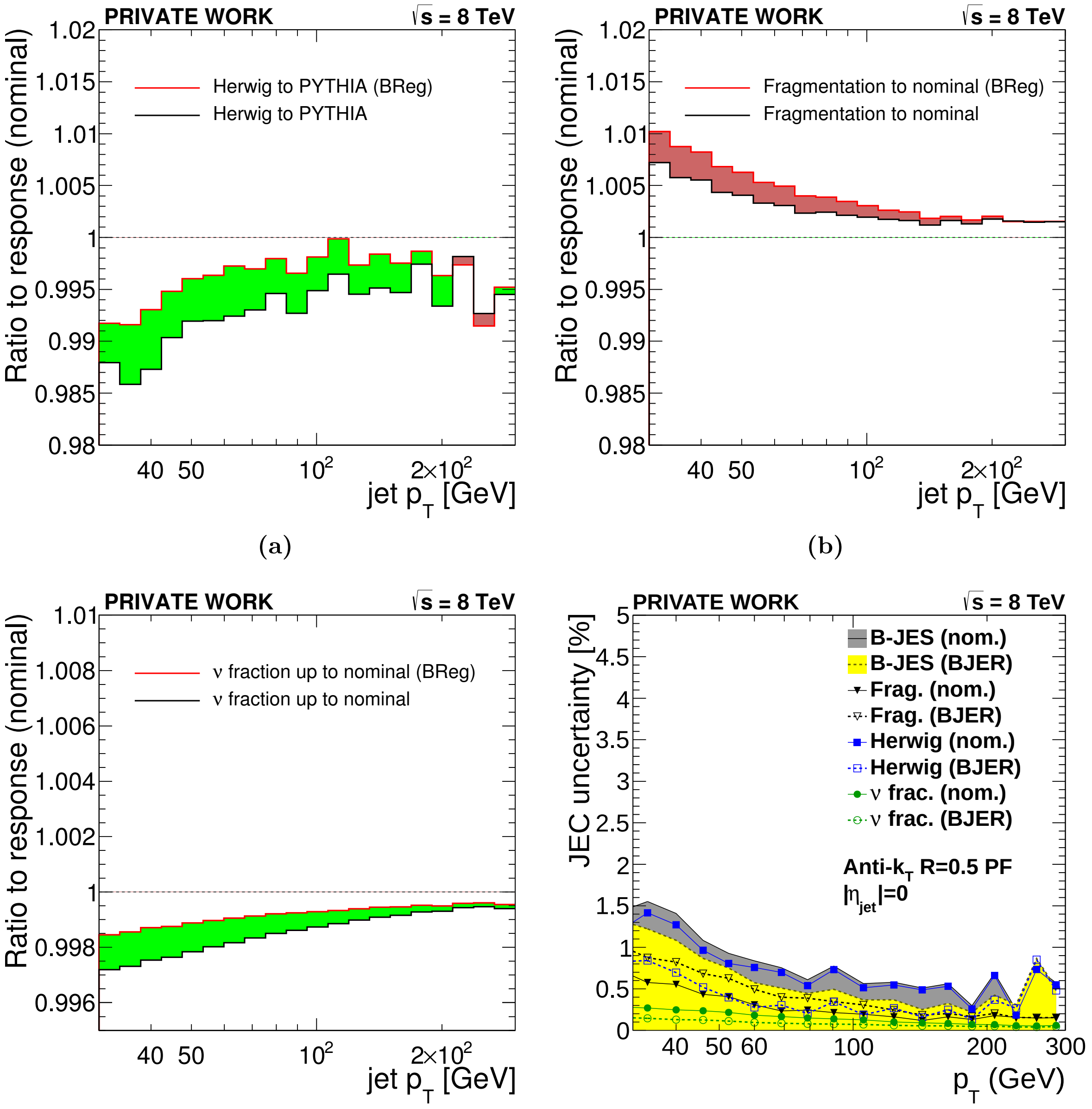

(a) (b) (c) (d)

Figure 7.19.: Deviations of the response from the nominal response for various systematic variations before (black line) and after (red line) applying the b-regression as a function of p_T. (a,b,c): If the application of the BJER reduces the response differences caused by the systematic variation, the improvement is indicated as green filled area. If the differences are enhanced, the fill area is colored red. (a): Comparison of the response in the POWHEG +PYTHIA and the POWHEG +HERWIG MC sample (b): Comparison of the response in the nominal MC sample with and without scaling the b-fragmentation. (c): Comparison of the response in the nominal MC sample with and without scaling the semileptonic branching fraction of B-hadrons (denoted with ν up in the legend). (d): Systematic uncertainty of b-response before / after applying the b-regression as a function of p_T. Contributions by variations of the b-fragmentation and neutrino fractions as well as a direct PYTHIA/HERWIG comparison are shown.

These preselections lead to an analysis-specific jet p_{T} spectrum. The jet p_{T} spectrum in combination with the jet-energy resolution is a known source for biases of the measured response. This is discussed for the preselection used in this analysis using a toy MC study in Section 7.5.3.

7.5.1. Influence of systematic variations on the input observables and their correlation with the b-jet response

The influence of the systematic variations on the input observable distributions and the correlation of the observables with the jet energy response before and after applying the regression correction is evaluated in order to pinpoint any potential larger deviations from the expected behavior. For most observables, the differences of the observable distributions among the systematic variations are small and the same behavior as discussed in Section 7.4 is observed: Response differences between PYTHIA and HERWIG are reduced while no improvement can be ascertained for the fragmentation variation. Jet properties particularly sensitive to the fragmentation modeling are the jet width $\sigma_{\varphi\varphi}$ and the particle multiplicities.

Exemplary, the charged hadron multiplicity, the width in φ, and the muon energy fraction distributions and the correlations of these observables with the response are shown in Figure 7.20. In contrast to Section 7.2, the hatched uncertainty band here only indicates the statistical uncertainty of the data (or the statistical uncertainty of the average response in the nominal MC in the correlation plots).

The description of the charged hadron multiplicity is improved by applying the fragmentation reweighting, but the description of the jet width is worsened. The differences in the description of the muon fraction are small. The effect of reducing the response differences after applying the regression correction is visible as a function of all three exemplary observables. Corresponding plots for all observables are listed in Appendix C.1.

7.5.2. Training to explicitly target fragmentation

When evaluating systematic uncertainties on the b-jet response in Section 7.4, the response differences between the nominal MC and the sample with a reweighted fragmentation increased slightly, if applying the BJER, as shown in Figure 7.19d. This effect has been observed for most training variations and could not be pinpointed to a single source, yet.

A dedicated training to address this observed behavior has been performed, including additional observables expected to be particularly sensitive to the b-fragmentation. Such observables are the relative secondary vertex p_{T} (the secondary vertex p_{T} was already part of the nominal training) and the energy fraction in the innermost 0.1 annulus of the jet as defined for the pileup jet identification [132]. The innermost annulus energy

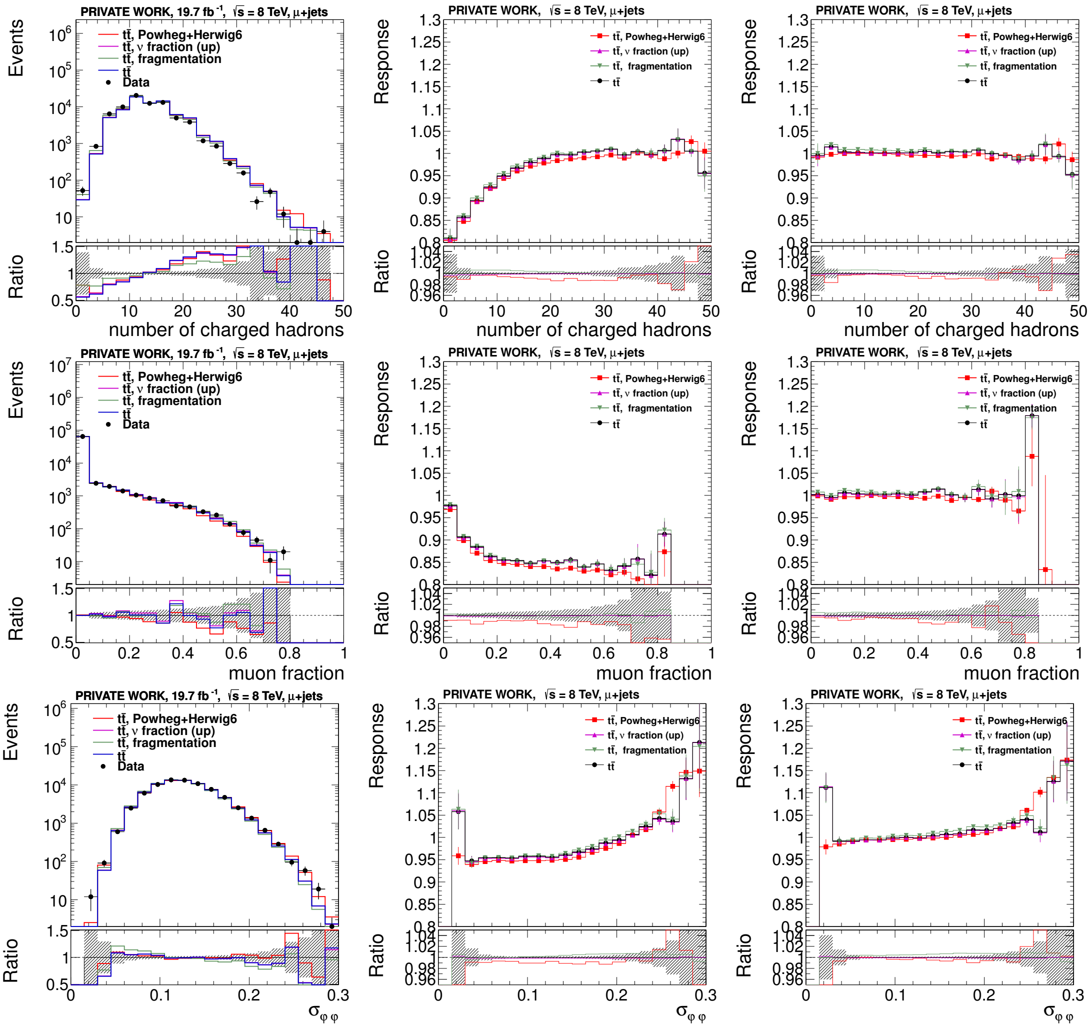

Figure 7.20.: Left column: Distribution of input observables with default MC and systematic variations in comparison to data. The lower pad shows the ratio of the MC variations to the data; Middle column: Correlation of input observables with jet energy response (standard JEC). The lower pad shows the ratio of the MC variations to the nominal MC; Right column: Correlation of input observables with jet energy response after applying the regression correction. The lower pad shows the ratio of the MC variations to the nominal MC.

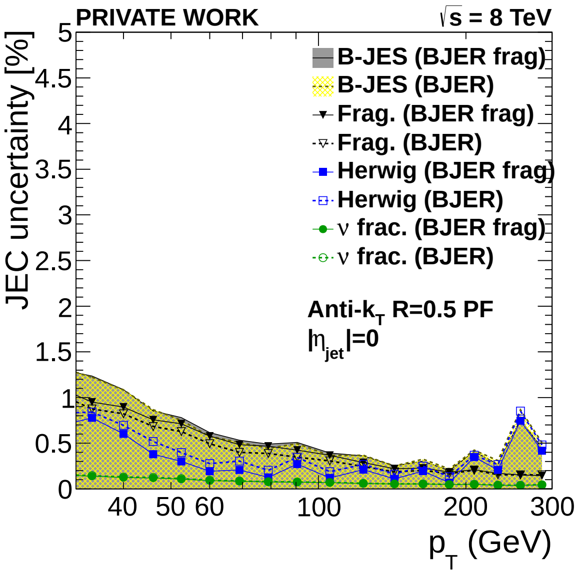

Figure 7.21.: Systematic uncertainty of b-response after applying the nominal b-regression (BJER) and after applying a cross-check training including the central annulus energy fraction and relative secondary vertex p_{T} (BJER frag) as a function of p_{T}. Contributions by variations of the b-fragmentation and neutrino fractions as well as a direct PYTHIA/HERWIG comparison are shown.

fraction shows a relatively strong correlation with the b-jet response, even after applying the nominal BJER as shown in Appendix C.1.5.

However, as depicted in Figure 7.21 the effect can not easily be reduced by this procedure and remains of approximately the same size, larger than without the regression. The reasons for this are not fully understood, but underline that the adopted regression method critically relies on a highly accurate simulation, incorporating measurements like those of the b-fragmentation function properly into the tuning of the simulation.

7.5.3. Discussion of the resolution bias

As mentioned in Section 7.3.2, a relatively strong correlation of the reconstructed jet p_{T} and the jet-energy response is observed. This can be understood using a simple toy MC model:

According to a given p_T^{gen}distribution, random p_T^{gen}values are sampled. For each p_T^{gen}entry, a jet-energy response is sampled according to a response model with a p_{T}-dependent jet-energy resolution. The resulting correlations of the jet-energy response and the “toy” reconstructed jet p_{T} can then be compared to the correlation observed after the selection specific to this analysis.

For this, two different p_{T}-spectra have been considered: the p_{T}-spectrum taken from the MC sample after the preselection and a purely exponential p_{T} spectrum, fitted to the high p_T-tail of the spectrum from MC. The sampled p_T-spectra for 1 mio. events are shown in Figure 7.22.(a).

In Figure 7.22.(b), the response distribution of the full $\mathrm{t}\bar{\mathrm{t}}$ MC sample is compared to the response distribution from the toy MC assuming the p_T-spectrum from the full simulation. For the toy MC, two different response models have been considered: a Gaussian response using a p_T-dependent jet-energy resolution parameterization (for the nominal QCD flavor mixture), and a crystal ball (CB) response model tuned to the response distribution of the full MC at $p_T^{gen} = 100$ GeV with the Gaussian response part scaled following the same p_T-dependent jet-energy resolution. While the Gaussian response model does not fit very well to the full MC, the crystal ball parameterization describes the b-jet specific low energy tails and only lacks in the description of the high response tail. However, this can be attributed to the threshold effect present in the full MC favoring upwards response fluctuations due to the cut of 30 GeV on the reconstructed jet p_T.

In Figure 7.22.(c), the mean response is depicted as a function of the reconstructed p_T for both response models assuming the p_T-spectrum from the full MC and the response as observed directly in the full simulation. While the simple Gaussian model does not describe the observed correlation of the response and the reconstructed p_T, the crystal ball response model describes the response fairly well. The long “turn-on” of the response is only described by this ball model as it takes into account the low response tails.

In Figure 7.22.(d), the mean response in the toy MC is shown as a function of p_T for the two different p_T-spectra depicted in Figure 7.22.(a). If threshold effects could be neglected, i.e. a purely exponential spectrum could be assumed, the bias to a lowered response would be much smaller in the low p_T-region.

Overall, the correlation of the response with the reconstructed p_T in the training MC sample can precisely be reproduced and explained using the toy MC model outlined above. The b-jet energy regression takes into account the p_T-spectrum and response shape and corrects for the observed correlation. Possible improvements that would help to make the regression independent of the p_T-spectrum and applicable to any event topology are discussed in Section 7.6.

7.6. Possible improvements and outlook

The b-jet energy regression technique discussed in this chapter has the potential to improve the jet-energy resolution while simultaneously decreasing the b-JES uncertainty. In the typical p_T-range of b-jets in top-quark analyses of $\approx 50\,\mathrm{GeV}$, the MC studies show a resolution improvement of 10-15%. If evaluated in the way as chosen in Section 7.4, it appears feasible to lower the systematic uncertainty associated with the b-JES slightly in case a BJER is applied to the b-jets.

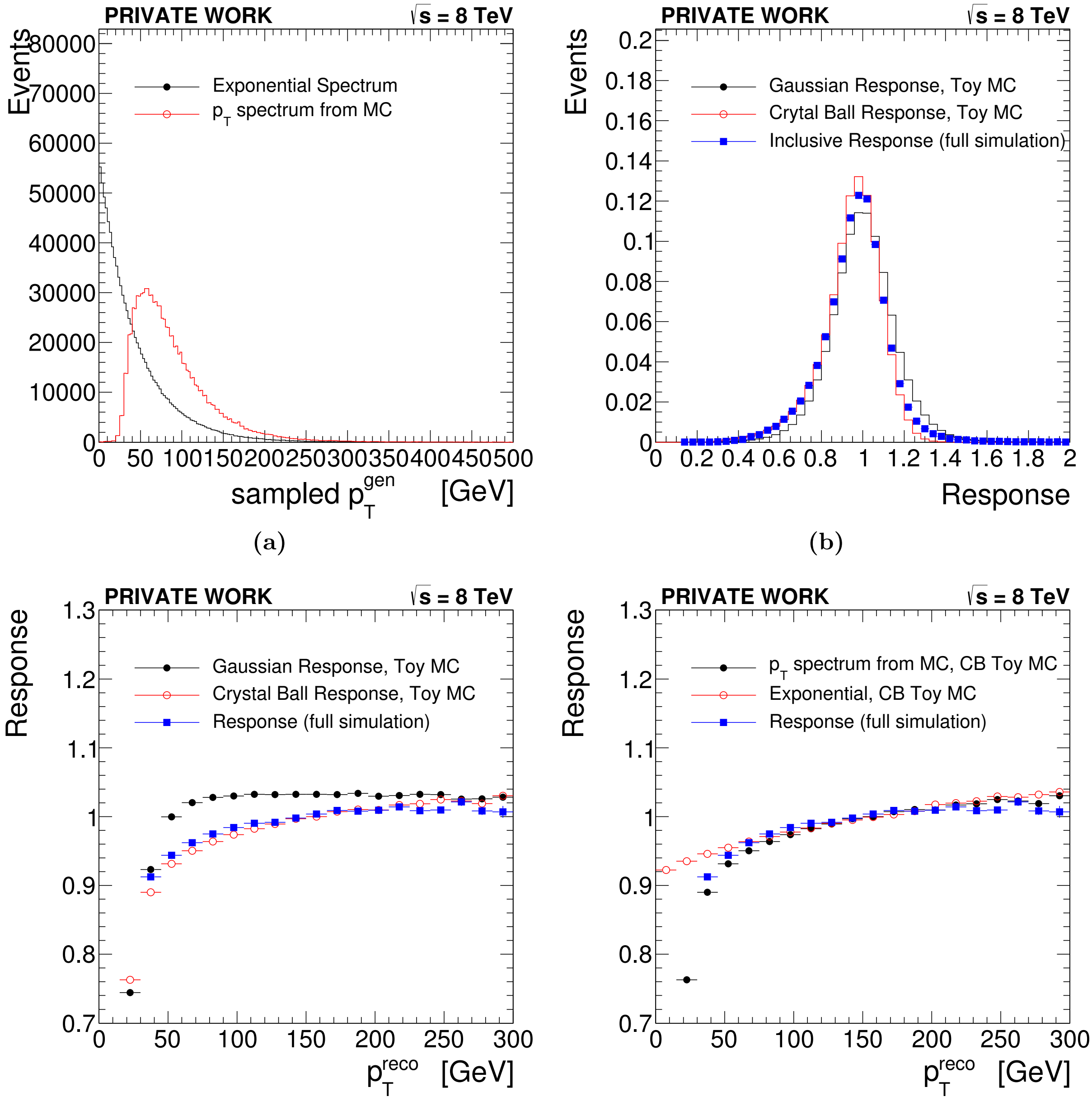

(a) **(b)**

(c) **(d)**

Figure 7.22.: (a): Different p_{T}-spectra used for the toy MC; (b): Response distribution integrated over the full p_{T}-spectrum from MC for a Gaussian and a “crystal ball” (CB) response model, compared to the inclusive response distribution from the full MC; (c): Mean response for p_{T}-spectrum from the full simulation convoluted with Gaussian response model and crystal ball response model, compared to the mean response from the full simulation; (d): Resulting response using a crystal ball response model tuned to the response distribution at $p_T^{gen} = 100$ GeV convoluted with the different spectra as shown in (a) compared to the observed response in MC;

However, several improvements to the actual implementation of such regression corrections are possible. This includes the careful choice or definition of additional b-jet properties which still show a correlation with the b-jet response after a BJER with a given set of observables is applied. For example, some of the observables used for the determination of the quark gluon discriminator or the pileup jet identification still show correlations with the response after applying the nominal BJER. Implementing them could help to increase the resolution improvement or to decrease the sensitivity to the fragmentation modeling.

As discussed in Section 7.3.3, a reduction of the number of input observables can be achieved without considerably reducing the performance of the regression. This would help to keep the complexity for monitoring the description of input observables at a reasonable level and improve the overall expected robustness of the BJER.

Following the discussion on the resolution bias inherent to the current approach of analysis-specific regression trainings in Section 7.3.2, it would appear advisable to devise a more general ansatz for a training to avoid such a bias. For example, with sufficiently large MC samples, it would be feasible to have multiple trainings binned in p_T^{gen}, avoiding the direct use of the reconstructed jet p_{T} in the training. Similarly to the derivation of MC truth L2L3 jet-energy corrections as discussed in Section 4.5.2, the corresponding training could then be selected according to p_{T}^{L1L2L3}. This would also lead to a more general applicability of such a regression in other topologies.

Such a b-jet energy regression applicable to other event topologies could be validated effectively using data-driven techniques like Z/γ+jet balancing and become an optional part of the CMS jet-energy correction chain.

Chapter 8

Measurement of the top-quark mass with BJER

The measurement of the top quark mass is scientifically highly important, but also a benchmark of the detector performance. At LHC experiments, the uncertainties on the measurement are dominated by systematic uncertainties. At 7 TeV, measurements in the all-hadronic channel and the lepton+jets channel by the University of Hamburg group using an ideogram method have been very successful [6, 175].

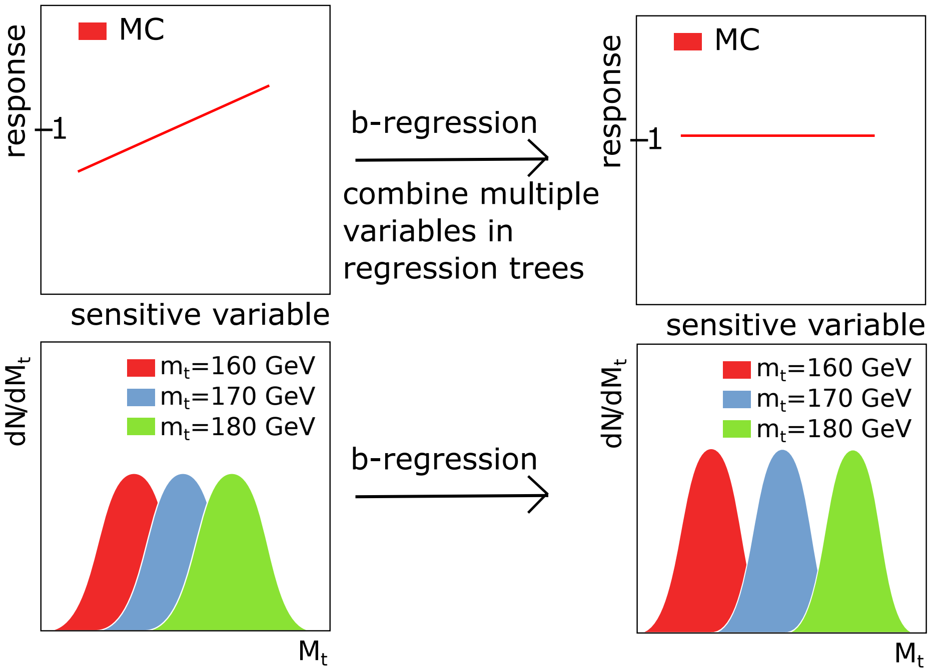

Figure 8.1.: Top: Basic idea of the b-jet energy regression: Find (many) jet properties sensitive to the jet-energy response and correct for the observed correlation using a multivariate regression technique like boosted regression trees; Bottom: Gain in the top-quark mass determination by improving the resolution of the fitted top-quark mass distribution and potentially reduce systematic uncertainties. Both adapted from [189].

Up to now, the measurements in the lepton+jets decay channel have lead to the most precise single measurements of the top-quark mass (currently the most precise single measurement is [72]). The dominant systematic uncertainty of the top-quark mass measurement [6] is the b-JES uncertainty with a value of 0.61 GeV. The total systematic uncertainty (adding 14 other sources to the b-JES uncertainty) was found to be 0.98 GeV. As a supplement to the ongoing main measurement at 8 TeV in the lepton+jets channel, for which a preliminary result has already been made public [7], the use of the b-jet energy regression (BJER) presented in the previous chapter in the analysis has been tested. By applying the b-jet energy regression, an improved top-quark mass resolution is expected as illustrated in Figure 8.1. This would lead to a reduced statistical uncertainty on the measurement. In addition, the systematic uncertainties related to the description of b-jets could potentially be reduced if the b-jet energy regression indeed leads to a reduced sensitivity of the analysis to systematic variations linked to the b-JES uncertainty. This is suggested by the studies in Chapter 7.

First, an introduction to the analysis strategy is given for the nominal analysis. Then, the existing analysis is repeated after adding the BJER to the analysis chain before the kinematic fit. The impact of the BJER on relevant distributions and selection efficiencies is discussed. As the application of the BJER shifts e.g. the fitted top-quark mass distribution, the full top mass analysis calibration is repeated and systematic uncertainties related to the b-JES uncertainty are re-evaluated. The results with and without applying the BJER are compared and the top-quark mass on data is determined in both cases.

8.1. Nominal top-quark mass measurement in the lepton+jets decay channel

In a $\mathrm{t\bar{t}}$-event, both top quarks decay with an almost 100% branching ratio weakly via $t \to bW$. Depending on the decay modes of the two W bosons, different event topologies are defined as discussed in Section 2.2.2. In the lepton+jets decay channel, one of the W bosons decays into a charged lepton and its corresponding neutrino, the other W boson decays into a quark-antiquark pair.

Imposing the requirement of two b-tagged jets (using the combined secondary vertex b tagger at the medium working point, CSVM) among the four leading jets with $p_\mathrm{T} > 30$ GeV and $|\eta| < 2.4$, and requiring exactly one isolated lepton with $p_\mathrm{T} > 33$ GeV results in a very clean sample which contains 94.3% $\mathrm{t\bar{t}}$ events [7].

The full analysis in the lepton+jets channel using an ideogram method is described in detail in [5–7]. Here, only the most important analysis steps relevant for the BJER application are touched on.

Kinematic fit: In order to improve the resolution of reconstructed quantities after the preselection and in order to estimate the compatibility of the reconstructed event with the

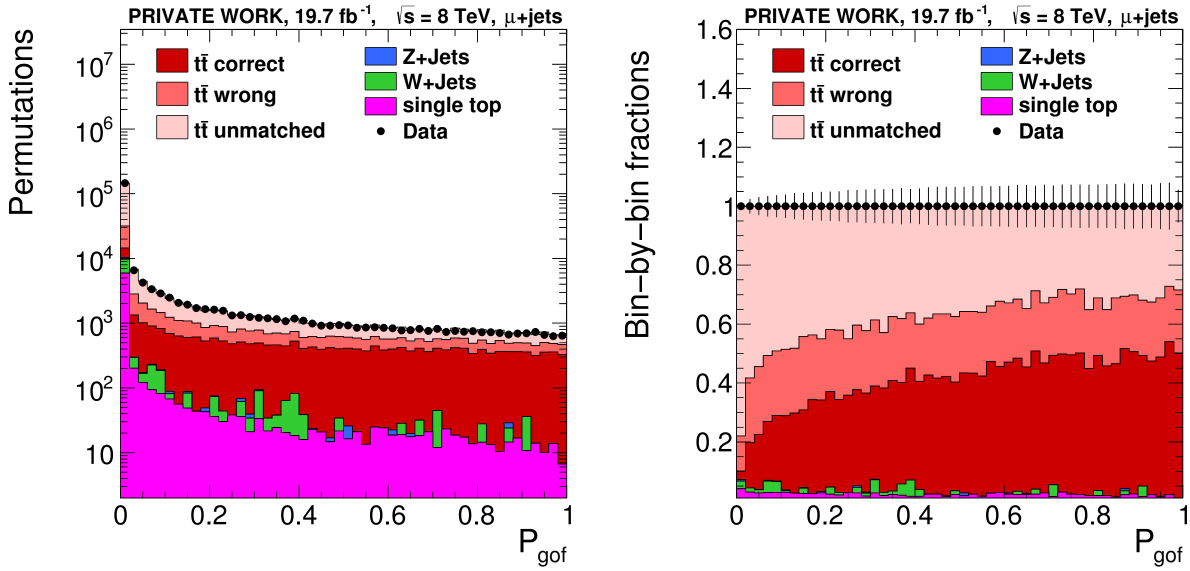

(a) (b)

Figure 8.2.: (a) P_{gof} distribution; (b): P_{gof} distribution normalized in each bin in P_{gof} to unity to visualize the P_{gof} dependence of the cp/wp/un-fractions

lepton+jets $\mathrm{t\bar{t}}$ hypothesis, a kinematic fit is applied. In the kinematic fit, the input four-vectors of the lepton, the four leading jets, and the missing transverse momentum (start value for the undetected neutrino) are modified within their respective object resolutions to best fit to the event hypothesis. Here, fit constraints on the two top masses ($m_t = m_{\bar{t}}$) and the subsequent decay into a W boson (with $m_W = 80.4$ GeV) and a b-quark are imposed. Subsequently, the kinematic fit minimizes $\chi^2 = (\mathbf{x} - \mathbf{x}^m)^T G (\mathbf{x} - \mathbf{x}^m)$ where $\mathbf{x}^m$ is the vector of measured observables, $\mathbf{x}$ the vector of fitted observables, and G is the inverse error matrix which is given by the resolutions of the observables.

With the two b-tagged jets as candidates for the b-quarks and two untagged jets as candidates for the hadronic W boson decay, two possible parton-jet assignments per event are possible and two solutions for the z-component of the neutrino momentum have to be considered (the reconstructed $\vec{E}_{\mathrm{T}}^{\text{miss}}$ can only provide start values for p_x^ν and p_y^ν).

Depending on the parton-jet assignment, three different permutation categories are used in the top-quark mass analysis: correct permutations (cp), wrong permutations (wp, swapped b-jet), and unmatched permutations (un). In the unmatched case at least one quark from the $\mathrm{t\bar{t}}$ decay could not be matched unambiguously to any of the four leading jets. As a measure of the compatibility of the permutation with the event hypothesis, a goodness-of-fit (gof) probability is defined as $P_{\text{gof}} = \exp\left(-\frac{1}{2}\chi^2\right)$. The distribution of the fit probability is shown in Figure 8.2. For higher values of P_{gof}, the fraction of correct permutations is increased considerably. As a compromise between statistical precision and increasing the cp fraction, a cut of $P_{\text{gof}} > 0.2$ was chosen. In order to enrich correct permutations further, the permutations are weighted by P_{gof}.

Ideogram method: In order to determine the top-quark mass, the $m_{\mathrm{t}}^{\mathrm{fit}}$ observable is a well-suited estimator. It is defined as the invariant mass of the sum of the four-vectors of the W boson candidate and the b-jet. However, the distribution of $m_{\mathrm{t}}^{\mathrm{fit}}$ is very sensitive to the jet-energy scale. Any jet-energy scale uncertainties propagate directly to the $m_{\mathrm{t}}^{\mathrm{fit}}$ distribution, leading to the fact that in most top-quark mass measurements, uncertainties related to the jet-energy scale are dominating systematic uncertainties. In the top-quark mass measurements pursued by the University of Hamburg group [6, 7, 71, 175], this is overcome by simultaneously fitting a jet-energy scale factor (JSF) on top of the standard jet-energy corrections. The JSF is constrained by the distribution of $m_{\mathrm{W}}^{\mathrm{reco}}$ defined as the invariant mass of the hadronic W boson candidate before applying the kinematic fit.

A detailed description of the specific implementation of the ideogram method and further calibration steps via pseudo-experiments to correct for small remaining biases is given in [6]. The ideogram method itself was first used by the DELPHI collaboration for measurements of the W boson mass and width [197] and first used for the measurement of the top quark mass in the lepton+jets decay channel at D0 [198].

Starting from the $m_{\mathrm{t}}^{\mathrm{fit}}$ and $m_{\mathrm{W}}^{\mathrm{reco}}$ distributions, the ideogram method is used to determine the most likely m_{t} and JSF values. The ideogram method takes into account different permutation cases for single events. For each event a likelihood is computed and the most likely m_{t} and JSF values are determined by maximizing $-2\ln\mathcal{L}\left(m_{\mathrm{t}},\mathrm{JSF}|\mathrm{sample}\right)$ where the likelihood for all events is given by

$$\mathcal{L}\left(\mathrm{sample}|m_{\mathrm{t}},\mathrm{JSF}\right) = \prod_{\mathrm{events}}\left(\sum_{i=1}^{n} P_{\mathrm{gof}}\left(i\right)\Big(\sum_{j} f_j P_j(m_{\mathrm{t},i}^{\mathrm{fit}}|m_{\mathrm{t}},\mathrm{JSF}) \times P_j(m_{\mathrm{W},i}^{\mathrm{reco}}|m_{\mathrm{t}},\mathrm{JSF})\Big)\right)^{w_{\mathrm{event}}}$$

Input to this likelihood are the $m_{\mathrm{t}}^{\mathrm{fit}}$ and $m_{\mathrm{W}}^{\mathrm{reco}}$ distributions determined from seven different m_{t} and three different JSF values. These distributions are described by fitting probability density functions (PDF) for each m_{t}/JSF-combination and for each permutation case: correct (cp), wrong (wp), or unmatched (un).

The dependence of the fit parameters on m_{t} and JSF is parameterized to obtain continuous functions $P_j(m_{\mathrm{t},i}^{\mathrm{fit}}|m_{\mathrm{t}},\mathrm{JSF})$ and $P_j(m_{\mathrm{W},i}^{\mathrm{reco}}|m_{\mathrm{t}},\mathrm{JSF})$. In the likelihood formulation n denotes the number of permutations in each event, j labels the permutation cases, and f_j represents their relative fraction as determined from the MC. In order to reduce the influence of events without correct permutations, the event weight $w_{\mathrm{event}} = c\sum_{i=1}^{n} P_{\mathrm{gof}}\left(i\right)$ is introduced, where c is a normalization constant.

Result of the nominal analysis in the μ+jets channel: For the comparison of the results of the nominal analysis with the slightly adapted version utilizing the b-jet energy regression presented in the previous chapter, an intermediate version of the nominal analysis has been used. For the μ+jets channel, this gives

$$\mu\text{+jets: } m_{\mathrm{t}} = 171.92 \pm 0.26\,(\mathrm{stat.}{+}\mathrm{JSF}); \qquad \mathrm{JSF} = 1.016 \pm 0.002\,(\mathrm{stat.})$$

as the central result on the full 2012 data. In the preliminary result [7], a set of MC samples with a higher number of generated events has been used as well as a p_{T}-dependent residual correction, explaining the small numerical differences in the obtained m_{t} and JSF values. However, for the comparison of the analysis with/without applying the b-jet energy regression as discussed in this chapter, the smaller size of the used MC samples is not expected to influence the results.

8.2. Full analysis chain with b-regression

In order to evaluate the resolution improvements observed in Chapter 7, the full analysis chain of the top-quark mass analysis has been followed in the μ+jets channel. The resulting correction factor from the b-jet energy regression is calculated and the kinematic fit is performed with the reconstructed b-jet four-vectors scaled by the BJER correction factor.

As a consequence of the application of the BJER, the number of correct permutations passing the fit probability cut increases by 2.5% and the fraction of correct permutations improves slightly from 41.7% to 42%. In addition, the top-quark mass resolution is expected to improve. The impact on the $m_{\mathrm{t}}^{\mathrm{fit}}$-distribution is shown in Figure 8.3(a)-(c) splitted up by permutation types. For the correct permutation type, the resolution as indicated by a Gaussian fit to the peak region is improved by 10% similar to the improvement observed in Chapter 7. For all permutation types, the mean of the distribution is shifted to higher masses. This behavior is caused by the BJER correction factor which amounts to $\approx +10\%$ at low p_{T} closely linked to the particular b-jet p_{T} spectrum in the analysis as discussed in Section 7.5.3. This shift is also visible in Figure 8.3(d)-(f) where the fitted b-jet p_{T} is shown.

The observed shifts necessitate the rederivation of templates and an updated calibration of the ideogram method using pseudoexperiments to derive final results. The determination of relevant systematic uncertainties directly linked to the uncertainties on the b-jet energy scale is also redone in order to evaluate possible changes to the uncertainties due to the application of the BJER.

8.2.1. Determination of probability density functions and calibration of the ideogram method

As outlined in Section 8.1, the probability density functions (PDF) are an important component of the likelihood from which m_{t} and the JSF are determined. The net upward shift of the invariant mass distribution requires a rederivation of the PDFs. These are fitted to the $m_{\mathrm{t}}^{\mathrm{fit}}$ and $m_{\mathrm{W}}^{\mathrm{reco}}$ distributions for seven different mass samples, three different JSF hypotheses, and the three different permutation types.

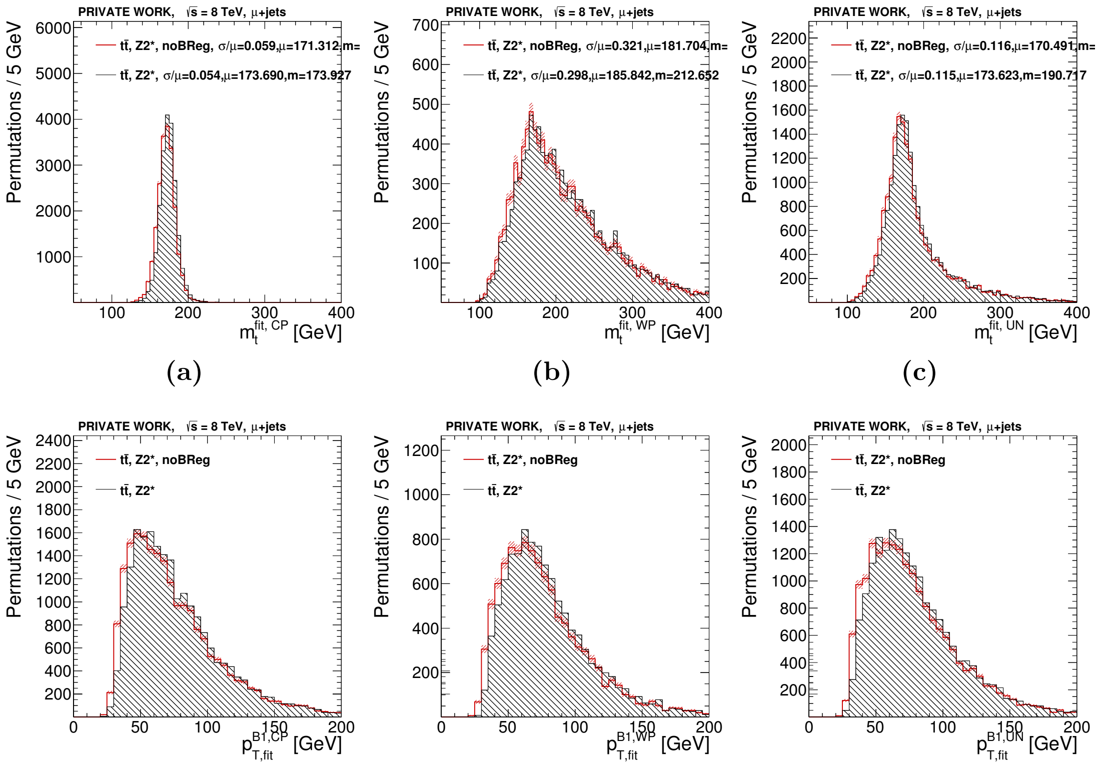

(a) **(b)** **(c)**

(d) **(e)** **(f)**

Figure 8.3.: Fitted top-quark mass distributions in MC with/without BJER for all permutations with $P_{\text{gof}} > 0.2$; (a): correct permutations; (b) wrong permutations; (c) unmatched.
Fitted b-jet p_{T} in MC with/without BJER for all permutations with $P_{\text{gof}} > 0.2$; (d): correct permutations; (e) wrong permutations; (f) unmatched.

For the $m_{\mathrm{t}}^{\mathrm{fit}}$ PDFs, the wrong permutation distribution is fitted by a Voigt profile, the correct and unmatched distributions are described by a crystal ball function. For the $m_{\mathrm{W}}^{\mathrm{reco}}$ PDFs, the distributions are fitted by asymmetric Gauss functions. In Figure 8.4, the distributions and fits are shown for the different permutation types for representative JSF and $m_{\mathrm{t}}^{\mathrm{gen}}$ variations. As expected, the $m_{\mathrm{t}}^{\mathrm{fit}}$ and $m_{\mathrm{W}}^{\mathrm{reco}}$ distributions after applying the b-jet energy regression can be approximated by the standard parameterizations.

In order to obtain continuous PDFs, the fit parameters themselves are parameterized linearly as a function of JSF and $m_{\mathrm{t}}^{\mathrm{gen}}$.

Following the analysis procedure of the nominal top-quark mass analysis, a calibration is done to correct for residual biases. About 10000 pseudoexperiments per $m_{\mathrm{t}}^{\mathrm{gen}}$/JSF variation are performed and the extracted values of m_{t} and the JSF to the input $m_{\mathrm{t}}^{\mathrm{gen}}$/JSF are evaluated. The resulting very small biases are depicted in Figure 8.5.(a). A bias correction depending linearly on m_{t}, JSF, and the product of m_{t} and JSF is fitted for m_{t} and JSF. After applying this bias correction and repeating the pseudoexperiments, a very good closure is observed as shown in Figure 8.5.(b) and the existing analysis framework can be used to compare the results before/after applying the b-jet energy regression.

8.2.2. Systematic uncertainties with/without b-regression

In order to evaluate changes in the systematic uncertainties due to the application of the b-jet energy regression, the b-JES related systematic uncertainties considered in Section 7.4 have been evaluated in the framework of the full top-quark mass analysis.

The resulting shifts for both analysis variants are listed in Table 8.1. It should be noted that the comparison between the POWHEG samples either interfaced with PYTHIA or HERWIG is only considered as a cross-check in the main analysis and the changes are not explicitly limited to the b-jet modeling. However, for the b-jet response a significant improvement was observed using the BJER in Section 7.4. The application of the BJER results in significantly reduced differences between PYTHIA and HERWIG in the full mass analysis.

As expected from the discussion in Section 7.4, the uncertainty due to semileptonic B-hadron decays is significantly reduced while the shift due to the imperfect modeling of the b-fragmentation is slightly increased.

In the 2D mass measurement with a floating JSF as well as in the 1D mass measurement with the JSF fixed to 1, significant improvements are observed: Quadratically adding up the three uncertainty sources would result in 2D mass uncertainties of 0.60 GeV vs. 0.30 GeV (with regression) and 1D mass uncertainties of 0.61 GeV vs. 0.21 GeV (with regression). In addition to the variations considered here, a larger set of uncertainties considered for the nominal top-quark mass analysis has been evaluated. Those results are quoted in Appendix D.1 and the observed shifts generally agree for both analysis variants within statistical uncertainties.

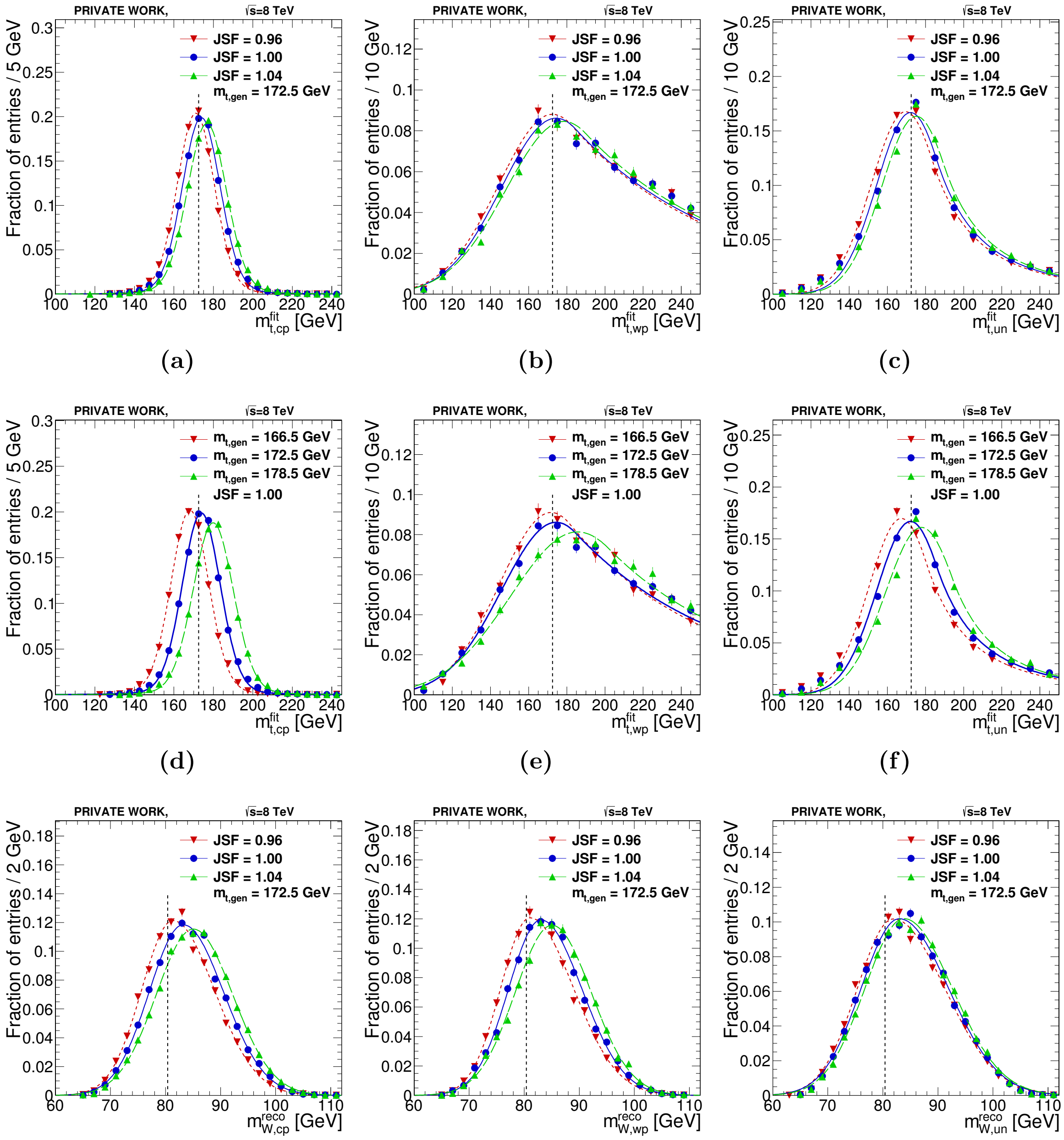

(a) (b) (c)

(d) (e) (f)

(g) (h) (i)

Figure 8.4.: (a-h) Distributions of $m_{\mathrm{t}}^{\mathrm{fit}}$ for mass and JSF variations and $m_{\mathrm{W}}^{\mathrm{reco}}$ for JSF variations for correct, wrong, and unmatched permutations.

Table 8.1.: List of systematic shifts considered as b-JES uncertainties in Section 7.4 for the muon+jets final states with/without applying the b-jet energy regression for the 2D-mass [GeV], the resulting JSF, and the resulting 1D-mass [GeV] (ideogram method with only m_t as free fit parameter and JSF fixed to 1). For statistically independent sample comparisons, the statistical uncertainties of the shift evaluation are quoted.

Uncertainty name	2D mass	JSF	1D mass
main analysis			
Powheg+Pythia6 vs. Powheg+Herwig6	0.58 ± 0.22	0.000 ± 0.002	0.59 ± 0.14
- shift	-0.58	-0.000	-0.59
Semi-leptonic B hadron decays	0.15 ± 0.00	0.000 ± 0.000	0.16 ± 0.00
- up	-0.15	-0.000	-0.16
- down	+0.09	+0.000	+0.09
b fragmentation	0.03 ± 0.00	0.001 ± 0.000	0.04 ± 0.00
- shift	+0.03	-0.001	-0.04
Quadratic sum of uncertainties	0.60	0.002	0.61
with b-jet energy regression			
Powheg+Pythia6 vs. Powheg+Herwig6	0.13 ± 0.20	0.000 ± 0.002	0.13 ± 0.13
- shift	-0.13 (0.20)	-0.000	-0.13
Semi-leptonic B hadron decays	0.05 ± 0.00	0.000 ± 0.000	0.05 ± 0.00
- up	-0.05	+0.000	-0.05
- down	+0.05	-0.000	+0.05
b fragmentation	0.19 ± 0.00	0.000 ± 0.000	0.15 ± 0.00
- shift	+0.19	-0.000	+0.15
Quadratic sum of uncertainties	0.30	0.002	0.21

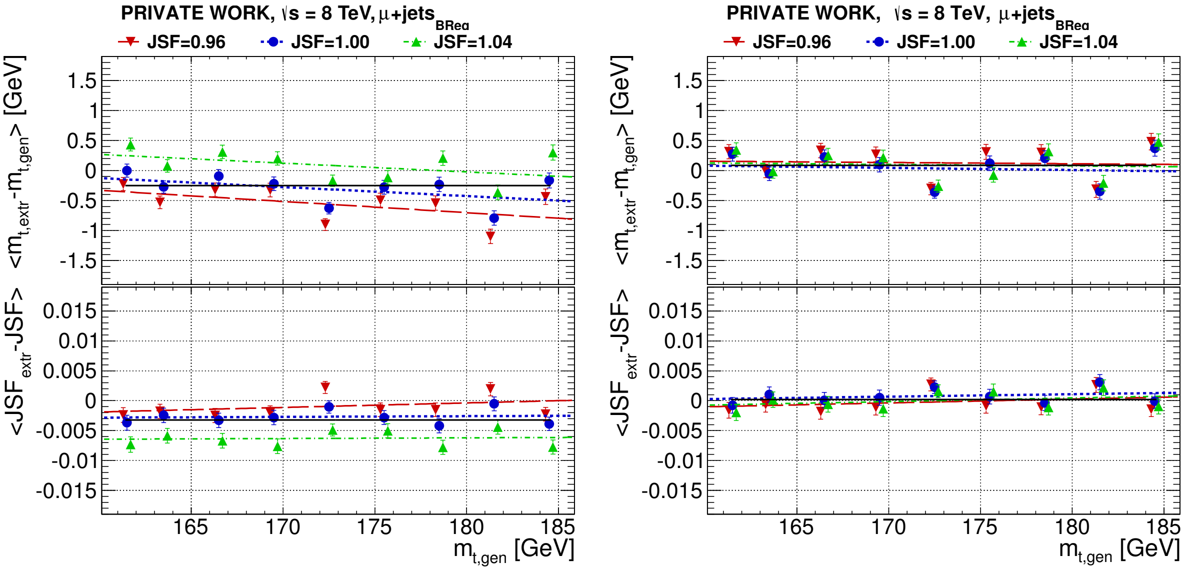

(a) (b)

Figure 8.5.: (a) Fit biases before calibration; (b) after calibration

8.3. Influence of the regression correction on $m_{\mathrm{t}}^{\mathrm{fit}}$ distribution and result on data

By applying the b-jet energy regression to the full top-quark mass analysis, an increased statistical sensitivity of the analysis due to an improved $m_{\mathrm{t}}^{\mathrm{fit}}$ resolution and potentially lowered systematic uncertainties linked to the b-JES were envisaged. An increased statistical sensitivity has been achieved as illustrated in Figure 8.6 by comparing the fitted top-quark mass distributions before/after applying the b-jet energy regression and by comparing the expected statistical uncertainty on the 2D mass result by performing pseudoexperiments. The statistical sensitivity can be improved by about 10 %.

The improved statistical precision is also observed in data: The $m_{\mathrm{t}}^{\mathrm{fit}}$ distribution is shown in Figure 8.7(a)-(b) which compares the distributions in data and MC with/without applying the b-jet energy regression. The resolution improvement of $m_{\mathrm{t}}^{\mathrm{fit}}$ can be ascertained by the increased number of events in the peak region for both, data and MC. The Data/MC comparison of the b-jet p_{T} in Figure 8.7(c)-(d) shows a good agreement before and after applying the BJER. The improvement in the $m_{\mathrm{t}}^{\mathrm{fit}}$ distribution of about 10 % is also ascertained when evaluating the top-quark mass and JSF using the full ideogram method:

$$\mu\text{+jets: } m_{\mathrm{t}} = 171.92 \pm 0.26\,(\text{stat.+JSF}); \quad \text{JSF} = 1.016 \pm 0.002\,(\text{stat.})$$
$$\mu\text{+jets (BReg): } m_{\mathrm{t}} = 172.19 \pm 0.24\,(\text{stat.+JSF}); \quad \text{JSF} = 1.017 \pm 0.002\,(\text{stat.})$$

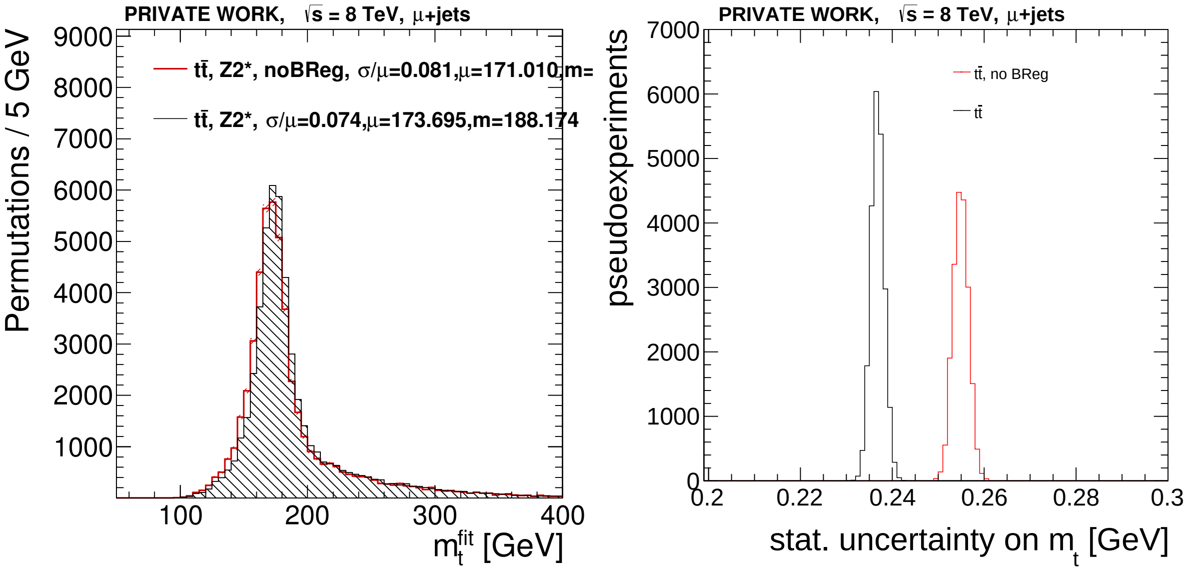

(a) (b)

Figure 8.6.: (a): Fitted top-quark mass distribution in MC with/without b-regression for all permutations with $P_{\text{gof}} > 0.2$; (b): Statistical uncertainty expected for the 2D mass determination from pseudoexperiments with/without b-regression.

This evaluation gives consistent results for the nominal and the BJER-supplemented analysis with slightly improved statistical precision when applying the BJER.

The possible gains in the total systematic uncertainty of the top-quark mass measurement are less straight forward to judge and there is always a tradeoff when introducing another step to the analysis chain: While the b-jet energy regression could potentially reduce the b-JES related uncertainties it is itself a rather complex procedure and could affect seemingly uncorrelated parts of the analysis, necessitating to weigh up the potential gain against the increased complexity.

In comparison to the 7 TeV analysis, improvements have been made regarding the determination of flavor-specific JES uncertainties. The evaluation of systematic uncertainties equivalent to the 2011 b-JES uncertainty (varying the b-jet response by the generic CMS flavor uncertainty) would result in an uncertainty of about 0.59 GeV.

In the preliminary result of the nominal analysis, the transverse momenta of the b-jets are scaled by the uncertainties provided for b-jets (based on a PYTHIA/HERWIG++ comparison in QCD events and the in-situ response from γ+jet, Z+jet, and dijet events, partially based on studies performed during the course of this thesis as discussed in Section 4.5.5). In addition, the variation of the semileptonic B-hadron decay fractions and the b-fragmentation as discussed in Section 8.2.2 are evaluated. If these three variations are summed up quadratically, this corresponds to a systematic uncertainty of about 0.35 GeV. Adding the additionally introduced variations of the gluon response and the udsc-quark response yields an uncertainty of 0.49 GeV. This means that the systematic

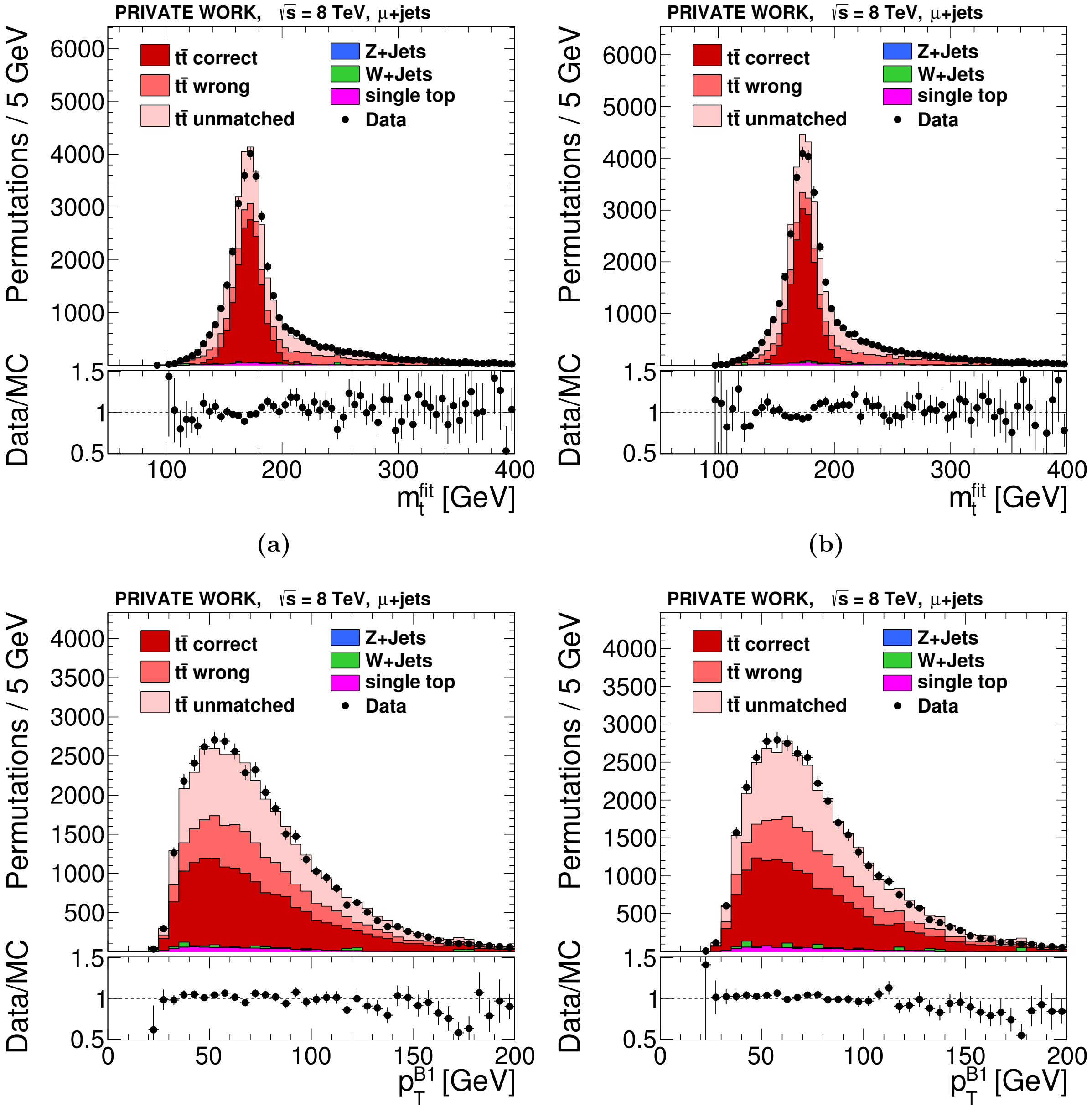

(a)

(b)

(c)

(d)

Figure 8.7.: Fitted top-quark mass distribution with(b)/without(a) b-regression for all permutations with $P_{\text{gof}} > 0.2$; fitted hadronic leg b-jet p_{T} distribution with(d)/without(c) b-regression for all permutations with $P_{\text{gof}} > 0.2$

uncertainties directly related to the b-JES could already be reduced by adopting a more detailed evaluation of systematic uncertainties.

Nevertheless, the evaluation of PYTHIA/HERWIG differences directly in $t\bar{t}$ events as performed in Section 7.4 can provide a further improved estimate of the uncertainty. The evaluation of the systematic uncertainties in the way proposed in Section 8.2.2 leads to b-JES related systematic uncertainties of 0.60 GeV without applying the BJER and 0.30 GeV with applying the BJER, i.e. a 50% reduction for this subset of uncertainties.

Due to the improved procedure in the nominal analysis, the potential gains for the b-JES systematic uncertainty are somewhat smaller than anticipated from the 7 TeV analysis. However, due to the full integration of the b-jet energy regression into the analysis framework shared by the University of Hamburg CMS group, it will be possible to compare the resulting total uncertainties with/without applying the regression presented here or a further improved iteration of the correction. Based on the outcome it could prove beneficial to implement the b-jet energy regression as default for future analyses of the top-quark mass at CMS.

Chapter 9

Conclusions and outlook

A cornerstone of the factorized jet-energy corrections at CMS are corrections based on simulated events covering the full phase space of jet occurences. Data-driven techniques are used to validate the jet-energy scale and to derive residual corrections compensating for any observed differences in the response between data and simulation. With cross sections significantly higher than those of Z+jet and γ+jet events, QCD-dijet events are an exquisite choice for a highly granular calibration of the jet-energy scale as a function of η relative to the central detector region. Despite the lack of an excellent-resolution reference object such as a Z boson or photon, they are a well-suited tool for this purpose reaching up to very high p_{T}.

In this thesis, the calibration using dijet events has been discussed in detail. Two complementary methods to determine the response have been used: The first method is the traditional p_{T} balance method that directly relates the p_{T} of a central and a forward jet to determine the response of the forward jet relative to the central jet. The second, the Missing Transverse Energy Projection Fraction (MPF) method, has been applied to dijet events at CMS for the first time in the course of this thesis. Due to the usage of $\vec{E}_{\mathrm{T}}^{\mathrm{miss}}$ to infer the response of forward jets it provides complementary results and is less succeptible to the radiation of additional jets.

Slight differences in the response observed in the comparison of data and simulations are compensated for by using MC/Data-ratios of the response estimator of both methods, corrected for the effect of additional event activity, to determine correction factors. These residual corrections have been continuously updated and provided centrally to the collaboration during the 2011 and early 2012 run in the course of this thesis. Cross-checks of the 2010 corrections using the p_{T} balance method are published in [133], the results for the 2011 calibration are publicly documented in [134, 148].

The residual corrections are generally below 2-3% in the detector region up to $|\eta| < 2$. The largest corrections have been ascertained in the endcap and forward region and at the boundaries between these regions at $|\eta| \approx 3$, reaching up to 20%. In the most forward regions, the statistical uncertainties of the measurement get large due to relatively high p_{T} thresholds for the dijet triggers, resulting in a lack of low p_{T} events. Systematic uncertainties related to the determination of the residual corrections have been found to be below 1% in the detector region up to $|\eta| < 2.5$ and of the order of 3% in the forward detector region. This is comparable to the precision achieved by ATLAS and D0 with their latest calibrations.

With the high number of dijet events in the region up to $|\eta| < 3$, detailed studies of the time stability of the jet-energy scale, considered as an additional systematic uncertainty on the jet-energy scale in 2011 and 2012, and even a highly-granular scan of the response on the level of single calorimeter cells could be performed. These studies of high-level objects like jets can and should be used to improve the calibration of the individual detector components. The analysis of the composition of jets in terms of Particle Flow candidates in dijet and other topologies can provide important insights in this context.

In the upcoming LHC run, the analysis of dijet events will remain an important area of study. However, due to the high instantaneous luminosities and resulting trigger limitations, the bulk of collected events will be at very high p_{T}. This will complicate the derivation of residual corrections in the forward region and precautions like dedicated central-forward triggers should be taken. An alternative interesting approach is that of the "matrix method" introduced by ATLAS, moderately improving the statistical precision at high $|\eta|$ by extending the reference region for the calibration of very forward jets.

The precise calibration of the jet-energy scale at HEP experiments is of utmost importance to the success of physics analyses with jets in their final state. Even for analyses not directly interested in jets, the ubiquity of jets in the high pileup environment of the LHC makes it almost impossible to avoid them. Actually, the continuously improved understanding of these signatures of quarks and gluons can help to make discoveries in the uncharted phase space now probed by the LHC.

Efforts to understand the correlations of jet-energy scale uncertainties among different experiments are an important prerequisite for optimal combinations of precision measurements with significant influence of such uncertainties. Even though ATLAS and CMS use different jet types, ATLAS using calorimeter based jets, CMS adopting the Particle Flow approach, the performance and calibration procedure is quite comparable at both experiments. The discussions among ATLAS and CMS summarized in this thesis and publicly documented in [172] have been used in combinations of measurements such as the top-quark mass [69]. They are a valuable starting point for further discussions on the correlations between ATLAS and CMS and triggered ideas for improvements of the calibration procedure in both collaborations, e.g. to consider an extrapolation to zero additional event activity in the ATLAS dijet analysis and to perform a p_{T}-dependent combination of different channels to derive the absolute scale in the central detector region in CMS.

Besides jet cross section measurements, top-quark mass measurements are a prime example of analyses particularly sensitive to uncertainties on the jet-energy scale. With constraints on the W mass widely used in measurements of the top-quark mass to reduce the bulk of these uncertainties, remaining systematic uncertainties related to the jet-energy scale of b-jets have become dominant.

A study of the description of b-jet properties in $\mathrm{t\bar{t}}$ events has been performed using 2012 data and shows a good description by simulation for most observables. In order to improve the reconstruction of b-jets relevant for measurements of the top-quark mass, an additional jet-energy correction specifically tailored for b-jets has been studied. The correction exploits the correlation of various b-jet properties with the response using multivariate regression techniques to gain a more precise measurement of the b-jets in terms of energy scale and resolution. The energy resolution improves by $10-15\%$ in the typical p_{T}-range of b-jets in top-quark mass analyses.

A more detailed evaluation of systematic uncertainties of the b-JES than used for 2011 measurements has been performed for the case of applying or not applying the regression correction. For this, PYTHIA/HERWIG response differences have been considered directly in $\mathrm{t\bar{t}}$ events as well as uncertainties related to the b fragmentation and semileptonic decays of B-hadrons have been taken into account. This evaluation yields slightly improved systematic uncertainties when applying the regression correction, amounting to 0.6% instead of 0.9% at a $p_T^{\mathrm{b\,jet}}$ of 60 GeV.

The regression correction has been added to the existing measurement of the top-quark mass [5–7] at CMS in the lepton+jets channel. A comparison of the analyis in the muon+jets channel with and without applying the regression correction has shown an improved statistical sensitivity if applying the regresion correction. This 10% improvement has been a direct consequence of the better jet-energy resolution for b-jets on the resolution of the top-quark mass. For the b-JES related systematic uncertainties evaluated as proposed in Section 8.2.2, an improvement of 50% from 0.6 GeV to 0.3 GeV is found if the BJER is applied. In the evaluation of other systematic uncertainties considered for the final result, no negative impact when applying the regression has been observed.

Regression corrections, especially for b-jets, are an active field of study in CMS and other HEP experiments. Improved iterations of these corrections, will prove beneficial for many precision measurements as they offer an improved performance without the need to modify any of the detector components. This can be achieved by extending the applicability to a wide variety of event topologies, developing an analysis-independent correction.

Appendix A

MC samples used for analyses

A.1. Data Samples used for the determination of relative residual corrections

Table A.1.: The primary data sets and lists of certified luminosity blocks (*JSON-file*) used in the main (CMSSW 44X-based) analysis with the corresponding (unprescaled) integrated luminosity L.

Primary data set	JSON-file	L (fb^{-1})
`/Jet/Run2011A-08Nov2011-v1/AOD`	`Cert_160404-180252_7TeV_ReRecoNov08_Collisions11_JSON.txt`	5.013
`/Jet/Run2011B-19Nov2011-v1/AOD`	`Cert_160404-180252_7TeV_ReRecoNov08_Collisions11_JSON.txt`	(runs $\geq$ 163337)

Simulated data samples	No. of events
`/QCD_Pt-15to3000_TuneZ2_Flat_7TeV_pythia6/Fall11-PU_S6_START44_V9B-v2`	10 mio.
`/QCD_Pt-15to3000_Tune23_Flat_7TeV_herwigpp/Fall11-PU_S6_START44_V9B-v1M`	10 mio.
`/QCD_Pt-15to3000_TuneZ2_Flat_7TeV_pythia6/Fall11-NoPileUp_START44_V9B-v1`	1 mio.

Table A.2.: The primary data sets and lists of certified luminosity blocks (*JSON-file*) used in the CMSSW 42X analysis with the corresponding (unprescaled) integrated luminosity L.

Primary data set	JSON-file	L (pb^{-1})
`/Jet/Run2011A-May10ReReco_v1`	`Cert_160404-163869_7TeV_May10ReReco_Collisions11_JSON_v2.txt`	134.2 (runs $\geq$ 163337)
`/Jet/Run2011A-PromptReco_v4`	`Cert_160404-167151_7TeV_PromptReco_Collisions11_JSON.txt`	970.1
`/Jet/Run2011A-05Aug2011-v1`	`Cert_170249-172619_7TeV_ReReco5Aug_Collisions11_JSON_v3.txt`	390.6
`/Jet/Run2011A-PromptReco-v6`	`Cert_160404-180252_7TeV_PromptReco_Collisions11_JSON.txt`	706.4
`/Jet/Run2011B-PromptReco-v1`	`Cert_160404-180252_7TeV_PromptReco_Collisions11_JSON.txt`	2741
Total		4942.3

Simulated data samples	No. of events
`/QCD_Pt-15to3000_TuneZ2_Flat_7TeV_pythia6/Fall11-PU_S6_START42_V14B-v1`	10 mio.

Table A.3.: The primary data sets and lists of certified luminosity blocks (*JSON-file*) used in the 2012 analysis analysis (CMSSW 53X ReReco dataset) with the corresponding integrated luminosity L.

Primary data set	JSON-file	L (fb^{-1})
`/Jet/Run2012A-22Jan2013-v1`	`Cert_190456-208686_8TeV_22Jan2013ReReco_Collisions12_JSON.txt`	0.889
`/JetHT/Run2012B-22Jan2013-v1` `+/JetMon/Run2012B-22Jan2013-v1`	`Cert_190456-208686_8TeV_22Jan2013ReReco_Collisions12_JSON.txt`	4.429
`/JetHT/Run2012C-22Jan2013-v1` `+/JetMon/Run2012C-22Jan2013-v1`	`Cert_190456-208686_8TeV_22Jan2013ReReco_Collisions12_JSON.txt`	7.152
`/JetHT/Run2012D-22Jan2013-v1` `+/JetMon/Run2012D-22Jan2013-v1`	`Cert_190456-208686_8TeV_22Jan2013ReReco_Collisions12_JSON.txt`	7.318
Total		19.789

Simulated data samples	No. of events
`/QCD_Pt-15to3000_TuneZ2_Flat_8TeV_pythia6/Summer12_DR53X-PU_S10_START53_V7A-v1`	10 mio.

A.2. MC Samples used for the training of the b-jet energy regression

Table A.4.: The simulated data samples used for the training of the b-jet energy regression

Simulated data samples	No. of events
`/TTJets_mass161_5_TuneZ2star_8TeV-madgraph-tauola ...`	5.4 mio.
`/TTJets_mass163_5_TuneZ2star_8TeV-madgraph-tauola ...`	5.4 mio.
`/TTJets_mass166_5_TuneZ2star_8TeV-madgraph-tauola ...`	4.5 mio.
`/TTJets_mass169_5_TuneZ2star_8TeV-madgraph-tauola ...`	5.2 mio.
`/TTJets_MassiveBinDECAY_TuneZ2star_8TeV-madgraph-tauola ...`	7.0 mio.
`/TTJets_mass175_5_TuneZ2star_8TeV-madgraph-tauola ...`	5.2 mio.
`/TTJets_mass178_5_TuneZ2star_8TeV-madgraph-tauola ...`	4.7 mio.
`/TTJets_mass181_5_TuneZ2star_8TeV-madgraph-tauola ...`	5.1 mio.
`/TTJets_mass184_5_TuneZ2star_8TeV-madgraph-tauola ...`	5.2 mio.
`... /Summer12_DR53X-PU_S10_START53_V7A-v1`	
Total	47.7 mio.

Appendix B

Control distributions of basic quantities and response estimator mean values in all considered $|\eta|$ bins for the dijet analysis

In Section B.1, control distributions of various quantitites in the dijet analysis are shown. They are compiled for the datasets listed in Table A.1.

In Figure B.1, the distributions are shown before and after the main selection cuts on $\Delta\varphi$ and $p_{\mathrm{T}}^{\mathrm{rel}}$. In Figure B.2, the distributions are compared after the $\Delta\varphi$ and after both cuts. In Figure B.3, the distributions are compared after the $p_{\mathrm{T}}^{\mathrm{rel}}$ and after both cuts.

The distributions before/after the pileup reweighting of the simulation are shown in Figure B.4. Control distributions after the selection cuts comparing PYTHIA and HERWIG++ are shown in Figure B.5. The resulting control distributions of the jet-energy resolution study are shown in Figure B.6.

All observables are shown once with a linear and once with a logarithmic y-axis. The list of obervables evaluated for the control plots includes:

- $\Delta\varphi$ between the two leading jets
- $p_{\mathrm{T}}^{\mathrm{rel}}$, the relative p_{T} of the third jet compared to the two leading jets
- p_{T}^{probe}, the transverse momentum of the probe jet
- p_{T}^{barrel}, the transverse momentum of the barrel jet
- p_{T,j_3}, the transverse momentum of the third jet
- $\overline{p}_{\mathrm{T}}$, the average transverse momentum of the two leading jets
- the number of reconstructed vertices in two p_{T}-ranges, where the lower edge corresponds to the 99% efficiency thresholds of the `HLT_DiJetAve60` and `HLT_DiJetAve300` triggers.

- the $|\eta|$ spectrum in the above p_{T}-ranges
- $\overline{p}_{\mathrm{T}}$ in two $|\eta|$ bins (not inclusive in η as above)
- $\mathcal{R}_{\mathrm{MPF}}$ and $\mathcal{R}_{\mathrm{rel}}$ distributions in two $|\eta|$ bins and two p_{T}-ranges for each $|\eta|$ bin.

In Section B.2, individual plots related to the relative response method are shown in all $|\eta|$ bins. These are

- the mean values of the relative response
- the k_{rad} extrapolations
- the p_{T}-dependence of the Data/MC-ratios of the relative response
- the p_{T}-dependence of the extrapolated Data/MC-ratios of the relative response, corresponding to the k_{rad} extrapolation.

Section B.3 shows the corresponding plots for the MPF method. In Section B.4, the dependence of the relative Data/MC ratios of the relative respnse and the MPF response on $p_{\mathrm{T}}^{\mathrm{rel}}$ are compared for using either PYTHIA or HERWIG++ as reference MC.

B.1. Control distributions

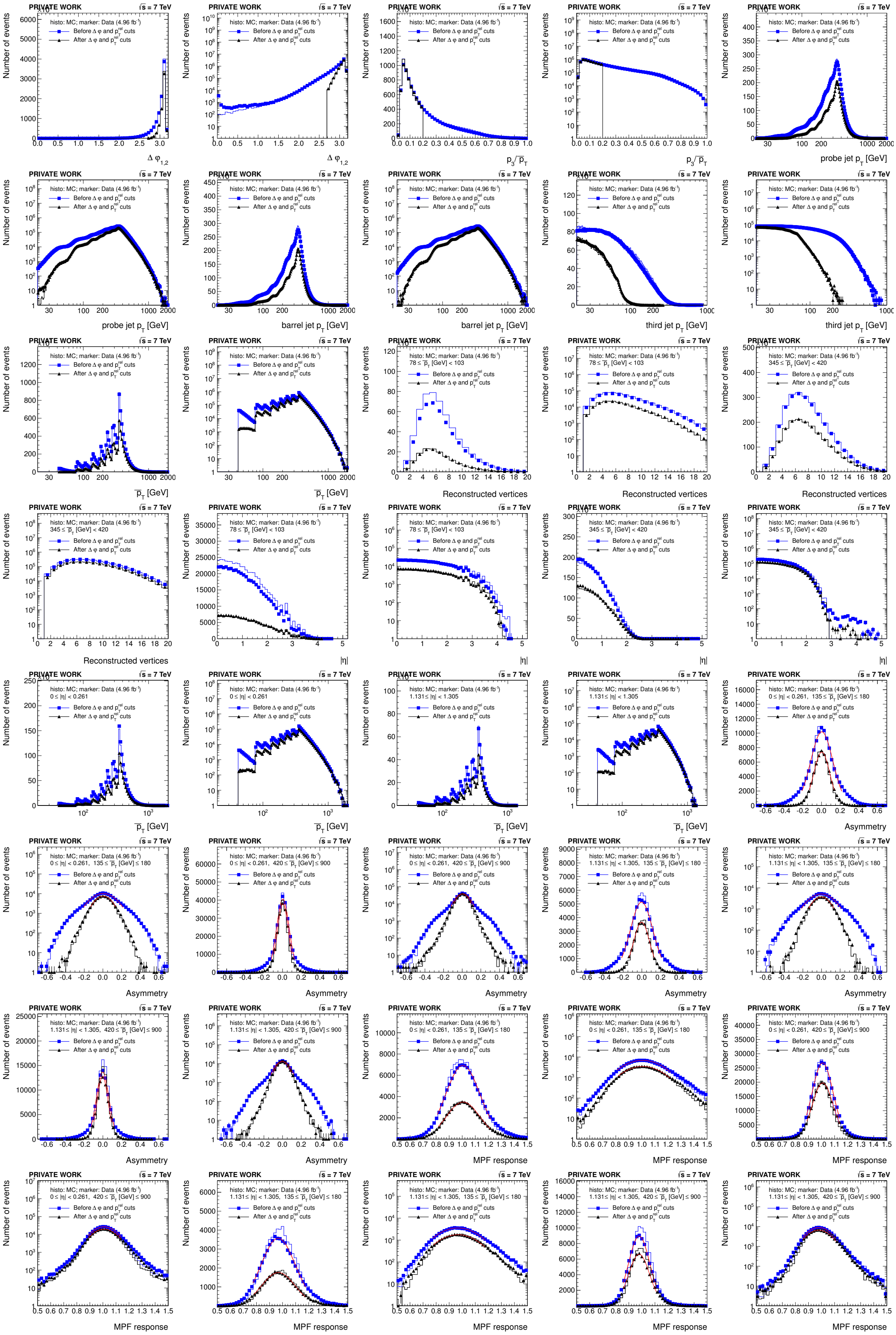

Figure B.1.: Various control plots comparing distibutions in data and MC "Before $\Delta\varphi$ and p_T^{rel} cuts" and "After $\Delta\varphi$ and p_T^{rel} cuts".

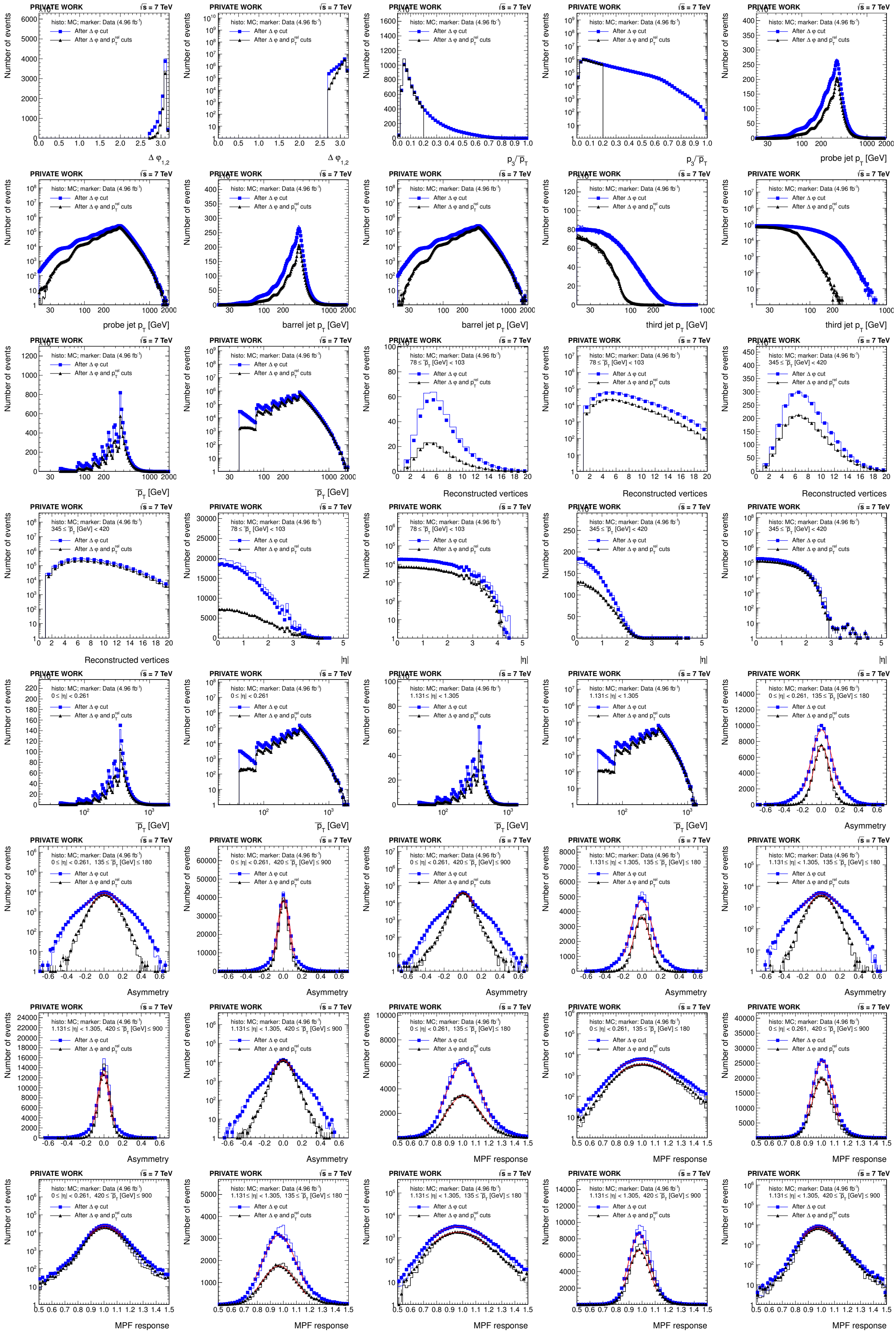

Figure B.2.: Various control plots comparing distibutions in data and MC "After $\Delta\varphi$ cut" and "After $\Delta\varphi$ and p_T^{rel} cuts".

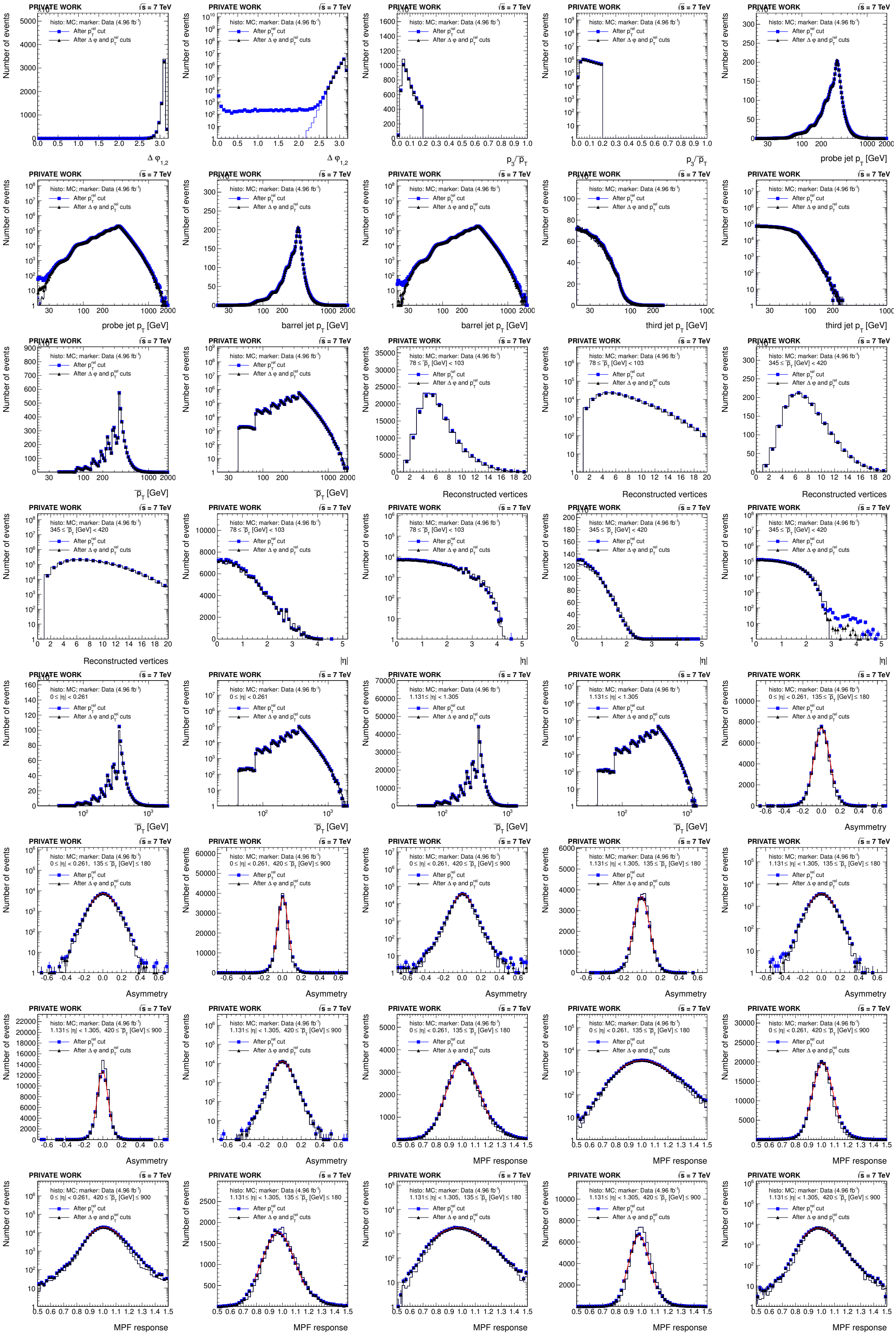

Figure B.3.: Various control plots comparing distibutions in data and MC "After p_T^{rel} cut" and "After $\Delta\varphi$ and p_T^{rel} cuts".

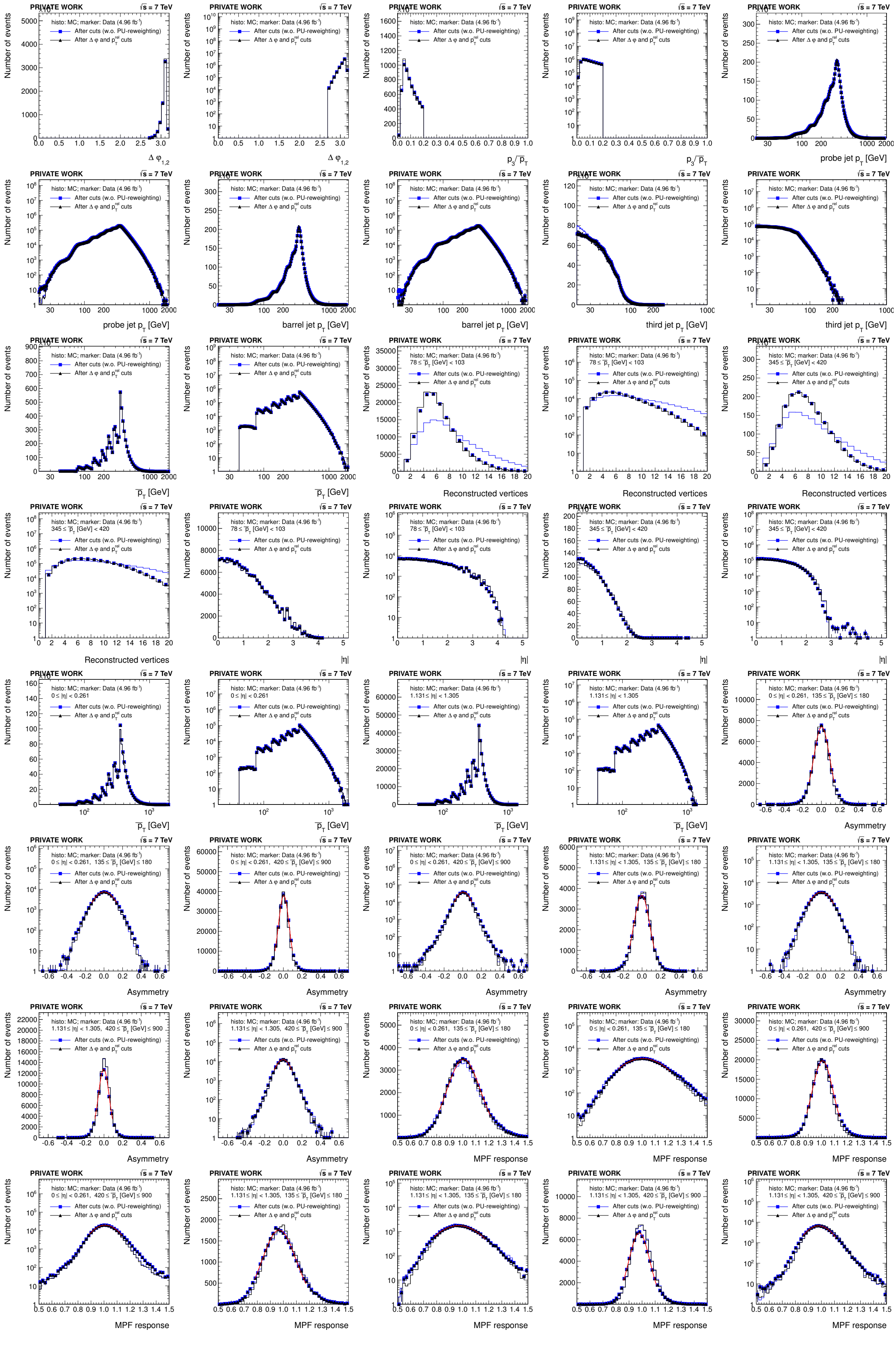

Figure B.4.: Various control plots comparing distibutions in data and MC "After cuts (w.o. PU-reweighting)" and "After $\Delta\varphi$ and p_T^{rel} cuts".

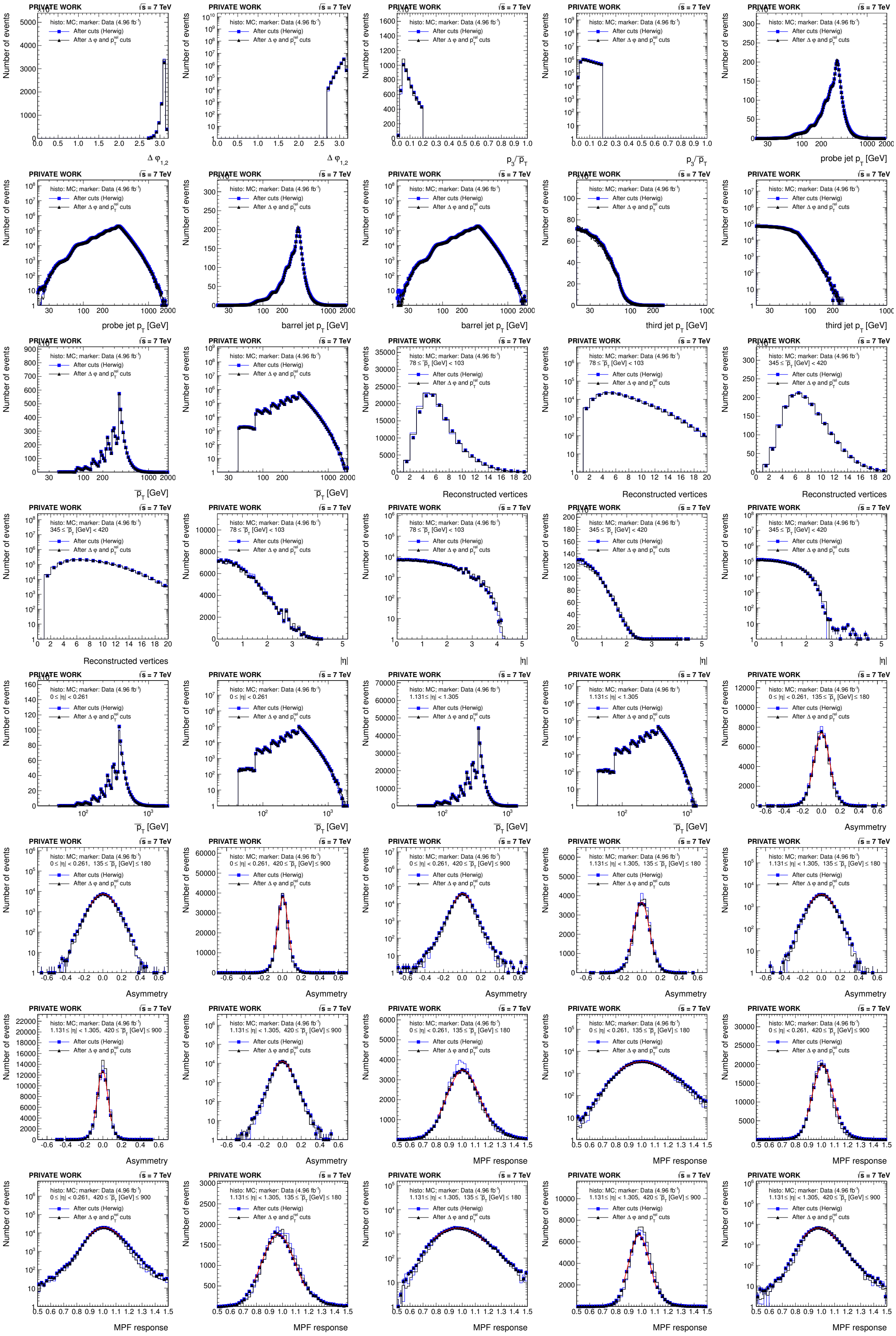

Figure B.5.: Various control plots comparing distibutions in data and MC "After cuts (Herwig)" and "After $\Delta\varphi$ and p_T^{rel} cuts".

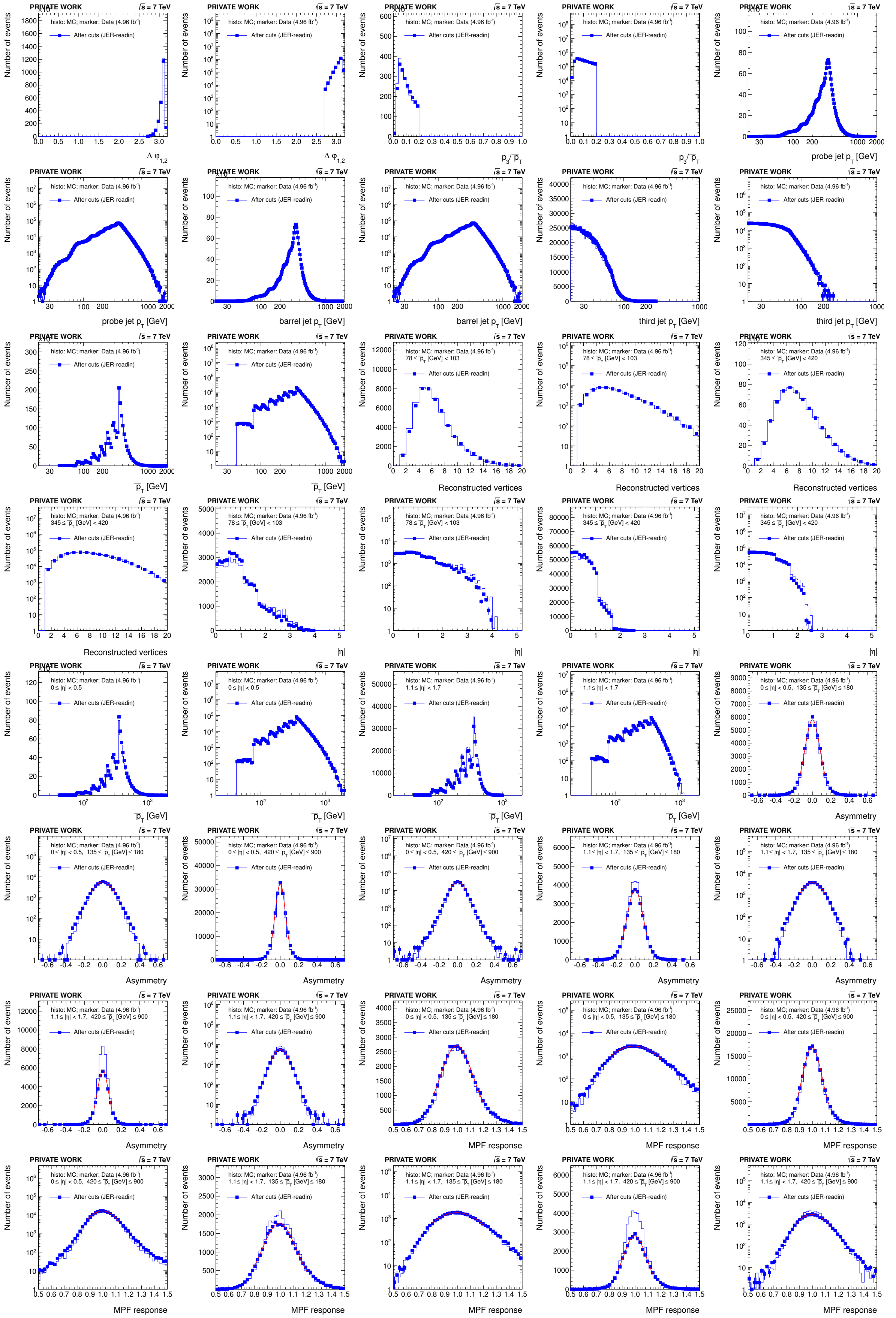

Figure B.6.: Various control plots comparing distibutions in data and MC "After cuts (JER-readin)" and "After cuts (JER-readin)".

B.2. Relative response plots in all $|\eta|$ bins

B.2.1. k_{rad} extrapolations

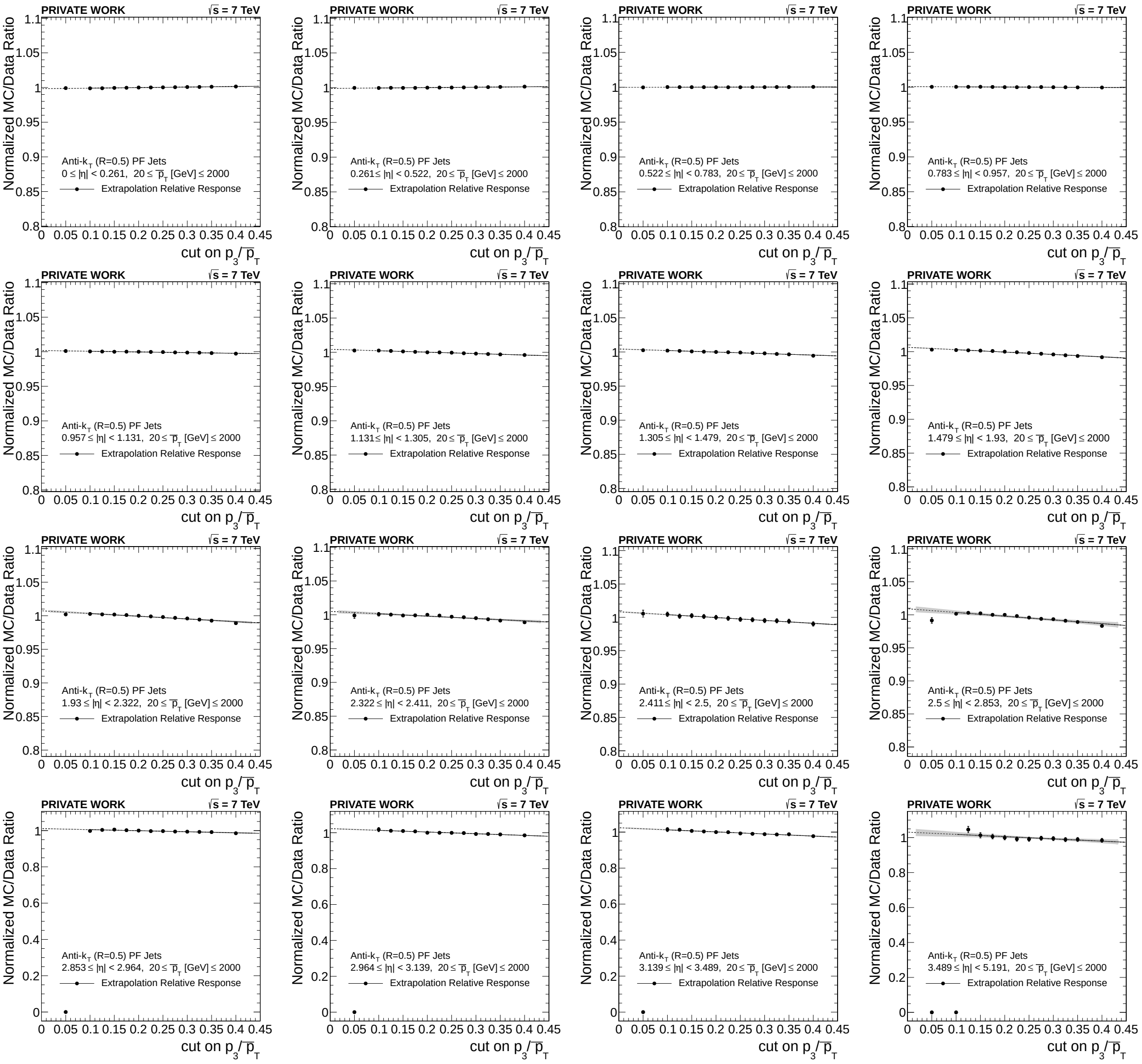

B.2.2. Mean values of the relative response

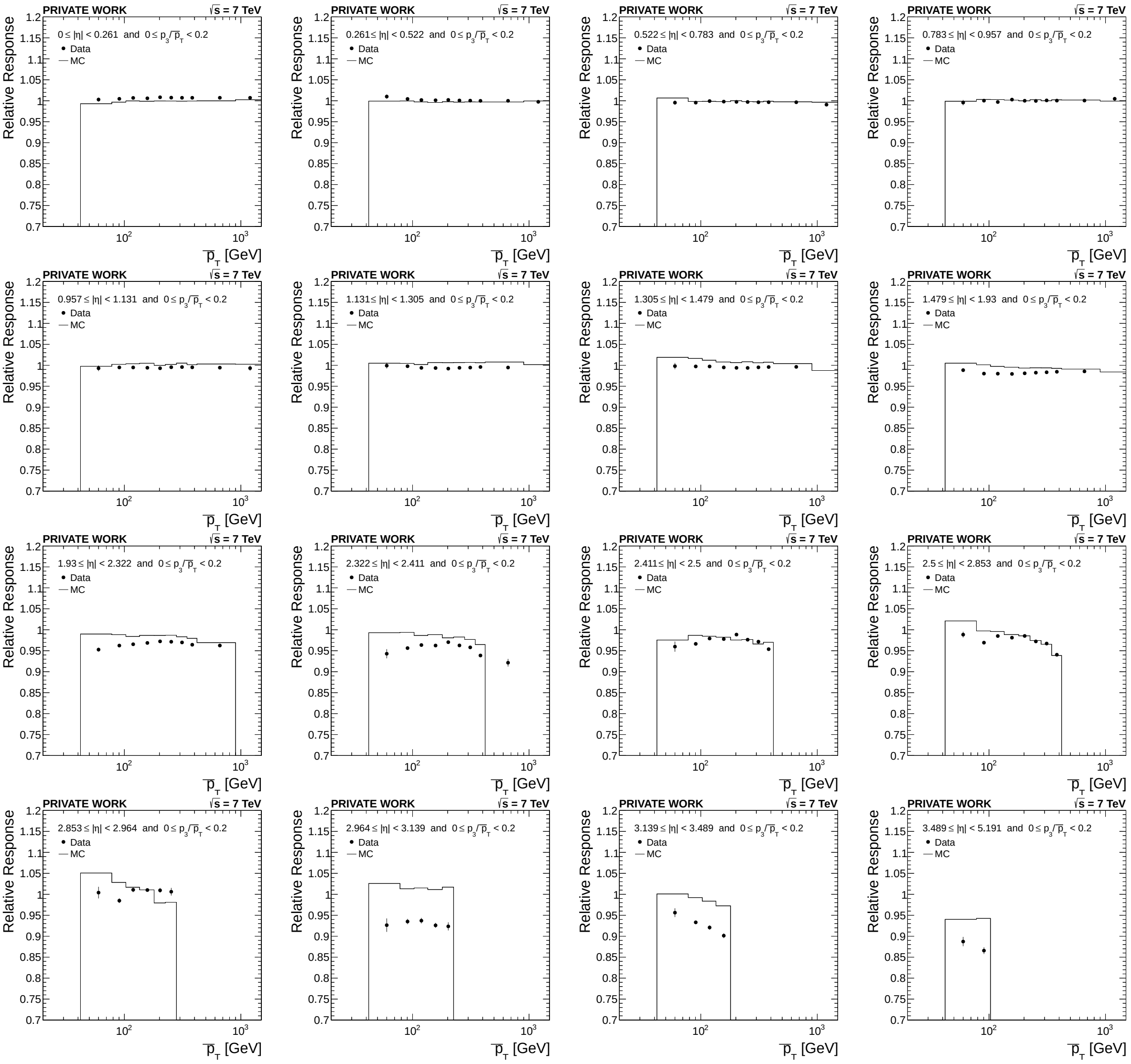

B.2.3. p_T-dependence of the Data/MC ratio of the relative response

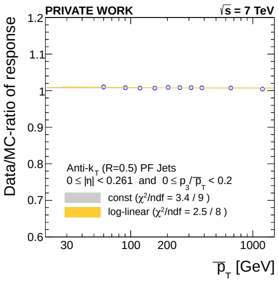

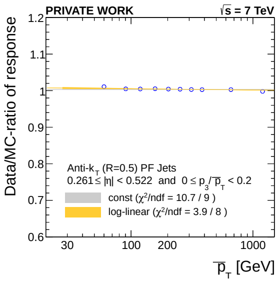

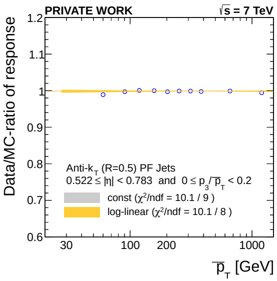

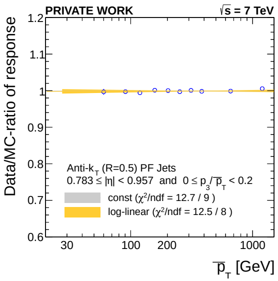

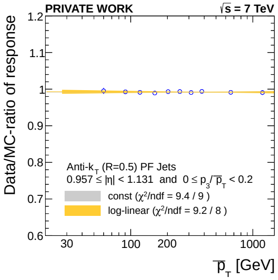

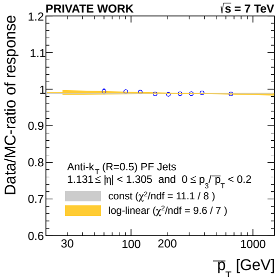

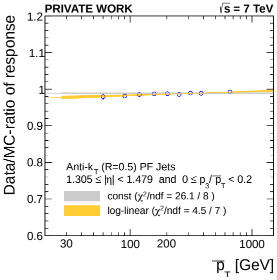

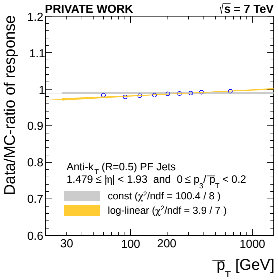

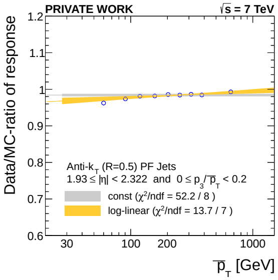

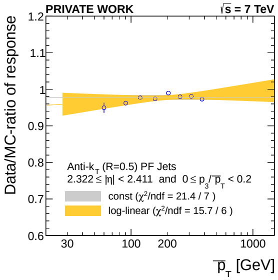

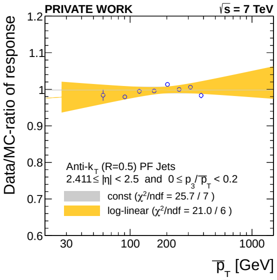

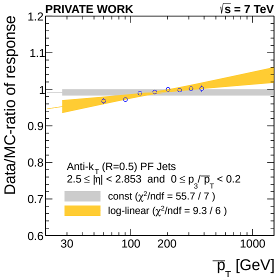

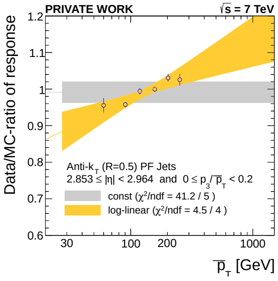

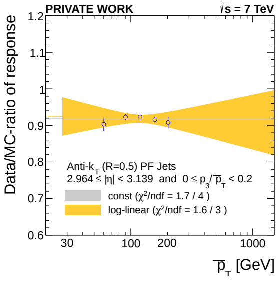

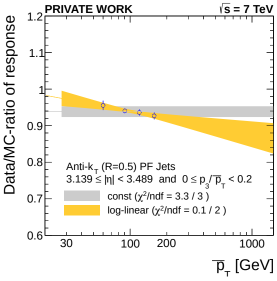

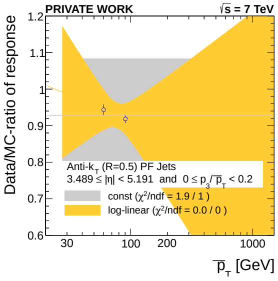

B.2.4. p_{T}-dependence of the k_{rad} correction for the relative response

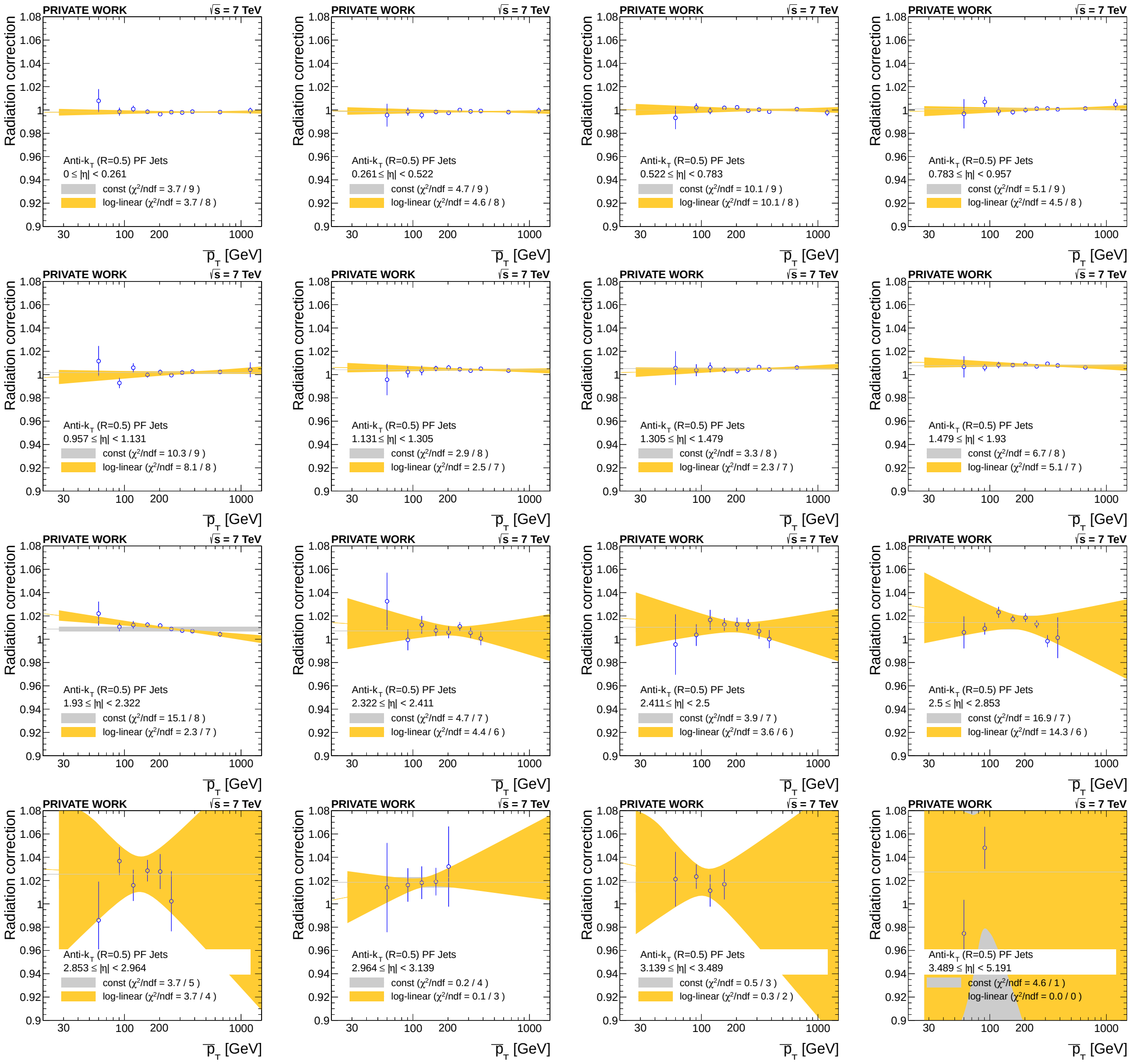

B.3. MPF response plots in all $|\eta|$ bins

B.3.1. k_{rad} extrapolations

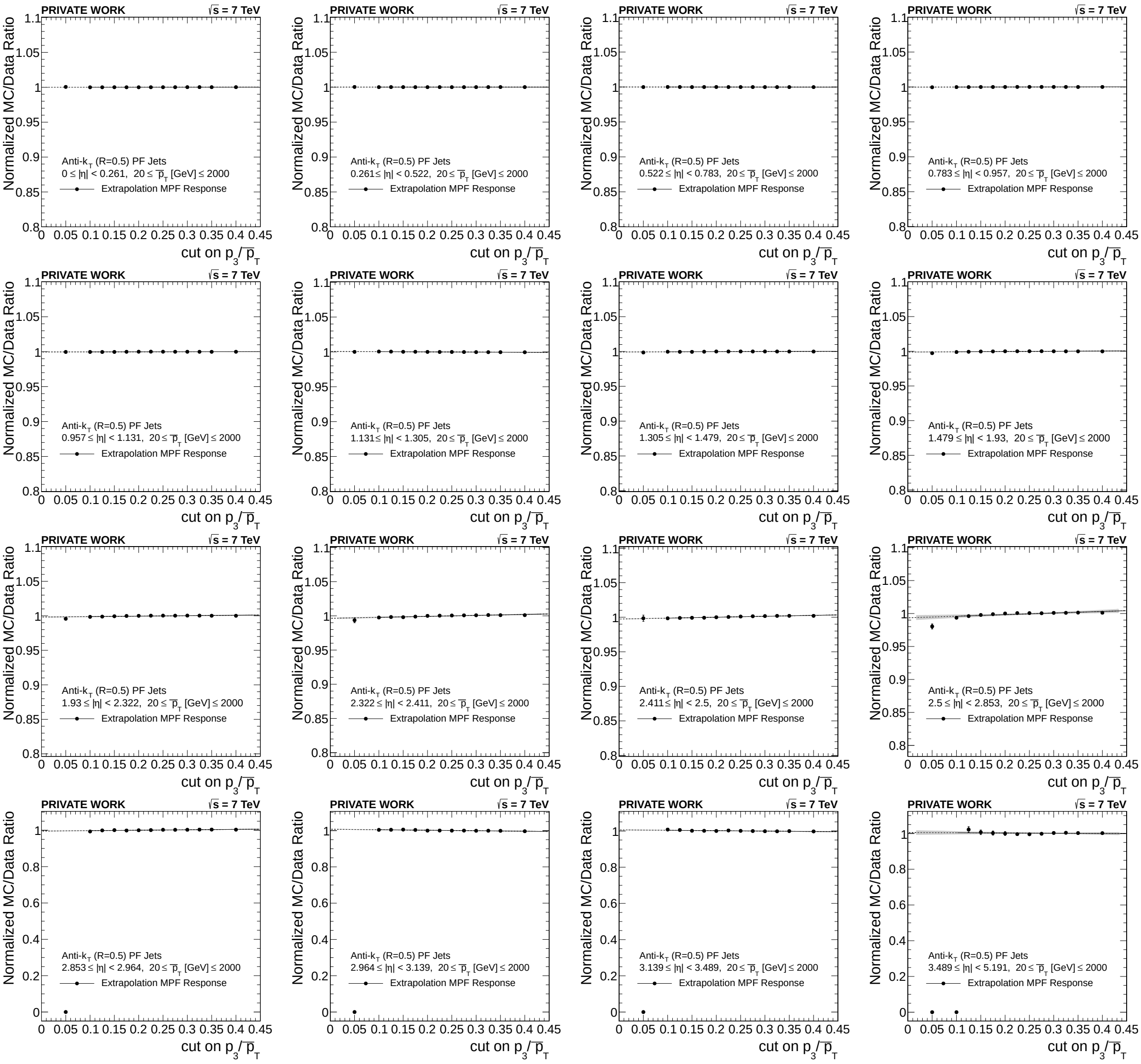

B.3.2. Mean values of the MPF response

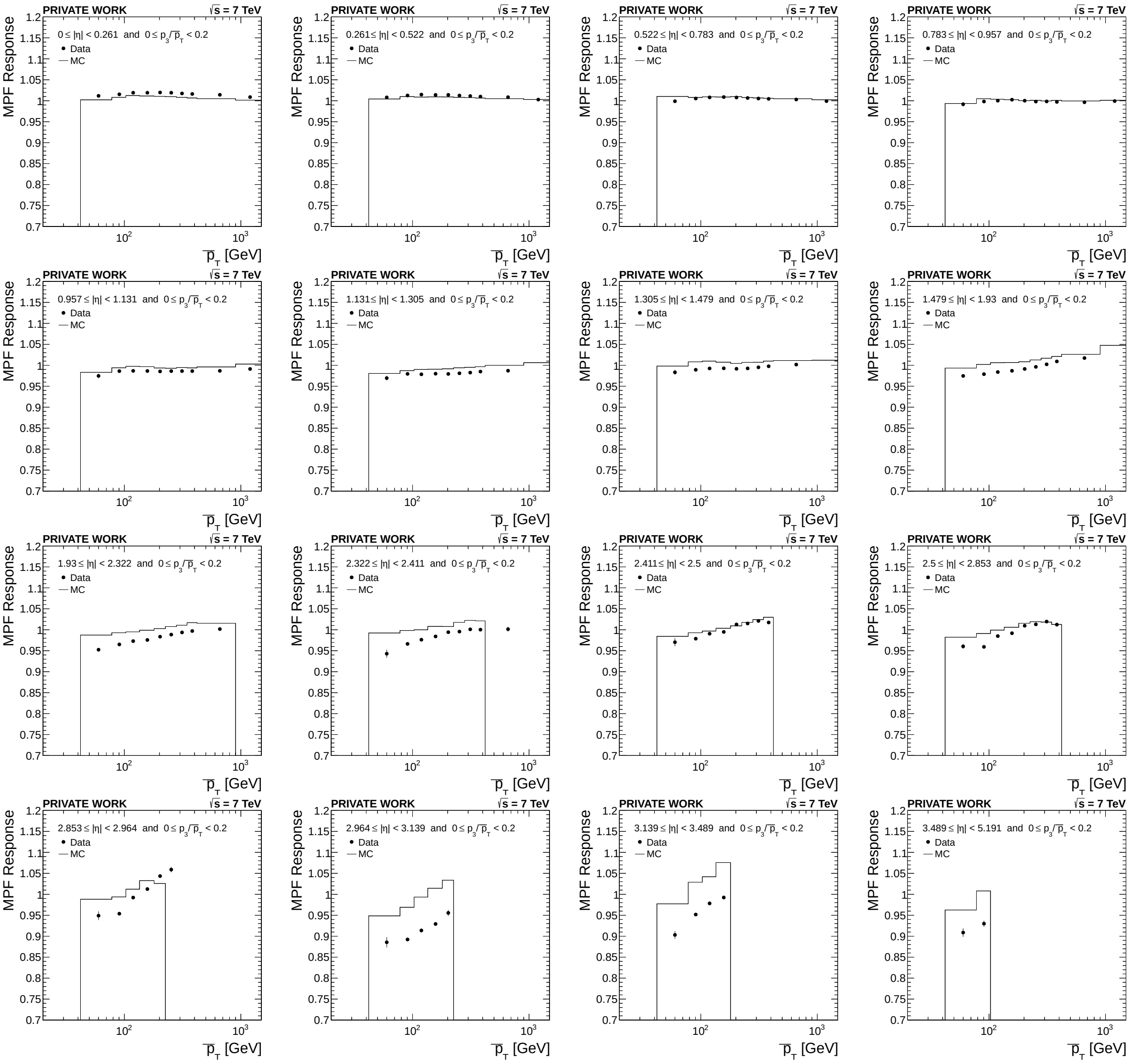

B.3.3. p_{T}-dependence of the Data/MC ratio of the MPF response

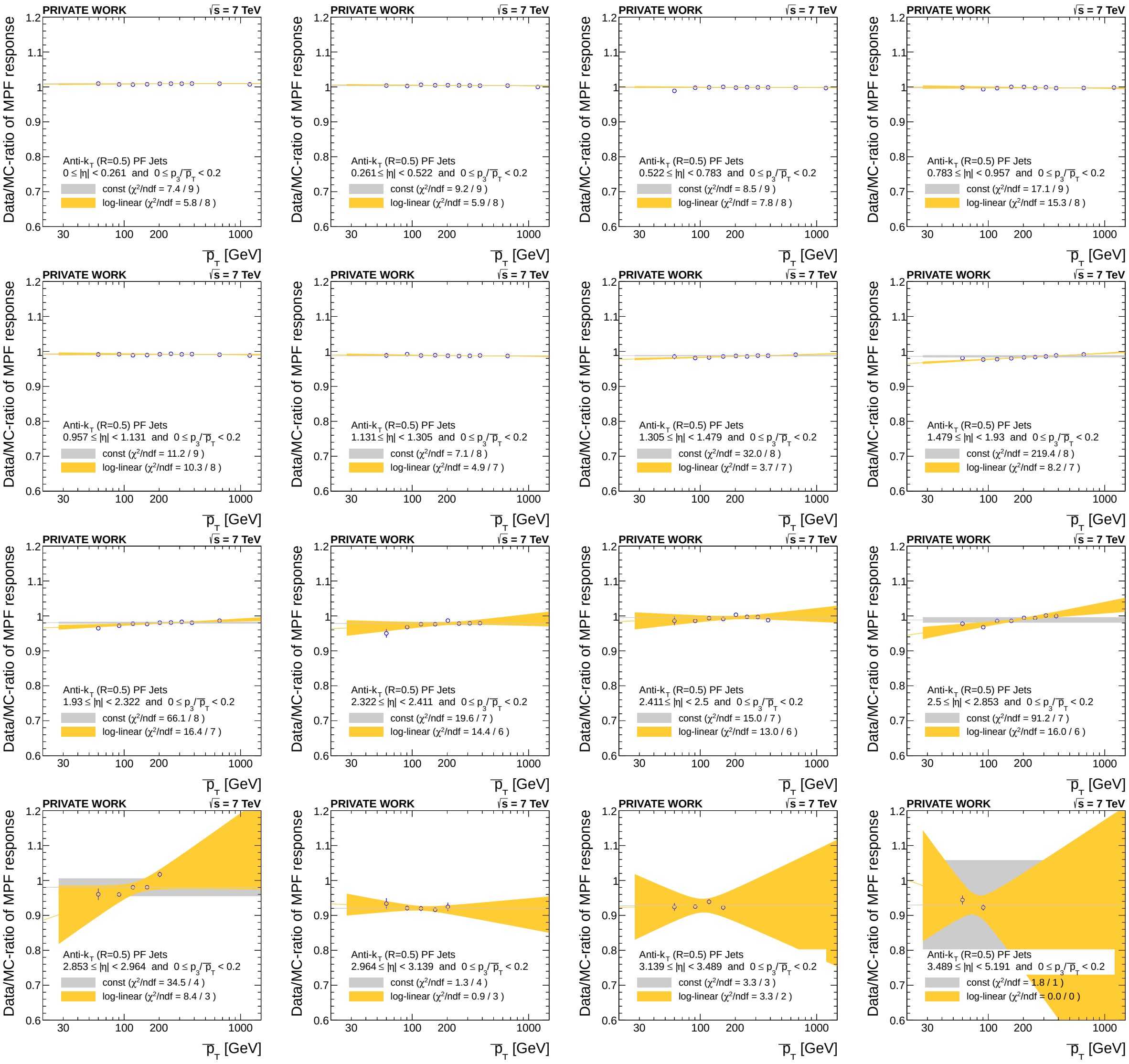

B.3.4. p_T-dependence of the k_{rad} correction for the MPF method

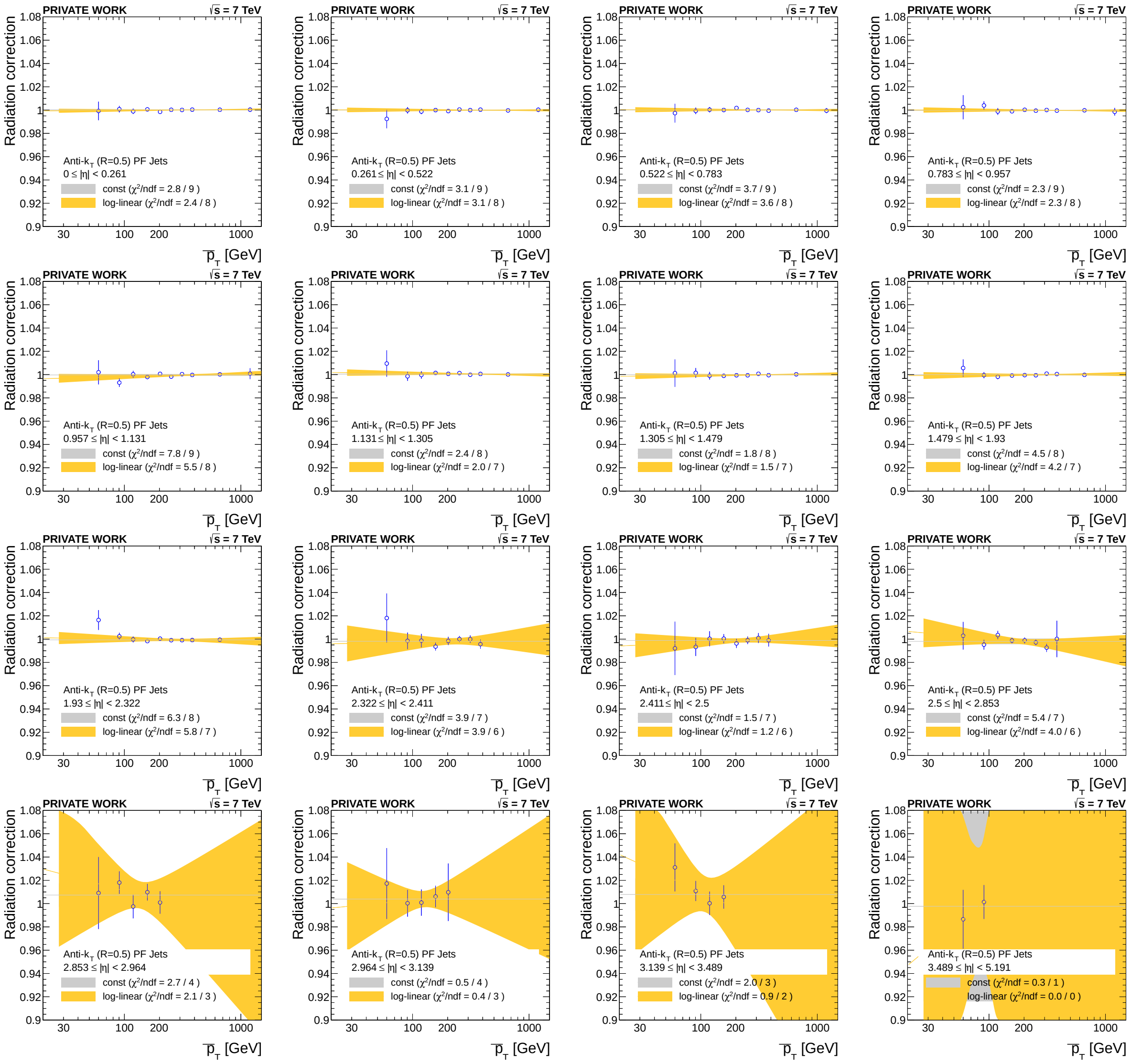

B.4. Comparison of the $p_{\mathrm{T}}^{\mathrm{rel}}$ dependence of MPF and relative response for PYTHIA and Herwig++ as reference MC

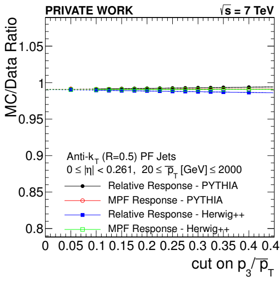

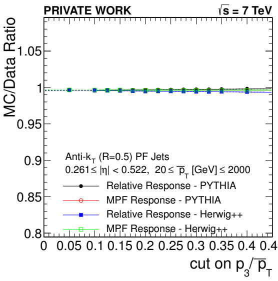

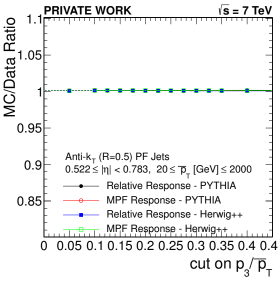

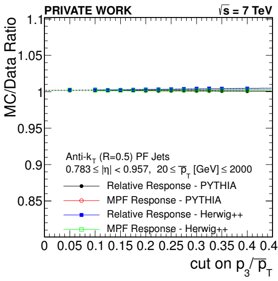

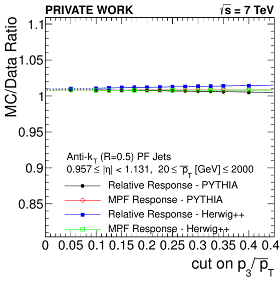

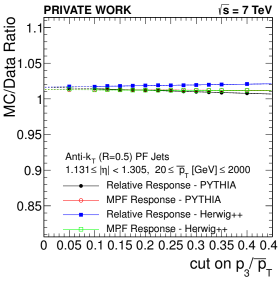

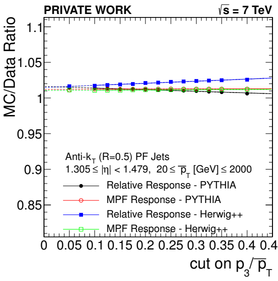

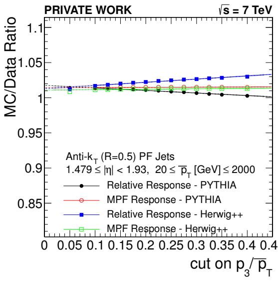

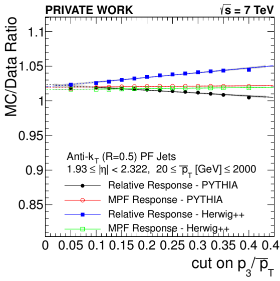

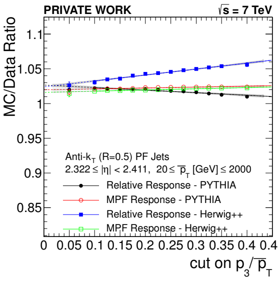

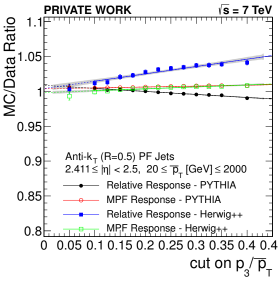

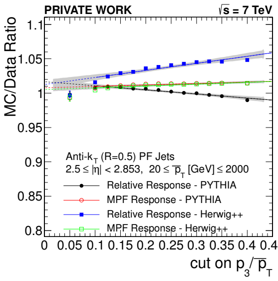

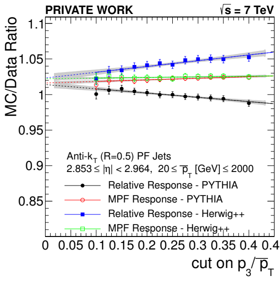

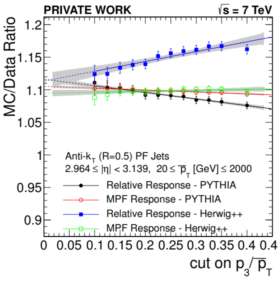

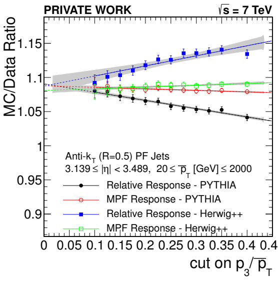

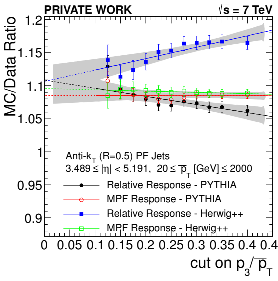

Appendix C

Control distributions of b-jet properties

C.1. Influence of systematic variations on the input variables and correlation with response

In the following sections, control distributions for all b-jet properties studied in the course of the determination of the b-jet energy regression are collected. Each left plot shows the distribution of the b-jet property in data and simulated events. The distribution is determined for the selected b-jets in the top-quark mass analysis, i.e. the two b-tagged jets considered as b-jets in the $\mathrm{t\bar{t}}$ event hypothesis. The number of events in simulation is normalized to the number of data events. The ratio to data is shown in the lower part of the plot, the hatched uncertainty bands only takes into account the statistical uncertainty of the data.

Each plot in the centre shows the correlation of the nominal jet-energy response with the b-jet property under study as observed for all true b-jets in the central MC-sample. The ratio to the nominal MC sample is shown in the lower part of the plot, the hatched uncertainty bands only takes into account the statistical uncertainty of the nominal MC sample.

Each right plot shows the correlation of the jet-energy response after applying the b-jet energy regression with the b-jet property under study as observed for all true b-jets in the central MC-sample. The ratio to the nominal MC sample is shown in the lower part of the plot, the hatched uncertainty bands only takes into account the statistical uncertainty of the nominal MC sample.

For all plots, the influence of the systematic variations discussed in Section 7.4 is indicated.

C.1.1. Lepton fractions

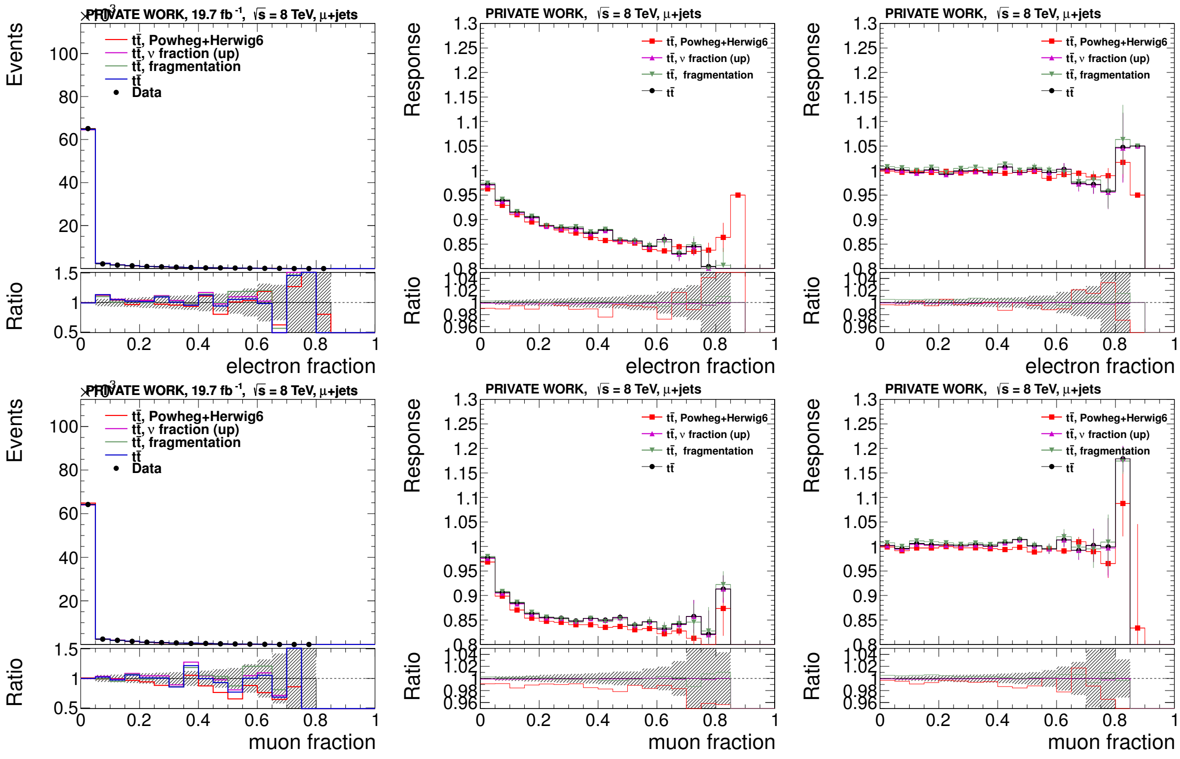

C.1.2. Other PF properties

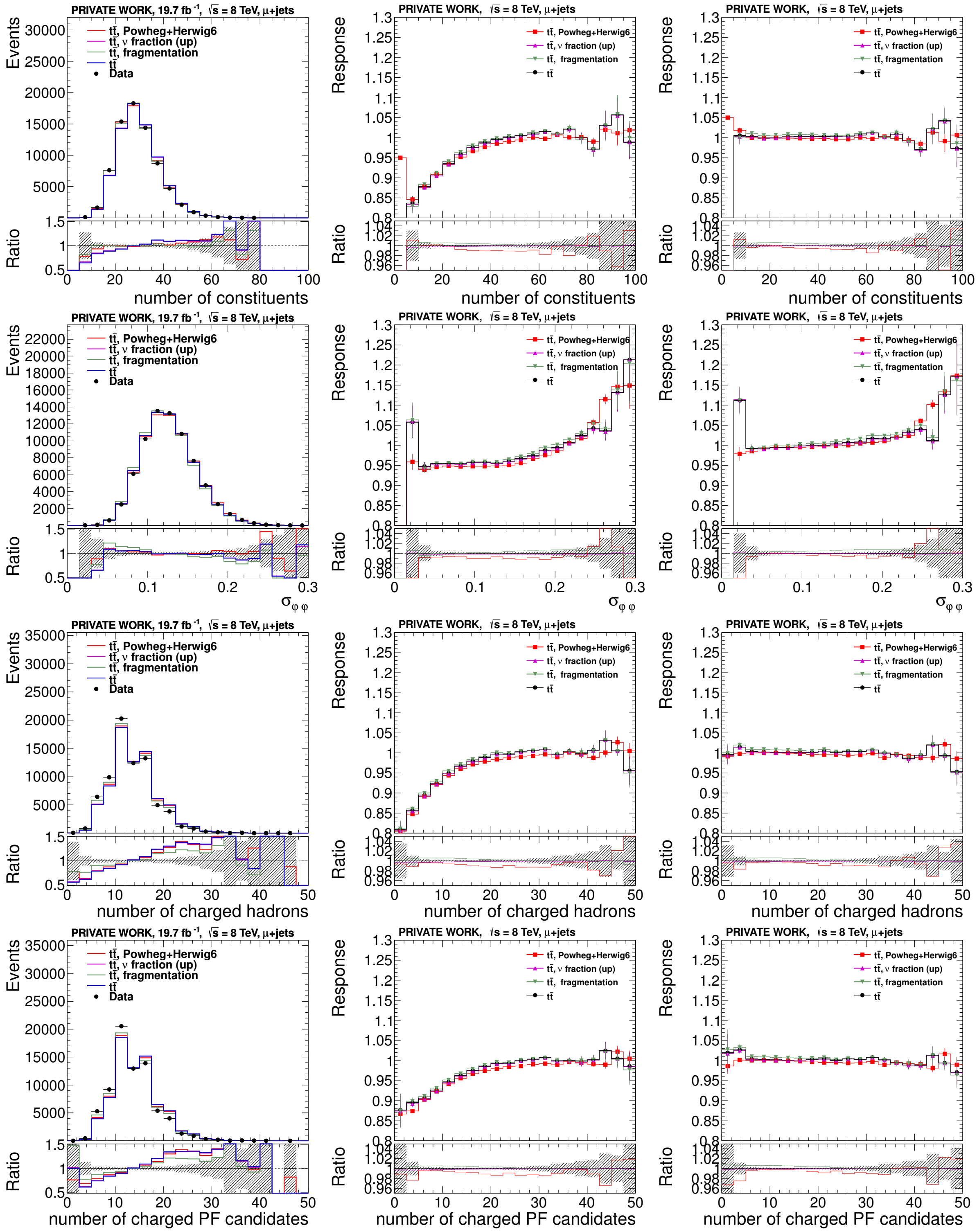

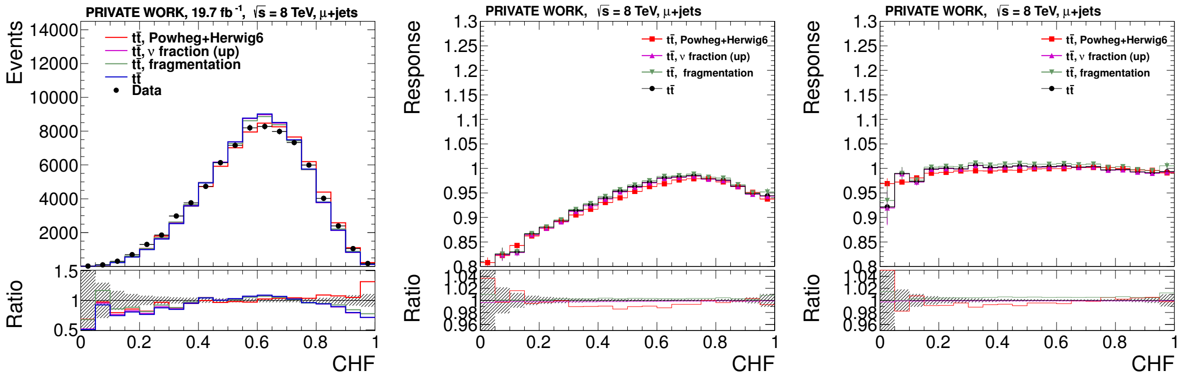

C.1.3. b-tagging related properties

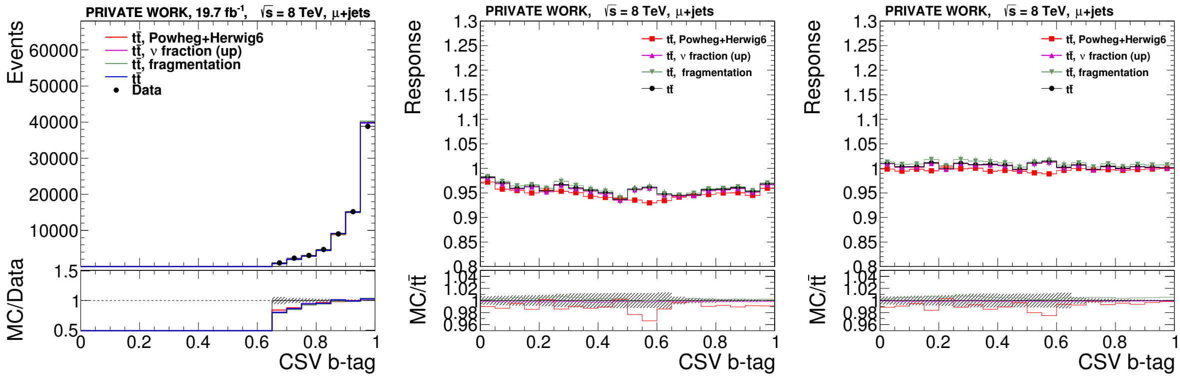

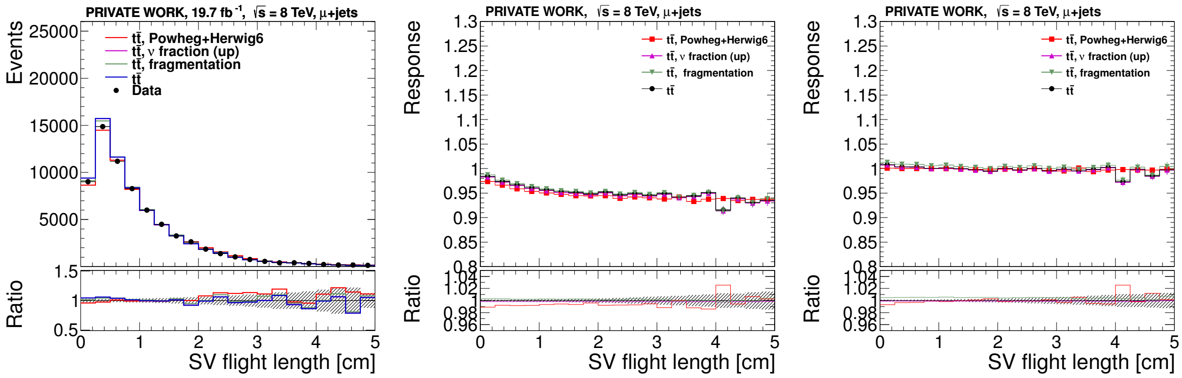

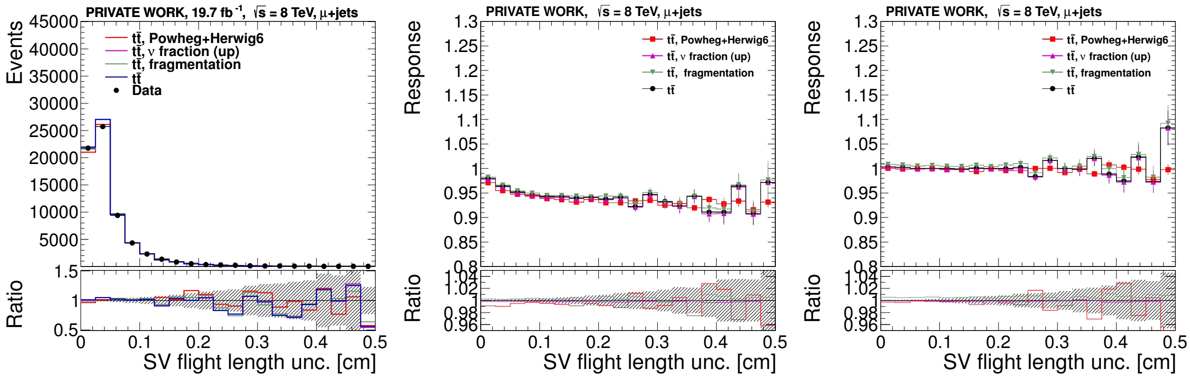

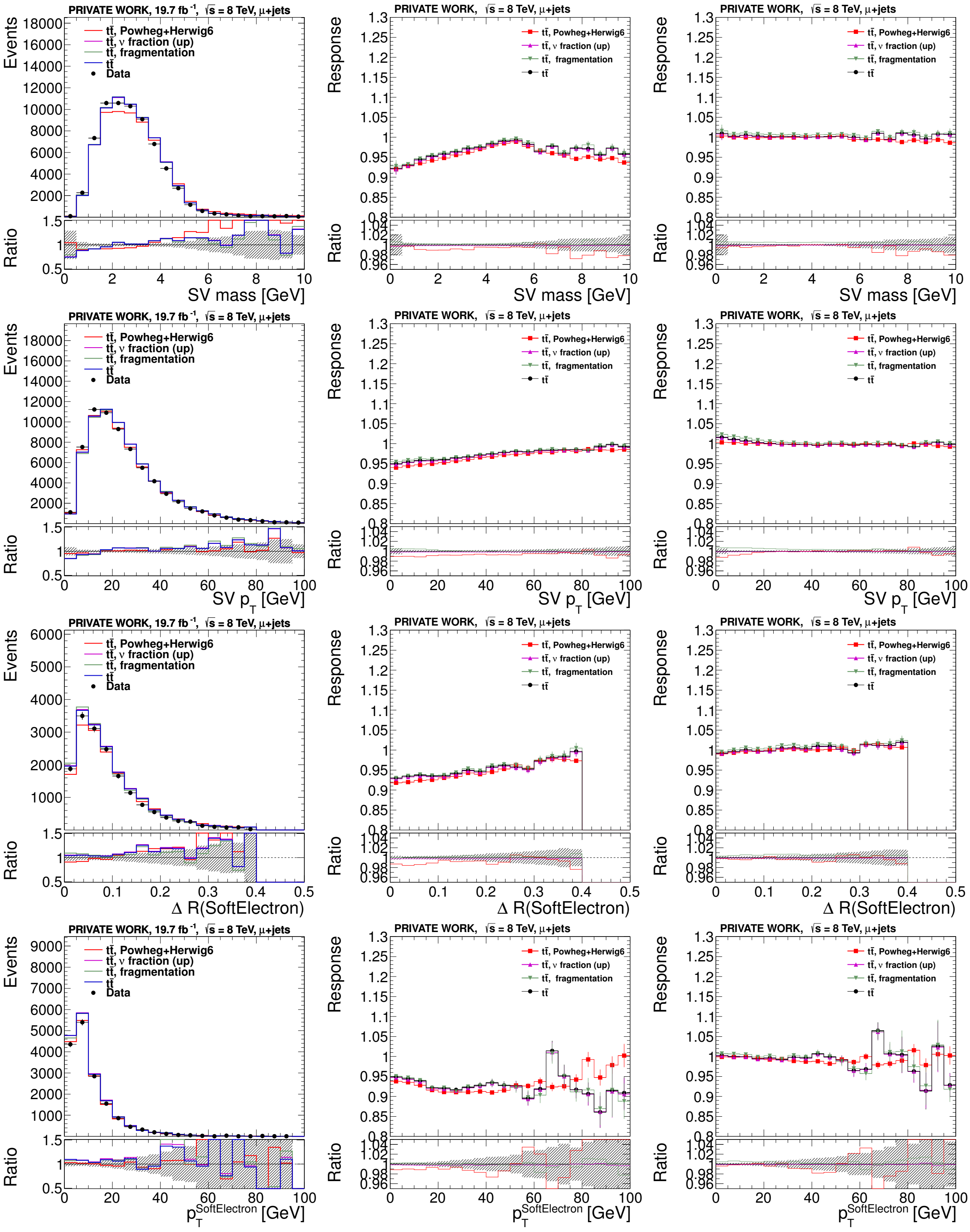
PRIVATE WORK, 19.7 fb^{-1}, $\sqrt{s}$ = 8 TeV, μ+jets
PRIVATE WORK, $\sqrt{s}$ = 8 TeV, μ+jets
tt̄, Powheg+Herwig6
tt̄, ν fraction (up)
tt̄, fragmentation
tt̄
Data
Events
Response
Ratio
SV mass [GeV]
SV p_T [GeV]
Δ R(SoftElectron)
$p_T^{SoftElectron}$ [GeV]

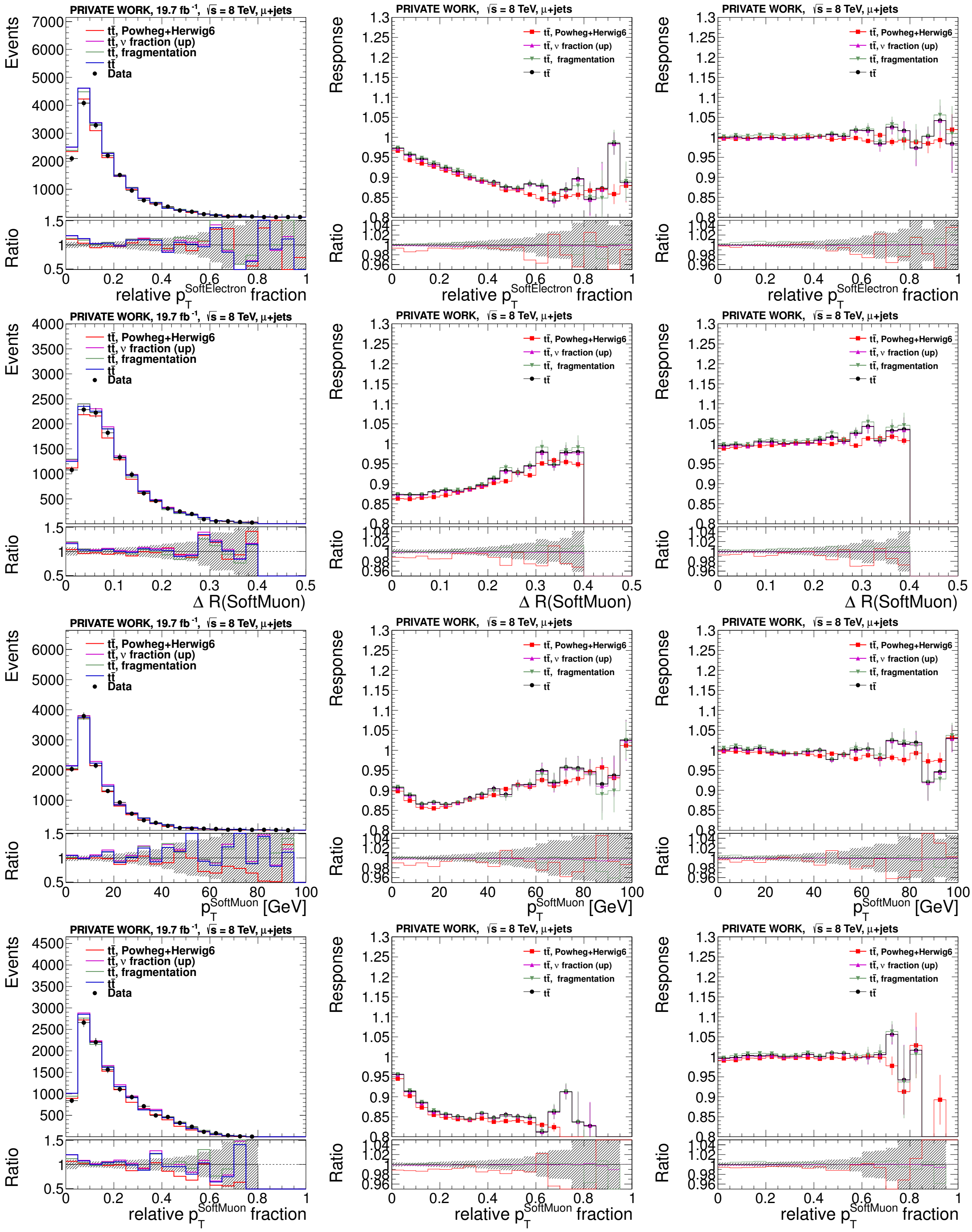
PRIVATE WORK, 19.7 fb^{-1}, $\sqrt{s}$ = 8 TeV, μ+jets
PRIVATE WORK, $\sqrt{s}$ = 8 TeV, μ+jets
Events
Response
Ratio
$t\bar{t}$, Powheg+Herwig6
$t\bar{t}$, ν fraction (up)
$t\bar{t}$, fragmentation
$t\bar{t}$
Data
relative $p_T^{SoftElectron}$ fraction
Δ R(SoftMuon)
$p_T^{SoftMuon}$ [GeV]
relative $p_T^{SoftMuon}$ fraction

C.1.4. Kinematic and pilup-correction related quantities

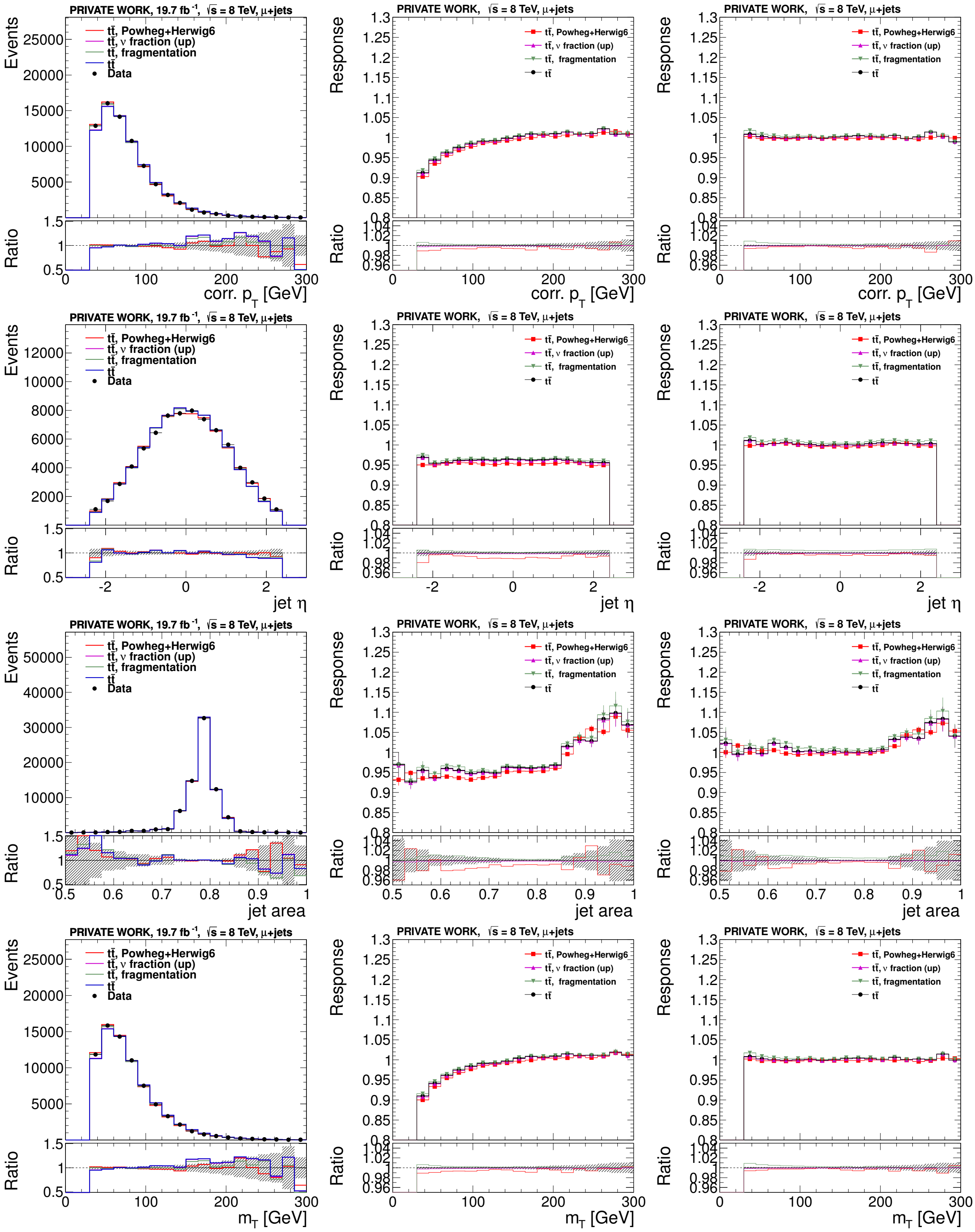

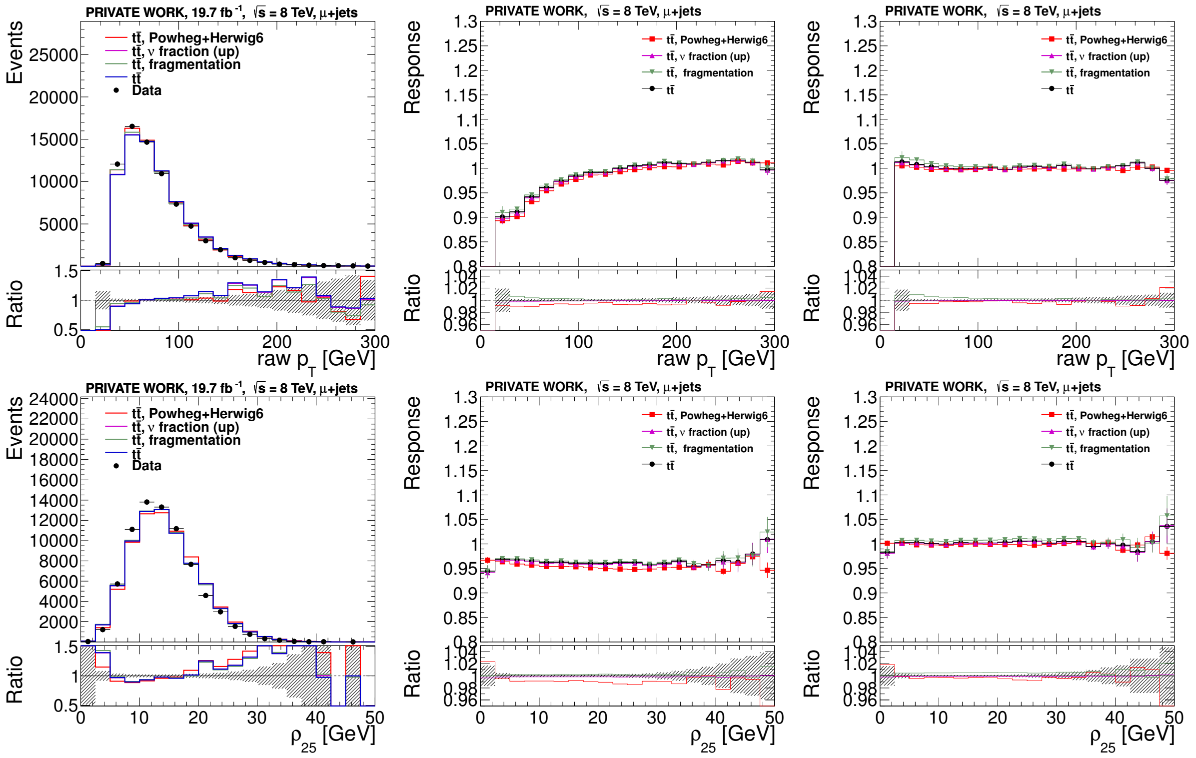

C.1.5. Observables not considered in the BJER

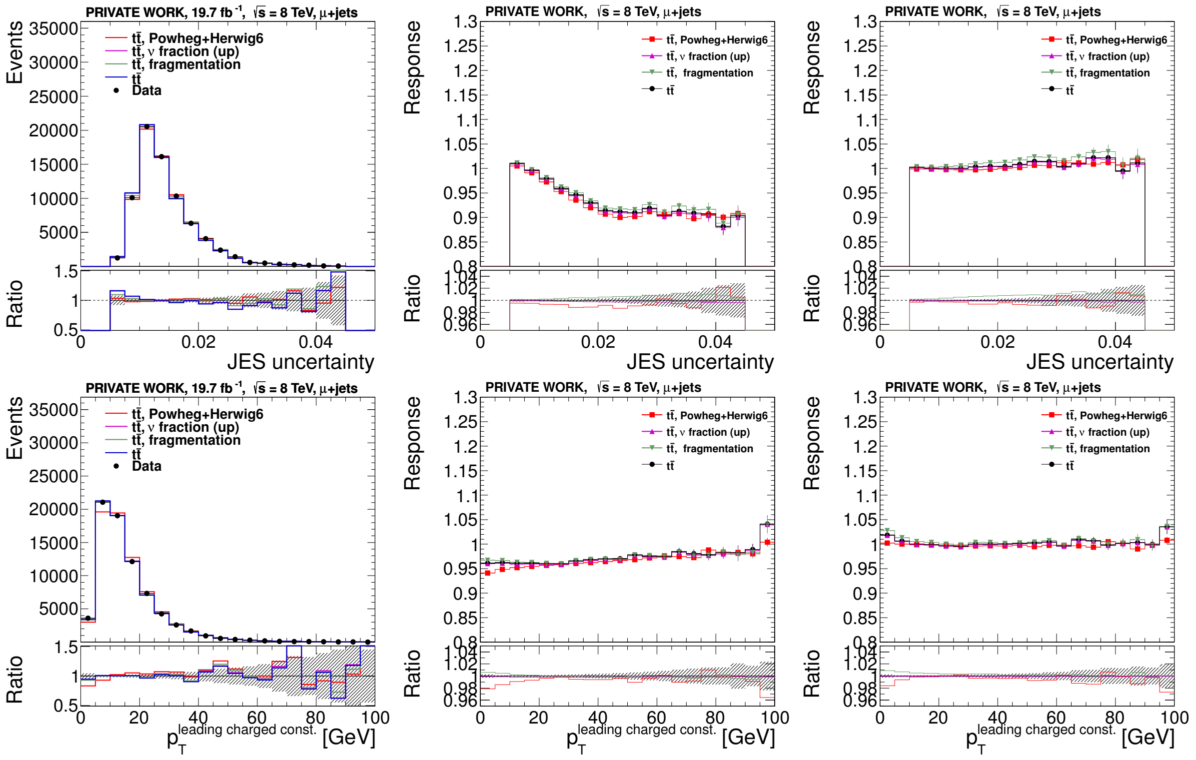

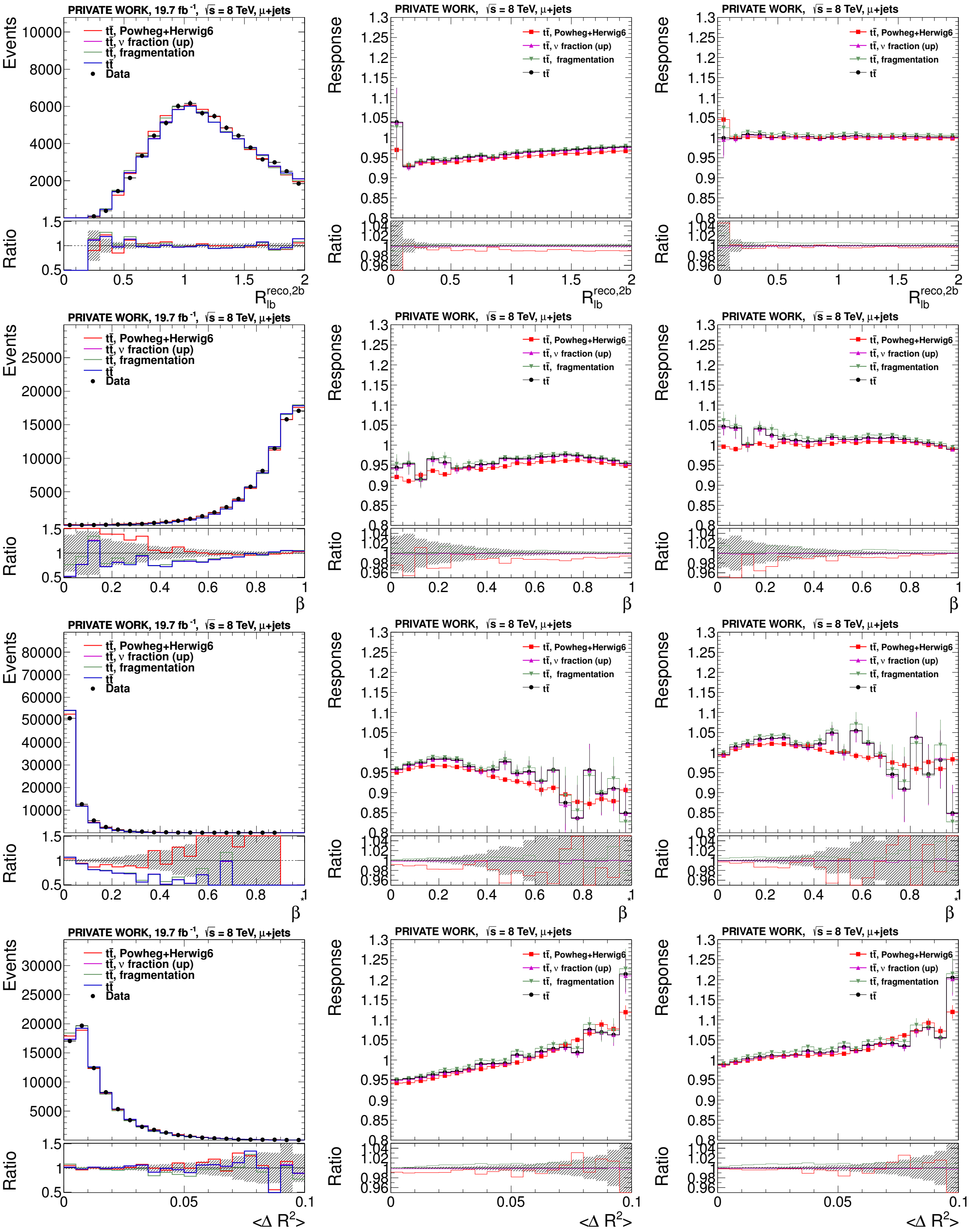
PRIVATE WORK, 19.7 fb^{-1}, $\sqrt{s}$ = 8 TeV, μ+jets
PRIVATE WORK, $\sqrt{s}$ = 8 TeV, μ+jets
$t\bar{t}$, Powheg+Herwig6
$t\bar{t}$, ν fraction (up)
$t\bar{t}$, fragmentation
$t\bar{t}$
Data
Events
Response
Ratio
$R_{lb}^{reco,2b}$
β
<Δ R^2>

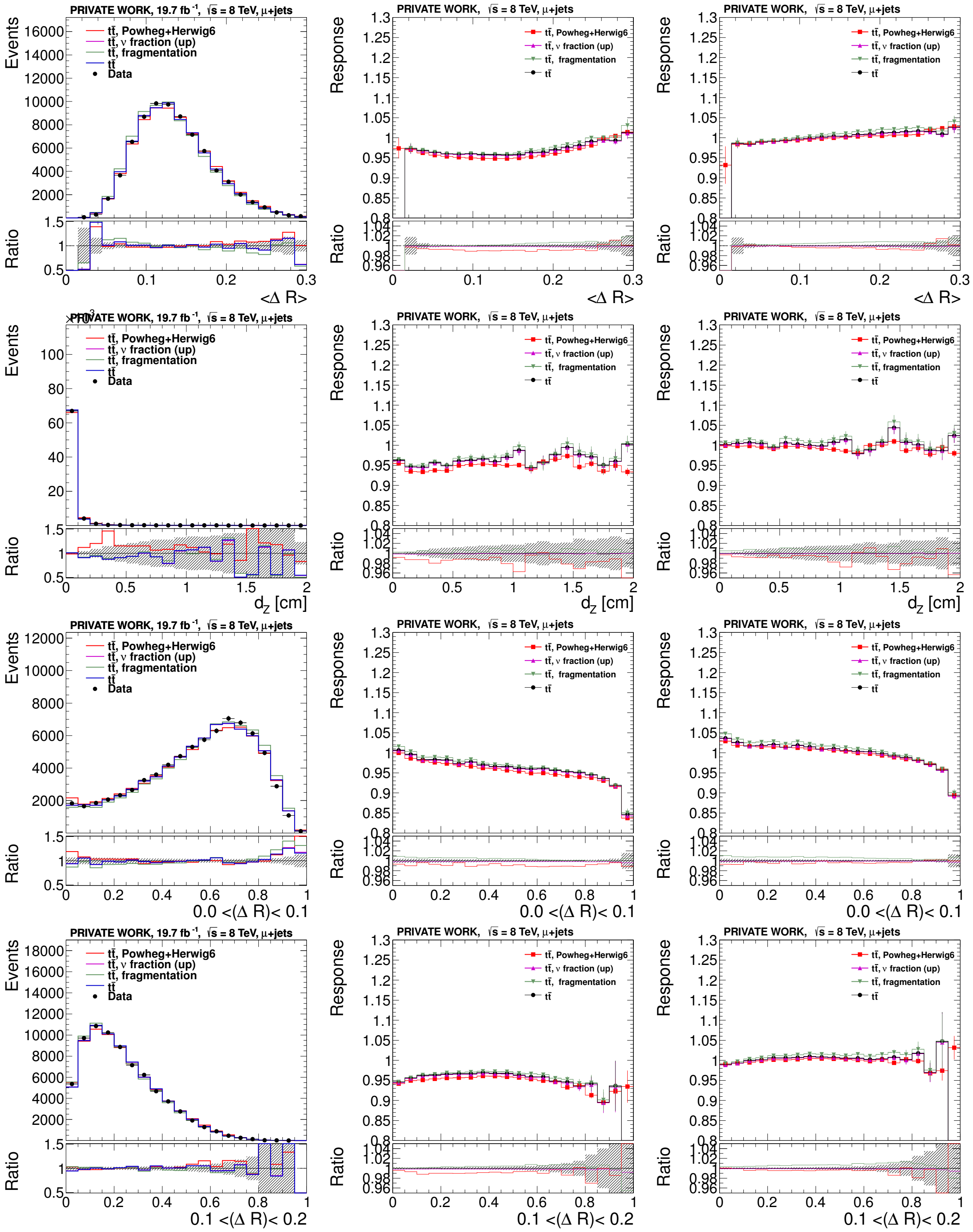
PRIVATE WORK, 19.7 fb^{-1}, $\sqrt{s}$ = 8 TeV, μ+jets
PRIVATE WORK, $\sqrt{s}$ = 8 TeV, μ+jets
tt̄, Powheg+Herwig6
tt̄, ν fraction (up)
tt̄, fragmentation
tt̄
Data
Events
Response
Ratio
×10^3
<Δ R>
d$_Z$ [cm]
0.0 <(Δ R)< 0.1
0.1 <(Δ R)< 0.2

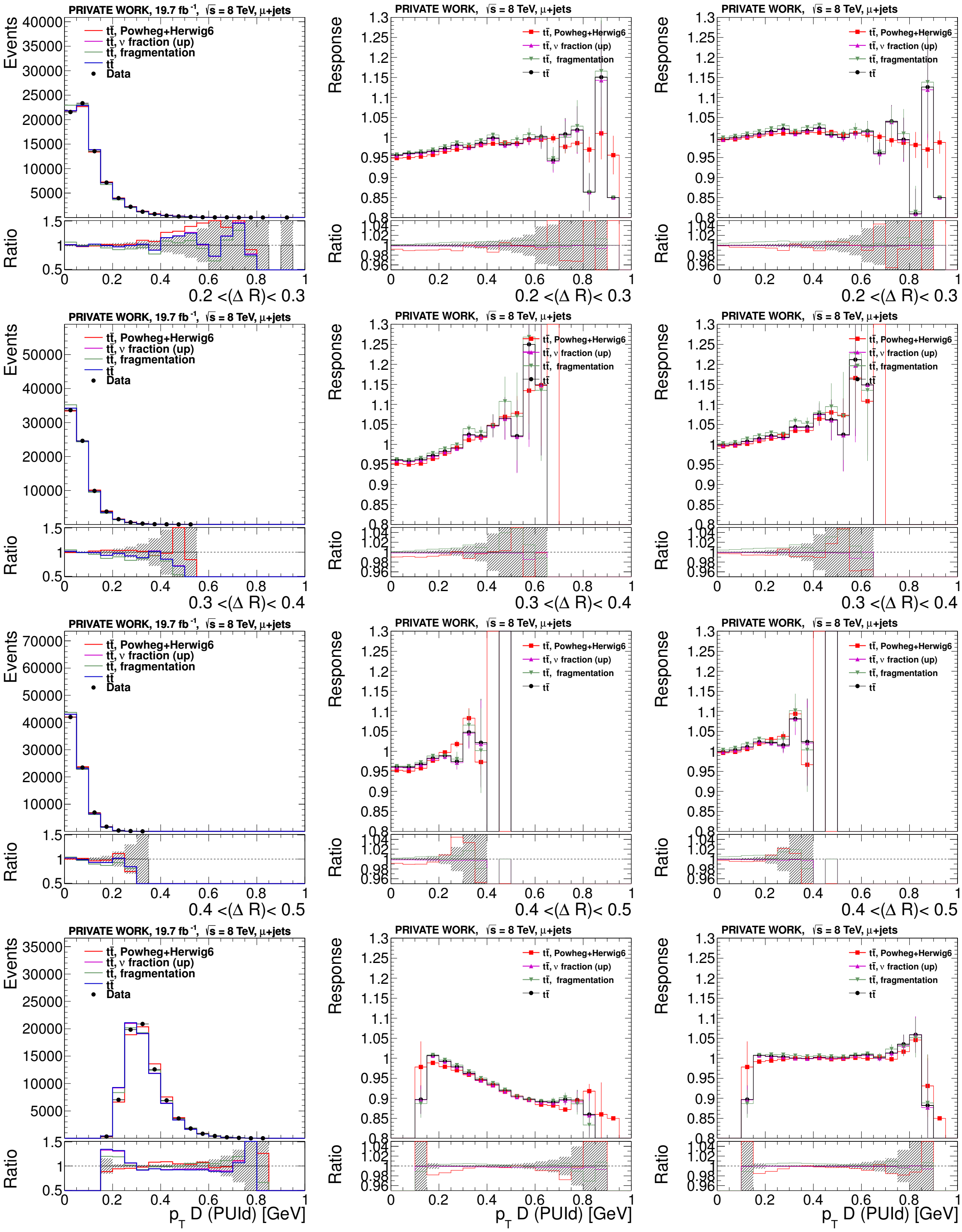
PRIVATE WORK, 19.7 fb^{-1}, $\sqrt{s}$ = 8 TeV, μ+jets
PRIVATE WORK, $\sqrt{s}$ = 8 TeV, μ+jets
Events
Response
Ratio
tt̄, Powheg+Herwig6
tt̄, ν fraction (up)
tt̄, fragmentation
tt̄
Data
0.2 <(Δ R)< 0.3
0.3 <(Δ R)< 0.4
0.4 <(Δ R)< 0.5
p_T D (PUId) [GeV]
0
0.2
0.4
0.6
0.8
1
0.5
1
1.5
0.8
0.85
0.9
0.95
1
1.05
1.1
1.15
1.2
1.25
1.3
0.96
0.98
1
1.02
1.04
5000
10000
15000
20000
25000
30000
35000
40000
50000
60000
70000

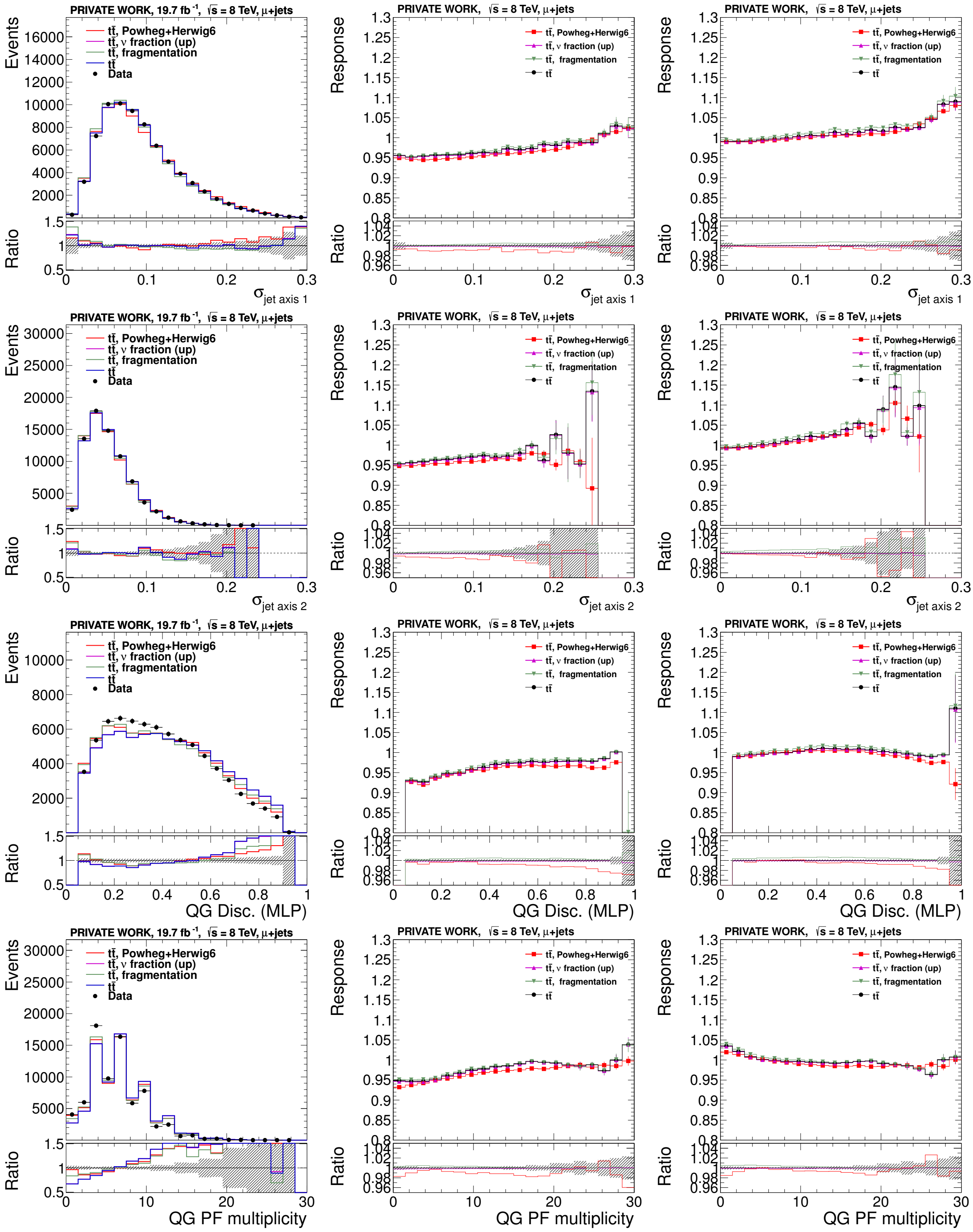
PRIVATE WORK, 19.7 fb^{-1}, $\sqrt{s}$ = 8 TeV, μ+jets
PRIVATE WORK, $\sqrt{s}$ = 8 TeV, μ+jets
tt̄, Powheg+Herwig6
tt̄, ν fraction (up)
tt̄, fragmentation
tt̄
Data
Events
Response
Ratio
$\sigma_{\text{jet axis 1}}$
$\sigma_{\text{jet axis 2}}$
QG Disc. (MLP)
QG PF multiplicity

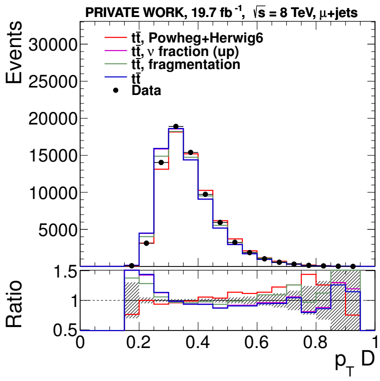
PRIVATE WORK, 19.7 fb^{-1}, $\sqrt{s}$ = 8 TeV, μ+jets
Events
tt̄, Powheg+Herwig6
tt̄, ν fraction (up)
tt̄, fragmentation
tt̄
Data
30000
25000
20000
15000
10000
5000
Ratio
1.5
1
0.5
0
0.2
0.4
0.6
0.8
1
p_T D

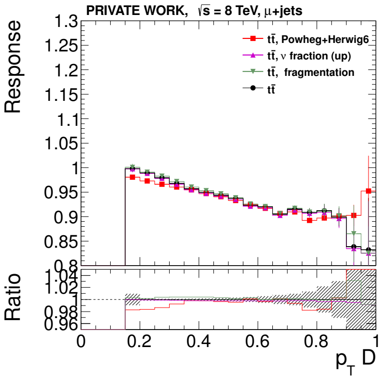
PRIVATE WORK, $\sqrt{s}$ = 8 TeV, μ+jets
Response
tt̄, Powheg+Herwig6
tt̄, ν fraction (up)
tt̄, fragmentation
tt̄
1.3
1.25
1.2
1.15
1.1
1.05
1
0.95
0.9
0.85
0.8
Ratio
1.04
1.02
1
0.98
0.96
0
0.2
0.4
0.6
0.8
1
p_T D

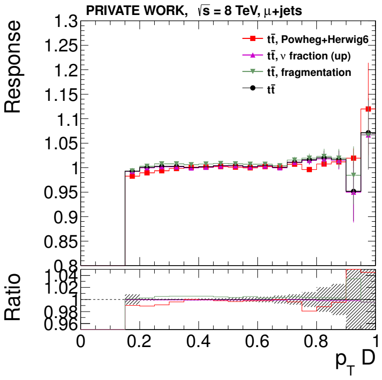
PRIVATE WORK, $\sqrt{s}$ = 8 TeV, μ+jets
Response
tt̄, Powheg+Herwig6
tt̄, ν fraction (up)
tt̄, fragmentation
tt̄
1.3
1.25
1.2
1.15
1.1
1.05
1
0.95
0.9
0.85
0.8
Ratio
1.04
1.02
1
0.98
0.96
0
0.2
0.4
0.6
0.8
1
p_T D

Appendix D

Supplementary material regarding the measurement of the top-quark mass (with/without BJER)

D.1. Additional systematic shifts evaluated with/without applying the regression correction

Table D.1.: Extended list of systematic shifts evaluated for the muon+jets final states with/without applying the b-jet energy regression for the 2D-mass, the resulting JSF, and the resulting 1D-mass (ideogram method with JSF fixed to 1). For statistically independent sample comparisons, the statistical uncertainties of the shift evaluation are quoted.

Uncertainty name	2D mass	JSF	1D mass
main analysis			
Q^2 scale	0.24 ± 0.32	0.006 ± 0.003	0.27 ± 0.19
- up	+0.08	-0.002	-0.05
- down	-0.24	+0.006	+0.27
Color reconnection	0.24 ± 0.21	0.001 ± 0.002	0.14 ± 0.12
- shift	-0.24	+0.001	-0.14
Jet energy response (gluon)	0.30 ± 0.00	0.004 ± 0.000	0.07 ± 0.00
- up	-0.30	+0.004	+0.07
- down	+0.22	-0.003	-0.00
Jet energy response (udsc)	0.15 ± 0.00	0.002 ± 0.000	0.04 ± 0.00
- up	+0.08	-0.001	-0.02
- down	-0.15	+0.002	+0.04
(cc) MC@NLO+Herwig6 vs. Powheg+Herwig6	0.54 ± 0.21	0.012 ± 0.002	0.51 ± 0.13
- shift	-0.54	+0.012	+0.51
ME generator	0.30 ± 0.19	0.001 ± 0.002	0.20 ± 0.11
- shift	-0.30	+0.001	-0.20

Continued on next page

Table D.1.: Extended list of systematic shifts evaluated for the muon+jets final states with/without applying the b-jet energy regression for the 2D-mass, the resulting JSF, and the resulting 1D-mass (ideogram method with JSF fixed to 1). For statistically independent sample comparisons, the statistical uncertainties of the shift evaluation are quoted.

Uncertainty name	2D mass	JSF	1D mass
main analysis			
ME-PS matching threshold	0.04 ± 0.31	0.002 ± 0.003	0.17 ± 0.18
- up	+0.01	+0.001	+0.07
- down	-0.04	+0.002	+0.17
(cc) MadGraph (no SC) vs. Powheg	0.05 ± 0.16	0.001 ± 0.001	0.00 ± 0.10
- shift	-0.05	+0.001	+0.00
Pileup (pp cross-section)	0.08 ± 0.00	0.001 ± 0.000	0.05 ± 0.00
- up	-0.07	+0.001	+0.05
- down	+0.08	-0.001	-0.05
(cc) Powheg+Pythia6 vs. MC@NLO+Herwig6	0.03 ± 0.22	0.012 ± 0.002	1.09 ± 0.13
- shift	-0.03	-0.012	-1.09
(cc) Powheg+Pythia6 vs. Powheg+Herwig6	0.58 ± 0.22	0.000 ± 0.002	0.59 ± 0.14
- shift	-0.58	-0.000	-0.59
(cc) Pythia Z2* vs. P11	0.05 ± 0.18	0.001 ± 0.002	0.01 ± 0.10
- shift	-0.05	+0.001	+0.01
Semi-leptonic B hadron decays	0.15 ± 0.00	0.000 ± 0.000	0.16 ± 0.00
- up	-0.15	-0.000	-0.16
- down	+0.09	+0.000	+0.09
Top-pt reweighting	0.11 ± 0.00	0.003 ± 0.000	0.12 ± 0.00
- shift	-0.11	+0.003	+0.12
Underlying event	0.10 ± 0.23	0.001 ± 0.002	0.08 ± 0.14
- up	+0.04	+0.001	+0.08
- down	-0.10	+0.000	-0.06
b fragmentation	0.03 ± 0.00	0.001 ± 0.000	0.04 ± 0.00
- shift	+0.03	-0.001	-0.04
Quadratic sum of uncertainties (cross-checks not considered)	0.75	0.009	0.49

Table D.2.: Extended list of systematic shifts evaluated for the muon+jets final states with/without applying the b-jet energy regression for the 2D-mass, the resulting JSF, and the resulting 1D-mass (ideogram method with JSF fixed to 1). For statistically independent sample comparisons, the statistical uncertainties of the shift evaluation are quoted.

Uncertainty name	2D mass	JSF	1D mass
with b-jet energy regression			
Q^2 scale	0.26 ± 0.30	0.005 ± 0.003	0.32 ± 0.17
- up	+0.26	-0.003	+0.06
- down	-0.08	+0.005	+0.32
Color reconnection	0.16 ± 0.19	0.001 ± 0.002	0.10 ± 0.12
- shift	-0.16	+0.001	-0.10
Jet energy response (gluon)	0.27 ± 0.00	0.004 ± 0.000	0.06 ± 0.00
- up	-0.25	+0.004	+0.06
- down	+0.27	-0.003	+0.04
Jet energy response (udsc)	0.13 ± 0.00	0.002 ± 0.000	0.07 ± 0.00
- up	+0.13	-0.001	+0.02
- down	-0.10	+0.002	+0.07
(cc) MC@NLO+Herwig6 vs. Powheg+Herwig6	0.35 ± 0.20	0.012 ± 0.002	0.63 ± 0.12
- shift	-0.35	+0.012	+0.63
ME generator	0.28 ± 0.18	0.001 ± 0.002	0.20 ± 0.11
- shift	-0.28	+0.001	-0.20
ME-PS matching threshold	0.22 ± 0.29	0.000 ± 0.003	0.26 ± 0.17
- up	+0.10	+0.000	+0.13
- down	+0.22	+0.000	+0.26
(cc) MadGraph (no SC) vs. Powheg	0.12 ± 0.15	0.000 ± 0.001	0.10 ± 0.09
- shift	+0.12	-0.000	+0.10
Pileup (pp cross-section)	0.04 ± 0.00	0.001 ± 0.000	0.07 ± 0.00
- up	-0.03	+0.001	+0.07
- down	+0.04	-0.001	-0.07
(cc) Powheg+Pythia6 vs. MC@NLO+Herwig6	0.22 ± 0.20	0.012 ± 0.002	0.77 ± 0.12
- shift	+0.22	-0.012	-0.77
(cc) Powheg+Pythia6 vs. Powheg+Herwig6	0.13 ± 0.20	0.000 ± 0.002	0.13 ± 0.13
- shift	-0.13	-0.000	-0.13
(cc) Pythia Z2* vs. P11	0.00 ± 0.16	0.001 ± 0.002	0.07 ± 0.10
- shift	-0.00	+0.001	+0.07
Semi-leptonic B hadron decays	0.05 ± 0.00	0.000 ± 0.000	0.05 ± 0.00
- up	-0.05	+0.000	-0.05
- down	+0.05	-0.000	+0.05
Top-pt reweighting	0.09 ± 0.00	0.003 ± 0.000	0.13 ± 0.00
- shift	-0.09	+0.003	+0.13

Continued on next page

Table D.2.: Extended list of systematic shifts evaluated for the muon+jets final states with/without applying the b-jet energy regression for the 2D-mass, the resulting JSF, and the resulting 1D-mass (ideogram method with JSF fixed to 1). For statistically independent sample comparisons, the statistical uncertainties of the shift evaluation are quoted.

Uncertainty name	2D mass	JSF	1D mass
with b-jet energy regression			
Underlying event	0.11 ± 0.22	0.001 ± 0.002	0.06 ± 0.13
- up	+0.01	+0.001	+0.06
- down	-0.11	+0.001	-0.06
b fragmentation	0.19 ± 0.00	0.000 ± 0.000	0.15 ± 0.00
- shift	+0.19	-0.000	+0.15
Quadratic sum of uncertainties (cross-checks not considered)	0.69	0.009	0.55

D.2. Control distributions of m_t^{fit}

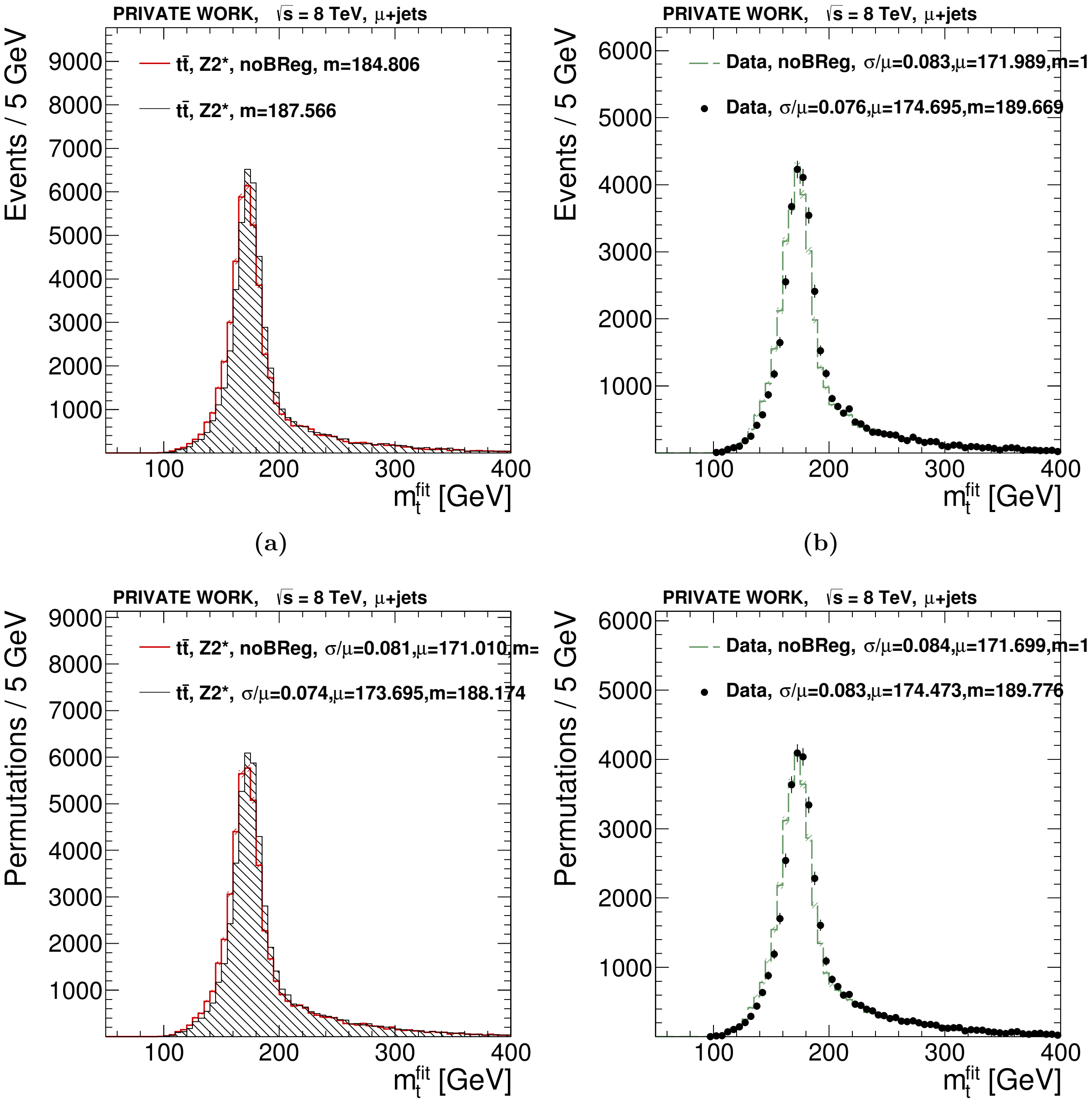

(a) (b)

(c) (d)

Figure D.1.: Fitted top mass distribution with/without b-regression; (a) best fit result, MC only, (b) best fit result in data, (c) all permutations with $P_{gof} > 0.2$ in MC, (d) all permutations with $P_{gof} > 0.2$ in data

Bibliography

[1] D. Mendeleev, “Über die Beziehungen der Eigenschaften zu den Atomgewichten der Elemente”, *Zeitschrift für Chemie* (1869) 405–406.

[2] J. L. Meyer, “Die Natur der chemischen Elemente als Function ihrer Atomgewichte”, *Annalen der Chemie und Pharmacie* (1870) 354–364.

[3] ATLAS collaboration, “Observation of a new particle in the search for the Standard Model Higgs boson with the ATLAS detector at the LHC”, *Physics Letters B* **716** (2012), no. 1, 1 – 29. `doi:10.1016/j.physletb.2012.08.020`.

[4] CMS collaboration, “Observation of a new boson at a mass of 125 GeV with the CMS experiment at the LHC”, *Physics Letters B* **716** (2012), no. 1, 30 – 61. `doi:10.1016/j.physletb.2012.08.021`.

[5] Markus Seidel, “Measurement of Top Quark Mass and Jet Energy Scale at the CMS Experiment using the Ideogram Method”, *diploma-thesis at University of Hamburg* **CERN-THESIS-2011-096, CMS-TS-2012-004** (2011).

[6] The CMS Collaboration, “Measurement of the top-quark mass in $\mathrm{t\bar{t}}$ events with lepton+jets final states in pp collisions at $\sqrt{s} = 7\,\mathrm{TeV}$”, *Journal of High Energy Physics* **2012** (2012), no. 12, 1–37. `doi:10.1007/JHEP12(2012)105`.

[7] CMS Collaboration, “Measurement of the top-quark mass in $t\bar{t}$ events with lepton+jets final states in pp collisions at $\sqrt{s} = 8\,\mathrm{TeV}$”, *CMS-PAS-TOP-14-001* (2014).

[8] D. Griffiths, “Introduction to Elementary Particles”. Wiley-VCH, 2nd edition, 10, 2008.

[9] B. Martin and G. Shaw, “Particle Physics (Manchester Physics Series)”. Wiley, 3rd edition, 12, 2008.

[10] F. Halzen and A. D. Martin, “Quarks and Leptons: An Introductory Course in Modern Particle Physics”. Wiley, 1st edition, 1, 1984.

[11] M. E. Peskin and D. V. Schroeder, “An Introduction To Quantum Field Theory (Frontiers in Physics)”, *Westview Press* (October, 1995).

[12] CERN Webfest 2012, “Standard Model infographic developed at the webfest”, *Website* (`https://cdsweb.cern.ch/record/1473657`, 8 June 2014).

[13] S. Weinberg, "The making of the Standard Model", *The European Physical Journal C - Particles and Fields* **34** (2004), no. 1, 5–13. `doi:10.1140/epjc/s2004-01761-1`.

[14] M. Gell-Mann, "A schematic model of baryons and mesons", *Physics Letters* **8** (1964), no. 3, 214 – 215. `doi:10.1016/S0031-9163(64)92001-3`.

[15] G. Zweig, "An SU_3 model for strong interaction symmetry and its breaking; Version 2", *CERN-TH-412* (Feb, 1964) 80 p.

[16] S. Weinberg, "A Model of Leptons", *Phys. Rev. Lett.* **19** (Nov, 1967) 1264–1266. `doi:10.1103/PhysRevLett.19.1264`.

[17] A. Salam, "Weak and electromagnetic interactions", *Proc. Nobel Symp.. 8* **C680519** (1968) 367–377.

[18] S. L. Glashow, "Partial-Symmetries of Weak Interactions", *Nucl. Phys. 22* (1961) 579. `doi:10.1016/0029-5582(61)90469-2`.

[19] J. Goldstone, "Field theories with Superconductor solutions", *Il Nuovo Cimento* **19** (1961), no. 1, 154–164. `doi:10.1007/BF02812722`.

[20] J. Goldstone, A. Salam, and S. Weinberg, "Broken Symmetries", *Phys. Rev.* **127** (Aug, 1962) 965–970. `doi:10.1103/PhysRev.127.965`.

[21] Nobelprize.org, Nobel Media AB, "The Nobel Prize in Physics 1979", *Website* (`http://nobelprize.org/nobel_prizes/physics/laureates/1979/`, 10 June 2014).

[22] D. Cundy, G. Myatt, F. Nezrick et al., "Upper limits for diagonal and neutral current couplings in the CERN neutrino experiments", *Physics Letters B* **31** (1970), no. 7, 478 – 480. `doi:10.1016/0370-2693(70)90158-9`.

[23] F. Hasert, S. Kabe, W. Krenz et al., "Observation of neutrino-like interactions without muon or electron in the gargamelle neutrino experiment", *Physics Letters B* **46** (1973), no. 1, 138 – 140. `doi:10.1016/0370-2693(73)90499-1`.

[24] Nobelprize.org, Nobel Media AB, "The Nobel Prize in Physics 2013", *Website* (`http://nobelprize.org/nobel_prizes/physics/laureates/2013/`, 10 June 2014).

[25] ALEPH Collaboration, CDF Collaboration, D0 Collaboration et al., "Precision Electroweak Measurements and Constraints on the Standard Model", *ArXiv e-prints* (December, 2010) `arXiv:1012.2367`.

[26] M. Baak, M. Goebel, J. Haller et al., "The electroweak fit of the standard model after the discovery of a new boson at the LHC", *The European Physical Journal C* **72** (2012), no. 11,. `doi:10.1140/epjc/s10052-012-2205-9`.

[27] F. Zwicky, "Die Rotverschiebung von extragalaktischen Nebeln", *Helv.Phys.Acta* **6**

(1933) 110–127.

[28] M. Markevitch, A. H. Gonzalez, D. Clowe et al., "Direct Constraints on the Dark Matter Self-Interaction Cross Section from the Merging Galaxy Cluster 1E 065756", *The Astrophysical Journal* **606** (2004), no. 2, 819. `doi:10.1086/383178`.

[29] Planck Collaboration, P. A. R. Ade, N. Aghanim et al., "Planck 2013 results. I. Overview of products and scientific results", *ArXiv e-prints* (March, 2013) `arXiv:1303.5062`.

[30] S. P. Martin, "A Supersymmetry primer", *Adv.Ser.Direct.High Energy Phys.* **21** (2010) 1–153, `arXiv:hep-ph/9709356`. `doi:10.1142/9789814307505_0001`.

[31] N. Arkani-Hamed, S. Dimopoulos, and G. Dvali, "The hierarchy problem and new dimensions at a millimeter", *Physics Letters B* **429** (1998), no. 34, 263 – 272. `doi:10.1016/S0370-2693(98)00466-3`.

[32] Henning Kirschenmann, "Exploitation of Jet Properties for Energy Scale Corrections for the CMS Calorimeters ", *diploma-thesis at University of Hamburg* **CMS-TS-2011-002** (2010).

[33] G. Dissertori, I. Knowles, and M. Schmelling, "Quantum Chromodynamics: High Energy Experiments and Theory (The International Series of Monographs on Physics)". Oxford University Press, USA, 4, 2003.

[34] R. K. Ellis, W. J. Stirling, and B. R. Webber, "QCD and Collider Physics (Cambridge Monographs on Particle Physics, Nuclear Physics and Cosmology)". Cambridge University Press, 12, 2003.

[35] G. Sterman and S. Weinberg, "Jets from Quantum Chromodynamics", *Phys. Rev. Lett.* **39** (Dec, 1977) 1436–1439. `doi:10.1103/PhysRevLett.39.1436`.

[36] S. D. Drell and T.-M. Yan, "Partons and their applications at high energies", *Annals of Physics* **66** (1971), no. 2, 578 – 623. `doi:10.1016/0003-4916(71)90071-6`.

[37] A. Buckley, J. Butterworth, S. Gieseke et al., "General-purpose event generators for LHC physics", *Physics Reports* **504** (July, 2011) 145–233, `arXiv:1101.2599`. `doi:10.1016/j.physrep.2011.03.005`.

[38] J. M. Campbell, J. W. Huston, and W. J. Stirling, "Hard interactions of quarks and gluons: a primer for LHC physics", *Reports on Progress in Physics* **70** (2007), no. 1, 89. `doi:10.1088/0034-4885/70/1/R02`.

[39] A. Ali and G. Kramer, "Jets and QCD: a historical review of the discovery of the quark and gluon jets and its impact on QCD", *The European Physical Journal H* **36** (2011), no. 2, 245–326. `doi:10.1140/epjh/e2011-10047-1`.

[40] Particle Data Group Collaboration, "Review of Particle Physics", *Phys. Rev. D* **86** (Jul, 2012) 010001. `doi:10.1103/PhysRevD.86.010001`.

[41] M. A. Dobbs, S. Frixione, E. Laenen et al., “Les Houches Guidebook to Monte Carlo Generators for Hadron Collider Physics”, *ArXiv e-prints* (March, 2004) `arXiv:arXiv:hep-ph/0403045`.

[42] G. Altarelli and G. Parisi, “Asymptotic Freedom in Parton Language”, *Nucl.Phys.* **B126** (1977) 298. `doi:10.1016/0550-3213(77)90384-4`.

[43] Y. L. Dokshitzer, “Calculation of the Structure Functions for Deep Inelastic Scattering and e+ e- Annihilation by Perturbation Theory in Quantum Chromodynamics.”, *Sov.Phys.JETP* **46** (1977) 641–653.

[44] V. N. Gribov and L. N. Lipatov, “Deep inelastic e p scattering in perturbation theory”, *Sov. J. Nucl. Phys.* **15** (1972) 438–450.

[45] J. Gao, M. Guzzi, J. Huston et al., “The CT10 NNLO Global Analysis of QCD”, *Phys.Rev.* **D89** (2014) 033009, `arXiv:1302.6246`. `doi:10.1103/PhysRevD.89.033009`.

[46] A. D. Martin, W. J. Stirling, R. S. Thorne et al., “Parton distributions for the LHC”, *European Physical Journal C* **63** (September, 2009) 189–285, `arXiv:0901.0002`. `doi:10.1140/epjc/s10052-009-1072-5`.

[47] H1 and ZEUS collaboration, “Combined measurement and QCD analysis of the inclusive ep scattering cross sections at HERA”, *Journal of High Energy Physics* **2010** (2010), no. 1,. `doi:10.1007/JHEP01(2010)109`.

[48] JW Stirling, “Private communication”, *Website* (`http://www.hep.ph.ic.ac.uk/~wstirlin/plots/plots.html`, June 2014).

[49] T. Sjöstrand, S. Mrenna, and P. Skands, “PYTHIA 6.4 Physics and Manual”, `arXiv:hep-ph/0603175`. `doi:10.1088/1126-6708/2006/05/026`.

[50] M. Bähr, S. Gieseke, M. A. Gigg et al., “Herwig++ physics and manual”, *European Physical Journal C* **58** (December, 2008) 639–707, `arXiv:0803.0883`. `doi:10.1140/epjc/s10052-008-0798-9`.

[51] M. L. Mangano, F. Piccinini, A. D. Polosa et al., “ALPGEN, a generator for hard multiparton processes in hadronic collisions”, *Journal of High Energy Physics* **2003** (2003), no. 07, 001. `doi:10.1088/1126-6708/2003/07/001`.

[52] J. Alwall, P. Demin, S. de Visscher et al., “MadGraph/MadEvent v4: the new web generation”, *Journal of High Energy Physics* **2007** (2007), no. 09, 028. `doi:10.1088/1126-6708/2007/09/028`.

[53] M. Wobisch, D. Britzger, T. Kluge et al., “Theory-Data Comparisons for Jet Measurements in Hadron-Induced Processes”, *ArXiv e-prints* (September, 2011) `arXiv:1109.1310`.

[54] D. Britzger, T. Kluge, K. Rabbertz et al., “fastNLO documentation”, *Website* (`http://fastnlo.hepforge.org/docs/`, June 2014).

[55] CMS collaboration, “Measurement of the underlying event activity at the LHC with $\sqrt{s} = 7\,\text{TeV}$ and comparison with $\sqrt{s} = 0.9\,\text{TeV}$”, *Journal of High Energy Physics* **2011** (2011), no. 9,. `doi:10.1007/JHEP09(2011)109`.

[56] W. Bernreuther, “Top-quark physics at the LHC”, *Journal of Physics G: Nuclear and Particle Physics* **35** (2008), no. 8, 083001. `doi:10.1088/0954-3899/35/8/083001`.

[57] J. R. Incandela, A. Quadt, W. Wagner et al., “Status and prospects of top-quark physics”, *Progress in Particle and Nuclear Physics* **63** (2009), no. 2, 239 – 292. `doi:10.1016/j.ppnp.2009.08.001`.

[58] F. P. Schilling, “Top quark physics at the LHC: A review of the first two years”, *International Journal of Modern Physics A* **27** (2012), no. 17, 1230016. `doi:10.1142/S0217751X12300165`.

[59] M. Kobayashi and T. Maskawa, “CP-Violation in the Renormalizable Theory of Weak Interaction”, *Progress of Theoretical Physics* **49** (February, 1973) 652–657. `doi:10.1143/PTP.49.652`.

[60] S. W. Herb, D. C. Hom, L. M. Lederman et al., “Observation of a Dimuon Resonance at 9.5 GeV in 400-GeV Proton-Nucleus Collisions”, *Phys. Rev. Lett.* **39** (Aug, 1977) 252–255. `doi:10.1103/PhysRevLett.39.252`.

[61] C. Quigg, “Top-ology”, *Physics Today* **50** (May, 1997) 20–26, `arXiv:hep-ph/9704332`. `doi:10.1063/1.881890`.

[62] CDF Collaboration Collaboration, “Observation of Top Quark Production in $p\bar{p}$ Collisions with the Collider Detector at Fermilab”, *Phys. Rev. Lett.* **74** (Apr, 1995) 2626–2631. `doi:10.1103/PhysRevLett.74.2626`.

[63] D0 Collaboration Collaboration, “Observation of the Top Quark”, *Phys. Rev. Lett.* **74** (Apr, 1995) 2632–2637. `doi:10.1103/PhysRevLett.74.2632`.

[64] T. Han, “The ”top” priority at the LHC”, *International Journal of Modern Physics A* **23** (2008), no. 25, 4107–4124. `doi:10.1142/S0217751X08042705`.

[65] M. Czakon, P. Fiedler, and A. Mitov, “Total Top-Quark Pair-Production Cross Section at Hadron Colliders Through $\mathcal{O}(\alpha_S^4)$”, *Phys. Rev. Lett.* **110** (Jun, 2013) 252004. `doi:10.1103/PhysRevLett.110.252004`.

[66] CMS Collaboration, “Top Quark Physics Summary Figures”, *CMS-TWiki* (`https://twiki.cern.ch/twiki/bin/view/CMSPublic/PhysicsResultsTOPSummaryPlots`, July 2014).

[67] D0 collaboration, “Useful Diagrams of Top Signals and Background”, *Website* (`http://www-d0.fnal.gov/Run2Physics/top/top_public_web_pages/top_feynman_diagrams.html`, July 2014).

[68] Tevatron Electroweak Working Group, CDF, and D0 Collaborations,

"Combination of CDF and DO results on the mass of the top quark using up to 8.7 fb^{-1} at the Tevatron", *ArXiv e-prints* (May, 2013) `arXiv:1305.3929`.

[69] The CMS Collaboration, "Combination of ATLAS and CMS results on the mass of the top quark using up to 4.9 fb^{-1} of data", *CMS-PAS-TOP-13-005* (2013).

[70] The ATLAS, CDF, CMS, and D0 Collaborations, "First combination of Tevatron and LHC measurements of the top-quark mass", *ArXiv e-prints* (March, 2014) `arXiv:1403.4427`.

[71] CMS Collaboration, "Measurement of the top mass in the fully hadronic channel at 8 TeV ", *CMS-PAS-TOP-14-002* (2014).

[72] D0 Collaboration, "Precision Measurement of the Top Quark Mass in $Lepton + Jets$ Final States", *Phys. Rev. Lett.* **113** (Jul, 2014) 032002. `doi:10.1103/PhysRevLett.113.032002`.

[73] CMS collaboration, "Determination of the top-quark pole mass and strong coupling constant from the $\mathrm{t\bar{t}}$ production cross section in pp collisions at $\sqrt{s} = 7$ TeV", *Physics Letters B* **728** (2014), no. 0, 496 – 517. `doi:10.1016/j.physletb.2013.12.009`.

[74] Baak, M. and Goebel, M. and Haller, J. and Hoecker, A. and Kennedy, D. and Kogler, R. and Mönig, K. and Schott, M. and Stelzer, J., "Results for the Global Electroweak Standard Model Fit", *Website* (`http://project-gfitter.web.cern.ch/project-gfitter/Standard_Model`, July 2014, September 2013 results).

[75] CMS Collaboration, "CMS Beyond-two-generations (B2G) Public Physics Results", *CMS-TWiki* (`https://twiki.cern.ch/twiki/bin/view/CMSPublic/PhysicsResultsB2G`, July 2014).

[76] CMS Collaboration, "CMS Exotica Public Physics Results", *CMS-TWiki* (`https://twiki.cern.ch/twiki/bin/view/CMSPublic/PhysicsResultsEXO`, July 2014).

[77] ATLAS Collaboration, "Exotics Public Results", *ATLAS-TWiki* (`https://twiki.cern.ch/twiki/bin/view/AtlasPublic/ExoticsPublicResults`, July 2014).

[78] E. Bruning et al., "LHC design report. Vol. I: The LHC main ring",. CERN-2004-003-V-1.

[79] L. Evans and P. Bryant, "LHC Machine", *Journal of Instrumentation* **3** (2008), no. 08, S08001.

[80] ATLAS Collaboration, "ATLAS detector and physics performance : Technical Design Report, 1", *ATLAS-TDR-014; CERN-LHCC-99-014*

(`http://cdsweb.cern.ch/record/391176`, 1999) 460.

[81] The ATLAS Collaboration, "The ATLAS Experiment at the CERN Large Hadron Collider", *Journal of Instrumentation* **3** (2008), no. 08, S08003. `doi:10.1088/1748-0221/3/08/S08003`.

[82] LHCb, "Technical Design Reports", *Website* (`http://lhcb.web.cern.ch/lhcb/TDR/TDR.htm`, 2010).

[83] The LHCb Collaboration, "The LHCb Detector at the LHC", *Journal of Instrumentation* **3** (2008), no. 08, S08005. `doi:10.1088/1748-0221/3/08/S08005`.

[84] P. Cortese, C. W. Fabjan, L. Riccati et al., "ALICE physics performance: Technical Design Report",.

[85] The ALICE Collaboration, "The ALICE experiment at the CERN LHC", *Journal of Instrumentation* **3** (2008), no. 08, S08002. `doi:10.1088/1748-0221/3/08/S08002`.

[86] R. Alemany-Fernandez, E. Bravin, L. Drosdal et al., "Operation and Configuration of the LHC in Run 1", *CERN-ACC-NOTE-2013-0041* (Nov, 2013).

[87] C. Lefvre, "The CERN accelerator complex. Complexe des acclrateurs du CERN", *CDS* (`http://cdsweb.cern.ch/record/1260465`, 2008).

[88] LEP EWWG, "The LEP Electroweak Working Group", *Website* (`http://lepewwg.web.cern.ch/LEPEWWG/`, March 2014).

[89] The ALEPH Collaboration, The DELPHI Collaboration, The L3 Collaboration et al., "Precision electroweak measurements on the Z resonance", *Phys. Rep.* **427** (May, 2006) 257–454, `arXiv:arXiv:hep-ex/0509008`. `doi:10.1016/j.physrep.2005.12.006`.

[90] CMS Collaboration, "Public CMS Luminosity Information", *CMS-TWiki* (`https://twiki.cern.ch/twiki/bin/view/CMSPublic/LumiPublicResults`, 2013).

[91] T. Bär, "Very Fast Losses of the Circulating LHC Beam, their Mitigation and Machine Protection", *PhD-thesis at University of Hamburg* **CERN-THESIS-2013-233** (2013).

[92] G. Iadarola, G. Arduini, V. Baglin et al., "Electron cloud and scrubbing studies for the LHC", *IPAC2013: Proceedings of the 4th International Particle Accelerator Conference* **CERN-ACC-2013-0054** (2013).

[93] D. Green, "At the Leading Edge: The ATLAS and CMS LHC Experiments". World Scientific, 2010.

[94] CMS Collaboration, "CMS 3-D image for inclusion in presentations - white

background", *CMS Document 2716-v3* (`https://cms-docdb.cern.ch/cgi-bin/DocDB/ShowDocument?docid=2716`, 2010).

[95] CMS Collaboration, "The CMS experiment at the CERN LHC", *JINST* **3** (2008) S08004. `doi:10.1088/1748-0221/3/08/S08004`.

[96] CMS Collaboration, "CMS Physics Technical Design Report Volume I: Detector Performance and Software", *CERN-LHCC-2006-001; CMS-TDR-008-1* (2006).

[97] CMS Collaboration, "CMS technical design report, volume II: Physics performance", *J. Phys.* **G34** (2007) 995–1579. `doi:10.1088/0954-3899/34/6/S01`.

[98] A. Dominguez, D. Abbaneo, K. Arndt et al., "CMS Technical Design Report for the Pixel Detector Upgrade", Technical Report CERN-LHCC-2012-016. CMS-TDR-11, CERN, Geneva, Sep, 2012.

[99] CMS Collaboration, "Tracking and Primary Vertex Results in First 7 TeV Collisions", *CMS-PAS-TRK-10-005* (2010).

[100] CMS Collaboration, "Energy calibration and resolution of the CMS electromagnetic calorimeter in pp collisions at $\sqrt{s} = 7\,\mathrm{TeV}$", *Journal of Instrumentation* **8** (2013), no. 09, P09009. `doi:10.1088/1748-0221/8/09/P09009`.

[101] The CMS-HCAL Collaboration, "Design, performance, and calibration of CMS hadron-barrel calorimeter wedges", *The European Physical Journal C* **55** (2008), no. 1, 159–171. `doi:10.1140/epjc/s10052-008-0573-y`.

[102] The CMS-HCAL Collaboration, "Design, performance, and calibration of the CMS hadron-outer calorimeter", *The European Physical Journal C* **57** (2008), no. 3, 653–663. `doi:10.1140/epjc/s10052-008-0756-6`.

[103] CMS Collaboration, A. Lobanov, "The CMS Outer HCAL SiPM Upgrade", Technical Report CMS-CR-2014-073, CERN, Geneva, May, 2014.

[104] The CMS-HCAL Collaboration, "Design, performance, and calibration of CMS forward calorimeter wedges", *The European Physical Journal C* **53** (2008), no. 1, 139–166. `doi:10.1140/epjc/s10052-007-0459-4`.

[105] The CMS-HCAL Collaboration, The CMS-HCAL Collaboration, "Design, Performance, and Calibration of CMS Hadron-Barrel Calorimeter Wedges", Technical Report CMS-NOTE-2006-138, CERN, Geneva, May, 2007.

[106] CMS Collaboration, "CMS Technical Design Report for the Phase 1 Upgrade of the Hadron Calorimeter", *CMS-TDR-010* (2012).

[107] The CMS collaboration, "Performance of CMS muon reconstruction in pp collision events at $\sqrt{s} = 7\,\mathrm{TeV}$", *Journal of Instrumentation* **7** (2012), no. 10, P10002.

`doi:10.1088/1748-0221/7/10/P10002`.

[108] CMS Collaboration, "Data Parking and Data Scouting at the CMS Experiment", *CMS-DP-2012-022* (2012).

[109] CMS Collaboration, "CMS The TriDAS Project: Technical Design Report, Volume 2: Data Acquisition and High-Level Trigger. CMS trigger and data-acquisition project", *CERN-LHCC-2002-026; CMS-TDR-6* (2002).

[110] T. Virdee, A. Petrilli, and A. Ball, "CMS High Level Trigger", Technical Report LHCC-G-134. CERN-LHCC-2007-021, CERN, Geneva, Jun, 2007.

[111] CMS Collaboration, "Tracking and Vertexing Results from First Collisions", Technical Report CMS-PAS-TRK-10-001, CERN, Geneva, 2010.

[112] The CMS collaboration, "CMS tracking performance results from early LHC operation", *The European Physical Journal C* **70** (2010), no. 4, 1165–1192. `doi:10.1140/epjc/s10052-010-1491-3`.

[113] CMS Collaboration, "Description and performance of track and primary-vertex reconstruction with the CMS tracker", *ArXiv e-prints* (May, 2014) `arXiv:1405.6569`.

[114] CMS Collaboration, "Slice through the detector with particle trajectories", *CMS Document Database* **5697-v2** (2011).

[115] CMS Collaboration, "Particle-Flow Event Reconstruction in CMS and Performance for Jets, Taus, and MET", *CMS PAS PFT-09/001* (2009).

[116] CMS Collaboration, "Commissioning of the Particle-Flow reconstruction in Minimum-Bias and Jet Events from pp Collisions at 7 TeV", *CMS PAS PFT-10/002* (2010).

[117] CMS Collaboration, "Study of tau reconstruction algorithms using pp collisions data collected at $\sqrt{s} = 7$ TeV", *CMS PAS PFT-10/004* (2010).

[118] Gavin P. Salam, "Towards jetography", *Eur. Phys. J. C* **67** (2010), no. 3-4, 637–686. `doi:10.1140/epjc/s10052-010-1314-6`.

[119] M. Cacciari, G. P. Salam, and G. Soyez, "FastJet user manual. (for version 3.0.2)", *European Physical Journal C* **72** (March, 2012) 1896, `arXiv:1111.6097`. `doi:10.1140/epjc/s10052-012-1896-2`.

[120] CMS Collaboration, "Search for Dijet Resonances in the Dijet Mass Distribution in pp Collisions at $\sqrt{s} = 7$ TeV", Technical Report CMS-PAS-EXO-10-001, CERN, 2010. Geneva, 2010.

[121] G. P. Salam and G. Soyez, "A practical seedless infrared-safe cone jet algorithm", *Journal of High Energy Physics* **5** (May, 2007) 86–+, `arXiv:0704.0292`. `doi:10.1088/1126-6708/2007/05/086`.

[122] M. Cacciari, G. P. Salam, and G. Soyez, “The anti-k_t jet clustering algorithm”, *Journal of High Energy Physics* (2008), no. 04, 063. `doi:10.1088/1126-6708/2008/04/063`.

[123] Matthias Schröder, “Private communication”,.

[124] M. Schröder, “Quality of Jet Measurements and Impact on a Search for New Physics at CMS”, *PhD-thesis at University of Hamburg* **CERN-THESIS-2012-176; CMS-TS-2012-040** (2012).

[125] The CMS Collaboration, “Performance of b tagging at $\sqrt{s} = 8$ TeV in multijet, $\mathrm{t\bar{t}}$ and boosted topology events”, Technical Report CMS-PAS-BTV-13-001, CERN, Geneva, 2013.

[126] The CMS collaboration, “Identification of b-quark jets with the CMS experiment”, *Journal of Instrumentation* **8** (2013), no. 04, P04013. `doi:10.1088/1748-0221/8/04/P04013`.

[127] OPAL Collaboration, “A model independent measurement of quark and gluon jet properties and differences”, *Zeitschrift für Physik C Particles and Fields* **68** (1995) 179–201. `doi:10.1007/BF01566667`.

[128] DELPHI Collaboration, “Investigation of the splitting of quark and gluon jets”, *The European Physical Journal C - Particles and Fields* **4** (1998) 1–17. `doi:10.1007/s100529800885`.

[129] CMS Collaboration, “Jet Transverse Structure and Momentum Distribution in pp Collisions at 7 TeV”, *CMS-PAS-QCD-10-014* (2010).

[130] G. Alexander, J. Allison, N. Altekamp et al., “A comparison of b and uds quark jets to gluon jets”, *Zeitschrift für Physik C Particles and Fields* **69** (1995) 543–560. `doi:10.1007/BF02907439`.

[131] CMS Collaboration, “Performance of quark/gluon discrimination in 8 TeV pp data”, Technical Report CMS-PAS-JME-13-002, CERN, Geneva, 2013.

[132] CMS Collaboration, “Pileup Jet Identification”, Technical Report CMS-PAS-JME-13-005, CERN, Geneva, 2013.

[133] CMS Collaboration, “Determination of jet energy calibration and transverse momentum resolution in CMS”, *Journal of Instrumentation* **6** (November, 2011) 11002, `arXiv:1107.4277`. `doi:10.1088/1748-0221/6/11/P11002`.

[134] CMS Collaboration, “Jet Energy Scale performance in 2011”, *CMS-DP-2012-006* (2012).

[135] CMS Collaboration, “Jet Energy Calibration in the 8 TeV *pp* data”, *CMS PAS JME-13/004* **In preparation** (2014).

[136] CMS Collaboration, “8 TeV Jet Energy Corrections and Uncertainties based on

$19.8\mathrm{fb}^{-1}$ of data in CMS", *CMS-DP-2013-033* (2013).

[137] CMS Collaboration, "Status of the 8 TeV Jet Energy Corrections and Uncertainties based on $11\mathrm{fb}^{-1}$ of data in CMS", *CMS-DP-2013-011* (2013).

[138] CMS Collaboration, "Jet Energy Corrections and Uncertainties. Detector Performance Plots for 2012.", *CMS-DP-2012-012* (2012).

[139] D. Bertolini, P. Harris, M. Low et al., "Pileup Per Particle Identification", `arXiv:1407.6013`.

[140] M. Cacciari and G. P. Salam, "Pileup subtraction using jet areas", *Physics Letters B* **659** (January, 2008) 119–126, `arXiv:0707.1378`. `doi:10.1016/j.physletb.2007.09.077`.

[141] S. Agostinelli, J. Allison, K. Amako et al., "G4–a simulation toolkit", *Nuclear Instruments and Methods in Physics Research Section A: Accelerators, Spectrometers, Detectors and Associated Equipment* **506** (2003), no. 3, 250 – 303. `doi:10.1016/S0168-9002(03)01368-8`.

[142] S. Banerjee, "Readiness of CMS Simulation Towards LHC Startup", *J.Phys.Conf.Ser.* **119** (2008) 032006. `doi:10.1088/1742-6596/119/3/032006`.

[143] CMS Collaboration Collaboration, "Validation and tuning of the CMS full simulation", *J.Phys.Conf.Ser.* **331** (2011) 032015. `doi:10.1088/1742-6596/331/3/032015`.

[144] CMS Collaboration, "MET performance in 8 TeV data", *CMS-PAS-JME-12-002* (2013).

[145] The CMS collaboration, "Missing transverse energy performance of the CMS detector", *Journal of Instrumentation* **6** (2011), no. 09, P09001. `doi:10.1088/1748-0221/6/09/P09001`.

[146] K. Kousouris, "Measurement of the Relative Jet Energy Scale in CMS with pp Collisions at 7 TeV", *(internal) CMS AN 2010/139* (2010).

[147] R. Harris and K. Kousouris, "Determination of the Relative Jet Energy Scale at CMS from Dijet Balance", *(internal) CMS AN 2008/031* (2009).

[148] Henning Kirschenmann on behalf of the CMS collaboration, "Determination of the Jet Energy Scale in CMS", *Journal of Physics: Conference Series* **404** (2012), no. 1, 012013. `doi:10.1088/1742-6596/404/1/012013`.

[149] University of Hamburg CMS group, "Kalibri Framework", *CMS-TWiki* (`https://twiki.cern.ch/twiki/bin/view/CMS/HamburgWikiAnalysisCalibration`, `http://wwwiexp.desy.de/groups/cms/kalibri/api/index.html`, 2007-2014).

[150] UA2 Collaboration, "Measurement of production and properties of jets at the CERN $\bar{p}p$ collider", *Zeitschrift für Physik C Particles and Fields* **20** (1983), no. 2,

117–134. `doi:10.1007/BF01573214`.

[151] D0 Collaboration, “Determination of the absolute jet energy scale in the D0 calorimeters”, *Nucl. Inst. Meth. A* **424** (1999) 352–394. `doi:10.1016/S0168-9002(98)01368-0`.

[152] D0 Collaboration, “Jet energy scale determination in the D0 experiment”, *ArXiv e-prints* (December, 2013) `arXiv:1312.6873`.

[153] CDF Collaboration, “Determination of the jet energy scale at the Collider Detector at Fermilab”, *Nucl. Inst. Meth. A* **566** (2006) 375–412. `doi:arXiv:hep-ex/0510047`.

[154] M. A. Voutilainen, “Measurement of the inclusive jet cross section in proton-antiproton collisions at the center-of-mass energy of 1.96 TeV”,.

[155] CDF Collaboration, “Dijet angular distribution in $p\bar{p}$ collisions at $\sqrt{s} = 1.8$ TeV”, *Phys. Rev. Lett.* **69** (Nov, 1992) 2896–2900. `doi:10.1103/PhysRevLett.69.2896`.

[156] CMS Collaboration, “Formulae for PF MET Type-I and Type-II Corrections”, *CMS-TWiki* (`https://twiki.cern.ch/twiki/bin/view/CMS/METType1Type2Formulae`, 01-Dec-2012).

[157] C. Autermann, C. Sander, P. Schleper et al., “Measurement of the Full Jet p_T Response Function in QCD Di-Jet Events”, *(internal) CMS AN 2011/330* (2011).

[158] CMS Collaboration, “Jet Identification”, *CMS-TWiki* (`https://twiki.cern.ch/twiki/bin/view/CMS/JetID`, March 2014).

[159] CMS JEC group, “Possible problems with Flat QCD+PU samples”, *(internal) CMS Hypernews* (`https://hypernews.cern.ch/HyperNews/CMS/get/jes/264.html`, 11-Aug-2011).

[160] CMS Collaboration, “Estimating Systematic Errors Due to Pileup Modeling”, *CMS-TWiki* (`https://twiki.cern.ch/twiki/bin/view/CMS/PileupSystematicErrors`, 2012).

[161] CMS Collaboration, “Jet Energy Resolution Measurement”, *CMS-TWiki* (`https://twiki.cern.ch/twiki/bin/viewauth/CMS/JetResolution`, 2013).

[162] K. Goebel, J. Haller, J. Ott et al., “Jet Transverse Momentum Resolution Measurement using Dijet Events at $\sqrt{s} = 8\,\mathrm{TeV}$”, *(internal) CMS AN 2013/416* (2010).

[163] CMS Collaboration, “2012 ECAL detector performance plots”,.

[164] The ATLAS Collaboration, “Jet energy measurement with the ATLAS detector in

proton-proton collisions at $\sqrt{\mathrm{s}} = 7$ TeV", *The European Physical Journal C* **73** (2013), no. 3, 1–118. `doi:10.1140/epjc/s10052-013-2304-2`.

[165] ATLAS Collaboration Collaboration, The ATLAS Collaboration, "Jet energy scale and its systematic uncertainty in proton-proton collisions at $\sqrt{(s)} = 7\,TeV$ with ATLAS 2011 data", Technical Report ATLAS-CONF-2013-004, CERN, Geneva, Jan, 2013.

[166] CMS Collaboration, "Boosted Top Jet Tagging at CMS", *CMS-PAS-JME-13-007* (2014), no. CMS-PAS-JME-13-007,.

[167] CMS Collaboration, "Identifying Hadronically Decaying Vector Bosons Merged into a Single Jet", *CMS-PAS-JME-13-006* (2013), no. CMS-PAS-JME-13-006,.

[168] CMS Collaboration, "Measurements of differential jet cross sections in proton-proton collisions at s=7 TeV with the CMS detector", *Phys. Rev. D* **87** (Jun, 2013) 112002. `doi:10.1103/PhysRevD.87.112002`.

[169] CMS Collaboration, "Measurement of the double-differential inclusive jet cross section at $\sqrt{s} = 8$ TeV with the CMS detector", *CMS-PAS-SMP-12-012* (2013).

[170] ATLAS collaboration, "Jet energy measurement with the ATLAS detector in proton-proton collisions at $\sqrt{\mathrm{s}} = 7$ TeV", *The European Physical Journal C* **73** (2013), no. 3,. `doi:10.1140/epjc/s10052-013-2304-2`.

[171] C. Doglioni, B. Malaesku, H. Kirschenmann et al., "Report on JES correlations ATLAS and CMS", *Open TOPLHCWG meeting* (`http://indico.cern.ch/event/245769/session/1/contribution/7/material/slides/0.pdf`, 2013).

[172] ATLAS collaboration and CMS collaboration, "Jet energy scale uncertainty correlations between ATLAS and CMS", *(in preparation) CMS-PAS-JME-14-003* (2014).

[173] ATLAS Collaboration, "Jet energy measurement and its systematic uncertainty in proton-proton collisions at $\sqrt{s} = 7$ TeV with the ATLAS detector", *ArXiv e-prints* (May, 2014) `arXiv:1406.0076`.

[174] ATLAS Collaboration, "Approved jet-energy resolution plots 2011", *ATLAS-TWiki* (`https://twiki.cern.ch/twiki/bin/view/AtlasPublic/JetEtmissApproved2013Jer2011`, 2013).

[175] CMS Collaboration, "Measurement of the top-quark mass in all-jets $t\bar{t}$ events in *pp* collisions at $\sqrt{s} = 7$ TeV", *The European Physical Journal C* **74** (2014), no. 4, 1–23. `doi:10.1140/epjc/s10052-014-2758-x`.

[176] T. Aaltonen, A. Buzatu, B. Kilminster et al., "Improved *b*-jet Energy Correction for $H \to b\bar{b}$ Searches at CDF", *ArXiv e-prints* (July, 2011) `arXiv:1107.3026`.

[177] CDF Collaboration Collaboration, "Precision Top-Quark Mass Measurement at CDF", *Phys. Rev. Lett.* **109** (Oct, 2012) 152003.

`doi:10.1103/PhysRevLett.109.152003`.

[178] CMS Collaboration, “Search for the standard model Higgs boson produced in association with a W or a Z boson and decaying to bottom quarks”, *Phys. Rev. D* **89** (Jan, 2014) 012003. `doi:10.1103/PhysRevD.89.012003`.

[179] T. Ravenscroft, “Using a Regression Analysis to Improve the b-Jet Energy Correction In $WH \to l\nu bb$ Searches at ATLAS”, *Institute of Physics 2014 Joint High Energy Particle Physics and Astro Particle Physics Groups Annual Meeting* (`https://indico.cern.ch/event/266149/session/23/contribution/57/material/slides/0.pdf`, 8 April 2014).

[180] Heavy Flavor Averaging Group, Y. Amhis, S. Banerjee et al., “Averages of b-hadron, c-hadron, and tau-lepton properties as of early 2012”, *ArXiv e-prints* (July, 2012) `arXiv:1207.1158`.

[181] A. Heister, S. Schael, R. Barate et al., “Study of the fragmentation of b quarks into B mesons at the Z peak”, *Physics Letters B* **512** (2001), no. 12, 30 – 48. `doi:10.1016/S0370-2693(01)00690-6`.

[182] J. Abdallah, P. Abreu, W. Adam et al., “A study of the b-quark fragmentation function with the DELPHI detector at LEP I and an averaged distribution obtained at the Z Pole”, *The European Physical Journal C* **71** (2011), no. 2, 1–29. `doi:10.1140/epjc/s10052-011-1557-x`.

[183] OPAL Collaboration, “Inclusive analysis of the b quark fragmentation function in Z decays at LEP”, *The European Physical Journal C - Particles and Fields* **29** (2003), no. 4, 463–478. `doi:10.1140/epjc/s2003-01229-x`.

[184] SLD Collaboration, “Measurement of the b-quark fragmentation function in Z^0 decays”, *Phys. Rev. D* **65** (May, 2002) 092006. `doi:10.1103/PhysRevD.65.092006`.

[185] Henning Kirschenmann, Peter Schleper, Markus Seidel et al., “Measurement of the top-quark mass in the lepton+jets channel”, *(internal) CMS AN 2013/383* (2013).

[186] The CMS Collaboration, “Measurement of differential top-quark-pair production cross sections in pp collisions at $\sqrt{s} = 7\,\text{TeV}$”, *The European Physical Journal C* **73** (2013), no. 3, 1–29. `doi:10.1140/epjc/s10052-013-2339-4`.

[187] CMS Collaboration, “Measurement of differential top-quark pair production cross sections in the lepton+jets channel in pp collisions at 8 TeV”, *CMS-PAS-TOP-12-027* (2013).

[188] The ATLAS Collaboration, “Measurement of the Top Quark Mass from $\sqrt{s} = 7$ TeV ATLAS Data using a 3-dimensional Template Fit”, *ATLAS-CONF-2013-046* (May, 2013).

[189] Markus Seidel, “Private communication”,.

[190] A. Hoecker, P. Speckmayer, J. Stelzer et al., "TMVA - Toolkit for Multivariate Data Analysis", *ArXiv e-prints* (March, 2007) `arXiv:0703039`.

[191] J. H. Friedman, "Greedy Function Approximation: A Gradient Boosting Machine", *Annals of Statistics* **29** (2001) 1189–1232. `doi:10.1214/aos/1013203451`.

[192] L. Breiman, "Classification and regression trees". The Wadsworth and Brooks-Cole statistics-probability series. Chapman & Hall, 1984.

[193] J. L. Bendavid, "Evidence for a narrow Higgs-like diphoton resonance with a mass of 125 GeV in pp collisions at $\sqrt{s} = 7$ - 8 TeV", *PhD-thesis at Massachusetts Institute of Technology. Department of Physics.* (`http://hdl.handle.net/1721.1/79539`, 2013).

[194] F. Beaudette, M. Dalchenko, C. Charlot et al., "Electron momentum determination using boosted regression trees", *(internal) CMS AN 2013/209* (2013).

[195] CDF and D0 Collaborations Collaboration, "Combination of the top-quark mass measurements from the Tevatron collider", *Phys. Rev. D* **86** (Nov, 2012) 092003. `doi:10.1103/PhysRevD.86.092003`.

[196] S. Alioli, P. Nason, C. Oleari et al., "A general framework for implementing NLO calculations in shower Monte Carlo programs: the POWHEG BOX", *Journal of High Energy Physics* **2010** (2010), no. 6, 1–58. `doi:10.1007/JHEP06(2010)043`.

[197] The DELPHI Collaboration, "Measurement of the W-pair cross-section and of the W mass in e^+e^- interactions at 172 GeV", *The European Physical Journal C - Particles and Fields* **2** (1998), no. 4, 581–595. `doi:10.1007/s100529800857`.

[198] D0 Collaboration, "Measurement of the top quark mass in the lepton+jets channel using the ideogram method", *Phys. Rev. D* **75** (May, 2007) 092001. `doi:10.1103/PhysRevD.75.092001`.

Danksagung

Ich möchte mich gerne bei all jenen bedanken, die direkt oder indirekt zum Gelingen dieser Arbeit beigetragen haben. Einige, längst nicht alle, möchte ich hier besonders hervorheben.

Einen herzlichen Dank möchte ich an Prof. Dr. Peter Schleper aussprechen für die Möglichkeit, in seiner Arbeitsgruppe meine Doktorarbeit anfertigen zu dürfen, und für die hilfreichen Kommentare während der Diplomanden- und Doktorandenzeit. Ich danke ihm wie auch Dr. Isabell-Alissandra Melzer-Pellmann für die Begutachtung der Dissertation. Prof. Dr. Erika Garutti und Jun.-Prof. Dr. Christian Sander haben freundlicherweise die Begutachtung der Disputation übernommen.

Ein besonders großer Dank gilt meinem Betreuer Dr. Hartmut Stadie. Er war stets für mich ansprechbar, freundlich und ausgesprochen hilfsbereit und die Diskussionen mit ihm, mal ganz nah und mal gar nicht nah an der Physik, waren immer erhellend und erfrischend.

Beim Zusammenschreiben der Arbeit habe ich von vielen Seiten hilfreiche Kommentare erhalten. Hervorheben möchte ich Prof. Dr. Robert Klanner, der sehr kurzfristig und kurz vor der Abgabe einen Großteil der Arbeit gelesen und kommentiert hat. Einen Großteil der Arbeit oder auch kürzere Abschnitte kommentiert haben außerdem Peter, Hartmut, Matthias, Denis, Markus und Holger. Vielen Dank dafür!

Ich habe mich in unserer Arbeitsgruppe sehr wohl gefühlt und die Zeit genossen. Neben dem Alltag mit Kantine, Flurgesprächen und Co. haben für mich auch die Dinge außer der Reihe wie Fußball, Spieleabende und Squash die gute Atmosphäre ausgemacht.

Ohne die Beiträge anderer ist so eine Arbeit gar nicht möglich. Ich habe viel profitiert von Vorarbeiten innerhalb der Gruppe, besonders durch Matthias und Hartmut, aber zum Beispiel auch von den Vorarbeiten in der JEC-Gruppe, besonders durch Mikko und Kostas. Meine spätere Mitarbeit an den Topmassenmessungen wurde erst durch die Vorarbeit von Markus, Hartmut und Eike möglich. Vielen Dank dafür!

Auch die Unterstützung durch Freunde und Familie hätte ich nicht missen wollen. Für den großartigen Rückhalt und die Geborgenheit gilt mein Dank meiner Frau Stefanie, meinem Sohn Lars, meinen Eltern, Traute und Gerd, meinen Geschwistern, Birgit, Holger und Harald, ihren Familien, meiner ganzen lieben Schwiegerfamilie und allen Freunden. Die Wochen vor und nach der Geburt waren unvergesslich und ich freue mich sehr, dass wir die Zeit als frischgebackene Familie - trotz beinahe gleichzeitiger Abgabe - intensiv erleben konnten. Vielen Dank dafür!